Nonequilibrium Quantum-Field Dynamics and Off-Shell Transport

Inaugural-Dissertation
zur
Erlangung des Doktorgrades
der Naturwissenschaftlichen Fakultät
der Justus-Liebig-Universität Gießen
Fachbereich 7 – Mathematik, Physik, Geographie

vorgelegt von
Sascha Juchem
aus Ochtendung

Gießen, 2003

D 26
Dekan: Prof. Dr. Volker Metag
I. Berichterstatter: Prof. Dr. Dr. Wolfgang Cassing
II. Berichterstatter: Prof. Dr. Werner Scheid
Tag der mündlichen Prüfung: 16. 12. 2003

Contents

Chapter 1

Introduction

Nonequilibrium many-body theory or quantum-field theory has become a major topic of research for transport processes in nuclear physics, in cosmological particle physics as well as condensed matter physics. The multidisciplinary aspect arises due to a common interest in the various relaxation phenomena of quantum dissipative systems. Important questions in high-energy nuclear or particle physics at the highest energy densities are: i) how do nonequilibrium systems in extreme environments evolve, ii) how do they eventually thermalize, iii) how do phase transitions occur in real-time with possibly nonequilibrium remnants, and iv) how do such systems evolve for unprecedented short and nonadiabatic timescales?

The very early history of the universe provides scenarios, where nonequilibrium effects might have played an important role, e.g. in the (post-)inflationary epoque or in the evolution of baryogenesis. In modern nuclear physics the understanding of the dynamics of heavy-ion collisions at various bombarding energies has always been a major motivation for research on nonequilibrium quantum many-body physics and relativistic quantum-field theories. The initial state of such collisions resembles an extreme nonequilibrium situation, whereas the final state might even exhibit a certain degree of thermalization. Indeed, at the presently highest energy heavy-ion collider experiments at the Relativistic Heavy-Ion Collider (RHIC), where one expects to create experimentally a transient deconfined state of matter denoted as quark-gluon plasma (QGP) there are experimental indications – like the build-up of collective flow – for an early thermalization accompanied with the generation of a very large pressure. Furthermore, the phenomenon of disoriented chiral condensates (DCC) during the chiral phase transition (from deconfined to ordinary hadronic matter) has lead to a considerable progress for our understanding of nonequilibrium phase transitions at short timescales over the last decade. All these examples demonstrate that one needs an *ab initio* description of the dynamics of out-of-equilibrium quantum-field theory.

An appropriate basis for the study of nonequilibrium quantum many-body physics is provided by the closed-time-path (CTP) functional integral ('Schwinger-Keldysh' [1, 2, 3, 4, 5]) formalism. The essential merit of this real-time Green function technique lies in its applicability to all kind of quantum nonequilibrium phenomena. Indeed, it has been used in various fields of nonrelativistic quantum nonequilibrium physics, such as condensed matter, plasma and nuclear physics, and in the context of relativistic quantum-field theories as well. Within this framework one can derive and find valid approximations – depending, of course, on the problem under consideration – by preserving overall consistency relations. In this context the most prominent role is played by the resulting causal Dyson-Schwinger equations of motion for the one-particle Green functions, i.e. the Kadanoff-Baym (KB) equations [6, 7, 8, 9, 10]. These equations might be considered as an ensemble average over the initial density matrix characterizing the preparation of the initial state of the system, which may be far out of equilibrium. The direct relation to the 'influence functional formalism' allows to address the stochastic aspects of the KB equations [11]. The presence of (quantum) noise and dissipation – related by a fluctuation-dissipation theorem – guarantees that the modes or particles of an open system become thermally populated on average in the long-time limit if coupled to an environmental heat bath.

A further important aspect of this formalism lies in the fact, that it serves as a basis for the derivation of generalized transport equations. Those kinetic equations – as obtained by means of appropriate Kadanoff-Baym equations within suitable approximations – play the central role in more or less all practical simulations of nonrelativistic and relativistic many-body nonequilibrium systems. Hence, a major impetus has been to derive semiclassical Boltzmann-like transport equations within the standard quasiparticle approximation [12, 13, 14]. Additionally, off-shell extensions by means of a gradient expansion in the space-time inhomogeneities – as already introduced by Kadanoff and Baym [6] – have been formulated for several systems: for a relativistic electron-photon plasma [15], for transport of electrons in a metal with external electrical field [16] and in semiconductors [10, 17], for transport of nucleons in heavy-ion reactions at intermediate energies [18], for transport of particles in ϕ^4-theory [9, 19] as well as for transport of partons in high-energy heavy-ion reactions [20, 21, 22, 23]. Within all these derivations the various forms assumed for the self-energy have to fulfill consistency relations in order to preserve symmetries of the fundamental Lagrangian [24, 25, 6].

In the nuclear physics context the quantum dynamics of the spectral function is a lively discussed issue in the microscopic modeling of hadronic resonances with a broad mass distribution. This is of particular relevance for simulations of heavy-ion reactions where e.g. the Δ-resonance or the ρ-meson already show a large decay width in vacuum. Especially the ρ vector meson is a promising hadronic particle for showing possible in-medium modifications in hot and compressed nuclear matter (see e.g. [26, 27]), since the leptonic decay products are of only weakly interacting electromagnetic nature. Indeed, the CERES experiment [28] at the Super-Proton-Synchrotron (SPS) at CERN has found a significant enhancement of lepton pairs for invariant masses below the pole of the ρ-meson, giving evidence for such modifications. Hence, a consistent formulation for the transport of extremely short-lived particles beyond the standard quasiparticle approximation is needed. On the one side, there exist purely formal developments starting from a first order gradient expansion of the underlying KB equations [29, 30, 31, 32], while on the other side already first practical realizations for various questions have emerged [33, 34, 35, 36, 37]. The general idea is to obtain a description for the propagation of the off-shell mass. However, a fully *ab initio* investigation without any further approximations, does not exist so far.

It has been found early in the investigations of heavy-ion collisions at low energies that collisions play a central role for the equilibration processes. Full time-dependent Hartree or Hartree-Fock descriptions [38] were insufficient to describe the reactions with increasing collision energy. In these cases additional Boltzmann-like collision terms had to be incorporated in order to provide a more adequate description of the collision processes. The same situation has been encountered for nonequilibrium quantum-field theories where typically the nonperturbative description of (second-order) phase transitions has been in the foreground by means of mean-field (Hartree) descriptions [39, 40, 41, 42, 43, 44]. Applications include the evolution of disoriented chiral condensates or the decay of the (oscillating) inflaton in the early reheating era. 'Effective' mean-field dissipation (and decoherence) – solving the so-called 'backreaction' problem – was incorporated by particle production through order parameters explicitly varying in time. However, it had been soon realized that such a dissipation mechanism, i.e. transferring collective energy from the time-dependent order parameter to particle degrees of freedom, can not lead to true dissipation and thermalization.

The incorporation of true collisions then has been formulated also for the various quantum-field theories [9, 45, 46, 47, 48]. In this respect a quite elegant way is provided by the two-particle-irreducible (2PI) effective action [9, 49, 50]. Including the background field and the correlation function on the same footing, collisions can be naturally included by taking into account contributions beyond the leading mean-field order of the generating functional. Due to the construction in terms of full Green functions this method ensures the validity of all essential conservation laws. The resulting equations of motion always do resemble the KB equations; in their general form (beyond the mean-field or Hartree(-Fock) approximation) they do break time invariance and thus lead to irreversibility. This macroscopic irreversibility arises from the truncations of the full theory to obtain the self-energy operators in a specific limit. As an example we mention the truncation of the (exact) Martin-Schwinger hierarchy in the derivation of the collisional operator in Ref. [18] or the truncation of the (exact) BBGKY hierarchy in terms of n-point functions [51, 52, 53, 54, 55, 56, 57, 58].

Although the Kadanoff-Baym equation has been of wide interest (numerical) studies of its full solution are rather scarce. In the nuclear and particle physics context pioneering work has been performed by Danielewicz [59] investigating the initial distribution of two occupied Fermi spheres in momentum space for spatially homogeneous systems in order to model the initial condition of a heavy-ion collision in the nonrelativistic domain. In comparison to a standard on-shell semiclassical Boltzmann equation the full quantum Kadanoff-Baym solution showed quantitative differences, i.e. a larger collective relaxation time for complete equilibration of the momentum distribution. This 'slowing down' of the quantum dynamics was attributed to quantum interference and off-shell effects. Similar quantum modifications in the equilibration and momentum relaxation have been found in [12] and for a relativistic situation in Ref. [60]. Particular emphasis was put in Refs. [60, 61] on non-local aspects (in time) of the collision process and thus the potential significance of memory effects on the nuclear dynamics. In the following, full and more detailed solutions of nonrelativistic KB equations have been performed by Köhler [62, 63] with special emphasis on the build-up of initial many-body correlations on short time scales. Moreover, the role of memory effects has been clearly shown experimentally by femtosecond laser spectroscopy in semiconductors [64] in the relaxation of excitons. Solutions of quantum transport equations for semiconductors [10, 65] – to explore relaxation phenomena on short time and distance scales – have become also a very active field of research [66].

During the last years the description of nonequilibrium real-time dynamics within the 2PI effective action formalism has regained strong interest. First numerical studies in this context for the time evolution of relativistic quantum-fields have been carried out for ϕ^4-theory in 1+1 dimensions within the three-loop approximation of the effective action [67, 68]. The method has been applied also to the homogeneous $O(N)$ model performing a systematic expansion in 1/N [69] or within the bare vertex approximation [70]. All these calculations exhibit thermalization since true scattering processes are included, i.e. beyond leading order. Thus the treatment within the 2PI effective action remedies the shortcomings of 1PI effective action approaches, that fail to show thermalization and do not reach the appropriate long-time limit [40, 71]. The investigations have been extended to the symmetry broken phase where the bare vertex approximation resums a larger series than contained in the 2PI-1/N expansion at next-to-leading order [72, 73, 74]. However, a detailed and quantitative interpretation of the time scales found was not given.

While the aforementioned studies restrict to homogeneous systems in space, there is a further branch dealing with general inhomogeneous settings. Especially the dynamical behaviour of relativistic scalar self-interacting field theories in 1+1 space-time dimensions is investigated within the Hartree and classical approximation in the symmetric or broken phase [75, 76, 77]. Since true collisions are absent at the Hartree level no thermalization is observed [75]. Only when additional ensemble averaging is invoked there are hints for quantum equilibration at intermediate times and classical equilibration at large times [76, 77].

As already stressed the present thesis will focus in particular on the full quantum dynamics of the spectral (i.e. 'off-shell') information contained in the nonequilibrium single-particle spectral function. In this respect we will study ab initio nonequilibrium time evolution in case of the scalar ϕ^4-theory in 2+1 space-time dimensions by means of the full Kadanoff-Baym equation. By employing a three-loop approximation for the 2PI effective action mean-field effects and scattering processes – as a necessary ingredient for equilibration – are included self-consistently. We will consider in detail the statistical and spectral aspects – as both contained in the Kadanoff-Baym formulation – of the thermalization process for far-from-equilibrium initial conditions. Here we want to show, how complete thermalization of all single-particle quantum fluctuations will be achieved. Furthermore, we will put special emphasis on the comparison of the full quantum solution to approximate schemes given first of all by the Boltzmann approximation in terms of quasiparticles. Such a comparison with the on-shell Boltzmann limit is – for the first time – performed for relativistic systems. Although the analogy of KB-type equations to a Boltzmann-like process is quite obvious, this relation is far from being trivial. The full quantum formulation contains much more information than a semiclassical (generally) on-shell Boltzmann equation. The dynamics of the spectral (i.e. 'off-shell') information is fully incorporated in the quantum dynamics while it is missing in the Bolzmann limit. A satisfying answer to the question of quantum equilibration can thus only be obtained by a detailed numerical solution of the quantum description itself. This is the basic aim of our present study. Additionally, we will investigate the off-shell extensions incorporated in generalized kinetic equations as obtained from a gradient expansion of the full Kadanoff-Baym equation. Although such generalized transport equations have already been used in the past, a check against the full solution is still lacking.

Before we will describe the structure of this work, we want to shortly motivate why we investigate the scalar ϕ^4-theory for the case of 2+1 space-time dimensions. On the one hand the study of the self-interacting bosonic theory in this dimensionality has a right on its own. On the other hand is contains two essential advantages:

1) It superceeds the rather artificial structure of the ϕ^4-theory in 1+1 dimensions, that has been investigated before. In the latter case on-shell scattering processes are purely (col-)linear and thus do not lead to an equilibration in accordance with an appropriate change of the momentum distribution. Thermalization in this dimensionality is only mediated by off-shell scattering processes. This is of course a rather unusual situation, since it is known from the investigation of heavy-ion collisions by means of quantum kinetic theories, that binary on-shell scattering plays an important role. In the 2+1 dimensional case both, on-shell and off-shell collisions influence the equilibration behaviour. Thus the theory in 2+1 dimensions is a well-suited laboratory in order to investigate the differences between the full Kadanoff-Baym theory and approximate schemes as given by the on-shell Boltzmann limit and by generalized off-shell transport equations.

2) The divergence structure of the ϕ^4-theory in 2+1 dimensions is such that one has full control over the renormalization procedure. As we will see in our investigations, only two self-energies – containing solely vacuum parts of Green functions – diverge in the ultraviolet regime. Thus the renormalization can be performed equivalently to the standard zero temperature vacuum case. This is different in 3+1 dimensions, where complete classes of self-energies are divergent, which incorporate non-vacuum parts of the Green functions as well. Thus actually more involved renormalization schemes should be used analogous to those constructed for self-consistent approximations at finite temperature [78, 79], which actually applies to the equilibrium case, only.

Our work is organized as follows: In Chapter 2 we will present the relevant equations for the nonequilibrium dynamics in case of the ϕ^4-theory. We will briefly derive the Kadanoff-Baym equations within the three-loop approximation of the 2PI effective action. Chapter 3 is devoted to numerical studies on equilibration phenomena within the full Kadanoff-Baym theory by employing different initial configurations. The structure of the quantum evolution is analyzed in detail by considering the statistical as well as the spectral aspects as contained in the full Kadanoff-Baym solution. The different time scales of the thermalization process are identified as given by an initial build-up of correlations, a kinetic equilibration at intermediate times and the approach to chemical equilibrium. Furthermore, it is shown that the solutions of the Kadanoff-Baym equations for $t \to \infty$ yield the proper off-shell thermal state, i.e. the Green functions fulfill the Kubo-Martin-Schwinger (KMS) relation in the long-time limit. The actual numerical algorithm used is described in Appendix A as well as the renormalization by counterterms in Appendix B in order to achieve ultraviolet convergent results. In Chapter 4 we present an efficient method for the calculation of self-consistent spectral functions at finite temperature in terms of real-time Green functions. Besides the issues of analyticity and coupling dependence of the spectral functions we will briefly present results for massless Bose fields in thermal equilibrium. The next parts of the work are dealing with approximate dynamical schemes and their relation to the full Kadanoff-Baym theory. Chapter 5 concentrates in particular on the well-known Boltzmann limit in terms of on-shell quasiparticles. The solutions of this approximation as well as a simple relaxation estimate will be confronted with the numerical results from the Kadanoff-Baym equations. The extension of the semiclassical kinetic theory to the off-shell case is presented in Chapter 6, where the generalized transport equations are derived within a first order gradient expansion from the full Kadanoff-Baym formulation in two different limits. The numerical studies – with very detailed comparison to the Kadanoff-Baym solution – of these generalized transport equations are contained in Chapter 7. Again we discuss the time evolution for both, the Green functions and the spectral functions as well as the relaxation of the chemical potential. Furthermore, we will shortly explore the validity of the underlying assumptions of the generalized transport schemes. In Chapter 8 we will implement the off-shell dynamics – inherent in the generalized kinetic theories – in a coupled-channel transport approach by means of evolution equations for testparticles. The resulting scheme will be exemplified for numerous model studies and for realistic heavy-ion collisions at intermediate and high energies. We close this work in Chapter 9 with a summary of our results and an outlook on future extensions.

Chapter 2

Nonequilibrium Dynamics for ϕ^4-Quantum-Field Theory

The scalar ϕ^4-theory is an example for a fully relativistic field theory of interacting scalar particles that allows to test theoretical approximations [54, 55, 56, 67, 68]. Its Lagrangian density is given by $(x = (t, \vec{x}))$

$$\mathcal{L}(x) \;=\; \frac{1}{2}\,\partial_\mu\phi(x)\,\partial^\mu\phi(x) \;-\; \frac{1}{2}\,m^2\,\phi^2(x) \;-\; \frac{\lambda}{4!}\,\phi^4(x)\;, \tag{2.1}$$

where m denotes the 'bare' mass and λ is the coupling constant determining the interaction strength of the scalar fields.

2.1 The Kadanoff-Baym Equations

As mentioned in the Introduction, a natural starting point for nonequilibrium quantum theory is provided by the closed-time-path (CTP) method. Here all quantities are given on a special real-time contour with the time argument running from $-\infty$ to $+\infty$ on the chronological branch $(+)$ and returning from $+\infty$ to $-\infty$ on the anti-chronological branch $(-)$ (cf. Fig. 2.1). In cases of systems prepared at time t_0 this value is (instead of $-\infty$) the start and end point of the real-time contour. In particular the path-ordered Green functions are defined as $(x_1 = (t_1, \vec{x}_1),\; x_2 = (t_2, \vec{x}_2))$

$$\begin{aligned} G(x_1, x_2) \;&=\; \langle\, T^p\,\{\, \phi(x_1)\,\phi(x_2)\,\}\,\rangle \qquad\qquad (2.2)\\ &=\; \Theta_p(t_1 - t_2)\;\langle\, \phi(x_1)\,\phi(x_2)\,\rangle \;+\; \Theta_p(t_2 - t_1)\;\langle\, \phi(x_2)\,\phi(x_1)\,\rangle\,, \end{aligned}$$

where the operator T^p orders the field operators according to the position of their arguments on the real-time path as accomplished by the path step-functions Θ_p

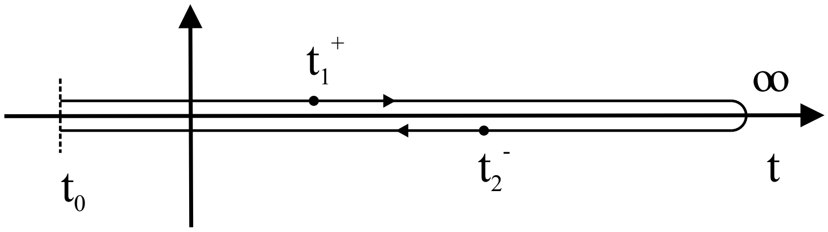

Figure 2.1: Closed real-time contour with upper chronological (+) branch and lower anti-chronological (−) branch. Time coordinates are characterized by their physical value and by the branch they belong to.

$$\Theta_p(t_1 - t_2) \;=\; \begin{cases} 1\,, & \text{if } t_1 \text{ is later on the contour as } t_2\,, \\ 0\,, & \text{if } t_2 \text{ is earlier on the contour as } t_1\,. \end{cases} \tag{2.3}$$

The expectation value in (2.2) is taken with respect to some given density matrix ρ_0, which is constant in time, while the operators in the Heisenberg picture contain the whole information of the time dependence of the nonequilibrium system.

Self-consistent equations of motion for these Green functions can be obtained with help of the two-particle-irreducible[1] (2PI) effective action $\Gamma[G]$. This functional is given by the double Legendre transform of the generating functional of connected Green functions W with respect to the local and bilinear external sources. In the case of a vanishing vacuum expectation value of the scalar field $\langle 0|\,\phi(x)\,|0\rangle \;=\; 0$ the effective action is a functional solely of the two-point Green function G and given by [24]

$$\Gamma[G] \;=\; \Gamma^0 \;+\; \frac{i}{2}\;[\,\ln(\,1 - \odot_p\, G_0 \odot_p \Sigma\,) \;+\; \odot_p\, G \odot_p \Sigma\,] \;+\; \Phi[G]\,. \tag{2.4}$$

In (2.4) Γ^0 depends only on free Green functions G_0 and is treated as a constant with respect to variation, while the symbols $\odot_p$ represent convolution integrals over space and the closed-time-path with the contour specified above (cf. Fig. 2.1). The functional Φ is the sum of all closed 2PI diagrams built up by full propagators G (and bare vertices) [24, 80]. It determines the resummed self-energy by functional variation as

$$\Sigma(x_1,x_2) \;=\; 2i\,\frac{\delta\Phi}{\delta G(x_2,x_1)}\,. \tag{2.5}$$

In general, the self-energy Σ contains a singular contribution Σ^δ on the contour and a non-local part, which can be expressed – analogously to the Green functions (2.2) – by a sum over Θ_p-functions

---

[1] n-particle-irreducible diagrams remain connected when n arbitrary internal lines are cut.

$$\Sigma(x_1,x_2) \;=\; \Sigma^{\delta}(x_1)\,\delta_p^{(d+1)}(x_1-x_2) \qquad (2.6)$$
$$\quad + \,\Theta_p(t_1-t_2)\,\Sigma^{>}(x_1,x_2) \;+\; \Theta_p(t_2-t_1)\,\Sigma^{<}(x_1,x_2)\,.$$

The δ_p-function on the closed-time-path is defined as

$$\delta_p^{(d+1)}(x_1-x_2) \;=\; \delta_p(t_1-t_2)\;\delta^{(d)}(\vec{x}_1-\vec{x}_2)\,, \qquad (2.7)$$

$$\delta_p(t_1-t_2) \;=\; \begin{cases} \delta(t_1-t_2)\,, & \text{if both } t_1 \text{ and } t_2 \text{ are on the upper } (+) \text{ branch}\,, \\ -\delta(t_1-t_2)\,, & \text{if both } t_1 \text{ and } t_2 \text{ are on the lower } (-) \text{ branch}\,, \\ 0\,, & \text{in other cases}\,, \end{cases}$$

in accordance with the contour integration. Here d denotes the spatial dimension of the problem ($d = 2$ in the case considered below). The equations of motion for the Green functions are obtained by the stationarity condition of the effective action (2.4)

$$\frac{\delta\,\Gamma}{\delta\,G} \;=\; 0\,, \qquad (2.8)$$

giving the Dyson-Schwinger equations for the full path-ordered Green functions

$$G(x_1,x_2) \;=\; G_0(x_1,x_2) \;+\; \int_p d^{d+1}y \int_p d^{d+1}z\;\; G_0(x_1,y)\;\Sigma(y,z)\;G(z,x_2)\,, \qquad (2.9)$$
$$G(x_1,x_2) \;=\; G_0(x_1,x_2) \;+\; \int_p d^{d+1}y \int_p d^{d+1}z\;\; G(x_1,y)\;\Sigma(y,z)\;G_0(z,x_2)\,.$$

Since the free propagator G_0 solves the Klein-Gordon equation as

$$[\,\partial_\mu^{x_1}\partial_{x_1}^\mu + m^2\,]\;\; G_0(x_1,x_2) \;=\; -\,\delta_p^{(d+1)}(x_1-x_2)\,, \qquad (2.10)$$

the equations of motion for the path-ordered Green functions read

$$-\,[\,\partial_\mu^{x_1}\partial_{x_1}^\mu + m^2\,]\;\; G(x_1,x_2) \;=\; \delta_p^{(d+1)}(x_1-x_2) \;+\; \int_p d^{d+1}z\;\; \Sigma(x_1,z)\;G(z,x_2)\,, \qquad (2.11)$$
$$-\,[\,\partial_\mu^{x_2}\partial_{x_2}^\mu + m^2\,]\;\; G(x_1,x_2) \;=\; \delta_p^{(d+1)}(x_1-x_2) \;+\; \int_p d^{d+1}z\;\; G(x_1,z)\;\Sigma(z,x_2)\,.$$

The functional Φ allows – by restricting to a particular set of diagrams – for the construction of effective theories, which are conserving and thermodynamically consistent [24, 81]. In our present calculation we take into account contributions up to the

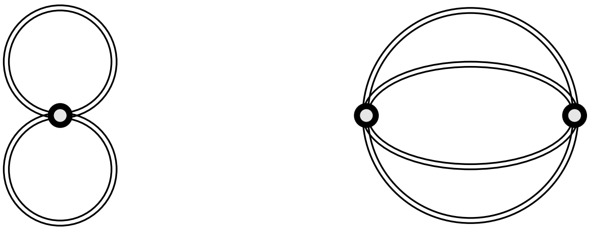

Figure 2.2: Contributions to the Φ-functional for the Kadanoff-Baym equation: two-loop contribution (l.h.s.) giving the tadpole self-energy and three-loop contribution (r.h.s.) generating the sunset self-energy. The Φ-functional is built up by full Green functions (double lines) while open dots symbolize the integration over the internal coordinates.

three-loop order for Φ-functional (cf. Fig. 2.2), which reads explicitly

$$i\Phi \;=\; \frac{i\lambda}{8}\int_p d^{d+1}x\;\, G(x,x)^2 \;-\; \frac{\lambda^2}{48}\int_p d^{d+1}x_1 \int_p d^{d+1}x_2\;\, G(x_1,x_2)^4\,. \tag{2.12}$$

This approximation corresponds to a weak coupling expansion such that we consider contributions up to the second superficial order in the coupling constant λ (cf. Fig. 2.3). For the superficial coupling constant order we count the explicit coupling factors λ associated with the visible vertices. The hidden dependence on the coupling strength – which is implicitly incorporated in the self-consistent Green functions that build up the Φ-functional and the self-energies – is ignored on that level. For our present purpose this approximation is sufficient since we include self-consistently the leading mean-field effects as well as the leading order scattering processes that pave the way to thermalization.

For the actual calculation it is advantageous to change to a single-time representation for the Green functions and (the non-local part of) the self-energies defined on the closed-time-path. In line with the position of the coordinates on the contour there exist four different two-point functions

$$\begin{aligned}
i\,G^{c}(x_1,x_2) &= i\,G^{++}(x_1,x_2) &&= i\,G(x_1^+,x_2^+) &&= \langle\, T^c\,\{\,\phi(x_1)\,\phi(x_2)\,\}\,\rangle\,, \qquad (2.13)\\
i\,G^{<}(x_1,x_2) &= i\,G^{+-}(x_1,x_2) &&= i\,G(x_1^+,x_2^-) &&= \langle\,\{\,\phi(x_2)\,\phi(x_1)\,\}\,\rangle\,,\\
i\,G^{>}(x_1,x_2) &= i\,G^{-+}(x_1,x_2) &&= i\,G(x_1^-,x_2^+) &&= \langle\,\{\,\phi(x_1)\,\phi(x_2)\,\}\,\rangle\,,\\
i\,G^{a}(x_1,x_2) &= i\,G^{--}(x_1,x_2) &&= i\,G(x_1^-,x_2^-) &&= \langle\, T^a\,\{\,\phi(x_1)\,\phi(x_2)\,\}\,\rangle\,.
\end{aligned}$$

Here $T^c\,(T^a)$ represent the (anti-)time-ordering operators in case of both arguments lying on the (anti-)chronological branch of the real-time contour. These four functions are not independent of each other. In particular the non-continuous functions G^c and G^a are built up by the Wightman functions $G^>$ and $G^<$ and the usual Θ-functions in the time coordinates

$$\begin{aligned} G^c(x_1,x_2) &= \Theta(t_1-t_2)\, G^>(x_1,x_2) \;+\; \Theta(t_2-t_1)\, G^<(x_1,x_2)\,, \\ G^a(x_1,x_2) &= \Theta(t_2-t_1)\, G^>(x_1,x_2) \;+\; \Theta(t_1-t_2)\, G^<(x_1,x_2)\,. \end{aligned} \tag{2.14}$$

Since for the real boson theory (2.1) the relation $G^>(x_1,x_2) = G^<(x_2,x_1)$ holds (2.13), the knowledge of the Green functions $G^<(x_1,x_2)$ for all x_1, x_2 characterizes the system completely. Nevertheless, we will give the equations for $G^<$ and $G^>$ explicitly since this is the familiar representation for general field theories [8, 18, 19].

By fixing the time arguments of the Green functions on different branches of the contour and resolving the time structure of the path-ordered quantities in the Dyson-Schwinger equations (2.11) we obtain the Kadanoff-Baym equations for the time evolution of the Wightman functions [19, 67]:

$$\begin{aligned} -\left[\partial_\mu^{x_1}\partial^\mu_{x_1} + m^2\right]\, G^{\gtrless}(x_1,x_2) &= \Sigma^\delta(x_1)\, G^{\gtrless}(x_1,x_2) \\ &\quad + \int_{t_0}^{t_1} dz_0 \int d^dz \;\; \left[\Sigma^>(x_1,z) - \Sigma^<(x_1,z)\right]\, G^{\gtrless}(z,x_2) \\ &\quad - \int_{t_0}^{t_2} dz_0 \int d^dz \;\; \Sigma^{\gtrless}(x_1,z)\; \left[G^>(z,x_2) - G^<(z,x_2)\right]\,, \\[1em] -\left[\partial_\mu^{x_2}\partial^\mu_{x_2} + m^2\right]\, G^{\gtrless}(x_1,x_2) &= \Sigma^\delta(x_2)\, G^{\gtrless}(x_1,x_2) \\ &\quad + \int_{t_0}^{t_1} dz_0 \int d^dz \;\; \left[G^>(x_1,z) - G^<(x_1,z)\right]\, \Sigma^{\gtrless}(z,x_2) \\ &\quad - \int_{t_0}^{t_2} dz_0 \int d^dz \;\; G^{\gtrless}(x_1,z)\; \left[\Sigma^>(z,x_2) - \Sigma^<(z,x_2)\right]\,, \end{aligned} \tag{2.15}$$

Within the three-loop approximation for the 2PI effective action (i.e. the Φ-functional (2.12)) we get two different self-energies: In leading order of the coupling constant only the local tadpole diagram (l.h.s. of Fig. 2.3) contributes and leads to the generation of an effective mass for the field quanta. This self-energy (in coordinate space) is given by

$$\Sigma^\delta(x) \;=\; \frac{\lambda}{2}\, i\, G^<(x,x)\,. \tag{2.16}$$

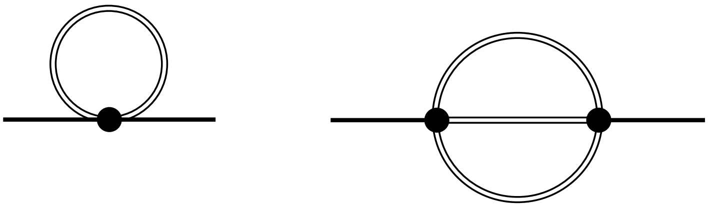

Figure 2.3: Self-energies of the Kadanoff-Baym equation: tadpole self-energy (l.h.s.) and sunset self-energy (r.h.s.). Since the lines represent full Green functions the self-energies are self-consistent (see text) with the external coordinates indicated by full dots.

In next order in the coupling constant (i.e. λ^2) the non-local sunset self-energy (r.h.s. of Fig. 2.3) enters the time evolution as

$$\Sigma^{\gtrless}(x_1,x_2) \;=\; -\frac{\lambda^2}{6}\, G^{\gtrless}(x_1,x_2)\, G^{\gtrless}(x_1,x_2)\, G^{\lessgtr}(x_2,x_1) \;=\; -\frac{\lambda^2}{6}\, \left[\, G^{\gtrless}(x_1,x_2)\, \right]^3. \tag{2.17}$$

Thus the Kadanoff-Baym equation (2.15) in our case includes the influence of a mean-field on the particle propagation – generated by the tadpole diagram – as well as scattering processes as inherent in the sunset diagram.

The Kadanoff-Baym equation (2.15) describes the full quantum nonequilibrium time evolution on the two-point level for a system prepared at an initial time t_0, i.e. when higher order correlations are discarded. The causal structure of this initial value problem is obvious since the time integrations are performed over the past up to the actual time t_1 (or t_2, respectively) and do not extend to the future.

Furthermore, also linear combinations of the Green functions in single-time representation are of interest. The retarded Green function G^R and the advanced Green function G^A are given as

$$\begin{aligned} G^R(x_1,x_2) \;&=\; \Theta(t_1-t_2)\;\left[\, G^>(x_1,x_2) - G^<(x_1,x_2)\,\right] \qquad (2.18)\\ &=\; \Theta(t_1-t_2)\;\langle\, [\, \phi(x_1)\,,\, \phi(x_2)\,]_-\,\rangle \\ &=\; G^c(x_1,x_2) \;-\; G^<(x_1,x_2) \;=\; G^>(x_1,x_2) \;-\; G^a(x_1,x_2)\,, \end{aligned}$$

$$\begin{aligned} G^A(x_1,x_2) \;&=\; -\,\Theta(t_2-t_1)\;\left[\, G^>(x_1,x_2) - G^<(x_1,x_2)\,\right] \qquad (2.19)\\ &=\; -\,\Theta(t_2-t_1)\;\langle\, [\, \phi(x_1)\,,\, \phi(x_2)\,]_-\,\rangle \\ &=\; G^c(x_1,x_2) \;-\; G^>(x_1,x_2) \;=\; G^<(x_1,x_2) \;-\; G^a(x_1,x_2)\,. \end{aligned}$$

These Green functions contain exclusively spectral, but no statistical information of the system. Their time evolution is determined by the Dyson-Schwinger equations (2.11) as well and given by

$$
\begin{aligned}
- \left[\partial_\mu^{x_1} \partial_{x_1}^\mu + m^2 + \Sigma^\delta(x_1)\right] \; G^R(x_1,x_2) \; &= \qquad\qquad (2.20)\\
& \delta^{(d+1)}(x_1 - x_2) \; + \; \int d^{d+1}z \;\; \Sigma^R(x_1,z) \;\; G^R(z,x_2)\,,
\end{aligned}
$$

$$
\begin{aligned}
- \left[\partial_\mu^{x_1} \partial_{x_1}^\mu + m^2 + \Sigma^\delta(x_1)\right] \; G^A(x_1,x_2) \; &= \qquad\qquad (2.21)\\
& \delta^{(d+1)}(x_1 - x_2) \; + \; \int d^{d+1}z \;\; \Sigma^A(x_1,z) \;\; G^A(z,x_2)\,,
\end{aligned}
$$

where the retarded and advanced self-energies Σ^R, Σ^A are defined via $\Sigma^>$, $\Sigma^<$ similar to the Green functions (2.18) and (2.19). Thus the retarded (advanced) Green functions are determined by retarded (advanced) quantities, only.

2.2 Homogeneous Systems in Space

In the following we will restrict to homogeneous systems in space. In order to obtain a numerical solution the Kadanoff-Baym equation (2.15) is transformed to momentum space:

$$
\begin{aligned}
\partial_{t_1}^2 \, G^<(\vec{p},t_1,t_2) \;\; &= \;\; - \left[\, \vec{p}^{\,2} + m^2 + \bar{\Sigma}^\delta(t_1) \,\right] \; G^<(\vec{p},t_1,t_2) \qquad\qquad (2.22)\\
& \quad - \int_{t_0}^{t_1} dt' \;\; \left[\, \Sigma^>(\vec{p},t_1,t') - \Sigma^<(\vec{p},t_1,t') \,\right] \; G^<(\vec{p},t',t_2)\\
& \quad + \int_{t_0}^{t_2} dt' \;\; \Sigma^<(\vec{p},t_1,t') \; \left[\, G^>(\vec{p},t',t_2) - G^<(\vec{p},t',t_2) \,\right]\\
&= \;\; - \left[\, \vec{p}^{\,2} + m^2 + \bar{\Sigma}^\delta(t_1) \,\right] \; G^<(\vec{p},t_1,t_2) \; + \; I_1^<(\vec{p},t_1,t_2)\,,
\end{aligned}
$$

where we have summarized both memory integrals into the function $I_1^<$. The equation of motion in the second time direction t_2 is given analogously.

In two-time and momentum space representation the self-energies in (2.22) read

$$\bar{\Sigma}^{\delta}(t) \;=\; \frac{\lambda}{2}\int\frac{d^dp}{(2\pi)^d}\; i\,G^{<}(\vec{p},t,t)\;, \tag{2.23}$$

$$\Sigma^{\gtrless}(\vec{p},t,t') \;=\; -\frac{\lambda^2}{6}\int\frac{d^dq}{(2\pi)^d}\int\frac{d^dr}{(2\pi)^d}\;\; G^{\gtrless}(\vec{q},t,t')\;\; G^{\gtrless}(\vec{r},t,t')\;\; G^{\gtrless}(\vec{p}-\vec{q}-\vec{r},t,t')\,. \tag{2.24}$$

For the numerical solution of the Kadanoff-Baym equations (2.22) we have developed a flexible and accurate algorithm, which is described in more detail in Appendix A. Furthermore, a straightforward integration of the Kadanoff-Baym equations (2.22) in time does not lead to meaningful results since in 2+1 space-time dimensions both self-energies (2.23,2.24) are ultraviolet divergent. We note, that due to the finite mass m adopted in (2.1) no problems arise from the infrared momentum regime. The ultraviolet regime, however, has to be renormalized by introducing proper counterterms. The details of the renormalization scheme are given in Appendix B as well as a numerical proof for the convergence in the ultraviolet regime.

Chapter 3

Numerical Studies on Equilibration

In the following Sections we will use the renormalized mass $m = 1$, which implies that times are given in units of the inverse mass or $t \cdot m$ is dimensionless. Accordingly, the coupling λ in (2.1) is given in units of the mass m such that λ/m is dimensionless, too.

As already observed in the 1+1 dimensional case [69] the mean-field term, generated by the tadpole diagram, does not lead to an equilibration of arbitrary initial momentum distributions since it only modifies the propagation of the particles by the generation of an effective mass. Our calculations lead to the same findings and thus we skip an explicit presentation of the actual results. Accordingly, thermalization in 2+1 dimensions requires the inclusion of the collisional self-energies as generated by the sunset diagram. All calculations to be shown in the following consequently involve both self-energies.

3.1 Initial Conditions

In order to investigate equilibration phenomena on the basis of the Kadanoff-Baym equations for our 2+1 dimensional problem, we first have to specify the initial conditions for the time integration. This is a problem of its own and discussed in more detail in Appendix C. For our present study we consider four different initial distributions that are all characterized by the same energy density (see Section 3.3 for an explicit representation). Consequently, for large times ($t \to \infty$) all initial value problems should lead to the same equilibrium final state. The initial equal-time Green functions $G^<(\vec{p}, t\!=\!0, t\!=\!0)$ adopted are displayed in Fig. 3.1 (upper part) as a function of the momentum p_x (for $p_y = 0$). We concentrate here on polar symmetric configurations due to the large numerical expense for this first investigation[1]. Since the equal-time Green functions $G^<(\vec{p}, t, t) \equiv G^<_{\phi\phi}(\vec{p}, t, t)$ are purely imaginary, we show only the real part of $i\, G^<$ in Fig. 3.1. Furthermore, the corresponding initial distribution functions in the occupation density $n(\vec{p}, t\!=\!0)$, related to $i\, G^<(\vec{p}, t\!=\!0, t\!=\!0)$ via

---

[1] In Section 5 we will present also calculations for non-symmetric systems.

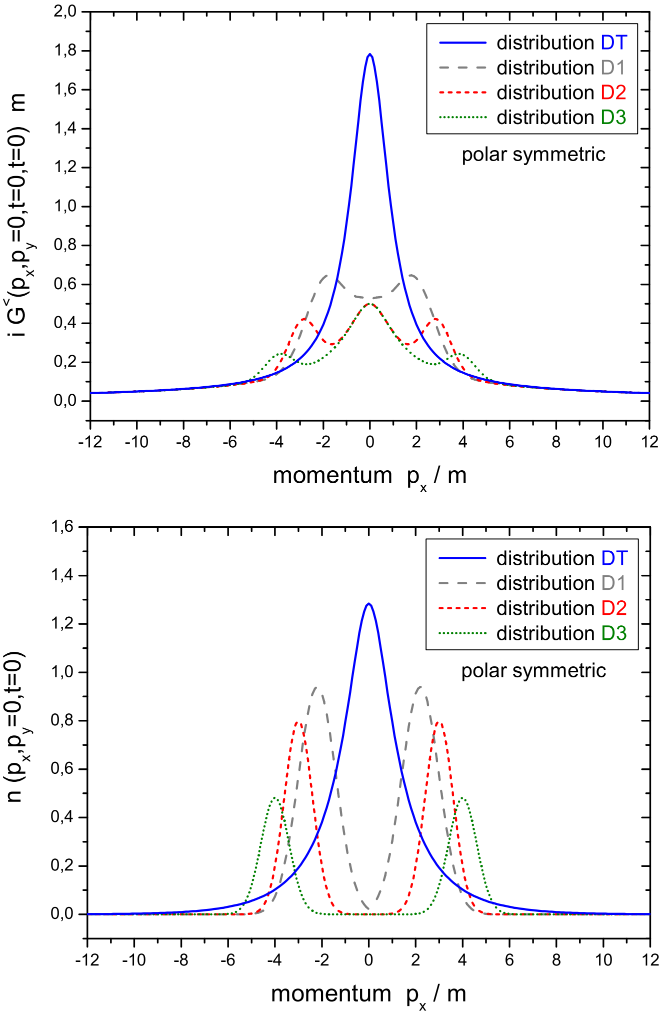

Figure 3.1: Initial Green functions $i\,G^<(|\,\vec{p}\,|, t\!=\!0, t\!=\!0)$ (upper part) and corresponding initial distribution functions $n(|\,\vec{p}\,|, t = 0)$ (lower part) for the distributions D1, D2, D3 and DT in momentum space (for a cut of the polar symmetric distribution in p_x direction for $p_y = 0$).

$$2\omega_{\vec{p}}\;\; i\,G^<_{\phi\phi}(\vec{p}, t\!=\!0, t\!=\!0) \;=\; n(\vec{p}, t\!=\!0) \;+\; n(-\vec{p}, t\!=\!0) \;+\; 1\,, \tag{3.1}$$

are shown in Fig. 3.1 in the lower part. For an explicit representation of the other Green functions $G^<_{\phi\pi}$, $G^<_{\pi\phi}$ and $G^<_{\pi\pi}$ (cf. Appendix A) at initial time t_0 we refer to the discussion of the general initial conditions in Appendix C.

While the initial distributions D1, D2, D3 have the shape of (polar symmetric) 'tsunami' waves [44] with maxima at different momenta in p_x, the initial distribution DT corresponds to a free Bose gas at a given initial temperature $T_0 \approx 1.736\,m$ that is fixed by the initial energy density. According to (3.1) the difference between the Green functions and the distribution functions is basically given by the vacuum contribution, which has its maximum at small momenta. Thus even for the distributions D1, D2, D3 the corresponding Green functions are non-vanishing for $|\vec{p}| \approx 0$.

Since we consider a finite volume $V = a^2$ we work in a basis of momentum modes characterized by the number of nodes in each direction. The number of momentum modes is typically in the order of 40; we checked that all our results are stable with respect to an increasing number of basis states and do not comment on this issue any more, since this is a strictly necessary condition for our analysis. For times $t < 0$ we consider the systems to be noninteracting and switch on the interaction ($\sim \lambda$) for $t = 0$ to explore the quantum dynamics of the interacting system for $t > 0$.

We directly step on with the actual numerical results.

3.2 Equilibration in Momentum Space

The time evolution of various (selected) momentum modes of the equal-time Green function for the different initial states D1, D2, D3 and DT is shown in Fig. 3.2, where the dimensionless time $t \cdot m$ is displayed on a logarithmic scale.

We observe that starting from very different initial conditions – as introduced in Fig. 3.1 – the single momentum modes converge to the same respective numbers for large times as characteristic for a system in equilibrium. As noted above, the initial energy density is the same for all distributions and energy conservation is fulfilled strictly in the time integration of the Kadanoff-Baym equations. The different momentum modes in Fig. 3.2 typically show a three-phase structure. For small times ($t \cdot m < 10$) one finds damped oscillations that can be identified with a typical switching-on effect at $t = 0$, where the system is excited by a sudden increase of the coupling constant to $\lambda/m = 18$. Here dephasing and relaxation of the initial conditions happen on a time scale of the inverse damping rate (cf. Appendix C). We note in passing that one might also start with an effective initial mass m^* including the self-consistent tadpole contribution [69], however, our numerical solutions showed no significant difference for the equilibration process such that we discard an explicit representation. The damping of the initial oscillations depends on the coupling strength λ/m and is more pronounced for strongly coupled systems.

For 'intermediate' time scales ($10 < t \cdot m < 500$) one observes a strong change of all momentum modes in the direction of the final stationary state. We address this phase to 'kinetic' equilibration and point out, that – depending on the initial conditions and the coupling strength – the momentum modes can temporarily even exceed their respective equilibrium value. This can be seen explicitly for the lowest momentum modes ($|\vec{p}|/m$ = 0.0, 0.8) of the distribution D1 (long dashed lines) in Fig. 3.2, which possesses initially maxima at small momentum. Thus the time evolution towards the final equilibrium value is – after an initial phase with damped oscillations – not necessarily monotonic. For different initial conditions this behaviour may be weakened significantly as seen for example in case of the initial distribution D2 (short dashed lines) in Fig. 3.2. Coincidently, both calculations D1 and D2 show approximately the same equal-time Green function values for times $t \cdot m > 80$. Note, that for the initial

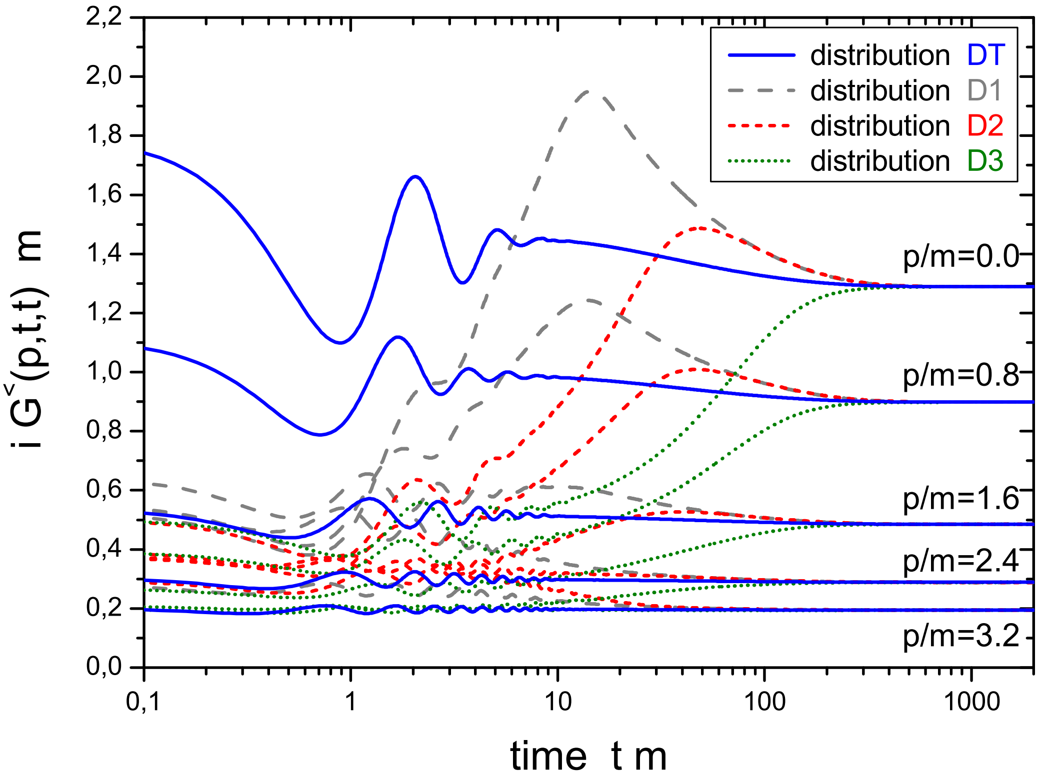

Figure 3.2: Time evolution of selected momentum modes of the equal-time Green function $|\vec{p}|/m = 0.0, 0.8, 1.6, 2.4, 3.2$ (from top to bottom) for four different initial configurations D1, D2, D3 and DT (characterized by the different line types) with the same energy density. For the rather strong coupling constant $\lambda/m = 18$ the initial oscillations – from switching on the interaction at $t = 0$ – are damped rapidly and disappear for $t \cdot m > 10$. Finally, all momentum modes assume the same respective equilibrium value for long times ($t \cdot m > 500$) independent of the initial state.

distribution D3 (dotted lines) the non-monotonic behaviour is not seen any more.

In general, we observe that only initial distributions (of the well type) show this feature during their time evolution, if the maximum is located at sufficiently small momenta. Initial configurations like the distribution DT (solid lines) – where the system initially is given by a free gas of particles at a temperature T_0 – do not show this property. We also remark that this 'overshooting' – as in the particular case of D1 – is *not* observed in a simulation with a kinetic Boltzmann equation (see Section 5.4). Hence this highly nonlinear effect must be attributed to quantal off-shell and memory effects not included in the standard Boltzmann limit. Although the DT distribution is not the equilibrium state of the interacting theory, the actual numbers are much closer to the equilibrium state of the interacting system than the initial distributions D1, D2 and D3. Therefore, the evolution for DT proceeds less violently. We point out, that in contrast to the calculations performed for ϕ^4-theory in 1+1 space-time dimensions [69] we find no power law behaviour for intermediate time scales.

The third phase, i.e. the late time evolution ($t \cdot m > 300$) is characterized by a smooth approach of the single momentum modes to their respective equilibrium values. As we will see in Section 3.6 this phase is adequately characterized by chemical equilibration processes.

The three phases addressed in context with Fig. 3.2 will be investigated and analyzed in more detail in the following Sections.

3.3 Build-up of Initial Correlations

The time evolution of the interacting system within the standard Kadanoff-Baym equations is characterized by the build-up of early correlations. This can be seen from Fig. 3.3 where all contributions to the energy density [24] are displayed separately as a function of time with the initial value at $t_0 = 0$ subtracted. The kinetic energy density ε_{kin} is represented by all parts of ε_{tot} that are independent of the coupling constant ($\propto \lambda^0$). All terms proportional to λ^1 are summarized by the tadpole energy density ε_{tad} including the actual tadpole term as well as the corresponding tadpole mass counterterm (cf. Appendix B). The contributions from the sunset diagram ($\propto \lambda^2$) – again given by the correlation integral as well as by the sunset mass counterterm (cf. Appendix B) – are represented by the sunset energy density ε_{sun}.

$$\varepsilon_{tot}(t) \;=\; \varepsilon_{kin}(t) \;+\; \varepsilon_{tad}(t) \;+\; \varepsilon_{sun}(t)\;, \tag{3.2}$$

$$\varepsilon_{kin}(t) \;=\; \frac{1}{2}\int\frac{d^dp}{(2\pi)^d}\;(\vec{p}^{\,2}+m^2)\;i\,G^{<}_{\phi\phi}(\vec{p},t,t)\;+\;\frac{1}{2}\int\frac{d^dp}{(2\pi)^d}\;i\,G^{<}_{\pi\pi}(\vec{p},t,t)\;,$$

$$\varepsilon_{tad}(t) \;=\; \frac{1}{4}\int\frac{d^dp}{(2\pi)^d}\;\bar{\Sigma}_{tad}(t)\;i\,G^{<}_{\phi\phi}(\vec{p},t,t)\;+\;\frac{1}{2}\int\frac{d^dp}{(2\pi)^d}\;\delta m^2_{tad}\;i\,G^{<}_{\phi\phi}(\vec{p},t,t)\;,$$

$$\varepsilon_{sun}(t) \;=\; \underbrace{-\frac{1}{4}\int\frac{d^dp}{(2\pi)^d}\;i\,I_1^{<}(\vec{p},t,t)}_{\varepsilon_{cor}(t)}\;+\frac{1}{2}\int\frac{d^dp}{(2\pi)^d}\;\delta m^2_{sun}\;i\,G^{<}_{\phi\phi}(\vec{p},t,t)\;.$$

The calculation in Fig. 3.3 has been performed for the initial distribution DT (which represents a free gas of Bose particles at temperature $T_0 \approx 1.736\,m$) with a coupling constant of $\lambda/m = 18$. This state is stationary in the well-known Boltzmann limit (cf. Section 5), but it is not for the Kadanoff-Baym equation. In the full quantum calculations the system evolves from an uncorrelated initial state and the correlation

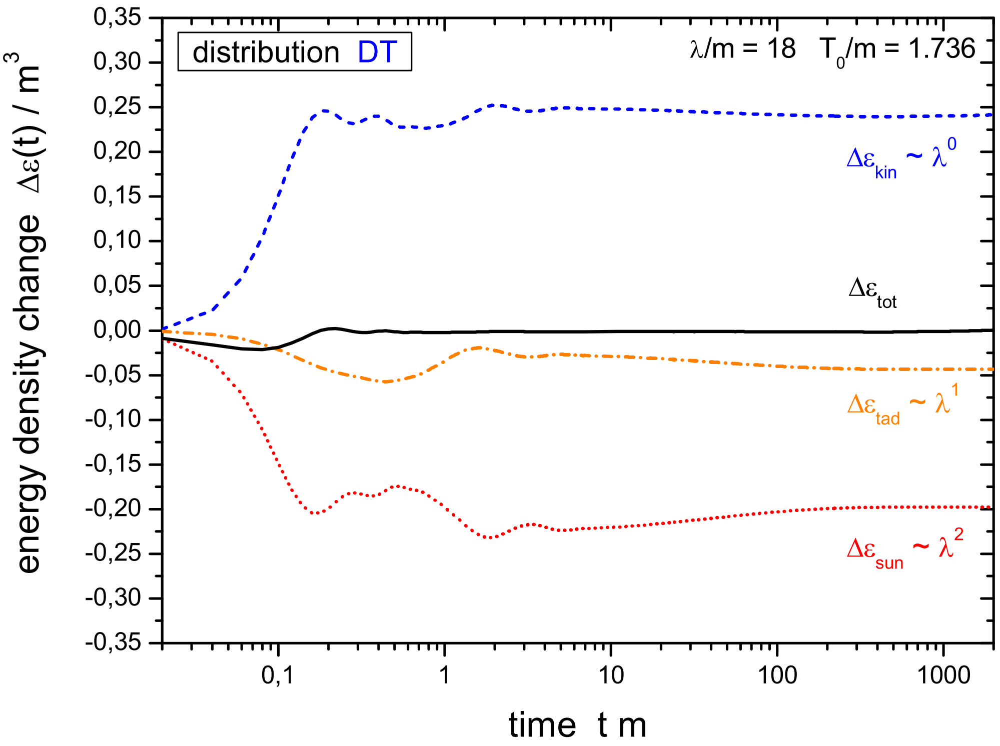

Figure 3.3: Change of the different contributions to the total energy density in time. The sunset energy density ε_{sun} decreases rapidly in time; this contribution is approximately compensated by an increase of the kinetic energy density ε_{kin}. Together with the smaller tadpole contribution ε_{tad} the total energy density ε_{tot} is conserved.

energy density ε_{sun} decreases rapidly with time. The decrease of the correlation energy ε_{sun} which is – with exception of the sunset mass counterterm contribution – initially zero is approximately compensated by an increase of the kinetic energy density ε_{kin}. Since the kinetic energy increases in the initial phase, the final temperature T_f is slightly higher than the initial 'temperature' T_0. The remaining difference is compensated by the tadpole energy density ε_{tad} such that the total energy density is conserved.

While the sunset energy density and the kinetic energy density always show a time evolution comparable to Fig. 3.3, the change of the tadpole energy density depends on the initial configuration and may be positive as well. Since the self-energies are obtained within a Φ-derivable scheme the fundamental conservation laws, as e.g. energy conservation, are respected to all orders in the coupling constant. When neglecting the $\propto \lambda^2$ sunset contributions and starting with a non-static initial state of identical energy density one observes the same compensating behaviour between the kinetic and the tadpole terms.

From Fig. 3.3 one finds that the system correlates in a very short time $(t \cdot m < 1)$ in comparison to the time for complete equilibration. The time to build up the correlations

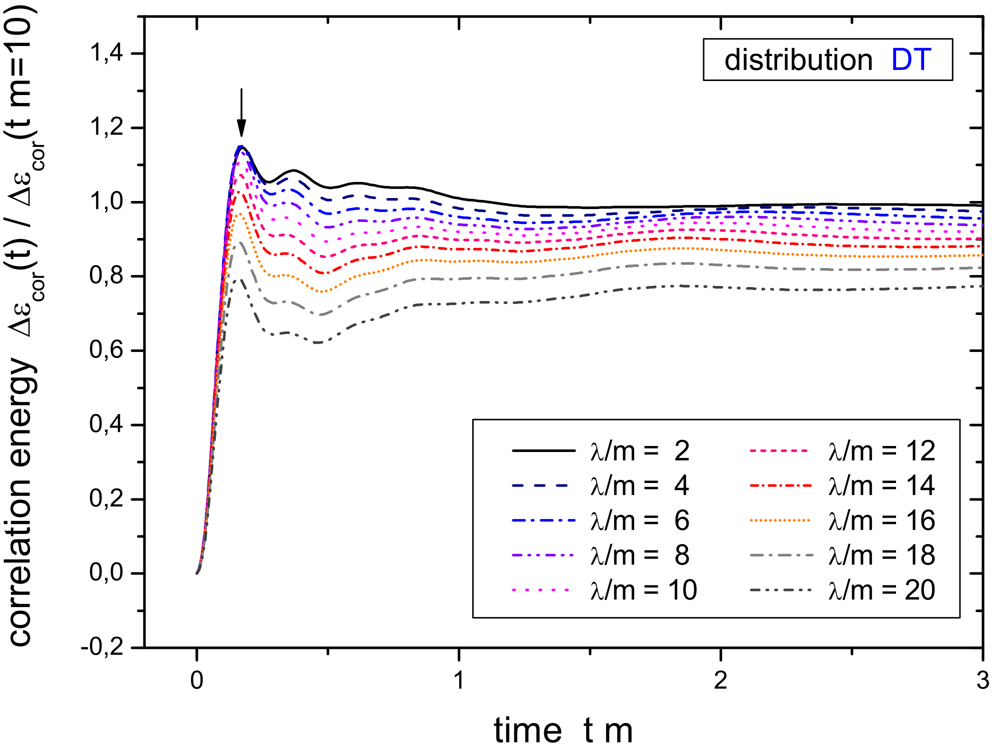

Figure 3.4: Normalized change of the correlation energy density ε_{cor} for various coupling constants $\lambda/m = 2 - 20$ in steps of 2 for the same initial distribution DT. The normalization has been performed with respect to the asymptotic correlation strength (for $t \cdot m > 10$). The systems correlate approximately independent from the coupling strength after $\tau_{cor} \cdot m \approx 0.16$.

τ_{cor} is rather independent of the interaction strength as seen from Fig. 3.4, where calculations with the same initial state DT are compared for several coupling constants $\lambda/m = 2 - 20$ in steps of 2. For all couplings λ/m the change of the correlation energy density here has been normalized to the asymptotic correlation strength ($t \cdot m > 10$). Fig. 3.4 shows that the correlation time τ_{cor} (which we define by the position of the first maximum) is approximately the same for all coupling constants. Within our definition the correlation time is $\tau_{cor} \cdot m \approx 0.16$ for all couplings λ. This result is in line with the KB studies of nonrelativistic nuclear matter problems, where the same independence from the coupling strength has been observed for the correlation time [63]. A similar result has, furthermore, been obtained within the correlation dynamical approach of Ref. [52]. Thus quantum systems apparently correlate on time scales that are very short compared to 'kinetic' or 'chemical' equilibration time scales.

The question now arises how such short time scales come about. We recall, that equations of motion containing memory integrals, like the Kadanoff-Baym equations, are the inevitable result of a reduction of multi-particle dynamics to the one-body level which induces phase correlations into the history of the system [82, 83]. This is similar to the situation encountered in the derivation of the standard Boltzmann equation, which only holds if one can separate between two time scales, $\tau_{cor} \ll \tau_{rel}$ (relaxation time scale), distinguishing between rapidly changing ('irrelevant') observables and smoothly behaving ('relevant') observables. Indeed, it had been shown for a nucleonic system [61] that such a finite memory in the collision process may have a profound influence on thermalization for medium-energy nuclear reactions. In any case, a finite correlation time is generated by first a constructive and then destructive interference of the various scattering channels building up for times going more and more in the past. For a fermionic system typical memory kernels for the collision integral are given in Refs. [60, 61, 62]). The structure of such memory kernels is governed by the off-shell behaviour and the phase-space average of the two-particle scattering amplitude, i.e.

$$\tau_{mem} \sim \frac{\hbar}{< \Delta E >} . \tag{3.3}$$

Of present concern is now the formation of the correlation energy and not the memory kernels of the collisional integrals, although they are closely related. The explicit correlation part of ε_{sun} contains the momentum integral over the function $I_1^<(\vec{p}, t, t)$, which itself is given by a memory integral over time as stated in (A.4) in Appendix A. From the explicit expression one notices that $I_1^<(\vec{p}, t = 0, t = 0) \equiv 0$ and for small times builds up coherently by the various 'scattering' contributions. For a fermionic system describing cold nuclear matter, similar expressions for the collisional energy density have been found and analyzed in detail by Köhler and Morawetz [63]. It has been found, that the time to build up the correlation energy by collisions from an initially uncorrelated system is given by $\tau_{cor} \approx 2\hbar/E_F$, where E_F denotes the Fermi energy. The memory integrals of $I_1^<$ – or those entering the quantal transport equations – can also contain classical contributions. For a dilute and equilibrated Maxwell-Boltzmann gas of nonrelativsitic particles at finite temperature T and assuming a static, Gaussian interaction potential $V(r) = V_0 \exp(-r^2/r_0^2)$, the various kernels can be worked out analytically [8, 83, 63]. The correlation time is then given by

$$\tau_{cor} \approx \sqrt{r_0^2 m/T + (\hbar/T)^2} . \tag{3.4}$$

The first part reflects the intuitive expectation, i.e. the time a classical particle passes through the range of a potential; the second part reflects the average temporal extent associated with the time-energy uncertainty relation induced by the characteristic (off-shell) energy scale in a typical collision. For our present situation, i.e. a relativistic bosonic theory interacting via a 4-point coupling, the temperature defines the only scale. Hence, $\tau_{cor} \approx \hbar/T$, which is a pure quantal effect. This estimate is also in agreement with our numerical findings.

3.4 Time Evolution of the Spectral Function

Within the Kadanoff-Baym calculations the full quantum information of the two-point functions is retained. Consequently, one has access to the spectral properties of the nonequilibrium system during its time evolution. The spectral function $A(x_1, x_2)$ for the present settings is given by

$$A(x_1,x_2) \;=\; \langle\, [\, \phi(x_1)\,,\, \phi(x_2)\,]_-\, \rangle \;=\; i\, [\, G^>(x_1,x_2) \;-\; G^<(x_1,x_2)\,]\,. \tag{3.5}$$

From our dynamical calculations the spectral function in Wigner space for each system time $t = (t_1 + t_2)/2$ is obtained via Fourier transformation with respect to the relative time coordinate $\Delta t = t_1 - t_2$:

$$\bar{A}(\vec{p}, p_0, t) \;=\; \int_{-\infty}^{\infty} d\Delta t \;\; \exp(i\, \Delta t\, p_0) \;\; A(\vec{p}, t_1 = t{+}\Delta t/2, t_2 = t{-}\Delta t/2). \tag{3.6}$$

We note, that a damping of the function $A(\vec{p}, t_1, t_2)$ in relative time Δt corresponds to a finite width $\bar{\Gamma}$ of the spectral function in Wigner space. This width in turn can be interpreted as the inverse life time of the interacting scalar particle. We recall, that the spectral function – for all times t and for all momenta $\vec{p}$ – obeys the normalization

$$\int_{-\infty}^{\infty} \frac{dp_0}{2\pi}\, p_0\, \bar{A}(\vec{p}, p_0, t) \;=\; 1 \qquad \forall\, \vec{p},\, t\,, \tag{3.7}$$

which is nothing but a reformulation of the equal-time commutation relation.

In Fig. 3.5 we display the time evolution of the spectral function for the initial distributions D1, D2, D3 and DT for two different momentum modes $|\,\vec{p}\,|/m = 0.0$ and $|\,\vec{p}\,|/m = 2.0$. Since the spectral functions are antisymmetric in energy for the momentum symmetric configurations considered, i.e. $\bar{A}(\vec{p}, -p_0, t) = -\bar{A}(\vec{p}, p_0, t)$, we only show the positive energy part. For our initial value problem in two-times and momentum space the Fourier transformation (3.6) is restricted for system times t to an interval $\Delta t \in [-2t, 2t\,]$. Thus in the very early phase the spectral function assumes a finite width already due to the limited support of the Fourier transform in the time interval and a Wigner representation is not very meaningful. We, therefore, present the spectral functions for various system times t starting from $t \cdot m = 15$ up to $t \cdot m = 480$.

For the free thermal initialization DT the evolution of the spectral function is very smooth and comparable to the smooth evolution of the equal-time Green function as discussed in Section 3.2. In this case the spectral function is already close to the equilibrium shape at small times being initially only slightly broader than for late times. The maximum of the spectral function (for all momenta) is higher than the (bare) on-shell value and nearly keeps its position during the whole time evolution.

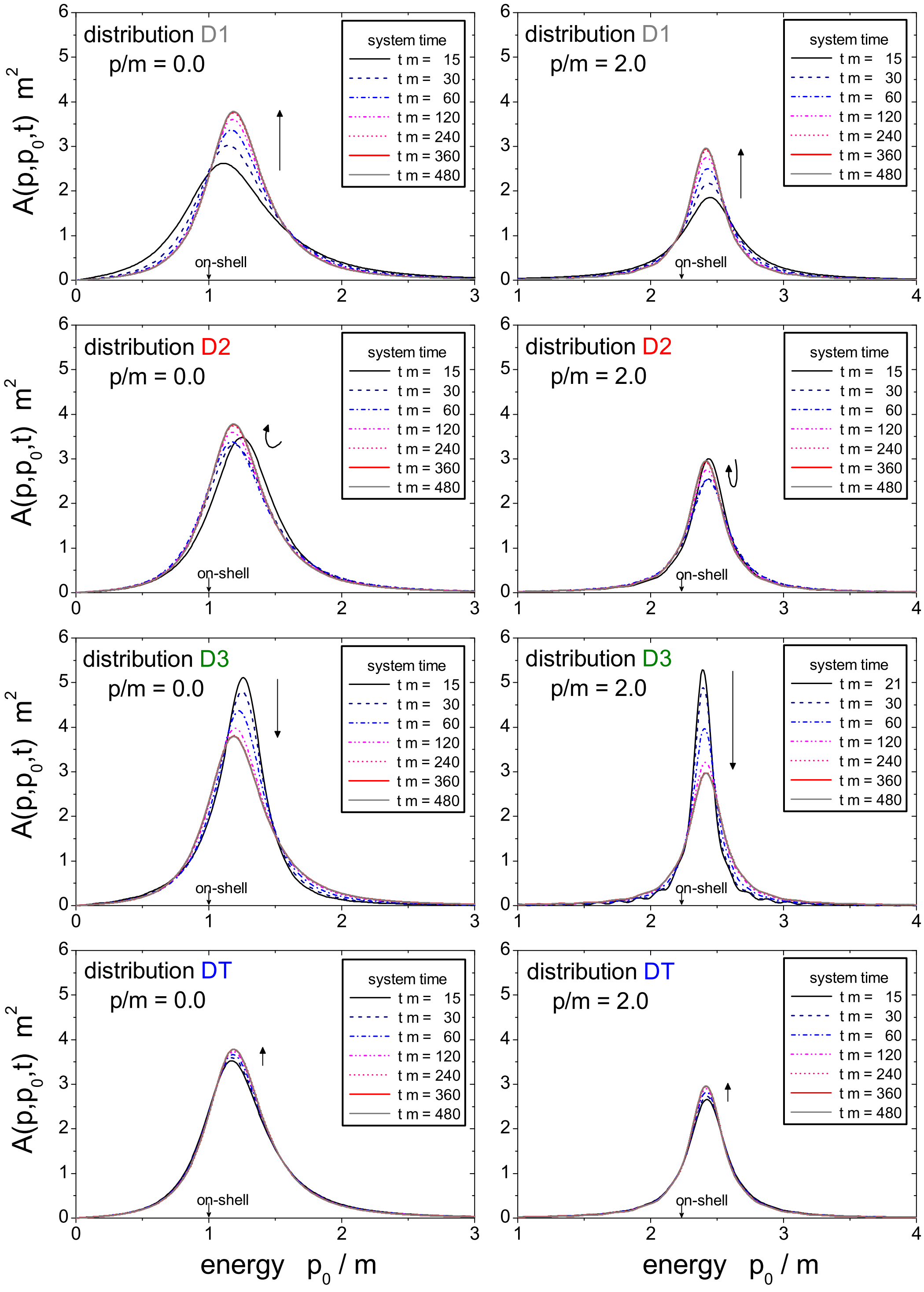

Figure 3.5: Time evolution of the spectral function $\bar{A}(\vec{p}, p_0, t)$ for the initial distributions D1, D2, D3 and DT (from top to bottom) with coupling constant $\lambda/m = 18$ and for the two momenta $|\,\vec{p}\,|/m = 0.0$ (l.h.s.) and $|\,\vec{p}\,|/m = 2.0$ (r.h.s.). The spectral function is shown for several times $t \cdot m = 15,\ 30,\ 60,\ 120,\ 240,\ 360,\ 480$ as indicated by the different line types.

This results from a positive tadpole mass shift, which is only partly compensated by a downward shift originating from the sunset diagram.

The time evolution for the initial distributions D1, D2 and D3 has a richer structure. For the distribution D1 the spectral function is broad for small system times (see the line for $t \cdot m = 15$) and becomes a little sharper in the course of the time evolution (as presented for the momentum mode $|\vec{p}|/m = 0.0$ as well as for $|\vec{p}|/m = 2.0$). In line with the decrease in width the height of the spectral function is increasing (as demanded by the normalization property (3.7)). This is indicated by the small arrow close to the peak position. Furthermore, the maximum of the spectral function (which is approximately the on-shell energy) is shifted slightly upwards for the zero-mode and shifted downwards for the mode with higher momentum being always higher than the vacuum on-shell value.

For the initial distribution D3 we find the opposite behaviour. Here the spectral function is quite narrow for early times and increases its width during the time evolution as observed for both momentum modes. Especially in the case of $|\vec{p}|/m = 2.0$ the width for early times is so small that the spectral function shows oscillations originating from the finite range of the Fourier transformation from relative time to energy. Although we have already increased the system time for the first curve to $t \cdot m = 21$ (for $t \cdot m = 15$ the oscillations are much stronger) the spectral function is not fully resolved, i.e. it is not sufficiently damped in relative time Δt in the interval available for the Fourier transform. For later times the oscillations vanish and the spectral function tends to the common equilibrium shape.

The time evolution of the spectral function for the initial distribution D2 is in between the last two cases. Here the spectral function develops (at intermediate times) a slightly higher width than in the beginning before it is approaching the narrower static shape again. The corresponding evolution of the maximum is again indicated by the (bent) arrow. Finally, all spectral functions show the (same) equilibrium form represented by the solid gray line.

As already observed in Section 3.2 for the equal-time Green functions, we emphazise, that there is no unique time evolution for the nonequilibrium systems. In fact, the evolution of the system during the equilibration process depends on the initial conditions. Our findings are slightly different from the conclusions drawn in [68] for the 1+1 dimensional case stating that the Wigner transformed spectral function is slowly varying, which might be due to the lower dimension. Still the time dependence of the spectral function is moderate enough, such that one might also work with some time-averaged or even the equilibrium spectral function. In order to investigate this issue in more quantitative detail, we concentrate on the maxima and widths of the spectral functions in the following.

Since the solution of the Kadanoff-Baym equation provides the full spectral information for all system times the evolution of the on-shell energies can be studied as well as the spectral widths. In Fig. 3.6 we display the time dependence of the on-shell energies $\omega(\vec{p}, t)$ – defined by the maximum of the spectral function – of the momentum modes $|\vec{p}|/m = 0.0$ (l.h.s.) and $|\vec{p}|/m = 2.0$ (r.h.s.) for the four initial distributions D1, D2, D3 and DT. We see that the on-shell energy for the zero momentum mode

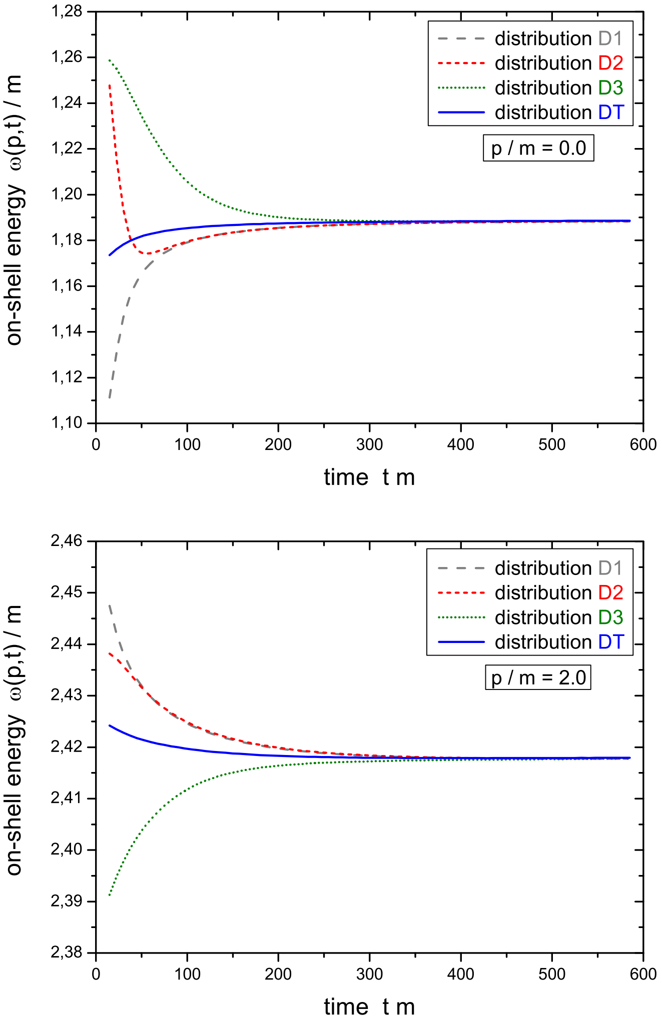

Figure 3.6: Time evolution of the on-shell energies $\omega(\vec{p}, t)$ of the momentum modes $|\vec{p}|/m = 0.0$ and $|\vec{p}|/m = 2.0$ for the different initializations D1, D2, D3 and DT with $\lambda/m = 18$. The on-shell self-energies are extracted from the maxima of the time-dependent spectral functions.

increases with time for the initial distribution D1 and to a certain extent for the free thermal distribution DT (as can be also extracted from Fig. 3.5). The on-shell energy of distribution D3 shows a monotonic decrease during the evolution while it passes through a minimum for distribution D2 before joining the line for the initialization D1. For momentum $|\vec{p}|/m = 2.0$ a rather opposite behaviour is observed. Here the on-shell energy for distribution D1 (and less pronounced for the distribution DT) are reduced in time whereas it is increased in the case of D3. The result for the initialization D2 is monotonous for this mode and matches the one for D1 already for moderate times. Thus we find, that the time evolution of the on-shell energies does not only depend on the initial conditions, but might also be different for various momentum modes. It turns out – for the initial distributions investigated – that the above described characteristics change around $|\vec{p}|/m = 1.5$ and are retained for larger momenta (not presented here).

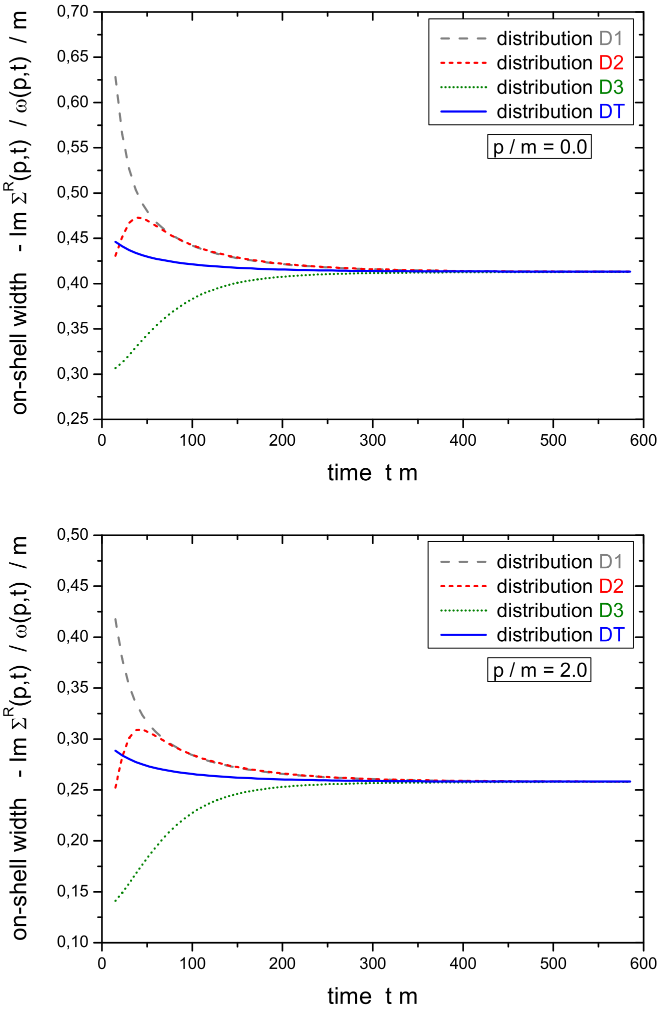

Figure 3.7: Time evolution of the on-shell widths $-Im\,\bar{\Sigma}^R(\vec{p},\omega(\vec{p},t),t)/\omega(\vec{p},t)$ of the momentum modes $|\,\vec{p}\,|/m = 0.0$ and $|\,\vec{p}\,|/m = 2.0$ for the different initializations D1, D2, D3 and DT with $\lambda/m = 18$.

Furthermore, we show in Fig. 3.7 the time evolution of the on-shell width for the usual momentum modes and different initial distributions. The on-shell width γ_ω is given by the imaginary part of the retarded sunset self-energy at the on-shell energy of each respective momentum mode as

$$\gamma_\omega(\vec{p},t) \;=\; \frac{-2\,Im\,\bar{\Sigma}^R(\vec{p},\omega(\vec{p},t),t)}{2\,\omega(\vec{p},t)} \;=\; \frac{\bar{\Gamma}(\vec{p},\omega(\vec{p},t),t)}{2\,\omega(\vec{p},t)}\,. \tag{3.8}$$

As already discussed in connection with Fig. 3.5 we observe for both momentum modes a strong decrease of the on-shell width for the initial distribution D1 (long dashed lines) associated with a narrowing of the spectral function. In contrast, the on-shell widths of distribution D3 (dotted lines) increase with time such that the corresponding spectral functions broaden towards the common stationary shape. For the initialization D2 (short dashed lines) we observe a non-monotonic evolution of the on-shell widths connected with a broadening of the spectral function at intermediate times. Similar to the case of the on-shell energies we find, that the results for the on-shell widths of the distributions D1 and D2 coincide well above a certain system time. As expected from the lower plots of Fig. 3.5, the on-shell width for the free thermal distribution DT (solid lines) exhibits only a weak time dependence with a slight decrease in the initial phase of the time evolution.

In summarizing this Section we point out, that there is no universal time evolution of the spectral functions for the initial distributions considered. Peak positions and widths depend on the initial configuration and evolve differently in time. However, we find only effects in the order of $< 10\%$ for the on-shell energies in the initial phase of the system evolution and initial variations of $< 50\%$ for the widths of the dominant momentum modes. Thus, depending on the physics problem of interest, one might eventually discard an explicit time dependence of the spectral functions and adopt the equilibrium shape.

3.5 The Equilibrium State

In Section 3.2 we have seen that arbitrary initial momentum configurations of the same energy density approach a stationary limit for $t \to \infty$, which is the same for all initial distributions. In this Section we will investigate, whether this stationary state is the proper thermal state for interacting Bose particles.

This question has already been addressed in Ref. [48] for an $O(N)$-invariant scalar field theory with unbroken symmetry. There it was shown that in the next-to-leading order (NLO) approximation the only translational invariant solutions are thermal ones. The importance of using the NLO approximation lies in the fact that – in contrast to the leading order (LO) calculation – scattering processes are included in the propagation which provide thermalization. Furthermore, the correlations induced by scattering lead to a non-trivial spectral function, whereas in the LO approximation one obtains the δ-function quasiparticle shape. Additionally, in the NLO calculation particle number non-conserving processes are allowed that lead to a change of the chemical potential μ, which approaches zero in the equilibrium state in agreement with the expectations for a neutral scalar theory without conserved quantum numbers.

As shown before, in our present calculations within the three-loop approximation of the 2PI effective action we describe kinetic equilibration via the sunset self-energies and also obtain a finite width for the particle spectral function. It is not obvious, however, if the stationary state obtained for $t \to \infty$ corresponds to the proper equilibrium state.

In order to clarify the nature of the asymptotic stationary state of our calculations we first change into Wigner space. The Green function and the spectral function in energy p_0 are obtained by Fourier transformation with respect to the relative time $\Delta t = t_1 - t_2$ at every system time $t = (t_1 + t_2)/2$ (cf. (3.6))

$$\bar{G}^{\gtrless}(\vec{p},p_0,t) \;=\; \int_{-\infty}^{\infty} d\Delta t \;\; \exp(i\,p_0\,\Delta t) \;\; G^{\gtrless}(\vec{p},t_1 = t+\Delta t/2, t_2 = t-\Delta t/2)\,, \qquad (3.9)$$

$$\bar{A}(\vec{p},p_0,t) \;=\; \int_{-\infty}^{\infty} d\Delta t \;\; \exp(i\,p_0\,\Delta t) \;\; A(\vec{p},t_1 = t+\Delta t/2, t_2 = t-\Delta t/2)\,. \qquad (3.10)$$

We recall, that the spectral function (3.10) can also be obtained directly from the Green functions in Wigner space by (3.5)

$$\bar{A}(\vec{p},p_0,t) \;=\; i\;\left[\,\bar{G}^{>}(\vec{p},p_0,t) \;-\; \bar{G}^{<}(\vec{p},p_0,t)\,\right]\,. \qquad (3.11)$$

Now we introduce the energy and momentum dependent distribution function $\bar{N}(\vec{p},p_0,t)$ at any system time t by

$$\begin{aligned} i\,\bar{G}^{<}(\vec{p},p_0,t) &= \bar{A}(\vec{p},p_0,t)\;\;\bar{N}(\vec{p},p_0,t)\,, \qquad (3.12)\\ i\,\bar{G}^{>}(\vec{p},p_0,t) &= \bar{A}(\vec{p},p_0,t)\;[\,\bar{N}(\vec{p},p_0,t)+1\,]\,. \end{aligned}$$

In equilibrium (at temperature T) the Green functions obey the Kubo-Martin-Schwinger relation (KMS) [84, 85] for all momenta $\vec{p}$

$$\bar{G}^{>}_{eq}(\vec{p},p_0) \;=\; \exp(p_0/T)\;\;\bar{G}^{<}_{eq}(\vec{p},p_0) \qquad\qquad \forall\,\vec{p}\,. \qquad (3.13)$$

If there exists a conserved quantum number in the theory we have, furthermore, a contribution of the corresponding chemical potential in the exponential function, which leads to a shift of arguments: $p_0/T \rightarrow (p_0-\mu)/T$. In the present case, however, there is no conserved quantum number and thus the equilibrium state has to give $\mu = 0$.

From the KMS condition of the Green functions (3.13) we obtain the equilibrium form of the distribution function (3.12) at temperature T as

$$\bar{N}_{eq}(\vec{p},p_0) \;=\; \bar{N}_{eq}(p_0) \;=\; \frac{1}{\exp(p_0/T)-1} \;=\; N_{bose}(p_0/T)\,, \qquad (3.14)$$

which is the well-known Bose distribution. As is obvious from (3.14) the equilibrium distribution can only be a function of energy p_0 and not of the momentum variable explicitly.

In Fig. 3.8 (lower part) we present the spectral function $\bar{A}(\vec{p},p_0,t)$ for the initial distribution D2 at late times $t\cdot m = 540$ for various momentum modes $|\,\vec{p}\,|/m = 0.0$,

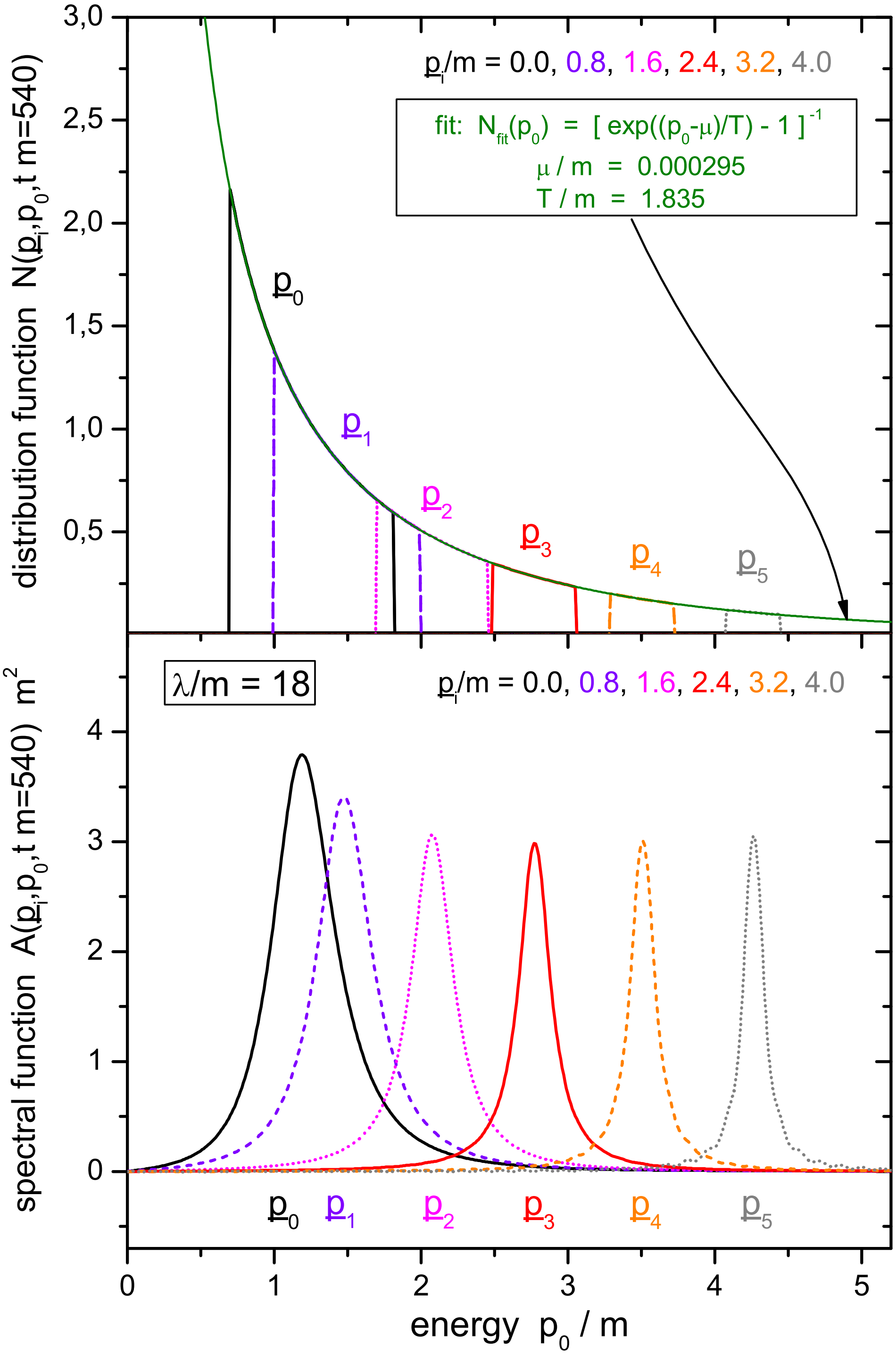

Figure 3.8: Spectral function $\bar{A}$ for various momentum modes $|\vec{p}\,|/m = 0.0$, 0.8, 1.6, 2.4, 3.2, 4.0 as a function of energy for late times $t \cdot m = 540$ (lower part). Corresponding distribution function $\bar{N}$ at the same time for the same momentum modes (upper part). All momentum modes can be fitted with a single Bose function of temperature $T_{eq}/m = 1.835$ and a chemical potential close to zero.

0.8, 1.6, 2.4, 3.2, 4.0 as a function of the energy p_0. We note, that for all other initial distributions – with equal energy density – the spectral function looks very similar at this time since the systems proceed to the same stationary state (cf. Section 3.2). We recognize that the spectral function is quite broad, especially for the low momentum modes, while for the higher momentum modes its width is slightly lower.

The distribution function $\bar{N}(p_0)$ as extracted from (3.12) is displayed in Fig. 3.8 (upper part) for the same momentum modes as a function of the energy p_0. The comparison is achieved by selecting a certain energy band around the maximum of each momentum mode considering all energies p_0 with $\bar{A}(|\vec{p}|, p_0) \cdot m^2 \geq 0.5$. We find that $\bar{N}(p_0)$ for all momentum modes can be fitted by a single Bose function with temperature $T/m = 1.835$. Thus the distribution function emerging from the Kadanoff-Baym time evolution for $t \to \infty$ approaches a Bose function in the energy p_0 that is independent of the momentum as demanded by the equilibrium form (3.14). Fig. 3.8 (upper part) demonstrates, furthermore, that the KMS-condition is fulfilled not only for on-shell energies, but for all p_0. We, therefore, have obtained the full off-shell equilibrium state by integrating the Kadanoff-Baym equations in time. In addition, the limiting stationary state is the correct equilibrium state for all energies p_0, i.e. also away from the quasiparticle energies.

We note in closing this Section, that the chemical potential μ – used as a second fit parameter – is already close to zero for these late times as expected for the correct equilibrium state of the neutral ϕ^4-theory which is characterized by a vanishing chemical potential μ in equilibrium. This, at first sight, seems rather trivial but we will show in the next Section that it is a consequence of our exact treatment. In contrast, the Boltzmann equation (cf. Section 5.4) in general leads to a stationary state for $t \to \infty$ with a finite chemical potential. We will attribute this failure of the Boltzmann approach to the absence of particle number non-conserving processes in the quasiparticle limit (see below).

3.6 Chemical Equilibration and Approach to KMS

As we have seen in the previous Section the chemical potential μ for the stationary state of the propagation at large times is close to zero in agreement with the properties of the neutral ϕ^4-theory. In this Section we will address the question of chemical equilibration in the late time evolution of the systems calculated before. In particular we are interested to examine, how the chemical potential μ vanishes with time for configurations initialized with finite chemical potentials $\mu \neq 0$ at $t = 0$.

To this aim we calculate the distribution function $N(p_0, t)$ for various system times t and extract the time-dependent chemical potential $\mu(t)$ by fitting a Bose function with parameters μ and T. The time evolution of the chemical potential μ (as extracted from the zero momentum mode) is displayed in Fig. 3.9 for various initial configurations and found to decrease almost exponentially with t to zero. For small times t the curves do not show an exponential behaviour since here we are still in the regime of kinetic nonequilibrium. Moreover, the chemical potential relaxation rate is nearly the same

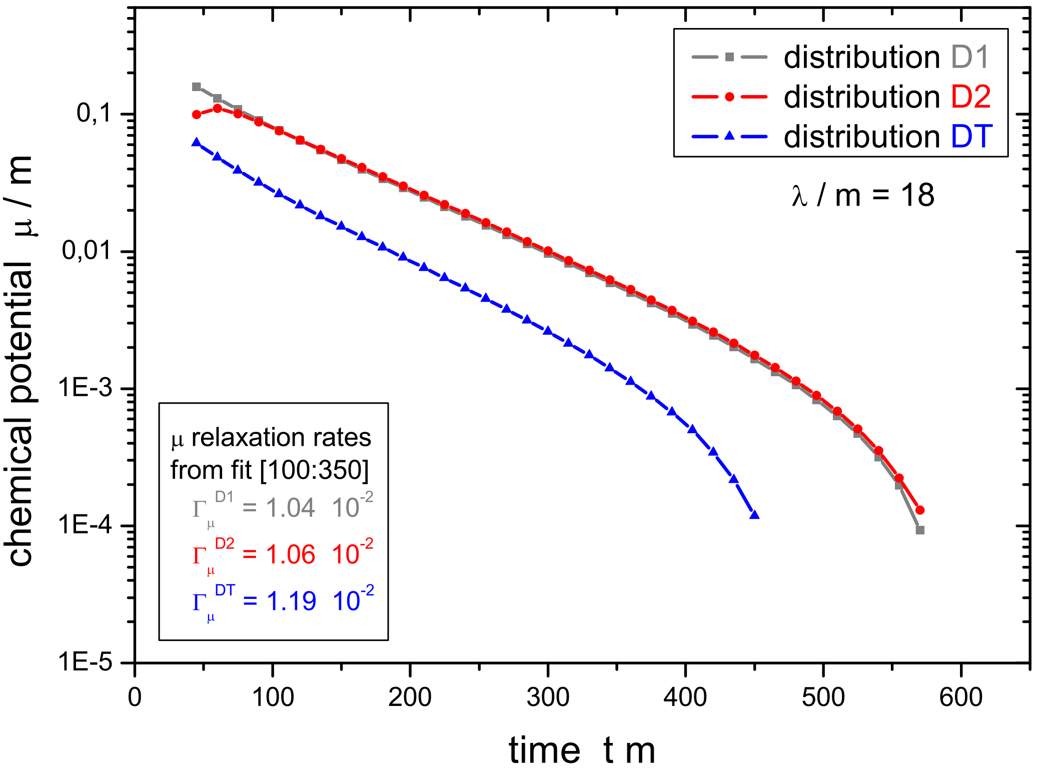

Figure 3.9: Logarithmic representation of the time evolution of the chemical potential μ for the initial distributions D1, D2 and DT. The corresponding relaxation rate $\Gamma_{\bar{\mu}}$ is determined from the exponential decrease.

for all initial configurations with the same energy density.

In order to understand the reason for this observation we calculate an estimate for this relaxation rate along the lines of Calzetta and Hu [48]. For reasons of transparency we first provide a brief derivation for the three-loop approximation of the 2PI effective action.

Since we are interested in the properties of the system close to equilibrium we again change to a Wigner representation for the Kadanoff-Baym equation. A first order gradient expansion of the Wigner transformed equation yields the following real valued transport equation (cf. Section 6.3 or [34, 35, 36])

$$\begin{aligned} &\{\, p^2 - m^2 - \bar{\Sigma}^{\delta}(t) - Re\,\bar{\Sigma}^R(p,t)\,,\, i\bar{G}^<(p,t)\,\} \;-\; \{\, i\bar{\Sigma}^<(p,t)\,,\, Re\,\bar{G}^R(p,t)\,\} \\ &\qquad = \; i\bar{G}^>(p,t)\, i\bar{\Sigma}^<(p,t) \;-\; i\bar{G}^<(p,t)\, i\bar{\Sigma}^>(p,t) \;=\; \bar{C}(p,t)\,. \end{aligned} \tag{3.15}$$

Here $\{\ ,\ \}$ denotes the $(d{+}1)$-dimensional representation of the general Poisson bracket. For the present case of spatially homogeneous systems all derivatives with respect to the mean spatial coordinates vanish. Thus it contains mean time and energy derivatives, only, and is given for arbitrary functions $\bar{F}_{1/2} = \bar{F}_{1/2}(p,t) = \bar{F}_{1/2}(\vec{p},p_0,t)$ as

$$\{\,\bar{F}_1\,,\,\bar{F}_2\,\} \;=\; \frac{\partial \bar{F}_1}{\partial p_0}\,\frac{\partial \bar{F}_2}{\partial t} \;-\; \frac{\partial \bar{F}_1}{\partial t}\,\frac{\partial \bar{F}_2}{\partial p_0}\,. \tag{3.16}$$

We first concentrate on the collision term $\bar{C}(p,t)$ – as given by the r.h.s. of equation (3.15) – for small deviations from thermal equilibrium. In our representation the correlation self-energies $i\bar{\Sigma}^{\gtrless}$ read in Wigner space

$$i\bar{\Sigma}^{\gtrless}(\vec{p},p_0,t) \;=\; \frac{\lambda^2}{6}\int\!\frac{d^{d+1}q}{(2\pi)^{d+1}}\int\!\frac{d^{d+1}r}{(2\pi)^{d+1}}\int\!\frac{d^{d+1}s}{(2\pi)^{d+1}}\;(2\pi)^{d+1}\delta^{(d+1)}(p-q-r-s) \tag{3.17}$$
$$i\bar{G}^{\gtrless}(\vec{q},q_0,t)\;\; i\bar{G}^{\gtrless}(\vec{r},r_0,t)\;\; i\bar{G}^{\gtrless}(\vec{s},s_0,t)\,,$$

where the energy and momentum integrals extend from $-\infty$ to ∞. In order to simplify the collision term we express the Green functions (similar to (3.12)) by the spectral function $\bar{A}$ and a distribution function $\tilde{N}$ via

$$i\bar{G}^{\gtrless}(\vec{p},p_0,t) \;=\; sign(p_0)\;\bar{A}(\vec{p},p_0,t)\;\Big[\,\Theta(\pm\,p_0) + \tilde{N}(\vec{p},p_0,t)\,\Big]\,. \tag{3.18}$$

The advantage of this representation is that the spectral function term $sign(p_0)\,\bar{A}(\vec{p},p_0,t)$ as well as the modified distribution function $\tilde{N}(\vec{p},p_0,t)$ are symmetric in the energy coordinate p_0 as can be deduced from $\bar{G}^{>}(\vec{p},p_0,t) = \bar{G}^{<}(-\vec{p},-p_0,t) = \bar{G}^{<}(\vec{p},-p_0,t)$ for the momentum symmetric ($\vec{p}\rightarrow -\vec{p}$) configurations considered here. The remaining asymmetric character of the Green functions is contained in the step-functions in energy. By this separation we may express the integrations over the full energy space in terms of integrations over the positive energy axis, only. Thus the collision term – additionally integrated over momenta and positive energies – can be written as

$$\int\!\frac{d^{d+1}p}{(2\pi)^{d+1}}\;\Theta(p_0)\;\bar{C}(p,t) \tag{3.19}$$
$$=\;\int\!\frac{d^{d+1}p}{(2\pi)^{d+1}}\;\Theta(p_0)\;\bar{A}(p,t)\;\Big\{\,[1{+}\tilde{N}(p,t)]\;\;i\bar{\Sigma}^{<}(p,t)\;-\;\tilde{N}(p,t)\;\;i\bar{\Sigma}^{>}(p,t)\,\Big\}$$
$$=\;\int\!Dp\;\Big\{\,[1{+}\tilde{N}(p,t)]\;\;i\bar{\Sigma}^{<}(p,t)\;-\;\tilde{N}(p,t)\;\;i\bar{\Sigma}^{>}(p,t)\,\Big\}$$
$$=\;\frac{\lambda^2}{3}\;\int\!Dp\int\!Dq\int\!Dr\int\!Ds\;\;(2\pi)^{d+1}\;\delta^{(d+1)}(p-q-r-s)$$
$$\times\Big\{\tilde{N}(p,t)\,[1{+}\tilde{N}(q,t)]\,[1{+}\tilde{N}(r,t)]\,[1{+}\tilde{N}(s,t)]\;-\;[1{+}\tilde{N}(p,t)]\,\tilde{N}(q,t)\,\tilde{N}(r,t)\,\tilde{N}(s,t)\Big\}\,.$$

Here we have introduced the short-hand notation:

$$\int\!Dp \;=\; \int\!\frac{d^{d+1}p}{(2\pi)^{d+1}}\,\Theta(p_0)\;\bar{A}(p,t) \;=\; \int\!\frac{dp_0}{(2\pi)}\,\Theta(p_0)\;\int\!\frac{d^dp}{(2\pi)^d}\;\bar{A}(\vec{p},p_0,t)\,. \tag{3.20}$$

We are interested especially in the very late time evolution, where the system is already close to equilibrium. Thus we can evaluate the integrated collision term with further approximations. First, we use the thermal spectral function $\bar{A}_{eq}(\vec{p},p_0)$ at the equilibrium temperature T_{eq}. This spectral function is calculated separately within a self-consistent scheme, which is explained in detail in Chapter 4. We note in passing, that the self-consistent thermal spectral functions (calculated numerically) are in excellent agreement with the dynamical spectral functions in the long-time limit of the nonequilibrium Kadanoff-Baym dynamics. Second, we adopt an equilibrium Bose function for the symmetrical nonequilibrium distribution function $\tilde{N}$ in energy, but allow for a small deviation in terms of a small chemical potential $\bar{\mu} = \mu/T$. This chemical potential $\bar{\mu}$ depends on the system time t as indicated by its relaxation observed in Fig. 3.9, but is assumed to be independent of energy and momentum. The near equilibrium distribution function is thus given by

$$\tilde{N}(p) \;\approx\; \tilde{N}^{\bar{\mu}}(p_0) \;=\; \frac{1}{\exp(|p_0|/T-\bar{\mu})-1} \quad \overset{\bar{\mu}\to 0}{\longrightarrow} \quad \tilde{N}^{0}(p_0) \;=\; N_{bose}(|p_0|/T)\,. \tag{3.21}$$

We now expand the integrated collision term with respect to the small parameter $\bar{\mu}$ around the equilibrium value $\bar{\mu}_{eq} = 0$. Since the zero-order contribution vanishes for the collision term in equilibrium, the first non-vanishing order is given by

$$\begin{aligned}\int\!\frac{d^{d+1}p}{(2\pi)^{d+1}}\,\Theta(p_0)\;\bar{C}(p,t) \;&=\; -\frac{\lambda^2}{3}\;2\,\bar{\mu}\;\int\!Dp_{eq}\int\!Dq_{eq}\int\!Dr_{eq}\int\!Ds_{eq} \\ &\times\,(2\pi)^{d+1}\,\delta^{(d+1)}(p-q-r-s)\;\;[1+\tilde{N}^0(p)]\;\tilde{N}^0(q)\;\tilde{N}^0(r)\;\tilde{N}^0(s)\end{aligned} \tag{3.22}$$

with the integration weighted by the thermal spectral function $\bar{A}_{eq}$ as

$$\int\!Dp_{eq} \;=\; \int\!\frac{d^{d+1}p}{(2\pi)^{d+1}}\,\Theta(p_0)\;\bar{A}_{eq}(p) \;=\; \int\!\frac{dp_0}{(2\pi)}\,\Theta(p_0)\;\int\!\frac{d^dp}{(2\pi)^d}\;\bar{A}_{eq}(\vec{p},p_0)\,. \tag{3.23}$$

On the left-hand-side of the transport equation we neglect, furthermore, the time derivative terms of the self-energies as well as the second Poisson bracket. The only contribution then stems from the drift term $2p_0\,\partial_t\,i\bar{G}^{<}(\vec{p},p_0,t)$, which might be extended by considering the energy derivative of the real part of the retarded self-energy.

The Green function is expressed again in terms of symmetric functions in energy (3.18), where the distribution function $\tilde{N}$ is given by the near equilibrium estimate (3.21) with a small time-dependent deviation $\bar{\mu}(t)$. Since the spectral function is approximated by its equilibrium form, the time derivative of the drift term gives only a contribution from the chemical potential. When integrating the complete drift term over momentum and (positive) energy space – as done above for the right-hand-side – we obtain in lowest order of the small chemical potential

$$\begin{aligned}\int\frac{d^{d+1}p}{(2\pi)^{d+1}}\,\Theta(p_0)\left\{2p_0\,\partial_t\,i\bar{G}^<(p,t)\right\} &\approx \int\frac{d^{d+1}p}{(2\pi)^{d+1}}\,\Theta(p_0)\;\bar{A}_{eq}(p)\;\;2p_0\;\partial_t\;\tilde{N}^{\bar{\mu}}(p,t) \qquad (3.24)\\ &\approx \frac{\partial\bar{\mu}(t)}{\partial t}\int\! Dp_{eq}\;\;2p_0\;\tilde{N}^0(p_0)\;[1+\tilde{N}^0(p_0)]\;.\end{aligned}$$

By taking also into account the energy derivative of the retarded self-energy we gain the improved result

$$\begin{aligned}&\int\frac{d^{d+1}p}{(2\pi)^{d+1}}\,\Theta(p_0)\left\{\left(2p_0-\partial_{p_0}Re\,\bar{\Sigma}^R_{eq}(p)\right)\;\partial_t\;i\bar{G}^<(p,t)\right\} \qquad (3.25)\\ \approx\;&\frac{\partial\bar{\mu}(t)}{\partial t}\int\! Dp_{eq}\;\;\left(2p_0-\partial_{p_0}Re\,\bar{\Sigma}^R_{eq}(p)\right)\;\tilde{N}^0(p_0)\;\;[1+\tilde{N}^0(p_0)]\;.\end{aligned}$$

Combining now both half-sides of the approximated transport equation we obtain

$$\frac{\partial\bar{\mu}(t)}{\partial t}\;\;K_1([A_{eq}(\lambda,T)];T)\;=\;-\,\bar{\mu}(t)\;\;K_2([A_{eq}(\lambda,T)];T,\lambda) \qquad (3.26)$$

with the temperature and coupling constant dependent functions

$$K_1([A_{eq}(\lambda,T)];T)\;=\;\int\! Dp_{eq}\;\;\left(2p_0-\partial_{p_0}Re\,\Sigma^R_{eq}(p)\right)\;\tilde{N}^0(p_0)\;\;[1+\tilde{N}^0(p_0)] \qquad (3.27)$$

$$\begin{aligned}K_2([A_{eq}(\lambda,T)];T,\lambda)\;&=\;\frac{2}{3}\,\lambda^2\int\! Dp_{eq}\int\! Dq_{eq}\int\! Dr_{eq}\int\! Ds_{eq}\;\;(2\pi)^{d+1}\;\delta^{(d+1)}(p-q-r-s)\\ &\qquad[1+\tilde{N}^0(p_0)]\;\;\tilde{N}^0(q_0)\;\;\tilde{N}^0(r_0)\;\;\tilde{N}^0(s_0) \qquad (3.28)\\ &=\;\frac{2}{3}\,\lambda^2\int\! Dp_{eq}\int\! Dq_{eq}\int\! Dr_{eq}\int\! Ds_{eq}\;\;(2\pi)^{d+1}\;\delta^{(d+1)}(p-q-r-s)\\ &\qquad\tilde{N}^0(p_0)\;[1+\tilde{N}^0(q_0)]\;[1+\tilde{N}^0(r_0)]\;[1+\tilde{N}^0(s_0)]\;.\end{aligned}$$

Thus the chemical potential decreases exponentially as

$$\bar{\mu}(t) \;=\; \exp(-K_2/K_1 \cdot t) \;=\; \exp(-\Gamma_{\bar{\mu}} \cdot t) \tag{3.29}$$

with the relaxation rate given by

$$\Gamma_{\bar{\mu}} = K_2/K_1 \,. \tag{3.30}$$

The equations above provide an explanation for the observed behaviour of the relaxation of the chemical potential. At first we recognize the exponential nature (3.29) of the processes seen in Fig. 3.9. The relaxation of the chemical potential originates – as seen from (3.28) – from particle number non-conserving $1 \leftrightarrow 3$ processes. This is easily recognized when considering the distribution functions $\tilde{N}$ assigned to incoming particles as well as the corresponding Bose enhancement factors $1 + \tilde{N}$ for the outgoing ones. Ordinary particle number conserving $2 \leftrightarrow 2$ scattering processes do not contribute. Thus it is not surprising, that a relaxation of the chemical potential is not described in the on-shell Boltzmann limit and the correct equilibrium state with vanishing chemical potential is missed (cf. Section 5.4).

The corresponding time evolution of the total particle number density n_{eff}^{tot} is shown in Fig. 3.10. It is obtained as the momentum space integral over the effective distribution function, which is defined for symmetric ($\vec{p} \to -\vec{p}$) configurations by the equal-time Green functions as [69]

$$n_{eff}(\vec{p},t) \;=\; \sqrt{G^{<}_{\phi\phi}(\vec{p},t,t)\;\; G^{<}_{\pi\pi}(\vec{p},t,t)} \;-\; \frac{1}{2}\,. \tag{3.31}$$

From Fig. 3.10 we clearly see that the particle number for the full Kadanoff-Baym equation is not constant in time, but changes due to $1 \leftrightarrow 3$ transitions. Finally, the distributions D1, D2 and DT show an excess of particles – related to their positive chemical potential – that is reduced until the common particle number is reached in the stationary limit. In contrast, the distribution D3 (dotted line) with initially well separated maxima in momentum space has too few particles, however, during the time evolution particles are produced such that the system reaches the common equilibrium state as well.

Furthermore, we point out the importance of the spectral function entering the relaxation rate (3.28) via the integral measures. Since $1 \leftrightarrow 3$ processes are responsible for the chemical equilibration, especially the shape of the spectral functions for high and low energies, i.e. above and below the three-particle threshold, is of great importance. From the formula above we also find an explanation for the fact, that all equal energy initializations – although starting with different absolute values of the chemical potential – show approximately the same relaxation rate. The spectral functions for the

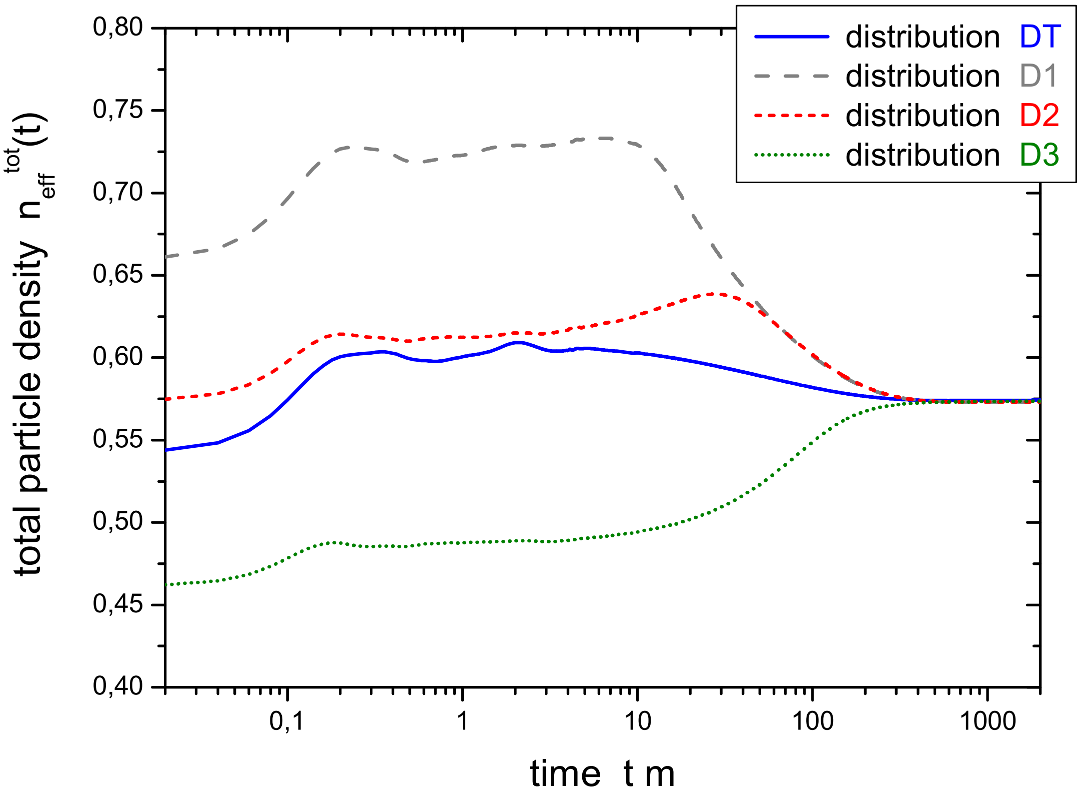

Figure 3.10: Total particle number density $n_{eff}^{tot}(t)$ for the initializations D1, D2, D3 and DT as a function of time. The particle number is not constant during the evolution, but changes due to non-conserving transitions ($1 \leftrightarrow 3$) that are allowed within the full Kadanoff-Baym dynamics.

different initializations have already almost converged to the thermal spectral function (for the equilibrium temperature of $T_{eq}/m = 1.835$ and coupling constant $\lambda/m = 18$) and are therefore comparable during the late stage of the evolution. The same holds approximately for the respective distribution functions, that approach Bose distribution functions at temperature T_{eq}. Thus we can deduce from (3.28) that the relaxation rate should be approximately the same for the different initial value problems considered.

Indeed, the estimate for the chemical relaxation (3.30) rate works rather well quantitatively. By calculating the thermal spectral functions independently within a self-consistent scheme at equilibrium temperature T_{eq} for coupling constant $\lambda/m = 18$ we find (together with the distribution functions of the same temperature) – by solving the multidimensional integrations – a value of $\Gamma_{\bar{\mu}}/m \approx 1.12 \cdot 10^{-2}$ (for the drift term only) and $\Gamma_{\bar{\mu}}/m \approx 1.17 \cdot 10^{-2}$ (when including additionally the energy dependence of the retarded self-energy) for the relaxation rate. The agreement with the results of the actual calculations in Fig. 3.9 given by $\Gamma_{\bar{\mu}}^{D1}/m \approx 1.04 \cdot 10^{-2}$, $\Gamma_{\bar{\mu}}^{D2}/m \approx 1.06 \cdot 10^{-2}$, and $\Gamma_{\bar{\mu}}^{DT}/m \approx 1.19 \cdot 10^{-2}$, is sufficiently good.

3.7 Dynamics Close to the Thermal State

In this Section we address the properties of systems close to thermal equilibrium. It is a widely used assumption that there exists a regime close to the thermal state, where the relaxation approximation is valid. Especially interesting are settings, where all momentum modes are in equilibrium, but only a single momentum mode $\vec{p}$ is out of equilibrium and deviates from its equilibrium value by a small amount δN. In such a case $\delta N(t)$ should decrease exponentially in time. The corresponding rate can be calculated in the usual quasiparticle approximation (i.e. starting from the standard Boltzmann equation) and is given by the on-shell width of the particle as determined from the imaginary part of the retarded self-energy at the on-shell energy (with respect to the momentum $\vec{p}$) as $\gamma_\omega(\vec{p}) = -Im\,\bar{\Sigma}^R(\vec{p},\omega(\vec{p}))/\omega(\vec{p})$.

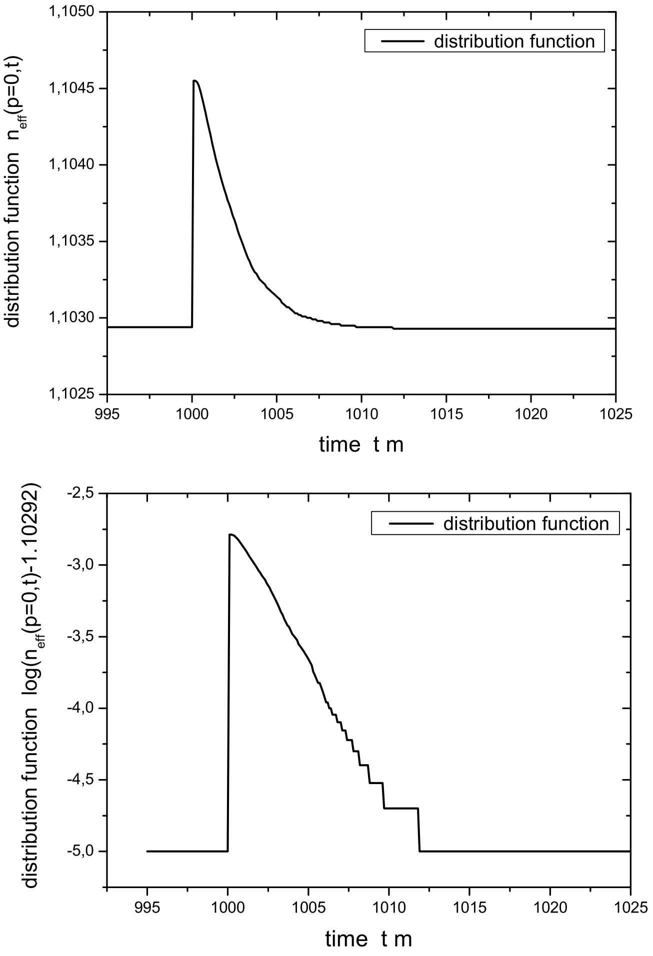

Figure 3.11: Time evolution of the zero momentum mode of the distribution function that has been excited at the system time $t_k \cdot m = 1000$ (upper part). From the exponential decrease of the deviation from the equilibrium value (that has been subtracted in the lower plot) the relaxation rate can be extracted.

In order to study the relaxation behaviour within the full Kadanoff-Baym theory we generate a corresponding initial state by the following procedure: We first start with a general nonequilibrium distribution at $t = 0$ and let it evolve in time. After a sufficiently long time period all momentum modes of the system get close to equilibrium. We then excite only a single momentum mode at a specific time t_k by multiplying the equal-time Green functions $G^<_{\phi\phi}(\vec{p}, t, t)$ and $G^<_{\pi\pi}(\vec{p}, t, t)$ at $t = t_k$ with a factor close to 1. As a result the corresponding effective occupation number $n_{eff}(\vec{p}, t)$ (3.31) differs slightly from its equilibrium value by $\Delta N(t_k)$.

For $t > t_k$ this deviation $\Delta N(t)$ indeed vanishes exponentially according to the full Kadanoff-Baym equations as shown in Fig. 3.11 for the zero momentum mode of the distribution function. For the specific case shown in Fig. 3.11 the equilibrium state has been generated by starting with the initial distribution DT for a coupling constant $\lambda/m = 18$. At the time $t_k \cdot m = 1000$ both Green functions have been changed simultaneously by only 10^{-3} in order to avoid large disturbances of the system. From the exponential decrease of the deviation one can directly extract the relaxation rate.

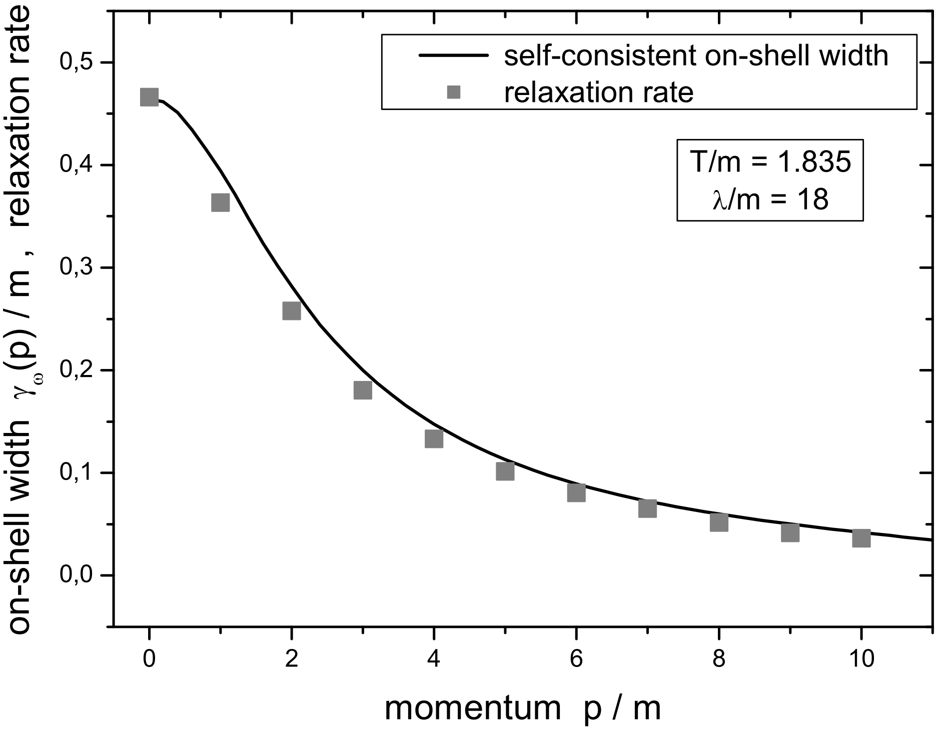

Figure 3.12: Comparison of the relaxation rates for single excited momentum modes (full dots) with the on-shell widths calculated at finite temperature for various momentum modes. The equilibrium state is characterized by $\lambda/m = 18$ and a temperature of $T_{eq}/m = 1.835$.

This extraction has been done for several momentum modes and leads to the numbers displayed in Fig. 3.12 by the full squares. In this plot, furthermore, the extracted relaxation rates are compared to the on-shell width of the particles as indicated by the line. The latter values have been obtained within an independent finite temperature calculation involving the self-consistent spectral function (and width). The exact method is described in detail in Section 4.1. We note, that – apart from the coupling constant – only the equilibrium temperature $T_{eq}/m = 1.835$ enters into the self-consistent scheme as input. It yields the on-shell energies $\omega(\vec{p})$ and the self-consistent width for all momenta and energies such that the on-shell width $\gamma_\omega(\vec{p})$ can be determined via (3.8). The comparison in Fig. 3.12 shows a very good agreement of the results for the relaxation rate obtained from a time-dependent single mode excitation of an equilibrated system with the findings for the on-shell width calculated within the self-consistent thermal approach. Thus the strong relation between both quantities has been shown explicitly for the case of a general off-shell nonequilibrium theory.

Chapter 4

Self-Consistent Spectral Functions at Finite Temperature

Whenever dealing with strongly interacting systems the single-particle spectral function is of great importance. In particular for systems at high temperature and/or high densities the spectral functions may exhibit a large width connected to a possibly complicated structure rather than showing a δ-function shape as in the case of on-shell quasiparticles.

For systems in equilibrium there are two standard approaches for calculating the spectral function: i) within the imaginary time formalism (ITF) by summation over discrete Matsubara frequencies, ii) within the real-time formalism (RTF), where the energy is considered as a real and continuous variable [85]. One great advantage of the approach ii) lies in the fact that it can be easily connected to the nonequilibrium situation. Therefore, we will use for our further developments the real-time formalism (RTF) as familiar from nonequilibrium calculations. We recall that the perturbative calculation of the sunset graph has been given in various works [86, 87, 88, 89]. Very recently a first self-consistent treatment of the ϕ^4-theory in 3+1 dimensions up to this order has been presented in [79].

4.1 The Iteration Scheme

In this Section we present a method for the calculation of self-consistent spectral functions, which i) treats different order contributions in the number of loops of the self-energy on the same footing and ii) incorporates the finite width due to the imaginary part of the self-energy. Thus the actual spectral function reenters the calculation and is iterated until self-consistency is reached.

Our iteration scheme is divided into the following steps:

1) The Green functions $\bar{G}^{\gtrless}$ are specified in energy-momentum space $(\vec{p}, p_0)$. In the initial step this can be done by assuming free Green functions (i.e. with δ-function like spectral functions) at the desired equilibrium temperature T.

2) We change to the mixed representation by Fourier transformation with respect to p_0 and calculate the Green functions $G^{\gtrless}$ as a function of momentum $\vec{p}$ and relative time Δt. Since we are interested in a (static) equilibrium situation, there is no dependence on a mean time variable. In case of the initial on-shell Green functions the mixed representation $(\vec{p}, \Delta t)$ is obtained analytically (5.1).

3) The collisional self-energies $\Sigma^{\gtrless}(\vec{p}, \Delta t)$ are calculated in the mixed representation with the Green functions $G^{\gtrless}(\vec{p}, \Delta t)$ via (2.24).

Additional remark: step 3) can be performed in several ways depending on the explicit structure of the self-energy diagrams. For the case of the sunset diagram in ϕ^4-theory we utilize another Fourier-method. Here the self-energies are first evaluated as a function of relative spatial (and time) coordinates, since the sunset self-energy is (in coordinate space) simply a product of coordinate space Green functions that are available by Fourier transformation with respect to the momentum. In the final step these self-energies are transformed by a spatial Fourier transformation back into the desired mixed representation.

4) From the collisional self-energies $\Sigma^{\gtrless}(\vec{p}, \Delta t)$ we determine the retarded self-energy

$$\Sigma^R(\vec{p}, \Delta t) \;=\; \Theta(\Delta t)\; [\, \Sigma^>(\vec{p}, \Delta t) \;-\; \Sigma^<(\vec{p}, \Delta t)\,]\,. \tag{4.1}$$

Thus the retarded self-energy is calculated in the mixed representation by explicit introduction of a step-function in relative time. As we will discuss below this is the main advantage of our scheme because it guarantees analyticity and thus the normalization of the self-consistent spectral function.

5) The retarded self-energy is Fourier transformed back into energy-momentum space $(\vec{p}, p_0)$ and separated into its real part $Re\, \bar{\Sigma}^R(\vec{p}, p_0)$ and its imaginary part, which is related to the width as $\bar{\Gamma}(\vec{p}, p_0) = -2\, Im\, \bar{\Sigma}^R(\vec{p}, p_0)$.

6) Calculating, furthermore, the real valued tadpole self-energy $\bar{\Sigma}^\delta$ the spectral function is given as

$$\bar{A}(\vec{p}, p_0) \;=\; \frac{\bar{\Gamma}(\vec{p}, p_0)}{[\, p_0^2 - \vec{p}^{\,2} - m^2 - \delta m^2 - \bar{\Sigma}^\delta - Re\, \bar{\Sigma}^R(\vec{p}, p_0)\,]^2 + \bar{\Gamma}^2(\vec{p}, p_0)/4}\,. \tag{4.2}$$

Here besides the initial physical mass m the mass counterterms $\delta m^2 = \delta m^2_{tad} + \delta m^2_{sun}$

enter, that have to be calculated independently (see Appendix B). The expression (4.2) for the spectral function is valid in general within a first order gradient expansion of the transport equation and is exact in equilibrium [34]. It is obtained as $\bar{A}(\vec{p},p_0) = -2\,Im\,\bar{G}^R(\vec{p},p_0)$ from the Green function that solves the retarded Dyson-Schwinger equation (2.20) (see also Section 6.2).

7) Now we can determine the Wightman functions $\bar{G}^{\gtrless}$ in the next iteration step in energy-momentum space by the relations

$$i\bar{G}^{<}(\vec{p},p_0) \;=\; \bar{N}(\vec{p},p_0)\,\bar{A}(\vec{p},p_0)\,, \qquad i\bar{G}^{>}(\vec{p},p_0) \;=\; [1+\bar{N}(\vec{p},p_0)]\,\bar{A}(\vec{p},p_0)\,. \tag{4.3}$$

The separation of the Wightman functions into distribution functions $\bar{N}$ and spectral function $\bar{A}$ is always possible and well-known from the derivation of transport equations [34]. We recall that in thermal equilibrium the distribution function N only depends on the energy variable p_0 and is independent of the momenta $\vec{p}$. It is given – for the scalar theory – by the Bose distribution

$$\bar{N}_{eq}(\vec{p},p_0) \;=\; \bar{N}_{eq}(p_0) \;=\; \frac{1}{\exp(p_0/T)-1} \;=\; N_{bose}(p_0/T)\,, \tag{4.4}$$

at equilibrium temperature T. The method is not restricted to finite temperature, but can be easily extended to finite densities. The presence of conserved quantities, as given for a charged complex scalar theory in the most simple case, can be accounted for by inclusion of a corresponding chemical potential μ in the Bose distribution function. In thermal equilibrium the Wightman functions are connected by the Kubo-Martin-Schwinger (KMS) periodicity condition

$$\bar{G}^{>}(\vec{p},p_0) \;=\; \exp(p_0/T)\;\;\bar{G}^{<}(\vec{p},p_0) \tag{4.5}$$

as inherent in the relations (4.3). The same holds for the collisional self-energies at finite temperature. Thus the calculations take slightly less effort than implied above.

By calculating the new Green functions in 7) we have closed the iteration loop. The iteration procedure is reentered at step 2), where the new Green functions are transformed to relative time space in order to calculate the corresponding new collisional self-energies. The alternating calculation of the Green function $G^{<}$ and of the spectral function A is performed until self-consistency is reached.

The scheme proposed above has one central advantage in comparison to the related approach given in [90]. In that case an iteration loop between the Green function and the spectral function or – to be more precise – the width is used as well. The width is determined from the imaginary part of the collisional self-energies directly in energy-momentum space and inserted into the equation for the spectral function. The real part, however, is either neglected or calculated by a dispersion relation in energy. The improvement of our method lies in using the mixed representation: Since the retarded self-energy is calculated in $(\vec{p}, \Delta t)$-space with an explicit Θ-function in relative time, analyticity is imposed automatically, i.e. the real part $Re\,\bar{\Sigma}^R(\vec{p}, p_0)$ and the imaginary part $Im\,\bar{\Sigma}^R(\vec{p}, p_0)$ of the retarded self-energy in energy-momentum space are connected by a dispersion relation. Furthermore, the spectral function A is normalized accordingly. This is not the case for some schemes that obtain the real part and the imaginary part of the retarded self-energy by different methods. Here problems with the normalization of the spectral function and analyticity may arise. Lateron we will illustrate this point in detail.

Within that context we also note that phenomenological models frequently use form factors, i.e. non-local vertices, to cure renormalization problems. Such form factors typically have poles in the complex energy plane. Using the form factors for the calculation of real and imaginary part of a self-energy therefore messes up the analyticity properties and in general destroys the normalization of the spectral function. A proper way out is indeed the calculation of only the imaginary part of the retarded self-energy from the corresponding loop expressions including form factors. The real part is calculated afterwards from a dispersion relation to insure the correct analyticity properties. Within our ϕ^4-theory renormalization is a well-defined concept. Hence in our case there is no need to resort to form factors. Therefore, we can use the computationally less expensive method discussed above for the iterative calculation of the self-energies and the two-point functions.

A further advantage lies in the fact that our method, especially in combination with the Fourier-prescription for the momentum integrals, is computationally fast in comparison to standard procedures of calculating multidimensional momentum integrals. Furthermore, due to the spherical symmetry of the equilibrium state it can be performed very efficiently. Moreover, it is easily applied to all temperatures and chemical potentials, i.e. as long as the distribution function $\bar{N}_{eq}(p_0, T, \mu)$ is specified.

Our scheme is appropriate for simple self-energies, as for example the sunset diagram. Basically it is applicable also for more complex diagrams since it always reduces the number of necessary integrations. The whole procedure profits from the fact that the appearing convolution integrals in momentum and energy correspond to ordinary products of coordinate space functions. Thus the required integrations to obtain the self-energy can be reduced considerably. In case of the sunset diagram, that has only two external points (given by the coordinates of the self-energy) but no internal points, integrations can be avoided completely besides the Fourier transformation itself. For more complicated diagrams one has to integrate over the space-time coordinates of all internal points. Nevertheless, at least the contributions from the external points can be handled in a multiplicative manner rather than performing time consuming energy-momentum integrations.

When discussing the range of applicability of our method one should note as well, that it is mainly suited for field theories that are void of complicated renormalization prescriptions. In our case of ϕ^4-theory in 2+1 space-time dimensions the renormalization can be done by simple mass counterterms since only the pure vacuum contributions of both self-energies diverge. This mass renormalization scheme can be easily included in the iteration procedure as seen by the representation for the spectral function (4.2). In cases of diverging diagrams, that contain temperature dependent parts, the renormalization procedure is much more involved [78, 79]. In such situations our method might be complicated significantly.

Our approach of using a mixed representation of momentum and relative time (instead of the energy) is related to a method used within the imaginary time formalism (ITF). In this case a mixed representation is established as well, which is known as the Saclay-method [91, 92]. The representation is obtained by transforming from discrete and imaginary energy variables – the Matsubara frequencies $\omega_n = 2\pi i\, nT$ (for bosons) – towards an imaginary time variable τ. Due to the discrete structure of the temperature dependent Matsubara frequencies the imaginary time variable is restricted by the temperature T as $\tau \in [0, 1/T]$. In contrast, in the real-time formalism (RTF) the relative time variable Δt is unbounded in accordance with the continuous energy variable p_0. The energy integrations of the RTF correspond in the ITF to summations over the infinite number of discrete Matsubara frequencies. In case of perturbative calculations there exist comfortable expressions for the latter series which make the calculation easier. In a self-consistent calculation the finite temperature Green functions assume a complicated structure rather than the simple on-shell form and a numerical evaluation is necessary. This is of course possible, but intricate, since the very high Matsubara-frequencies give still a considerable contribution to the series. Thus it is necessary to include all these large modes even if the retarded self-energies are rather small at high frequencies. In order to reduce the large computing time one might calculate the retarded self-energy only up to a certain Matsubara frequency ignoring the small retarded self-energy for all higher modes. For the higher modes the Green function of the next iteration step is determined by inclusion of the frequency and momentum independent – and thus for large frequencies non-vanishing – tadpole self-energy, only. As we have tested, this prescription seems to lead to a sufficient accuracy with a reduced computational time.

4.2 Finite Temperature Spectral Functions

In the following we show the actual results calculated within the self-consistent scheme described above. The tadpole self-energy as well as the retarded sunset self-energy are included self-consistently using the renormalization prescription of Appendix B. In Fig. 4.1 the width $\bar{\Gamma}$ is displayed as a function of the energy p_0 for four different momentum modes $|\vec{p}|/m =$ 0, 2, 4, 6 for a temperature of $T/m = 1.835$ and a coupling constant of $\lambda/m = 18$. This configuration corresponds to the thermalized state obtained by the time evolution of the polar symmetric initial momentum distributions D1, D2, D3 and DT in Section 3. For comparison we present, furthermore, the width as obtained by a perturbative calculation (as indicated by the dashed lines) for the same momentum modes, and with the same external parameters T and λ. The results have been obtained with the (self-consistent) effective mass $m^*_{tad,it}/m = 1.490$ on the tadpole level, i.e. by the iterative solution of the tadpole gap equation. This is in the spirit of Wang and

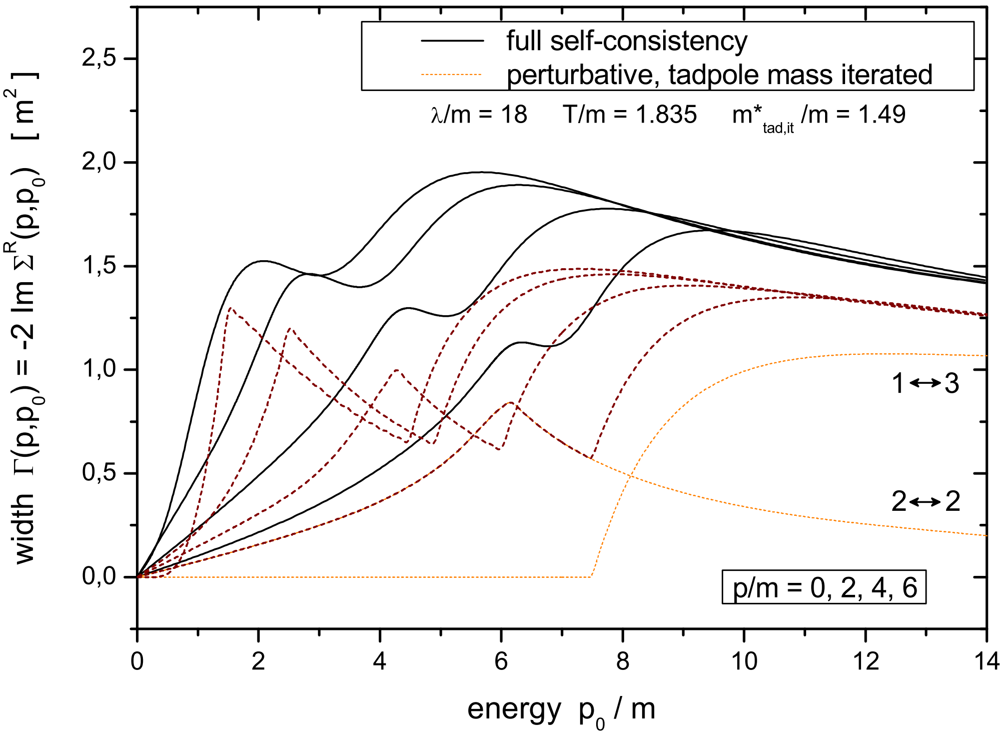

Figure 4.1: Self-consistent width (solid lines) and perturbative width (dashed lines) as a function of the energy p_0/m for various momentum modes $|\vec{p}|/m = 0,\ 2,\ 4,\ 6$ for a thermal system at temperature $T/m = 1.835$ with coupling constant $\lambda/m = 18$. For the highest momentum mode $|\vec{p}|/m = 6$ of the perturbative calculation, the collision contribution $(2 \leftrightarrow 2)$ and the decay contribution $(1 \leftrightarrow 3)$ to the width are explicitly displayed.

Heinz [88] who firstly determined the effective mass in lowest order (also in a self-consistent way) and inserted this mass in the following into the expressions for the width calculated within the next order. We see from Fig. 4.1 that the perturbative width shows a similar (two maxima) shape for all momentum modes (for the given case of $m^* < T_{eq}$). It is characterized by an increase towards a maximum around the on-shell energy $\omega^*_{\vec{p}} = \sqrt{\vec{p}^{\,2} + m^{*\,2}}$ and falling off beyond. This behaviour stems from the $2 \leftrightarrow 2$ processes in the self-energies as indicated for the highest momentum mode $|\vec{p}|/m = 6$ by the thin line. Particles can be scattered by other particles – present in the system at finite temperature – such that they achieve the shown (collisional) damping width. This collision contribution vanishes for a system at temperature $T = 0$. Furthermore, particles with sufficient energy can decay into three other particles. Above the threshold of $p_{0,th}(\vec{p}) = \sqrt{\vec{p}^{\,2} + (3\,m^*)^2}$ these $1 \leftrightarrow 3$ processes lead to an increase of the width (as marked for the highest momentum mode by the second thin line). Finally, the width Γ decreases for larger energies and assumes a momentum-independent constant value

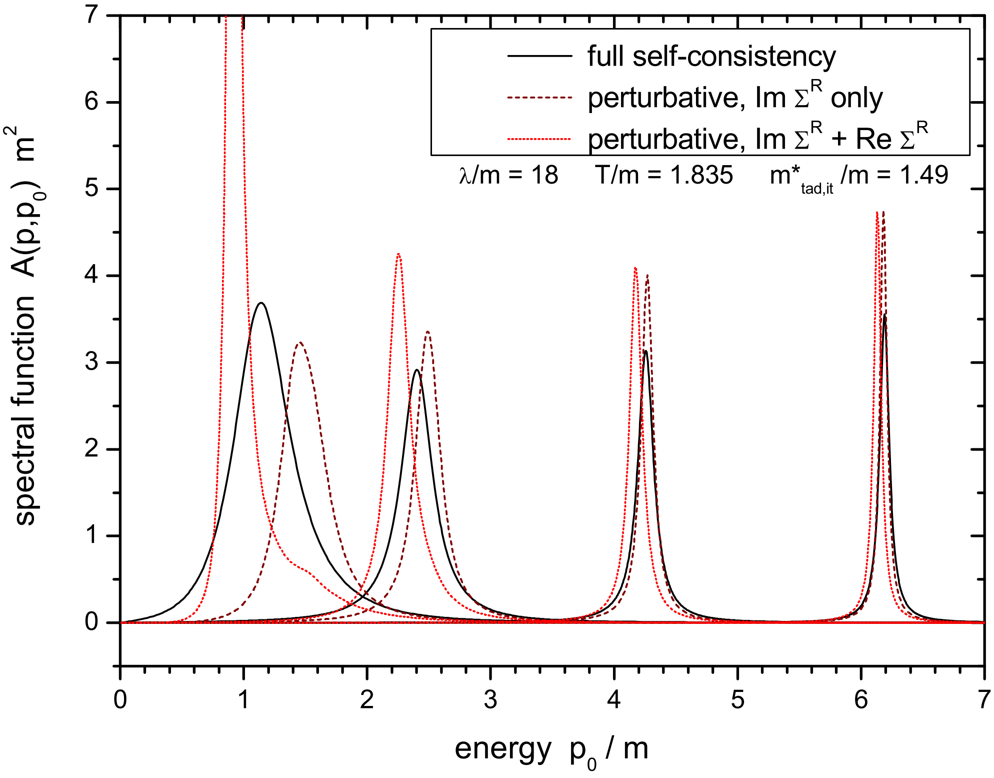

Figure 4.2: Self-consistent spectral function as a function of the energy p_0/m for various momentum modes $|\vec{p}|/m = 0, 2, 4, 6$ for a thermal system at temperature $T/m = 1.835$ with coupling constant $\lambda/m = 18$ (solid lines). Furthermore, spectral functions as obtained in a perturbative calculation with (dotted lines) and without (dashed lines) inclusion of the real part of the retarded self-energy are shown in comparison.

in the high energy limit. This behaviour is in contrast to the case of 3+1 dimensions, where the width shows a monotonous increase for very high energies.

In comparison, the width calculated within the self-consistent scheme shows a similar two maximum shape. Here, both processes are incorporated although they cannot be separated easily due to the self-consistent iteration. Apparently, the sharp structures present in the perturbative calculation have been washed out considerably. The kink structures resulting from threshold effects slightly disappear since the (broad) spectral function reenters the evaluation in this iteration scheme. Furthermore, also the position of the first maximum can be moved, as seen especially for the low momentum modes. This is an effect of the self-consistent spectral function that accounts also for mass shifts caused by the tadpole self-energy and the real part of the retarded sunset self-energy. Overall, Fig. 4.1 shows that the width in the self-consistent calculation can be significantly larger than in the corresponding perturbative estimate. However, the differences are reduced for smaller coupling constants in agreement with results

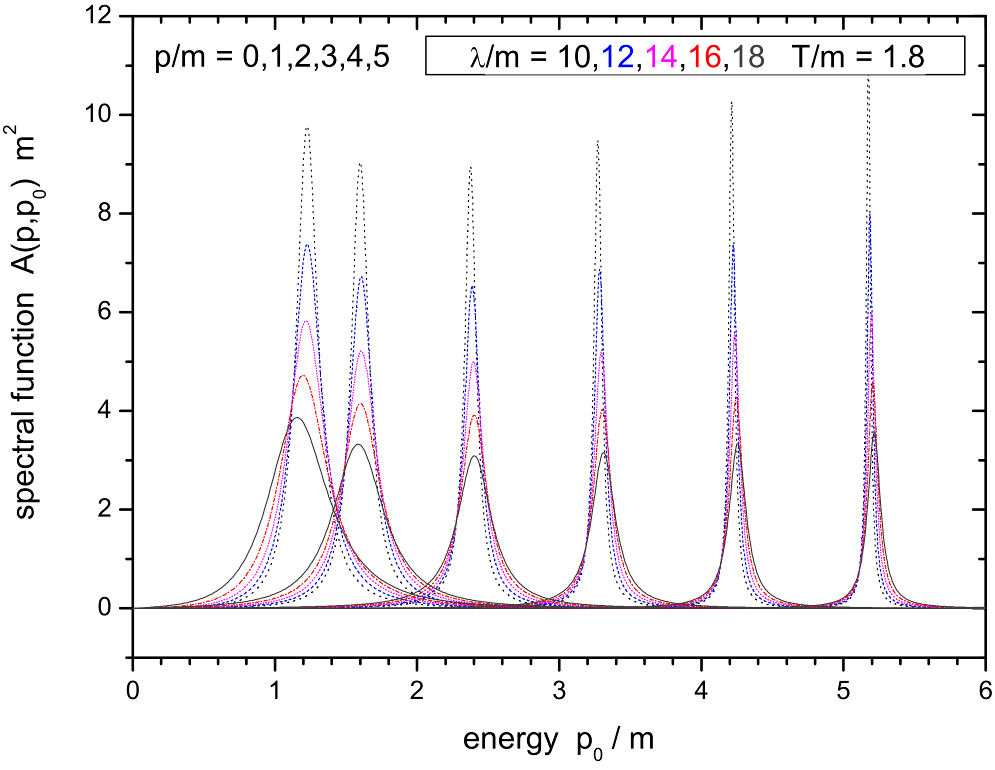

Figure 4.3: Self-consistent spectral function as a function of the energy p_0/m for coupling constants $\lambda/m = 10$, 12, 14, 16, 18 at temperature $T/m = 1.8$. With increasing interaction strength the spectral functions become broader for all momentum modes $|\vec{p}|/m = 0$, 1, 2, 3, 4, 5.

obtained within the classical approximation [93].

In Fig. 4.2 we present the corresponding spectral functions for the system at temperature $T/m = 1.835$ and coupling constant $\lambda/m = 18$. The spectral functions are displayed as a function of the energy for the same four momentum modes of $|\vec{p}|/m =$ 0, 2, 4, 6. We observe that the larger width of the full self-consistent calculation (solid lines) in comparison to the perturbative result (dashed lines in Fig. 4.2) reflects itself in a slightly broader spectral function. Furthermore, the perturbative spectral function is located at higher energies compared to the full result, in particular for the low momentum modes. This is due to the fact, that in the perturbative calculation the effective mass of the particles is fixed before evaluating the width by a solution of the tadpole gap equation. Mass modifications due to the interactions of higher order are neglected within this approximation in line with [88], where the spectral function is determined solely by the imaginary part of the retarded self-energy. On the other hand, the reduction of the effective mass due to the real part of the retarded sunset self-energy is included in the self-consistent approach leading to a shift of the spectral function maxima to lower on-shell energies. Moreover, the tadpole mass shift is not fixed in that calculation but modified during the iteration process as well. In the present case the momentum and energy independent tadpole mass shift within the self-consistent second order calculation is given as $\Delta m_{tad}^2/m^2 = 1.094$ in comparison to the value obtained for the first order calculation by the tadpole gap equation of $\Delta m_{tad}^2/m^2 = 1.220$. This indicates already a shift of the spectral function to lower on-shell energies although the size is small compared to the effect coming from the second order self-energy. Thus both spectral functions are getting closer again for higher momenta where the sunset mass shift is smaller.

At this point we emphasize that the spectral function obtained by the self-consistent scheme obeys the normalization condition to high accuracy (3.7). This is not the case for a perturbative calculation where only the imaginary part of the retarded self-energy is taken into account as in [88]. When inserting only the expression for the width into the equilibrium form of the spectral function but neglecting the real part of the retarded self-energy, the normalization condition may be violated strongly. In the present perturbative calculation the correct normalization is underestimated by $\approx 20\%$ for the small momentum modes. Thus these kinds of spectral functions, furthermore, strongly violate the desired analyticity properties. In order to show the importance of the real part of the retarded self-energy even on the shape of the spectral function we present in Figure 4.2 a calculation which takes this contribution explicitly into account. Calculating the complete retarded self-energy perturbatively with an effective mass of $m_{tad,it}^*/m = 1.490$ yields the spectral function displayed for the same momentum modes with dotted lines. We see that the shape of the spectral function is strongly affected in particular for the small momentum modes. The inclusion of the real part causes a significant shift of the spectral function to lower energies. Since the width is smaller in that region (cf. Fig. 4.1), the spectral function assumes – especially for the low momentum modes – a much narrower shape. Nevertheless, the inclusion of the real part of the retarded self-energy leads to a proper normalization of the corresponding spectral functions. Still there is a significant disagreement between the improved perturbative (dotted line) and the self-consistent solution (solid line).

In order to illustrate the dependence on the interaction strength we show in Fig. 4.3 the spectral function at temperature $T/m = 1.8$ for coupling constants $\lambda/m =$ 10, 12, 14, 16, 18. As expected, the spectral functions are significantly broader for increasing interaction strength. Again the low lying momentum modes achieve the broadest shape, respectively. Furthermore, the on-shell value is changing with λ, which is easily visible for the small momentum modes. Here two effects are superimposed: The upward mass shift generated by the tadpole diagram is competing with the negative shift from the retarded self-energy, which gives a significant contribution primarily in the low momentum regime. With increasing coupling strength the higher order term dominates, which results in a lowering of the on-shell energies for small momenta as seen in Fig. 4.3. In the high momentum region – where the real part of the retarded self-energy is small – the constant tadpole mass shift dominates and leads to an increase of the effective mass with the coupling constant. This effect can already be seen for the modes $|\vec{p}|/m = 4, 5$ and is even stronger for higher momenta (not displayed here).

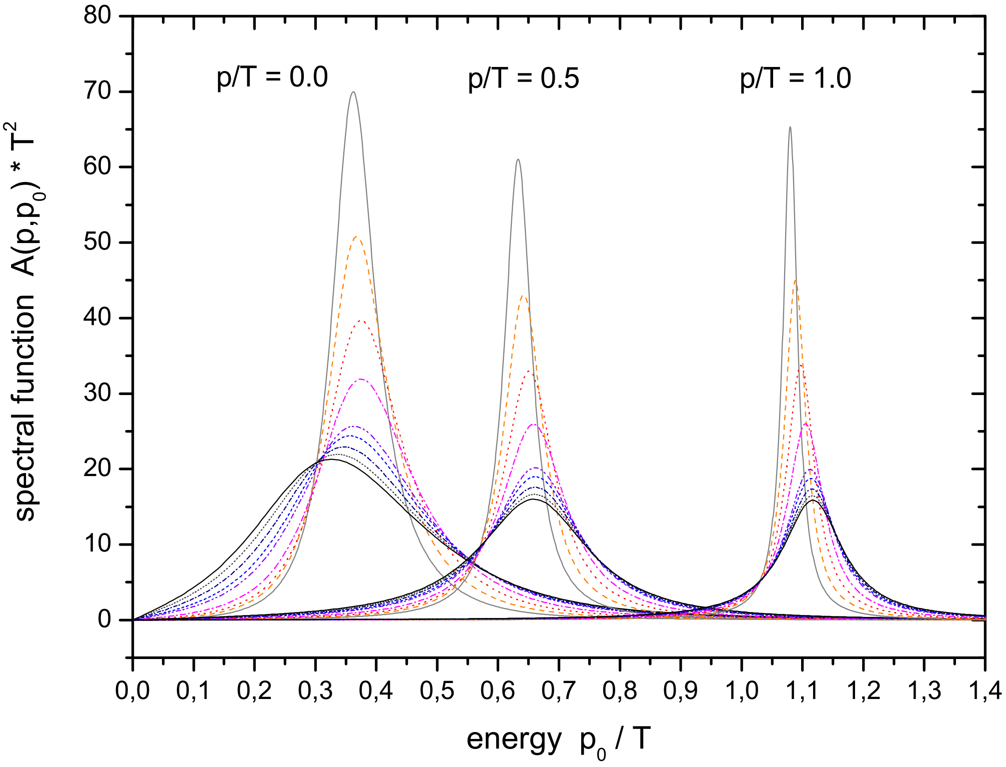

Figure 4.4: Spectral functions of three momentum modes $|\vec{p}|/T = 0.0,\ 0.5,\ 1.0$ for different coupling constants $\lambda/T = 2,\ 2.5,\ 3,\ 3.5,\ 4,\ 4.1,\ 4.2,\ 4.25,\ 4.265$ as a function of energy for the massless case $m = 0$. With increasing coupling λ/T the spectral function of the zero momentum mode becomes broader and moves to lower energies.

4.3 The Massless Case

As the final part of this Chapter we consider the case of massless scalar fields in the Lagrangian (2.1). The dynamics of massless quantum field theory has been extensively discussed over the last years especially for the dynamics of the soft, infrared modes which might be described by classical wave dynamics. In particular the diffusion rate of the topological charge in electroweak theory has been calculated within classical simulations [94]. The connection between classical and quantal correlation functions has then been worked out in a variety of papers [95]. Also it was shown recently within ϕ^4-theory that the classical wave dynamics is equivalent to a standard Boltzmann description for the soft modes when including the correct Bose statistics and staying in the weak coupling regime [96].

From our (numerical) studies we find no qualitative difference in the dynamics of massless fields compared to the one with finite masses for moderate couplings, which is due to the generation of an effective thermal mass by the leading tadpole diagram as suggested in [97]. We note that there is a logarithmic divergence in the infrared sector for the sunset self-energy in vacuum for 2+1 dimensions (cf. (B.2)) and thus a sublety, which we have cured by evaluating the vacuum counterterm in our renormalization description at a very small but finite mass.

In the following we concentrate on the structure of the spectral function with respect to the coupling strength λ/T. In Fig. 4.4 the spectral function of three low momentum modes $|\vec{p}|/T = 0.0, 0.5, 1.0$ for various coupling constants $\lambda/T = 2, 2.5, 3, 3.5, 4, 4.1, 4.2, 4.25, 4.265$ as a function of energy p_0/T is displayed. Since the temperature represents the scale for the massless case, we give all quantities in units of T. We find that the spectral function is shifted to larger energies with increasing and still moderate coupling strength ($\lambda/T \leq 3.5$). However, in the strong coupling regime ($\lambda/T > 3.5$) especially the spectral function of the zero momentum mode moves downward again, leading to a major reduction of the effective mass. Simultaneously, the spectral width grows with the coupling constant λ/T. Thus for large couplings the on-shell width becomes comparable to the effective mass (as given by the maximum position of the zero-mode spectral function).

To summarize our findings we show in Fig. 4.5 (upper part) the evolution of the on-shell energy of the zero momentum mode as a function of the coupling constant λ/T. The effective mass – as given by the maximum of the spectral function – increases with λ/T up to moderate couplings $\lambda/T \approx 3.5$ which is – as already discussed for the non-zero mass case – essentially an effect of the mass generation by the tadpole self-energy. For larger couplings $\lambda/T > 3.5$ the contribution from the retarded self-energy plays a more important role and results in a decrease of the effective mass. The reduction of the effective mass becomes rather strong for couplings $\lambda/T \geq 4.25$ indicating a significant shift of the corresponding self-consistent spectral function to smaller energies. This behaviour is accompanied by a strong increase of the on-shell width $\gamma_\omega(|\vec{p}| = 0)$ of the zero momentum mode as seen from Fig. 4.5 (middle part). While the width grows smoothly with the coupling constant for moderate couplings, we find a strong steepening in the high coupling regime as well. Thus the zero-mode spectral function for high coupling constants becomes extremely broad with an on-shell width comparable to or even larger than its effective mass.

As seen from Fig. 4.5 the evolution of the self-consistent spectral function in the strong coupling regime becomes singular and critical, such that the iteration processes do not lead to a convergent result for $\lambda/m \approx 4.266$. We address this effect to the onset of Bose condensation. In order to illustrate this interpretation we show in Fig. 4.5 (lower part) the change of the effective occupation number (as obtained from the equal-time Green functions (3.31)) with the coupling λ/T for four different momentum modes $|\vec{p}|/T = 0.0, 0.5, 1.0, 1.5$. Whereas the effective particle number of the higher momentum modes remain approximately constant, the occupation number of the zero momentum mode changes rapidly for $\lambda/T > 4.26$ indicating a preferential occupation of the condensate mode for higher couplings.

We recall that such an onset of a Bose condensation is possible for the massless relativistic theory in 2+1 space-time dimensions. Although the effective mass is not identical to zero we observe significant spectral support at low energies due to the broad spectral functions for the strongly interacting system. We note that in the present description the system has to stay in the symmetric phase, where no coherent field can develop. However, when including additionally a non-vanishing field expectation value [55], the symmetry will be broken and the system might enter a new phase. A detailed investigation of the issue we delay to a future study.

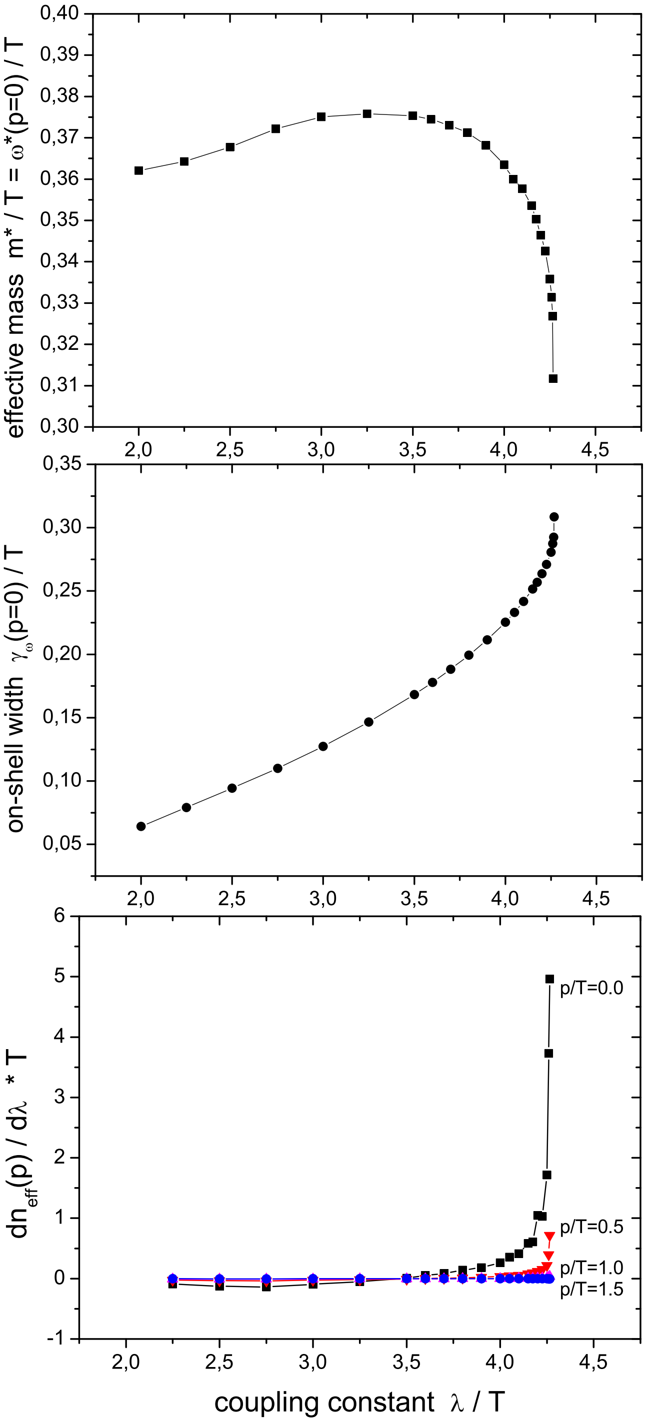

Figure 4.5: Effective mass (upper plot) and on-shell width of the zero momentum mode (middle plot) as a function of the coupling constant λ/T for a massless theory. With increasing coupling λ/T the occupation number of the zero momentum mode grows considerably in contrast to higher momentum modes (lower plot) indicating the onset of Bose condensation for $\lambda/T > 4.26$.

Chapter 5

Full versus Approximate Dynamics

The Kadanoff-Baym equations studied in the previous Chapters represent the full quantum field theoretical equations with the chosen topology for the self-consistent dissipative self-energy on the single-particle level. However, its numerical solution is quite involved and it is of interest to investigate, in how far approximate schemes deviate from the full calculation. Nowadays, transport models are widely used in the description of quantum system out of equilibrium (cf. Introduction). Most of these models work in the 'quasiparticle' picture, where all particles obey a fixed energy-momentum relation and the energy is no independent degree of freedom anymore; it is determined by the momentum and the (effective) mass of the particle. Accordingly, these particles are treated with their δ-function spectral shape as infinitely long living, i.e. stable objects. This assumption is rather questionable e.g. for high-energy heavy-ion reactions, where the particles achieve a large width due to the frequent collisions with other particles in the high density and/or high energy regime. Furthermore, this is doubtful for particles that are unstable even in the vacuum. The question, in how far the quasiparticle approximation influences the dynamics in comparison to the full Kadanoff-Baym calculation, is of general interest [59, 62].

5.1 Derivation of the Boltzmann Approximation

In the following we will give a short derivation of the Boltzmann equation starting directly from the Kadanoff-Baym dynamics in the two-time and momentum space representation as employed within this work. This derivation is briefly reviewed since we want i) to emphasize the link of the full Kadanoff-Baym equation with its approximated version and ii) to clarify the assumptions that enter the Boltzmann equation. The conventionally employed derivation of the (equivalent) Boltzmann equation will be discussed later on.

Since the Boltzmann equation describes the time evolution of distribution functions for quasiparticles we first consider the quasiparticle Green functions in two-time representation for homogeneous systems:

$$
\begin{aligned}
G^{\gtrless}_{\phi\phi,qp}(\vec{p},t_1,t_2) &= \frac{-i}{2\omega_{\vec{p}}}\, \{\, N_{qp}(\mp\vec{p})\, \exp(\pm i\,\omega_{\vec{p}}\,(t_1-t_2)) \\
&\qquad + [\, N_{qp}(\pm\vec{p})+1\,]\, \exp(\mp i\,\omega_{\vec{p}}\,(t_1-t_2))\,\} \\
G^{\gtrless}_{\phi\pi,qp}(\vec{p},t_1,t_2) &= \frac{1}{2}\, \{\, \mp N_{qp}(\mp\vec{p})\, \exp(\pm i\,\omega_{\vec{p}}\,(t_1-t_2)) \\
&\qquad \pm [\, N_{qp}(\pm\vec{p})+1\,]\, \exp(\mp i\,\omega_{\vec{p}}\,(t_1-t_2))\,\} \\
G^{\gtrless}_{\pi\phi,qp}(\vec{p},t_1,t_2) &= \frac{1}{2}\, \{\, \pm N_{qp}(\mp\vec{p})\, \exp(\pm i\,\omega_{\vec{p}}\,(t_1-t_2)) \\
&\qquad \mp [\, N_{qp}(\pm\vec{p})+1\,]\, \exp(\mp i\,\omega_{\vec{p}}\,(t_1-t_2))\,\} \\
G^{\gtrless}_{\pi\pi,qp}(\vec{p},t_1,t_2) &= \frac{-i\,\omega_{\vec{p}}}{2}\, \{\, N_{qp}(\mp\vec{p})\, \exp(\pm i\,\omega_{\vec{p}}\,(t_1-t_2)) \\
&\qquad + [\, N_{qp}(\pm\vec{p})+1\,]\, \exp(\mp i\,\omega_{\vec{p}}\,(t_1-t_2))\,\}\,.
\end{aligned}
\tag{5.1}
$$

For each momentum $\vec{p}$ the Green functions are freely oscillating in relative time $t_1 - t_2$ with the on-shell energy $\omega_{\vec{p}}$. The time-dependent quasiparticle distribution functions are given with the energy variable fixed to the on-shell energy as $N_{qp}(\vec{p},t) \equiv N(\vec{p},p_0 = \omega_{\vec{p}},t)$, where the on-shell energies $\omega_{\vec{p}}$ might depend on time as well. Such a time variation e.g. might be due to an effective mass as generated by the (renormalized) time-dependent tadpole self-energy. In this case the on-shell energy reads

$$
\omega_{\vec{p}}(t) = \sqrt{\vec{p}^{\,2} + m^2 + \bar{\Sigma}^{\delta}_{ren}(t)}\,. \tag{5.2}
$$

Vice versa we can define the quasiparticle distribution function by means of the quasiparticle Green functions at equal times t as [11]

$$
\begin{aligned}
N_{qp}(\vec{p},t) &= \left[\, \frac{\omega_{\vec{p}}(t)}{2}\, i\, G^{<}_{\phi\phi,qp}(\vec{p},t,t) \;+\; \frac{1}{2\omega_{\vec{p}}(t)}\, i\, G^{<}_{\pi\pi,qp}(\vec{p},t,t)\,\right] \\
&\quad - \frac{1}{2}\left[\, G^{<}_{\pi\phi,qp}(\vec{p},t,t) \;-\; G^{<}_{\phi\pi,qp}(\vec{p},t,t)\,\right].
\end{aligned}
\tag{5.3}
$$

Using the equations of motions for the Green functions in diagonal time direction (A.2) (exploiting $G^{<}_{\phi\pi}(\vec{p},t,t) = -[\, G^{<}_{\pi\phi}(\vec{p},t,t)\,]^*$) the time evolution of this distribution function is given by

$$\partial_t\, N_{qp}(\vec{p},t) \;=\; -\,Re\left\{\, I^{<}_{1\,;\,qp}(\vec{p},t,t)\,\right\} - \frac{1}{\omega_{\vec{p}}(t)}\; Im\left\{\, I^{<}_{1,2\,;\,qp}(\vec{p},t,t)\,\right\}\,. \tag{5.4}$$

The time derivatives of the on-shell energies cancel out since the quasiparticle Green functions obey

$$G^{<}_{\pi\pi}(\vec{p},t,t) \;=\; \omega^2_{\vec{p}}(t)\; G^{<}_{\phi\phi}(\vec{p},t,t) \tag{5.5}$$

as seen from (5.1). Furthermore, we remark that contributions containing the energy $\omega^2_{\vec{p}}$ – as present in the equation of motion for the Green functions (A.2) – no longer show up. The time evolution of the distribution function is entirely determined by (equal-time) collision integrals containing (time derivatives of the) Green functions and self-energies,

$$I^{<}_{1;qp}(\vec{p},t,t) \;=\; \int_{t_0}^{t}\! dt'\;\; \Sigma^{<}_{qp}(\vec{p},t,t')\; G^{>}_{\phi\phi,qp}(\vec{p},t',t) \;-\; \Sigma^{>}_{qp}(\vec{p},t,t')\; G^{<}_{\phi\phi,qp}(\vec{p},t',t)\,, \tag{5.6}$$

$$I^{<}_{1,2;qp}(\vec{p},t,t) \;=\; \int_{t_0}^{t}\! dt'\;\; \Sigma^{<}_{qp}(\vec{p},t,t')\; G^{>}_{\phi\pi,qp}(\vec{p},t',t) \;-\; \Sigma^{>}_{qp}(\vec{p},t,t')\; G^{<}_{\phi\pi,qp}(\vec{p},t',t)\,.$$

Since we are dealing with a system of on-shell quasiparticles within the Boltzmann approximation, the Green functions in the collision integrals (5.6) are given by the respective quasiparticle quantities of (5.1). This holds for the collisional self-energies as well and is indicated by the index $\cdot_{qp}$

$$\Sigma^{\gtrless}_{qp}(\vec{p},t_1,t_2) \;=\; -i\frac{\lambda^2}{6}\int\!\frac{d^dq}{(2\pi)^d}\int\!\frac{d^dr}{(2\pi)^d}\int\!\frac{d^ds}{(2\pi)^d}\;(2\pi)^d\,\delta^{(d)}(\vec{p}-\vec{q}-\vec{r}-\vec{s})\;\frac{1}{2\omega_{\vec{q}}\,2\omega_{\vec{r}}\,2\omega_{\vec{s}}} \tag{5.7}$$

$$\begin{aligned}
\times\Big\{\;& N_{qp}(\mp\vec{q})\quad N_{qp}(\mp\vec{r})\quad N_{qp}(\mp\vec{s})\quad \exp(+i\,[\,t_1-t_2\,]\,[\,\pm\omega_{\vec{q}}\pm\omega_{\vec{r}}\pm\omega_{\vec{s}}\,])\\
+\,3\;\;& N_{qp}(\mp\vec{q})\quad N_{qp}(\mp\vec{r})\quad [\,N_{qp}(\pm\vec{s})+1\,]\quad \exp(+i\,[\,t_1-t_2\,]\,[\,\pm\omega_{\vec{q}}\pm\omega_{\vec{r}}\mp\omega_{\vec{s}}\,])\\
+\,3\;\;& N_{qp}(\mp\vec{q})\quad [\,N_{qp}(\pm\vec{r})+1\,]\quad [\,N_{qp}(\pm\vec{s})+1\,]\quad \exp(+i\,[\,t_1-t_2\,]\,[\,\pm\omega_{\vec{q}}\mp\omega_{\vec{r}}\mp\omega_{\vec{s}}\,])\\
+\;\;& [\,N_{qp}(\pm\vec{q})+1\,]\quad [\,N_{qp}(\pm\vec{r})+1\,]\quad [\,N_{qp}(\pm\vec{s})+1\,]\quad \exp(+i\,[\,t_1-t_2\,]\,[\,\mp\omega_{\vec{q}}\mp\omega_{\vec{r}}\mp\omega_{\vec{s}}\,])\;\Big\}\,.
\end{aligned}$$

For a free theory the distribution functions $N_{qp}(\vec{p})$ are obviously constant in time which, of course, is no longer valid for an interacting system out of equilibrium. Thus one has to specify the above expressions for the quasiparticle Green functions (5.1) to account for the time dependence of the distribution functions.

The actual Boltzmann approximation is defined in the limit, that the distribution functions have to be taken always at the latest time argument of the two-time Green function [60, 62]. Accordingly, for the general nonequilibrium case we introduce the ansatz for the Green functions in the collision term,

$$
\begin{aligned}
G^{\gtrless}_{\phi\phi,qp}(\vec{p},t_1,t_2) &= \frac{-i}{2\omega_{\vec{p}}}\,\{\; N_{qp}(\mp\vec{p},t_{max})\;\exp(\pm\, i\,\omega_{\vec{p}}\,(t_1-t_2)) \\
&\qquad + [\,N_{qp}(\pm\vec{p},t_{max})+1\,]\;\exp(\mp\, i\,\omega_{\vec{p}}\,(t_1-t_2))\;\}\,, \qquad (5.8) \\
G^{\gtrless}_{\phi\pi,qp}(\vec{p},t_1,t_2) &= \frac{1}{2}\,\{\; \mp N_{qp}(\mp\vec{p},t_{max})\;\exp(\pm\, i\,\omega_{\vec{p}}\,(t_1-t_2)) \\
&\qquad \pm [\,N_{qp}(\pm\vec{p},t_{max})+1\,]\;\exp(\mp\, i\,\omega_{\vec{p}}\,(t_1-t_2))\;\}\,,
\end{aligned}
$$

with the maximum time $t_{max} = max(t_1,t_2)$. The same ansatz is employed for the time-dependent on-shell energies which enter the representation of the quasiparticle two-time Green functions (5.8) with their value at t_{max}, i.e. $\omega_{\vec{p}} = \omega_{\vec{p}}(t_{max} = max(t_1,t_2))$.

The collision term contains a time integration which extends from an initial time t_0 to the current time t. All two-time Green functions and self-energies depend on the current time t as well as on the integration time $t' \leq t$. Thus only distribution functions at the current time, i.e. the maximum time of all appearing two-time functions, enter the collision integrals and the evolution equation for the distribution function becomes local in time. Since the distribution functions are given at fixed time t, they can be taken out of the time integral. When inserting the expressions for the self-energies and the Green functions in the collision integrals the evolution equation for the quasiparticle distribution function reads:

$$
\begin{aligned}
\partial_t\, N_{qp}(\vec{p},t) &= \frac{\lambda^2}{3}\int\!\frac{d^dq}{(2\pi)^d}\int\!\frac{d^dr}{(2\pi)^d}\int\!\frac{d^ds}{(2\pi)^d}\;(2\pi)^d\,\delta^{(d)}(\vec{p}-\vec{q}-\vec{r}-\vec{s})\;\frac{1}{2\omega_{\vec{p}}\,2\omega_{\vec{q}}\,2\omega_{\vec{r}}\,2\omega_{\vec{s}}} \qquad (5.9) \\
&\times \Big\{\;[\,\hat{N}_{\vec{p},t}\,\hat{N}_{-\vec{q},t}\,\hat{N}_{-\vec{r},t}\,\hat{N}_{-\vec{s},t} - N_{\vec{p},t}\,N_{-\vec{q},t}\,N_{-\vec{r},t}\,N_{-\vec{s},t}]\int_{t_0}^{t}\!dt'\;\cos([\,t-t'\,]\,[\,\omega_{\vec{p}}+\omega_{\vec{q}}+\omega_{\vec{r}}+\omega_{\vec{s}}\,]) \\
&+3\,[\,\hat{N}_{\vec{p},t}\,\hat{N}_{-\vec{q},t}\,\hat{N}_{-\vec{r},t}\;N_{\vec{s},t}\;-N_{\vec{p},t}\,N_{-\vec{q},t}\,N_{-\vec{r},t}\;\hat{N}_{\vec{s},t}\,]\int_{t_0}^{t}\!dt'\;\cos([\,t-t'\,]\,[\,\omega_{\vec{p}}+\omega_{\vec{q}}+\omega_{\vec{r}}-\omega_{\vec{s}}\,]) \\
&+3\,[\,\hat{N}_{\vec{p},t}\,\hat{N}_{-\vec{q},t}\;N_{\vec{r},t}\;\;N_{\vec{s},t}\;-N_{\vec{p},t}\,N_{-\vec{q},t}\;\hat{N}_{\vec{r},t}\;\;\hat{N}_{\vec{s},t}\,]\int_{t_0}^{t}\!dt'\;\cos([\,t-t'\,]\,[\,\omega_{\vec{p}}+\omega_{\vec{q}}-\omega_{\vec{r}}-\omega_{\vec{s}}\,]) \\
&+[\,\hat{N}_{\vec{p},t}\;\;N_{\vec{q},t}\;\;N_{\vec{r},t}\;\;N_{\vec{s},t}\;-N_{\vec{p},t}\;\;\hat{N}_{\vec{q},t}\;\;\hat{N}_{\vec{r},t}\;\;\hat{N}_{\vec{s},t}\,]\int_{t_0}^{t}\!dt'\;\cos([\,t-t'\,]\,[\,\omega_{\vec{p}}-\omega_{\vec{q}}-\omega_{\vec{r}}-\omega_{\vec{s}}\,])\;\Big\}\,,
\end{aligned}
$$

where we have introduced the abbreviation $N_{\vec{p},t} = N_{qp}(\vec{p},t)$ for the quasiparticle distribution function at current time t and $\hat{N}_{\vec{p},t} = N_{qp}(\vec{p},t) + 1$ for the according Bose factor.

Furthermore, a possible time dependence of the on-shell energies is suppressed in the above notation.

The terms in the collision term (5.9) for particles of momentum $\vec{p}$ are ordered as they describe different types of scattering processes where, however, we always find the typical gain and loss structure. The first line in (5.9) corresponds to the production and annihilation of four on-shell particles ($0 \to 4$, $4 \to 0$), where a particle of momentum $\vec{p}$ is produced or destroyed simultaneous with three other particles with momenta $\vec{q}, \vec{r}, \vec{s}$. The second line and the forth line describe ($1 \to 3$) and ($3 \to 1$) processes where the quasiparticle with momentum $\vec{p}$ is the single one or appears with two other particles. The relevant contribution in the Boltzmann limit is the third line which respresents ($2 \leftrightarrow 2$) scattering processes; quasiparticles with momentum $\vec{p}$ can be scattered out of their momentum cell by collisions with particles of momenta $\vec{q}$ (second term) or can be produced within a reaction of on-shell particles with momenta $\vec{r}$, $\vec{s}$ (first term).

The time evolution of the quasiparticle distribution is given as an initial value problem for the function $N_{qp}(\vec{p})$ prepared at initial time t_0. For large system times t (compared to the initial time) the time integration over the trigonometric function results in an energy conserving δ-function.

$$\lim_{t-t_0\to\infty} \int_{t_0}^{t} dt' \;\cos((t-t')\,\hat{\omega}) \;=\; \lim_{t-t_0\to\infty} \frac{1}{\hat{\omega}} \;\sin((t-t_0)\,\hat{\omega}) \;=\; \pi\,\delta(\hat{\omega})\,. \tag{5.10}$$

Here $\hat{\omega} = \omega_{\vec{p}} \pm \omega_{\vec{q}} \pm \omega_{\vec{r}} \pm \omega_{\vec{s}}$ represents the energy sum which is conserved in the limit $t - t_0 \to \infty$ where the initial time t_0 is considered as fixed. In this limit the time evolution of the distribution function amounts to

$$\begin{aligned}
\partial_t\, N_{qp}(\vec{p},t) \;=\; & \frac{\lambda^2}{6} \int\!\frac{d^dq}{(2\pi)^d}\int\!\frac{d^dr}{(2\pi)^d}\int\!\frac{d^ds}{(2\pi)^d}\;(2\pi)^{d+1}\;\frac{1}{2\omega_{\vec{p}}\,2\omega_{\vec{q}}\,2\omega_{\vec{r}}\,2\omega_{\vec{s}}} \qquad (5.11)\\
\times\Big\{ & \;[\hat{N}_{\vec{p},t}\,\hat{N}_{\vec{q},t}\,\hat{N}_{\vec{r},t}\,\hat{N}_{\vec{s},t} \;-\; N_{\vec{p},t}\,N_{\vec{q},t}\,N_{\vec{r},t}\,N_{\vec{s},t}]\;\delta^{(d)}(\vec{p}+\vec{q}+\vec{r}+\vec{s})\;\;\delta(\omega_{\vec{p}}+\omega_{\vec{q}}+\omega_{\vec{r}}+\omega_{\vec{s}})\\
+3\; & [\hat{N}_{\vec{p},t}\,\hat{N}_{\vec{q},t}\,\hat{N}_{\vec{r},t}\,N_{\vec{s},t} \;-\; N_{\vec{p},t}\,N_{\vec{q},t}\,N_{\vec{r},t}\,\hat{N}_{\vec{s},t}]\;\delta^{(d)}(\vec{p}+\vec{q}+\vec{r}-\vec{s})\;\;\delta(\omega_{\vec{p}}+\omega_{\vec{q}}+\omega_{\vec{r}}-\omega_{\vec{s}})\\
+3\; & [\hat{N}_{\vec{p},t}\,\hat{N}_{\vec{q},t}\,N_{\vec{r},t}\,N_{\vec{s},t} \;-\; N_{\vec{p},t}\,N_{\vec{q},t}\,\hat{N}_{\vec{r},t}\,\hat{N}_{\vec{s},t}]\;\delta^{(d)}(\vec{p}+\vec{q}-\vec{r}-\vec{s})\;\;\delta(\omega_{\vec{p}}+\omega_{\vec{q}}-\omega_{\vec{r}}-\omega_{\vec{s}})\\
+\; & [\hat{N}_{\vec{p},t}\,N_{\vec{q},t}\,N_{\vec{r},t}\,N_{\vec{s},t} \;-\; N_{\vec{p},t}\,\hat{N}_{\vec{q},t}\,\hat{N}_{\vec{r},t}\,\hat{N}_{\vec{s},t}]\;\delta^{(d)}(\vec{p}-\vec{q}-\vec{r}-\vec{s})\;\;\delta(\omega_{\vec{p}}-\omega_{\vec{q}}-\omega_{\vec{r}}-\omega_{\vec{s}})\Big\}\,.
\end{aligned}$$

In the energy conserving long-time limit (5.10) only the $2 \leftrightarrow 2$ scattering processes (third line in (5.9)) are contributing. All other terms vanish since the corresponding energy δ-functions can not be fulfilled for on-shell quasiparticles. In the following we will solve the energy conserving Boltzmann equation for on-shell particles:

$$\partial_t \, N_{qp}(\vec{p},t) \;=\; \frac{\lambda^2}{2} \int \! \frac{d^dq}{(2\pi)^d} \int \! \frac{d^dr}{(2\pi)^d} \int \! \frac{d^ds}{(2\pi)^d} \; (2\pi)^{d+1} \; \frac{1}{2\omega_{\vec{p}} \, 2\omega_{\vec{q}} \, 2\omega_{\vec{r}} \, 2\omega_{\vec{s}}} \tag{5.12}$$

$$[\, \hat{N}_{\vec{p},t} \, \hat{N}_{\vec{q},t} \, N_{\vec{r},t} \, N_{\vec{s},t} \;-\; N_{\vec{p},t} \, N_{\vec{q},t} \, \hat{N}_{\vec{r},t} \, \hat{N}_{\vec{s},t} \,] \;\; \delta^{(d)}(\vec{p}+\vec{q}-\vec{r}-\vec{s}) \;\; \delta(\omega_{\vec{p}}+\omega_{\vec{q}}-\omega_{\vec{r}}-\omega_{\vec{s}}) \, .$$

The system evolution given by (5.12) is explicitly local in time since it depends only on the current configuration; there are no memory effects from the integration over past times as present in the full Kadanoff-Baym equation.

We point out, that the numerical algorithm for the time integration of (5.12) is basically the same as the one employed for the solution of the Kadanoff-Baym equation (cf. Appendix A). Energy conservation can be assured by a precalculation including a shift of the lower boundary t_0 to earlier times. Even small time shifts suffice to keep the kinetic energy conserved. We note, that in contrast to the Kadanoff-Baym equation no correlation energy is generated in the Boltzmann limit.

In addition to the procedure presented above, we calculate the actual momentum-dependent on-shell energy for every momentum mode by a solution of the dispersion relation including contributions from the tadpole and the real part of the (retarded) sunset self-energy. In this way one can guarantee that at every time t the particles are treated as quasiparticles with the correct energy-momentum relation.

Before presenting the actual numerical results we like to comment on the derivation of the Boltzmann equation within the conventional scheme that is different from ours. Here, at first the Kadanoff-Baym equation (in coordinate space) is transformed to the Wigner representation by Fourier transformation with respect to the relative coordinates in space and time (for ϕ^4-theory see Refs. [19, 11]). The problem then is formulated in terms of energy and momentum variables together with a single system time. For non-homogeneous systems a mean spatial coordinate is necessary as well. As a next step the 'semiclassical approximation' is introduced, which consists of a gradient expansion of the convolution integrals in coordinate space within the Wigner transformation. For the time evolution only contributions up to first order in the gradients are kept (cf. (3.15)). Finally, the quasiparticle assumption is introduced as follows: The Green functions appearing in the transport equation – explicitly or implicitly via the self-energies – are written in Wigner representation as a product of a distribution function N and the spectral function A (cf. Section 3.6). The quasiparticle assumption is then realized by employing a δ-like form for the spectral function which connects the energy variable to the momentum. By integrating the first order transport equation over all (positive) energies, furthermore, the Boltzmann equation for the time evolution of the on-shell distribution function (5.12) is obtained.

Inspite of the fact, that the Bolzmann equation (5.12) can be obtained in different subsequent approximation schemes, it is of basic interest, how its actual solutions compare to those from the full Kadanoff-Baym dynamics.

5.2 Boltzmann vs. Kadanoff-Baym Dynamics

In the following we will compare the solutions of the Boltzmann equation with the solution of the Kadanoff-Baym theory. We start with a presentation of the nonequilibrium time evolution of two colliding particle accumulations (tsunamis) [44] within the full Kadanoff-Baym calculation (cf. Fig. 5.1). Such configurations are also used for simulations in the heavy-ion physics context [59, 44, 60, 61, 62].

During the time evolution the bumps at finite momenta (in p_x direction) gradually disappear, while the one close to zero momentum – which initially stems from the vacuum contribution to the Green function – is increased as seen for different snapshots at times $t \cdot m = 0,\ 15,\ 30,\ 45,\ 75,\ 150$ in Fig. 5.1. The system with initially apparent collision axis slowly merges – as expected – into an isotropic final distribution in momentum space.

For the comparison between the full Kadanoff-Baym dynamics and the Boltzmann approximation we concentrate on equilibration times. To this aim we define a quadrupole moment for a given momentum distribution $N(\vec{p})$ at time t as

$$Q(t) \;=\; \frac{\displaystyle\int \frac{d^2p}{(2\pi)^2}\ [p_x^2 - p_y^2]\ N(\vec{p},t)}{\displaystyle\int \frac{d^2p}{(2\pi)^2}\ N(\vec{p},t)}\,, \tag{5.13}$$

which vanishes for the equilibrium state. For the Kadanoff-Baym case we use in (5.13) the effective distribution function $n_{eff}(\vec{p},t)$, which is determined by the equal-time Green functions (3.31). When constructing the distribution function by means of equal-time Green functions the energy variable has been effectively integrated out. This has the advantage that the distribution function is given independently of the actual on-shell energies. We note, that a calculation with the on-shell energies basically leads to the same results.

The relaxation of the quadrupole moment (5.13) has been studied for two different initial distributions: The evolution of distribution d2 is displayed in Fig. 5.1 while for distribution d1 the position and the width of the two particle bumps have been modified. The calculated quadrupole moment (5.13) shows a nearly exponential decrease with time (see Fig. 5.2) and we can extract a relaxation rate Γ_Q via the relation

$$Q(t) \;\propto\; \exp(-\Gamma_Q \cdot t)\,. \tag{5.14}$$

Fig. 5.3 shows for both initializations that the relaxation in the full quantum calculation occurs faster for large coupling constants λ than in the quasi-classical approximation, whereas for small couplings the equilibration times of the full and the approximate evolutions are comparable. We find that the scaled relaxation rate Γ_Q/λ^2 is nearly constant in the Boltzmann case, but increases with the coupling strength in the Kadanoff-Baym calculation (especially for the initial distribution d2).

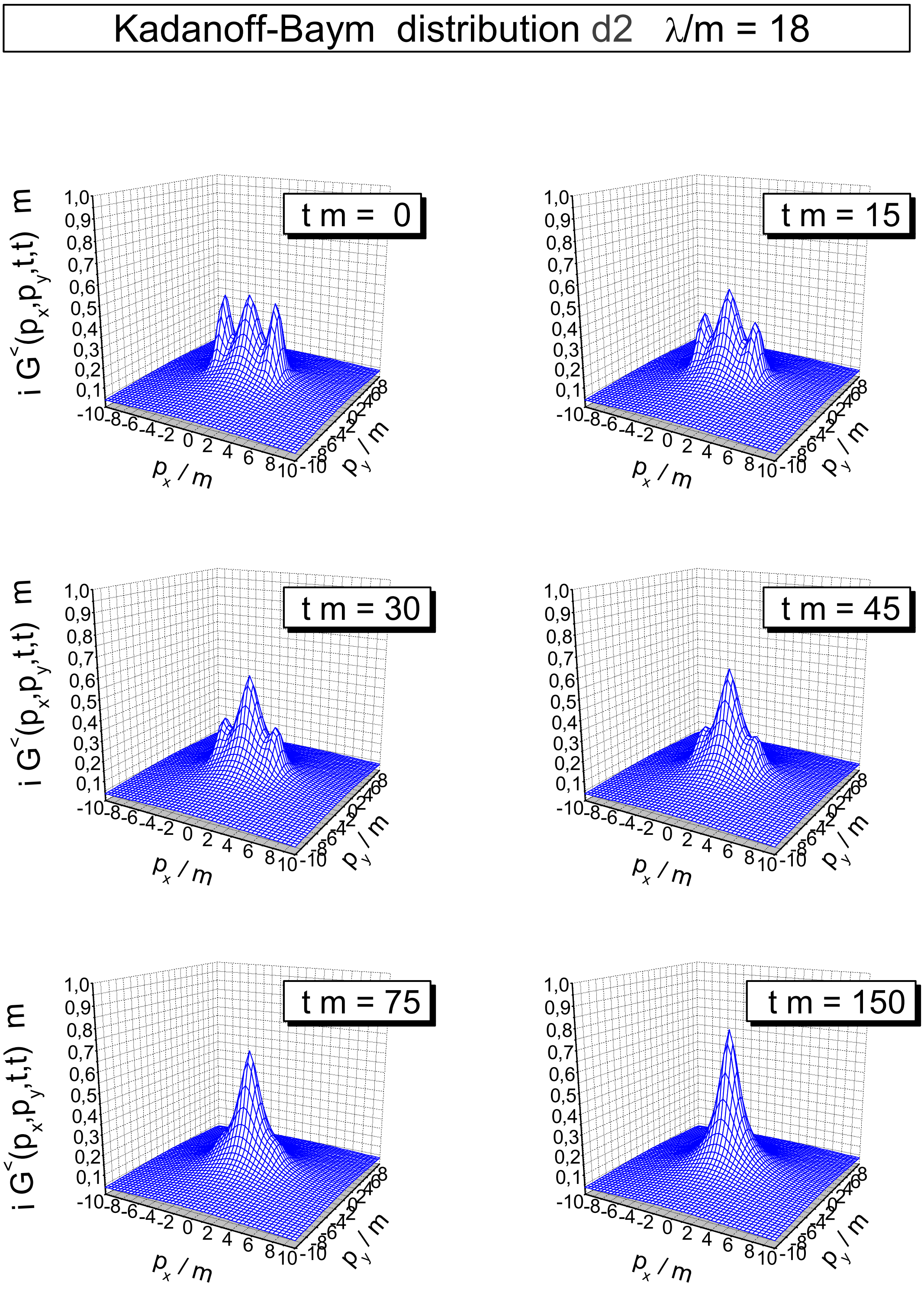

Figure 5.1: Evolution of the Green function in momentum space within the full Kadanoff-Baym dynamics. The equal-time Green function is displayed for various times $t \cdot m$ = 0, 15, 30, 45, 75, 150. Starting from an initially non-isotropic shape it develops towards a rotational symmetric distribution in momentum space.

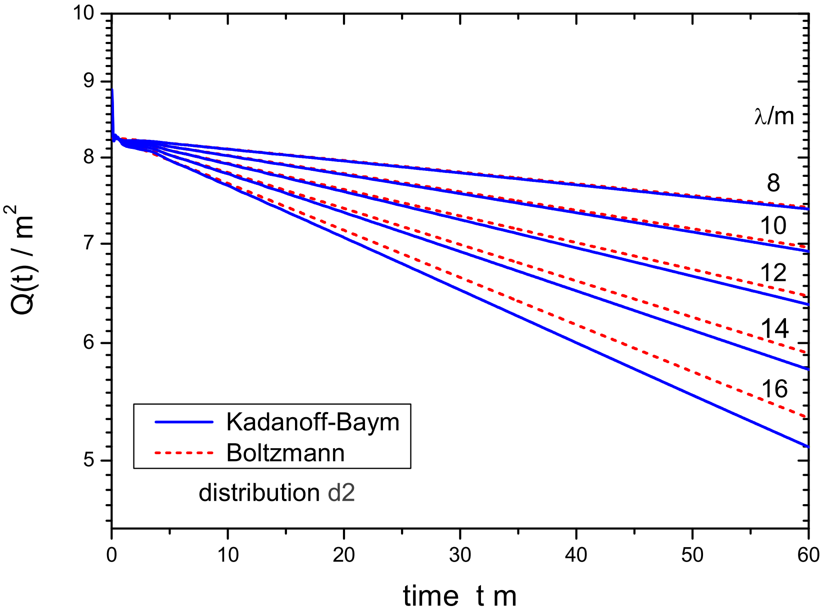

Figure 5.2: Decrease of the quadrupole moment in time for different coupling constants $\lambda/m = 8 \rightarrow 16$ in steps of 2 for the full Kadanoff-Baym calculation (solid lines) and the Boltzmann approximation (dashed lines).

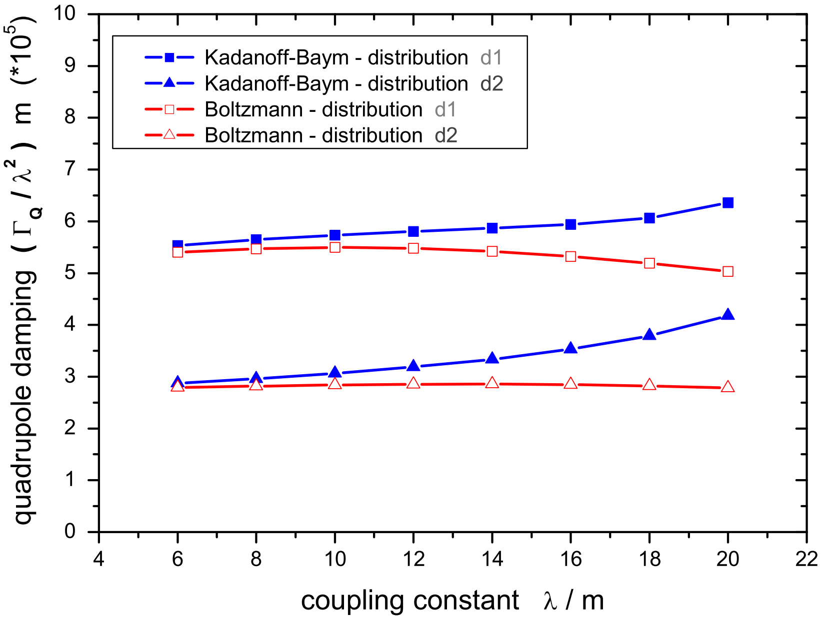

Figure 5.3: Relaxation rate (divided by the coupling λ squared) for Kadanoff-Baym and Boltzmann calculations as a function of the interaction strength. For the two different initial configurations the full Kadanoff-Baym evolution leads to a faster equilibration.

These findings are explained as follows: Since the free Green function – as used in the Boltzmann calculation – has only support on the mass-shell, only $(2 \leftrightarrow 2)$ scattering processes are described in the Boltzmann limit. All other processes with a different number of incoming and outgoing particles vanish (as noted before). Within the full Kadanoff-Baym calculation this is different, since here the spectral function – determined from the self-consistent Green function (cf. Section 3.5) – aquires a finite width. Thus the Green function has support at all energies although it drops fast far off the mass shell. Especially for large coupling constants, where the spectral function is sufficiently broad, the three particle production process gives a significant contribution to the collision integral. Since the width of the spectral function increases with the interaction strength, such processes become more important in the high coupling regime. As a consequence the difference between both approaches is larger for stronger interactions as observed in Fig. 5.3. For small couplings λ/m in both approaches basically the usual $2 \leftrightarrow 2$ scattering contributes and the results for the rate Γ_Q are quite similar.

In summarizing this Section we point out that the full solution of the Kadanoff-Baym equations does include $0 \leftrightarrow 4$, $1 \leftrightarrow 3$ and $2 \leftrightarrow 2$ off-shell collision processes which – in comparison to the Bolzmann on-shell $2 \leftrightarrow 2$ collision limit – become important when the spectral width of the particles reaches $\sim 1/3$ of the particle mass. On the other hand, the simple Boltzmann limit works surprisingly well for smaller couplings and those cases, where the spectral function is sufficiently narrow.

5.3 Estimate for the Quadrupole Relaxation

In this Section we concentrate on the quadrupole relaxation rates observed for the full Kadanoff-Baym and the Boltzmann approximation in order to provide a simple and intuitive explanation for the actual values extracted in the last Section. To this aim we study an idealized initial state given by two δ-functions in momentum space. For symmetry reasons they are placed on the positive and negative p_x-axis at $p_y = 0$. Thus the initial distribution function reads

$$N^{\delta}(\vec{p}, t=0) \;=\; N_0^{\delta}\; \delta(p_y)\; \left[\, \delta(p_x - p_{ini}) + \delta(p_x + p_{ini}) \,\right] \,, \qquad (5.15)$$

where N_0^{δ} is a normalization constant. We are now interested in the time evolution of this distribution function in particular in view of the relaxation rate of the quadrupole moment. For simplicity we will explore this question employing the Boltzmann equation, since the differences between the full and the quasiparticle calculation are rather moderate.

The special form of the initial distribution N^{δ} (5.15) has the particular advantage, that the collision term of the Boltzmann equation can be calculated analytically at the beginning of the evolution. We find for the time evolution of momentum moments within the Boltzmann approximation in 2+1 space-time dimensions:

$$\frac{d}{dt} < \mathcal{O} > (t) \; = \; \frac{d}{dt} \int \frac{d^2p}{(2\pi)^2} \; \mathcal{O} \; N(\vec{p},t) \; = \; \int \frac{d^2p}{(2\pi)^2} \; \mathcal{O} \; \frac{d}{dt} \; N(\vec{p},t) \tag{5.16}$$

$$= \; \frac{\lambda^2}{2} \int \frac{d^2p}{(2\pi)^2} \int \frac{d^2q}{(2\pi)^2} \int \frac{d^2r}{(2\pi)^2} \int \frac{d^2s}{(2\pi)^2} \; \mathcal{O} \; \frac{1}{2\omega_{\vec{p}} \, 2\omega_{\vec{q}} \, 2\omega_{\vec{r}} \, 2\omega_{\vec{s}}} \, (2\pi)^{2+1} \, \delta^{(2+1)}(p+q-r-s)$$

$$\Big\{ [1+N(\vec{p},t)] \, [1+N(\vec{q},t)] \, N(\vec{r},t) \, N(\vec{s},t) \; - \; N(\vec{p},t) \, N(\vec{q},t) \, [1+N(\vec{r},t)] \, [1+N(\vec{s},t)] \Big\} \; .$$

Here $\mathcal{O}$ can be a function of the momentum coordinates, but is assumed to be independent of time, e.g. $\mathcal{O} \in \{1, p_x^2, p_y^2\}$. Furthermore, the energy is fixed in this quasiparticle calculation by the momentum as $p_0 = \omega_{\vec{p}} = \sqrt{m^2 + \vec{p}^{\,2}}$. For our special initial state N^δ and for the chosen operators $\mathcal{O}$ all contributions of products of more than two distribution functions cancel out. Thus the derivative of the mean value is given by

$$\frac{d}{dt} < \mathcal{O} > (t) \; = \; \frac{\lambda^2}{32} \int \frac{d^2p}{(2\pi)^2} \int \frac{d^2q}{(2\pi)^2} \int \frac{d^2r}{(2\pi)^2} \int \frac{d^2s}{(2\pi)^2} \; \mathcal{O} \; \frac{1}{\omega_{\vec{p}} \, \omega_{\vec{q}} \, \omega_{\vec{r}} \, \omega_{\vec{s}}} \tag{5.17}$$

$$\times \, (2\pi)^{2+1} \, \delta^{(2+1)}(p+q-r-s) \;\; \{ \; N^\delta(\vec{r},t) \, N^\delta(\vec{s},t) \; - \; N^\delta(\vec{p},t) \, N^\delta(\vec{q},t) \; \} \; .$$

By inserting the explicit form of the initial conditions and performing the integrations over the momentum δ-functions we obtain for the gain term

$$\frac{d}{dt} < \left\{ \begin{array}{c} p_x^2 \\ p_y^2 \\ 1 \end{array} \right\} >_{gain} \; = \; N_0^{\delta\,2} \, \frac{\lambda^2}{32} \int \frac{d^2p}{(2\pi)^5} \left\{ \begin{array}{c} p_x^2 \\ p_y^2 \\ 1 \end{array} \right\} \left[\; 2 \frac{1}{\omega_{\vec{p}}^2 \, \omega_{ini}^2} \, \delta(2\omega_{\vec{p}} - 2\omega_{ini}) \right. \tag{5.18}$$

$$\left. + \; \frac{1}{\omega_{\vec{p}} \, \omega_{ini}^2 \, \omega_{\vec{p}_+}} \, \delta(\omega_{\vec{p}} + \omega_{\vec{p}_+} - 2\omega_{ini}) \; + \; \frac{1}{\omega_{\vec{p}} \, \omega_{ini}^2 \, \omega_{\vec{p}_-}} \, \delta(\omega_{\vec{p}} + \omega_{\vec{p}_-} - 2\omega_{ini}) \; \right] ,$$

where we take into account explicitly the different choices for the operator $\mathcal{O} \in \{1, p_x^2, p_y^2\}$. In (5.18) we have introduced the on-shell energy of the initial particle localization in momentum space

$$\omega_{ini} \; = \; \sqrt{m^2 + p_{ini}^2} \tag{5.19}$$

as well as the energies

$$\omega_{\vec{p}_\pm} \; = \; \sqrt{m^2 + (p_x \pm 2p_{ini})^2 + p_y^2} \; . \tag{5.20}$$

Since the integration over the last two δ-functions in energy yields zero, the only contribution to the integral stems from the first term, which can be evaluated as

$$\frac{d}{dt} < \left\{ \begin{array}{c} p_x^2 \\ p_y^2 \\ 1 \end{array} \right\} >_{gain} \; = \; N_0^{\delta 2} \, \frac{\lambda^2}{64\,(2\pi)^4} \, \frac{1}{\omega_{ini}^3} \left\{ \begin{array}{c} p_{ini}^2 \\ p_{ini}^2 \\ 2 \end{array} \right\} . \tag{5.21}$$

For the loss term we find (after carrying out the momentum space integrals)

$$\frac{d}{dt} < \left\{ \begin{array}{c} p_x^2 \\ p_y^2 \\ 1 \end{array} \right\} >_{loss} \; = \; N_0^{\delta 2} \, \frac{\lambda^2}{32} \int \frac{d^2 r}{(2\pi)^5} \left\{ \begin{array}{c} p_{ini}^2 \\ 0 \\ 1 \end{array} \right\} \Bigg[\, 2 \frac{1}{\omega_{\vec r}^2 \, \omega_{ini}^2} \, \delta(2\omega_{\vec r} - 2\omega_{ini}) \tag{5.22}$$

$$+ \; \frac{1}{\omega_{\vec r} \, \omega_{ini}^2 \, \omega_{\vec r_+}} \, \delta(\omega_{\vec r} + \omega_{\vec r_+} - 2\omega_{ini}) \; + \; \frac{1}{\omega_{\vec r} \, \omega_{ini}^2 \, \omega_{\vec r_-}} \, \delta(\omega_{\vec r} + \omega_{\vec r_-} - 2\omega_{ini}) \Bigg]$$

with the energy functions $\omega_{\vec r_\pm}$ given as above. Due to the appearance of $N^\delta(\vec p)$ in the loss term the integration over the momentum $\vec p$ is performed directly such that the values of the operator are fixed. Again only the first term of the integral gives a non-zero result and we get for the loss term in the early time evolution

$$\frac{d}{dt} < \left\{ \begin{array}{c} p_x^2 \\ p_y^2 \\ 1 \end{array} \right\} >_{loss} \; = \; N_0^{\delta 2} \, \frac{\lambda^2}{64\,(2\pi)^4} \, \frac{1}{\omega_{ini}^3} \left\{ \begin{array}{c} 2\,p_{ini}^2 \\ 0 \\ 2 \end{array} \right\} . \tag{5.23}$$

From (5.21) and (5.23) we find – in agreement with the general properties of the Boltzmann equation – that the total particle number is conserved for our particular initial state

$$\frac{d}{dt} N_{tot}(t) \; = \; \int \frac{d^2 p}{(2\pi)^2} \, \frac{d}{dt} N(\vec p) \bigg|_{t=0} \; = \; 0 \, . \tag{5.24}$$

Thus the total particle number is given by $N_{tot}(t) = 2N_0^\delta/(2\pi)^2$ for all times t. Furthermore, for the reduction of the quadrupole moment (calculated with the initial distribution N^δ) we obtain

$$\frac{d}{dt} Q(t) \bigg|_{t=0} \; = \; \frac{1}{N_{tot}} \int \frac{d^2 p}{(2\pi)^2} \, [p_x^2 - p_y^2] \, \frac{d}{dt} N(\vec p) \bigg|_{t=0} \; = \; - N_0^\delta \, \frac{\lambda^2}{64\,(2\pi)^2} \, \frac{p_{ini}^2}{\omega_{ini}^3} \, , \tag{5.25}$$

where the gain term does not give a contribution due to the symmetry in the momentum coordinates p_x and p_y.

As indicated by the numerical studies shown in the last Section the quadrupole moment decreases nearly exponentially in time. Thus assuming a decrease of the quadrupole moment of the form $Q(t) = Q_0 \exp(-\Gamma_Q \cdot t)$ we can determine the relaxation rate as

$$\Gamma_Q \;=\; -\frac{\dot{Q}(t=0)}{Q(t=0)} \;=\; N_0^\delta \, \frac{\lambda^2}{64\,(2\pi)^2} \, \frac{1}{\sqrt{m^2+p_{ini}^2}^{\,3}} \tag{5.26}$$

with the initial value $Q(t=0) = p_{ini}^2$. In order to connect this result to the initial distributions employed in our calculations

$$n(\vec{p}, t=0) \;=\; n_0 \;\exp(-(|p_x| - p_{ini})^2/2\sigma_x^2)\;\exp(-p_y^2/2\sigma_y^2) \tag{5.27}$$

we avail the corresponding representation of the δ-function and identify $N_0^\delta = 2\pi\, n_0\, \sigma_x\, \sigma_y$. Thus we can estimate the relaxation rate for the distribution d1 ($n_0 = 1$, $\sigma_x = 0.75$, $\sigma_y = 0.75$, $p_{ini} = 2.5$) as $\Gamma_Q^{d1} \approx 7.16 \cdot 10^{-5} \cdot \lambda^2$ and for distribution d2 ($n_0 = 1$, $\sigma_x = 0.5$, $\sigma_y = 1.0$, $p_{ini} = 3.0$) as $\Gamma_Q^{d2} \approx 3.93 \cdot 10^{-5} \cdot \lambda^2$, respectively. In both cases an initial mass $m = 1$ has been used. A comparison of this rather rough estimate with the results from the actual calculations shows a remarkably good agreement. When taking into account, that the effective mass slightly increases with the coupling λ/m in the full calculations, the agreement is even better.

Thus momentum relaxation in the full Kadanoff-Baym equations as well as in the Boltzmann limit can be understood in rather simple terms. Turning the argument around, we can conclude that relaxation phenomena – as described by the Kadanoff-Baym equations – do not differ very much in comparison to semiclassical limits though the full quantum off-shell propagation is invoked.

In addition, we note that the relaxation time for the quadrupole moment is one order of magnitude larger than the typical inverse damping width, which dictates the relaxation of a single mode out of equilibrium (see Section 3.7). Going from the equation (5.16) to equation (5.17) one notices that the Bose enhancement factors have dropped out for the further estimate of the quadrupole relaxation rate. On the other hand these factors enter crucially in the total width. For a 2+1 dimensional system these Bose factors are of special importance and increase significantly the damping width. This explains the obvious difference between the quadrupole relaxation – characterizing kinetic equilibration of a far-from-equilibrium system – and the relaxation of a single mode out of equilibrium.

5.4 Stationary State of the Boltzmann Evolution

In Sections 3.2 and 3.7 we have described the characteristics of equilibration within the full Kadanoff-Baym theory. In this Section we additionally show the nonequilibrium evolution in the Boltzmann limit and in particular work out the differences in both approaches.

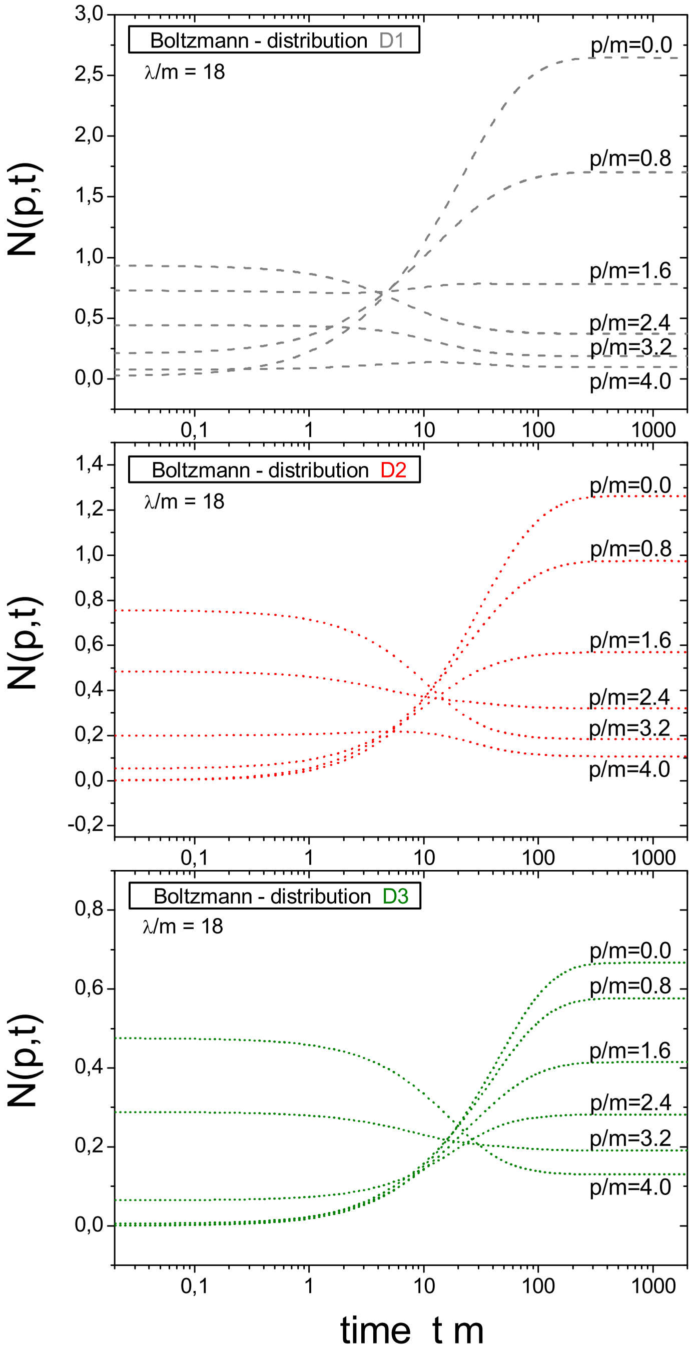

Figure 5.4: Time evolution of momentum modes $|\vec{p}|/m = 0.0,\, 0.8,\, 1.6,\, 2.4,\, 3.2,\, 4.0$ of the on-shell distribution function $N(\vec{p},t)$ for initializations D1 (upper plot), D2 (middle plot) and D3 (lower plot) in the Boltzmann approximation for $\lambda/m = 18$. All initial configurations (of the same energy) equilibrate, but lead to different stationary states (note the different scales for $N(\vec{p},t)$).

In Fig. 5.4 we present the time evolution of various momentum modes for the initial momentum space distributions D1, D2, D3 within the Boltzmann equation. In these calculations the effective on-shell energies are determined by including the time-dependent renormalized tadpole self-energy. The distributions D1, D2, D3 have been modified relative to our study of the Kadanoff-Baym dynamics in Chapter 3 such that they i) have the same energy density with respect to the modified total energy (where all sunset contributions are absent) and ii) are self-consistent with respect to the effective tadpole mass in order to avoid strong initial oscillations induced by a sudden change of the on-shell energies at very early times. For completeness we note, that the initial effective masses are determined by the solution of a gap equation taking into account the energy- and momentum-independent tadpole self-energy for the given initial momentum distribution.

We see from Fig. 5.4 that the time evolution given by the on-shell Boltzmann approximation deviates in several aspects from the Kadanoff-Baym dynamics. At first we find that in case of the Boltzmann equation the equal-energy initial distributions D1, D2 and D3 equilibrate towards different stationary states for $t \to \infty$. It can directly be read off from Fig. 5.4 when comparing the final occupation numbers of the various momentum modes. This behaviour is in contrast to the Kadanoff-Baym evolution where all initial distributions with the same energy reach a common stationary state (cf. Fig. 3.2). As pointed out in Section 3.6 this is an effect of the chemical equilibration mediated by particle number non-conserving processes, which are included in the Kadanoff-Baym dynamics since the full spectral function is taken into account. For the on-shell Boltzmann approximation, however, the particle number is strictly conserved and thus the initializations D1, D2, D3, that contain different number of particles, can not approach the same final state. Accordingly, the stationary state of the non-thermal initializations D1, D2, D3 exhibits a finite chemical potential (see below). Without explicit representation we note that the self-consistent initial configuration DT is already the thermal state of the Boltzmann equation and all momentum modes remain constant in time, whereas within the Kadanoff-Baym dynamics the 'free' thermal initialization DT evolves in time due to the generation of correlations (cf. Section 3.3).

In order to demonstrate, that the time evolution on the basis of the Boltzmann equation leads to a thermal state of quasiparticle excitations, we show in Fig. 5.5 the on-shell distribution $N(\vec{p},t)$ as a function of the time-dependent on-shell energy $\omega_{\vec{p}}(t)$ for various times $t \cdot m =$ 25, 50, 75, 100, 150, 200, 300, 500 for the initialization D1 and coupling strength $\lambda/m = 18$. We have displayed the quantity

$$F(\vec{p},t) \;=\; \ln(1+1/N(\vec{p},t)) \tag{5.28}$$

in order to obtain a straight line with slope $1/T$ and intersection point $-\mu/T$ in case of a Bose distribution $N = 1/(\exp((\omega_{\vec{p}} - \mu)/T) - 1)$ with temperature T and chemical potential μ. We see from Fig. 5.5 that the distribution at early times ($t \cdot m = 25$) is small for very low and very high momenta as reflected by the high values of the quantity F in the low and high energy regime. The particle accumulation at finite momentum for initialization D1 (cf. Fig. 3.1 (lower part)) shows up as a small dip in the curve. In

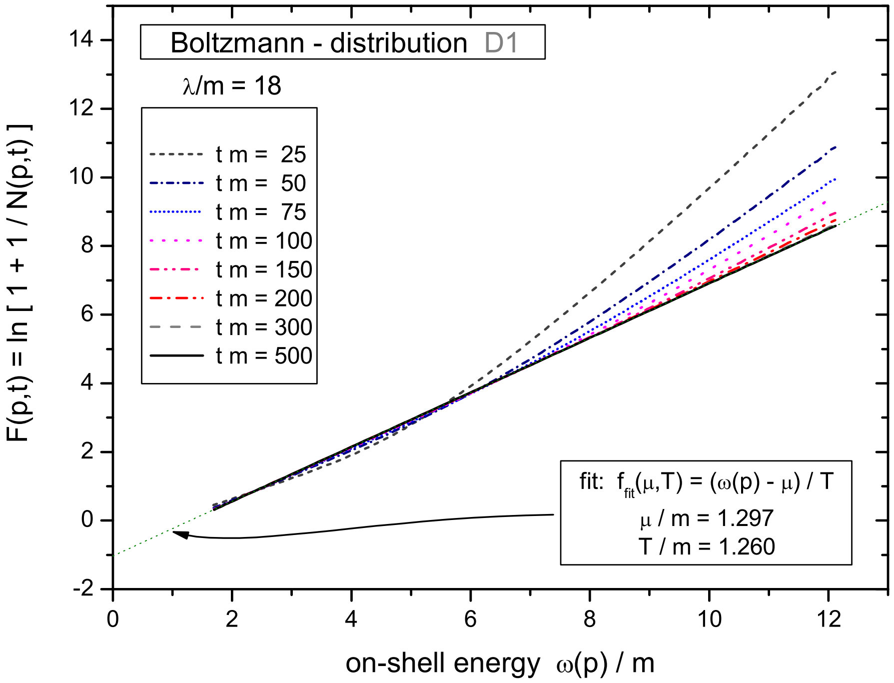

Figure 5.5: Distribution function F as a function of the time-dependent on-shell energy $\omega_{\vec{p}}(t)$ for various times $t \cdot m = 25, 50, 75, 100, 150, 200, 300, 500$ starting from an initial configuration D1 with coupling constant $\lambda/m = 18$. For large times a thermal state – characterized by a straight line in this representation – is reached with temperature $T/m = 1.260$ and finite chemical potential $\mu/m = 1.297$ as indicated by the fitting function (dotted line).

course of the time evolution these structures slowly vanish such that finally a straight line is reached (see lines for $t \cdot m = 300, 500$) indicating that the stationary limit is indeed a thermal distribution (at temperature $T/m = 1.260$). However, the chemical potential of the stationary distribution is non-vanishing – as recognized by the non-zero intersect of the dotted fit function – as $\mu/m = 1.297$. The initializations D2, D3 achieve different asymptotic temperatures which are given by $T/m = 1.562$ for D2 and $T/m = 2.218$ for D3. The chemical potential of the stationary state for these distributions is non-zero as well and has the values $\mu/m = 0.658$ for D2 and $\mu/m = -0.521$ for D3. We recall, that systems with large chemical potential distribute the total energy on many particles such that the final temperature is considerably lower. Thus, in general, the Boltzmann approximation does not drive the system to the proper equilibrium state of the neutral ϕ^4-theory, which is characterized by a vanishing chemical potential.

Furthermore, we see from Fig. 5.4 that in the Boltzmann limit the momentum modes evolve monotonically in time; there is no overshooting of the stationary limit as observed in the Kadanoff-Baym picture (cf. Fig. 3.2). Thus the non-monotonic behaviour shows up as a quantum phenomenon that is missing in the semiclassical treatment.

Chapter 6

Derivation of Generalized Transport Equations

In the previous Chapter we have discussed the Boltzmann equation as a rather crude – but frequently used – approximation to the full quantum theory. It treats the system evolution in terms of on-shell quasiparticles with fixed energy-momentum relation. As we have seen above this approximation exhibits also thermalization with comparable quadrupole relaxation rates for moderate coupling constants. However, characteristic features of the dynamics within the full Kadanoff-Baym equation are not observed for the Boltzmann case, such as the overshooting of low momentum equal-time Green function modes or complete chemical equilibration to the proper equilibrium state. The latter phenomenon is mediated by broad spectral functions and thus can not be obtained within the on-shell Boltzmann approach.

From the point of applications to experimental heavy-ion collisions there are further objections against the Boltzmann limit. Since it includes only on-shell particles, it is not able to treat resonances with their finite width in a consistent way. This extends to (in vacuum) stable particles (like protons) that assume a considerable width in the dense and/or hot medium due to collisions. Therefore it is also of practical interest to formulate transport theory in a more general way in order to include a consistent treatment of particles with broad dynamical spectral functions. In the following we will thus present a generalized transport equation based on a first order gradient expansion scheme. The quasiparticle assumption, employed in the standard derivation of the Boltzmann equation additionally, is not applied such that the semiclassical approach is able to deal with unstable particles as well. We will perform the derivation for an arbitrary (scalar) quantum-field theory containing only one elementary field and demand no restrictions on translational invariance in space or time.

The derivation of the generalized transport equation is based on the Kadanoff-Baym equation for the Wightman functions in coordinate space $(x_1 = (t_1, \vec{x}_1), x_2 = (t_2, \vec{x}_2))$

$$[\,\partial^{\mu}_{x_1}\partial^{x_1}_{\mu} + m^2 + \Sigma^{\delta}(x_1)\,]\;\; iG^{\gtrless}(x_1,x_2) \;=\; i\,I^{\gtrless}_1(x_1,x_2)\,. \tag{6.1}$$

The collision terms are given in $D = d + 1$ space-time dimensions by convolution integrals over coordinate space self-energies and Green functions:

$$I_1^{\gtrless}(x_1, x_2) = - \int_{t_0}^{t_1} d^D z \; [\Sigma^>(x_1, z) - \Sigma^<(x_1, z)] \; G^{\gtrless}(z, x_2) \tag{6.2}$$

$$+ \int_{t_0}^{t_2} d^D z \; \Sigma^{\gtrless}(x_1, z) \; [G^>(z, x_2) - G^<(z, x_2)] \, .$$

In the general case of an arbitrary (scalar) quantum field theory Σ^δ is the local part of the path self-energy while $\Sigma^{\gtrless}$ resemble the non-local collisional self-energy contributions. They are kept unspecified in the further derivation, but have to be fixed for actual applications. In the representation (6.2) the integration boundaries are exclusively given for the time coordinates. The integration starts at an initial time t_0 and ends at the current time coordinates of the Green function (t_1, t_2) indicating the causal structure of the Kadanoff-Baym equation. However, the convolution of the spatial coordinates extends over the whole spatial volume from $-\infty$ to $+\infty$, which is not indicated explicitly in (6.2).

6.1 Wigner Representation

Transport theories a usually formulated in phase-space. Thus one changes in the following to the Wigner representation via Fourier transformation with respect to the rapidly varying relative coordinate $\Delta x = x_1 - x_2$ and treats the system evolution in terms of the mean space-time coordinate $x = (x_1 + x_2)/2$ and the four-momentum $p = (p_0, \vec{p})$. The functions in Wigner space are obtained as

$$\bar{F}(p, x) = \int_{-\infty}^{\infty} d^D \Delta x \quad e^{+i\,\Delta x_\mu\, p^\mu} \; F(x_1 = x + \Delta x/2,\, x_2 = x - \Delta x/2) \, , \tag{6.3}$$

with the corresponding back transformation to coordinate space given by

$$F(x_1, x_2) = \int_{-\infty}^{\infty} \frac{d^D p}{(2\pi)^D} \quad e^{-i\,\Delta x_\mu\, p^\mu} \; \bar{F}(p, x) \, . \tag{6.4}$$

For the formulation of transport theory in the Wigner representation we have to focus not only on the transformation properties of ordinary two-point functions as given in (6.3), but also of convolution integrals as appearing in the equation of motion (6.2). A convolution integral in D dimensions (for arbitrary functions F, G),

$$H(x_1, x_2) = \int_{-\infty}^{\infty} d^D z \;\; F(x_1, z) \;\; G(z, x_2) \tag{6.5}$$

transforms as

$$\begin{aligned}
\bar{H}(p,x) &= \int_{-\infty}^{\infty} d^D\Delta x \quad e^{+i\,\Delta x_\mu\, p^\mu} \; H(x_1,x_2) \qquad (6.6)\\
&= \int_{-\infty}^{\infty} d^D\Delta x \quad e^{+i\,\Delta x_\mu\, p^\mu} \; \int_{-\infty}^{\infty} d^D z \;\; F(x_1,z) \;\; G(z,x_2)\\
&= \quad e^{+i\,\frac{1}{2}\,(\partial_p^\mu \cdot\, \partial_\mu^{x'} \,-\, \partial_x^\mu \cdot\, \partial_\mu^{p'})} \; \left[\, \bar{F}(p,x) \;\; \bar{G}(p',x') \,\right]\Big|_{x'=x,\, p'=p} \; .
\end{aligned}$$

In accordance with the standard assumption of transport theory we assume that all functions only smoothly evolve in the mean space-time coordinates and thus restrict to first order derivatives. All terms proportional to second or higher order derivatives in the mean space-time coordinates (also mixed ones) will be dropped. Thus the Wigner transformed convolution integrals are given in *first order gradient approximation* by

$$\bar{H}(p,x) \;=\; \bar{F}(p,x)\;\; \bar{G}(p,x) \;+\; i\,\frac{1}{2}\,\{\, \bar{F}(p,x)\,,\, \bar{G}(p,x)\,\} \;+\; \mathcal{O}(\partial_x^2)\,, \qquad (6.7)$$

with the relativistic generalization of the Poisson bracket

$$\{\, \bar{F}(p,x)\,,\, \bar{G}(p,x)\,\} \;=\; \partial_\mu^p\, \bar{F}(p,x)\cdot \partial_x^\mu\, \bar{G}(p,x) \;-\; \partial_x^\mu\, \bar{F}(p,x)\cdot \partial_\mu^p\, \bar{G}(p,x)\;. \qquad (6.8)$$

Thus the Wigner transformed convolution integral of two functions is given by the product of the Wigner transformed functions plus gradient corrections including derivatives with respect to energy-momentum and space-time coordinates.

Writing the Wigner transformation in explicit units (and not for the standard units using $\hbar = 1$), it explicitly contains the Planck constant in the exponential term as $\exp(i\,\Delta x\, p\,/\,\hbar)$. From the expression for the corresponding series operator $\exp(i\,\hbar\,[\,\partial_p^\mu\, \partial_\mu^{x'} - \partial_x^\mu\, \partial_\mu^{p'})\,]/2)$ we find that the first Poisson bracket term contains a factor $\hbar$ as well $i/2\,\{\bar{F},\bar{G}\} \to i/2\,\hbar\,\{\bar{F},\bar{G}\}$. Therefore the Poisson bracket can be interpreted as a first order correction in $\hbar$ to the purely multiplicative contribution of the Wigner transformed convolution integral. The results obtained in a first order gradient expansion are thus also referred to as the *semiclassical approximation.*

Furthermore, the Klein-Gordon derivative operator – applied to some arbitrary function F – transforms in Wigner representation to

$$\int_{-\infty}^{\infty} d^D\Delta x \;\; e^{i\,\Delta x_\mu\, p^\mu}\; [\,\partial_{x_1}^\mu \partial_\mu^{x_1} + m^2\,]\;\; F(x_1,x_2) \;=\; [\,-p^2 - i\,p^\mu\,\partial_\mu^x + \underbrace{\frac{1}{4}\,\partial_x^2}_{\approx\,0} + m^2\,]\;\bar{F}(p,x)\,, \qquad (6.9)$$

where the second order space-time derivatives have to be neglected in the first order gradient scheme.

6.2 Approximate Dynamics of the Spectral Function

Before we will come to the derivation of the actual transport equation we discuss the time evolution of the spectral properties of the system. In order to obtain the dynamics within the approximate scheme we start with the Dyson-Schwinger equations for the retarded and advanced Green functions in coordinate space (2.20,2.21)

$$\begin{aligned}
&-\left[\partial^{x_1}_{\mu}\partial^{\mu}_{x_1} + m^2 + \Sigma^{\delta}(x_1)\right]\ G^R(x_1,x_2) && (6.10)\\
&\qquad = \ \delta^{(D)}(x_1-x_2) + \int_{-\infty}^{\infty} d^Dz\ \Sigma^R(x_1,z)\ G^R(z,x_2)\,, \\
&-\left[\partial^{x_1}_{\mu}\partial^{\mu}_{x_1} + m^2 + \Sigma^{\delta}(x_1)\right]\ G^A(x_1,x_2) \\
&\qquad = \ \delta^{(D)}(x_1-x_2) + \int_{-\infty}^{\infty} d^Dz\ \Sigma^A(x_1,z)\ G^A(z,x_2)\,. && (6.11)
\end{aligned}$$

The time evolution of the retarded (advanced) Green function $G^{R(A)}$ is determined – apart from the time local term Σ^{δ} – by retarded (advanced) self-energies $\Sigma^{R(A)}$, only. The convolution integrals in (6.10) and (6.11) extend over the whole space and time range in contrast to the equations of motion for the Wightman functions given in (6.1) and (6.2).

The further procedure consists in the following steps: at first we i) transform the above equations into the Wigner representation and apply the first order gradient approximation. In this limit the convolution integrals yield the product terms and the general Poisson bracket of the self-energies and the Green functions $\{\Sigma^{R/A}, G^{R/A}\}$. We, furtheron, represent both equations in terms of real quantities, only, by the decomposition of the retarded and advanced Green functions and self-energies as

$$\begin{aligned}
\bar{G}^{R/A} &= Re\,\bar{G}^R \pm i\,Im\,\bar{G}^R = Re\,\bar{G}^R \mp i\,\bar{A}/2\,, & \bar{A} &= \mp 2\,Im\,\bar{G}^{R/A}\,,\\
\bar{\Sigma}^{R/A} &= Re\,\bar{\Sigma}^R \pm i\,Im\,\bar{\Sigma}^R = Re\,\bar{\Sigma}^R \mp i\,\bar{\Gamma}/2\,, & \bar{\Gamma} &= \mp 2\,Im\,\bar{\Sigma}^{R/A}\,.
\end{aligned} \qquad (6.12)$$

We find that in Wigner space the real parts of the retarded and advanced Green functions and self-energies are equal, while the imaginary parts have opposite sign and are proportional to the spectral function $\bar{A}$ and the width $\bar{\Gamma}$, respectively. The next step consists in ii) the separation of the real part and the imaginary part of the two equations for the retarded and advanced Green functions, that have to be fulfilled independently. Thus we obtain four real-valued equations for the self-consistent retarded and advanced Green functions. In the last step iii) we get simple relations by linear combination of these equations, i.e. by adding/subtracting the relevant equations.

This finally leads to two algebraic relations for the spectral function $\bar{A}$ and the real part of the retarded Green function $Re\,\bar{G}^R$ in terms of the width $\bar{\Gamma}$ and the real part of the retarded self-energy $Re\,\bar{\Sigma}^R$ as:

$$[\,p_0^2 - \vec{p}^{\,2} - m^2 - \bar{\Sigma}^\delta + Re\,\bar{\Sigma}^R\,]\;Re\,\bar{G}^R \;=\; 1 + \frac{1}{4}\,\bar{\Gamma}\,\bar{A}\,, \tag{6.13}$$

$$[\,p_0^2 - \vec{p}^{\,2} - m^2 - \bar{\Sigma}^\delta + Re\,\bar{\Sigma}^R\,]\;\bar{A} \;=\; \bar{\Gamma}\;Re\,\bar{G}^R\,. \tag{6.14}$$

A first consequence of (6.13) and (6.14) is a direct relation between the real and the imaginary parts of the retarded/advanced Green function, which reads (for $\bar{\Gamma} \neq 0$):

$$Re\,\bar{G}^R \;=\; \frac{p_0^2 - \vec{p}^{\,2} - m^2 - \bar{\Sigma}^\delta - Re\,\bar{\Sigma}^R}{\bar{\Gamma}}\;\bar{A}\,. \tag{6.15}$$

Furthermore, the solution of (6.13) and (6.14) yields the following result for the spectral function and the real part of the retarded Green function

$$\bar{A} \;=\; \frac{\bar{\Gamma}}{[\,p_0^2 - \vec{p}^{\,2} - m^2 - \bar{\Sigma}^\delta - Re\,\bar{\Sigma}^R\,]^2 + \bar{\Gamma}^2/4} \;=\; \frac{\bar{\Gamma}}{\bar{M}^2 + \bar{\Gamma}^2/4}\,, \tag{6.16}$$

$$Re\,\bar{G}^R \;=\; \frac{[\,p_0^2 - \vec{p}^{\,2} - m^2 - \bar{\Sigma}^\delta - Re\,\bar{\Sigma}^R\,]}{[\,p_0^2 - \vec{p}^{\,2} - m^2 - \bar{\Sigma}^\delta - Re\,\bar{\Sigma}^R\,]^2 + \bar{\Gamma}^2/4} \;=\; \frac{\bar{M}}{\bar{M}^2 + \bar{\Gamma}^2/4}\,, \tag{6.17}$$

where we have introduced the mass-function $\bar{M}$ in Wigner space:

$$\bar{M}(p,x) \;=\; p_0^2 - \vec{p}^{\,2} - m^2 - \bar{\Sigma}^\delta(x) - Re\,\bar{\Sigma}^R(p,x)\,. \tag{6.18}$$

The (6.16) spectral function shows a typical Breit-Wigner shape with energy- and momentum-dependent self-energy terms. Although the above equations are purely algebraic solutions and contain no derivative terms, they are valid up to the first order in the gradients. Moreover, subtraction of the real parts and adding up the imaginary parts lead to the time evolution equations

$$p^\mu\,\partial_\mu^x\,\bar{A} \;=\; \frac{1}{2}\,\{\,\bar{\Sigma}^\delta + Re\,\bar{\Sigma}^R\,,\,\bar{A}\,\} \;+\; \frac{1}{2}\,\{\,\bar{\Gamma}\,,\,Re\,\bar{G}^R\,\}\,, \tag{6.19}$$

$$p^\mu\,\partial_\mu^x\,Re\,\bar{G}^R \;=\; \frac{1}{2}\,\{\,\bar{\Sigma}^\delta + Re\,\bar{\Sigma}^R\,,\,Re\,\bar{G}^R\,\} \;-\; \frac{1}{8}\,\{\,\bar{\Gamma}\,,\,\bar{A}\,\}\,. \tag{6.20}$$

The Poisson bracket containing the mass-function $\bar{M}$ leads to the well-known drift operator $p^\mu \, \partial^x_\mu \, \bar{F}$ (for an arbitrary function $\bar{F}$), i.e.

$$\{ \bar{M} \, , \, \bar{F} \} \;=\; \{ p_0^2 - \vec{p}^{\,2} - m^2 - \bar{\Sigma}^\delta - Re \, \bar{\Sigma}^R \, , \, \bar{F} \} \tag{6.21}$$

$$\;=\; 2 \, p^\mu \, \partial^x_\mu \, \bar{F} \; - \; \{ \bar{\Sigma}^\delta + Re \, \bar{\Sigma}^R \, , \, \bar{F} \} \, , \tag{6.22}$$

such that the first order equations (6.19) and (6.20) can be written in a more comprehensive form as

$$\{ \bar{M} \, , \, \bar{A} \} \;=\; \{ \bar{\Gamma} \, , \, Re \, \bar{G}^R \} \, , \tag{6.23}$$

$$\{ \bar{M} \, , \, Re \, \bar{G}^R \} \;=\; - \frac{1}{4} \{ \bar{\Gamma} \, , \, \bar{A} \} \, . \tag{6.24}$$

When inserting (6.16) and (6.17) we find that these first order time evolution equations are solved by the algebraic expressions. In this case the following relations hold:

$$\{ \bar{M} \, , \, \bar{A} \} \;=\; \{ \bar{\Gamma} \, , \, Re \, \bar{G}^R \} \;=\; \{ \bar{M} \, , \, \bar{\Gamma} \} \; \frac{\bar{M}^2 - \bar{\Gamma}^2/4}{[\, \bar{M}^2 + \bar{\Gamma}^2/4 \,]^2} \, , \tag{6.25}$$

$$\{ \bar{M} \, , \, Re \, \bar{G}^R \} \;=\; - \frac{1}{4} \{ \bar{\Gamma} \, , \, \bar{A} \} \;=\; \{ \bar{M} \, , \, \bar{\Gamma} \} \; \frac{\bar{M} \, \bar{\Gamma}/2}{[\, \bar{M}^2 + \bar{\Gamma}^2/4 \,]^2} \, . \tag{6.26}$$

Thus we have derived the proper structure of the spectral function (6.16) within the semiclassical approximation. Together with the explicit form for the real part of the retarded Green function (6.17) we have now access to the dynamics of the spectral properties which is consistent up the first order in the gradients.

6.3 Derivation of the Semiclassical Transport Equation

In this Section we will derive the transport equations for the phase-space distribution in the first order gradient approximation. For this aim we start, as already mentioned, with the Kadanoff-Baym equation for the Green functions $G^{\gtrless}$. In order to apply the relations for the Wigner transformation of convolution integrals (6.7) we rewrite the memory terms such that the time integrations extend from $-\infty$ to $+\infty$. In this respect we consider the initial time $t_0 = -\infty$ whereas the upper time boundaries t_1, t_2

are taken into account by Θ-functions:

$$\begin{aligned}
I_1^{\gtrless}(x_1,x_2) &= - \int_{-\infty}^{\infty} d^Dx' \;\; \Theta(t_1-t')\; [\Sigma^{>}(x_1,x') - \Sigma^{<}(x_1,x')] \;\; G^{\gtrless}(x',x_2) \\
&\quad + \int_{-\infty}^{\infty} d^Dx' \;\; \Sigma^{\gtrless}(x_1,x') \;\; \Theta(t_2-t') \;\; [G^{>}(x',x_2) - G^{<}(x',x_2)] \\
&= - \int_{-\infty}^{\infty} d^Dx' \;\; \Sigma^{R}(x_1,x')\, G^{\gtrless}(x',x_2) \; + \; \Sigma^{\gtrless}(x_1,x')\, G^{A}(x',x_2)\,. \qquad (6.27)
\end{aligned}$$

We now perform the analogous steps as invoked in the preceeding Section for the retarded and advanced Dyson-Schwinger equations. We start with a first order gradient expansion of the Wigner transformed Kadanoff-Baym equation using (6.27) for the memory integrals. Again we separate the real and the imaginary parts in the resulting equation, which have to be satisfied independently. At the end of this procedure we obtain a generalized transport equation:

$$\begin{aligned}
\underbrace{2\,p^{\mu}\,\partial_{\mu}^{x}\, i\bar{G}^{\gtrless} \; - \; \{\,\bar{\Sigma}^{\delta} + Re\,\bar{\Sigma}^{R},\, i\bar{G}^{\gtrless}\,\}} \; - \{\, i\bar{\Sigma}^{\gtrless},\, Re\,\bar{G}^{R}\} \;\; &= \;\; i\bar{\Sigma}^{<}\, i\bar{G}^{>} \; - \; i\bar{\Sigma}^{>}\, i\bar{G}^{<} \\
\{\,\bar{M}\,,\, i\bar{G}^{\gtrless}\,\} \qquad\qquad\qquad - \{\, i\bar{\Sigma}^{\gtrless},\, Re\,\bar{G}^{R}\} \;\; &= \;\; i\bar{\Sigma}^{<}\, i\bar{G}^{>} \; - \; i\bar{\Sigma}^{>}\, i\bar{G}^{<} \qquad (6.28)
\end{aligned}$$

as well as a generalized mass-shell equation

$$\underbrace{[\,p^2 - m^2 - \bar{\Sigma}^{\delta} - Re\,\bar{\Sigma}^{R}\,]}_{\bar{M}} \;\; i\bar{G}^{\gtrless} \; = \; i\bar{\Sigma}^{\gtrless}\; Re\,\bar{G}^{R} \; + \; \frac{1}{4}\{\, i\bar{\Sigma}^{>},\, i\bar{G}^{<}\,\} \; - \; \frac{1}{4}\{\, i\bar{\Sigma}^{<},\, i\bar{G}^{>}\,\} \qquad (6.29)$$

with the mass-function $\bar{M}$ specified in (6.18). Since the Green function $G^{\gtrless}(x_1,x_2)$ consists of an antisymmetric real part and a symmetric imaginary part with respect to the relative coordinate $x_1 - x_2$, the Wigner transform of this function is purely imaginary. It is thus convenient to represent the Wightman functions in Wigner space furtheron by the real-valued quantities $i\bar{G}^{\gtrless}(p,x)$. Since the collisional self-energies obey the same symmetry relations in coordinate space and in phase-space, they will be kept also as $i\bar{\Sigma}^{\gtrless}(p,x)$ furtheron.

In the transport equation (6.28) one recognizes on the l.h.s. the drift term $p^{\mu}\,\partial_{\mu}^{x}\, i\bar{G}^{\gtrless}$, as well as the Vlasov term with the local self-energy $\bar{\Sigma}^{\delta}$ and the real part of the retarded self-energy $Re\,\bar{\Sigma}^{R}$. On the other hand the r.h.s. represents the collision term with its typical 'gain and loss' structure. The loss term $i\bar{\Sigma}^{>}\; i\bar{G}^{<}$ (proportional to the Green function itself) describes the scattering out of a respective phase-space cell whereas the gain term $i\bar{\Sigma}^< \, i\bar{G}^>$ takes into account scatterings into the actual cell. The last term on the l.h.s. $\{\, \bar{\Sigma}^R, Re\, \bar{G}^R \,\}$ is very peculiar since it does not contain directly the distribution function $i\bar{G}^<$. This second Poisson bracket vanishes in the quasiparticle approximation and thus does not appear in the on-shell Boltzmann limit. As we will discuss in detail in Chapter 8 the second Poisson bracket $\{\, i\bar{\Sigma}^{\gtrless}, Re\, \bar{G}^R \,\}$ governs the evolution of the off-shell dynamics for nonequilibrium systems.

Although the generalized transport equation (6.28) and the generalized mass-shell equation (6.29) have been derived form the same Kadanoff-Baym equation in a first order gradient expansion, both equations are not exactly equivalent. Instead, they deviate from each other by contributions of higher gradient order (see below). This raises the question: *which one of these two equations has be considered to higher priority?* The question is answered in praxis by the prescription of solving the generalized transport equation (6.28) for $i\bar{G}^<$ in order to study the dynamics of the nonequilibrium system in phase-space. Since the dynamical evolution of the spectral properties is taken into account by the equations derived in first order gradient expansion from the retarded and advanced Dyson-Schwinger equations, one can neglect the generalized mass-shell equation (6.29). Thus for actual numerical studies we will lateron use the generalized transport equation (6.28) supported by the algebraic relations (6.16) and (6.17).

For the neutral ϕ^4-theory $G^<(x_1,x_2) = G^>(x_2,x_1)$ holds in coordinate space and thus $i\bar{G}^<(p,x) = i\bar{G}^>(-p,x)$ for the Wigner transformed functions. Hence it is sufficient (in case of a neutral theory) to solve the evolution for the Wightman function $i\bar{G}^<$, only. The evolution equations are presented here for both functions for the sake of completeness. Furthermore, one recognizes by subtraction of the $i\bar{G}^>$ and $i\bar{G}^<$ mass-shell and transport equations, that the dynamics of the spectral function $\bar{A} = i\bar{G}^> - i\bar{G}^<$ is determined in the same way as derived from the retarded and advanced Dyson-Schwinger equations (6.16) and (6.23). The inconsistency between the two equations (6.28) and (6.29) vanishes due to the subtractions since the differences are contained in the collisional contributions on the r.h.s..

In order to evaluate the $\{\, i\bar{\Sigma}^<, Re\, \bar{G}^R \,\}$-term on the l.h.s. of (6.28) it is useful to introduce distribution functions for the Green functions and self-energies as

$$i\bar{G}^<(p,x) \;=\; \bar{N}(p,x)\, \bar{A}(p,x)\,, \qquad i\bar{G}^>(p,x) \;=\; [\,1 + \bar{N}(p,x)\,]\, \bar{A}(p,x)\,, \tag{6.30}$$

$$i\bar{\Sigma}^<(p,x) \;=\; \bar{N}^{\Sigma}(p,x)\, \bar{\Gamma}(p,x)\,, \qquad i\bar{\Sigma}^>(p,x) \;=\; [\,1 + \bar{N}^{\Sigma}(p,x)\,]\, \bar{\Gamma}(p,x)\,. \tag{6.31}$$

In equilibrium the distribution function with respect to the Green functions $\bar{N}$ and the self-energies $\bar{N}^{\Sigma}$ are given as Bose functions in the energy p_0 at given temperature and thus are equal. Following the argumentation of Botermans and Malfliet [18] the distribution functions $\bar{N}$ and $\bar{N}^{\Sigma}$ in (6.30) should be identical within the second term of the l.h.s. of (6.28) within a consistent first order gradient expansion. In order to demonstrate their argument we write

$$i\bar{\Sigma}^< \;=\; \bar{\Gamma}\,\bar{N}^\Sigma \;=\; \bar{\Gamma}\,\bar{N} \,+\, \bar{K}\,. \tag{6.32}$$

The 'correction' term $\bar{K}$ is proportional to the collision term (r.h.s.) of the generalized transport equation (6.28),

$$\bar{K} \;=\; \bar{\Gamma}\,(\,\bar{N}^\Sigma \,-\, \bar{N}\,) \;=\; (\,i\bar{\Sigma}^<\,i\bar{G}^> \,-\, i\bar{\Sigma}^>\,i\bar{G}^<\,)\,\bar{A}^{-1}\,, \tag{6.33}$$

which itself is of first order in the gradients. Thus, whenever a distribution function $\bar{N}^\Sigma$ appears within a Poisson bracket the difference term $(\bar{N}^\Sigma - \bar{N})$ becomes of second order in the gradients and should be omitted for consistency. As a consequence $\bar{N}^\Sigma$ can be replaced by $\bar{N}$ and thus the self-energy $\bar{\Sigma}^<$ by $\bar{G}^< \cdot \bar{\Gamma}/\bar{A}$ in the Poisson bracket term $\{\bar{\Sigma}^<, Re\,\bar{G}^R\}$. The generalized transport equation (6.28) then can be written in short-hand notation

$$\frac{1}{2}\bar{A}\,\bar{\Gamma}\,\left[\{\,\bar{M}\,,\; i\bar{G}^<\,\} \,-\, \frac{1}{\bar{\Gamma}}\,\{\,\bar{\Gamma}\,,\; \bar{M}\cdot i\bar{G}^<\,\}\right] \;=\; i\bar{\Sigma}^<\,i\bar{G}^> \,-\, i\bar{\Sigma}^>\,i\bar{G}^< \tag{6.34}$$

with the mass-function $\bar{M}$ (6.18).

The transport equation (6.34) within the Botermans-Malfliet (BM) form resolves the discrepancy between the generalized mass-shell equation (6.29) and the generalized transport equation in its original (so-called Kadanoff-Baym (KB)) form (6.28). Indeed, the solution of (6.34) is in full consistency with the corresponding mass-shell equation.

Furthermore, the consistent Botermans-Malfliet form will be the starting point for the derivation of an efficient transport approach for the description of realistic heavy-ion collisions. Together with a test-particle ansatz this equation allows for the study of the time evolution of phase-space densities including the approximate dynamics of the spectral function. As we will see in Section 8.3 the incorporation of the off-shell dynamics will have significant influence when testing theoretical approaches against experimental data.

Chapter 7

Dynamics within the Generalized Transport Equation

In this Chapter we will perform numerical studies of the dynamics inherent in the generalized transport equations derived in Chapter 6. Again we perform the calculations for the ϕ^4-theory in 2+1 space-time dimensions within the three-loop approximation for the effective action. This fixes the self-energies $\bar{\Sigma}^{\delta}$ and $i\bar{\Sigma}^{\gtrless}$ in (6.28) and (6.29) to be the same as in the case of the full Kadanoff-Baym theory given by the tadpole and the sunset contributions, respectively. For the first investigation we concentrate on the dynamics of the generalized transport equation (6.28) that has been obtained by gradient expansion of the Wigner transformed Kadanoff-Baym equation. As in Chapter 3 we restrict ourselves to homogeneous systems in space. Consequently the derivatives with respect to the mean spatial coordinate $\vec{x}$ vanish, such that the generalized transport equation (6.28) reduces to

$$2\,p_0\,\partial_t\,i\bar{G}^{<} \;-\; \{\,\bar{\Sigma}^{\delta}{+}Re\,\bar{\Sigma}^{R}\,,\,i\bar{G}^{<}\,\} \;-\; \{\,i\bar{\Sigma}^{<}\,,\,Re\,\bar{G}^{R}\,\} \;=\; i\bar{\Sigma}^{<}\,i\bar{G}^{>} \;-\; i\bar{\Sigma}^{>}\,i\bar{G}^{<} \qquad (7.1)$$

with the simplified Poisson brackets (for arbitrary functions $\bar{F},\bar{G}$)

$$\begin{aligned} &\{\,\bar{F}(\vec{p},p_0,t)\,,\,\bar{G}(\vec{p},p_0,t)\,\} \qquad (7.2)\\ &\quad=\;\partial_{p_0}\,\bar{F}(\vec{p},p_0,t)\;\partial_t\,\bar{G}(\vec{p},p_0,t)\;-\;\partial_t\,\bar{F}(\vec{p},p_0,t)\;\partial_{p_0}\,\bar{G}(\vec{p},p_0,t)\;. \end{aligned}$$

7.1 The Initial State

In order to specify the problem for the first order transport equation in time, the initial state has to be fixed, i.e. the initial Green function $i\bar{G}^{<}(\vec{p},p_0,t=0)$ has to be specified for all momenta $\vec{p}$ and all energies p_0.

To this aim, we first assume a given initial distribution function $n(\vec{p}, t\!=\!0)$ in momentum space equivalent to those used in the investigation of the full Kadanoff-Baym theory in order to allow for a comparison of the two schemes. Next, the complete initial phase-space distribution function $\bar{N}(\vec{p}, p_0, t\!=\!0)$ has to be specified as a function of the energy p_0 as well. We achieve this by the most simple ansatz of $\bar{N}$ being constant in the energy variable p_0 as a starting point. In order to determine the initial Green function we employ the self-consistent iteration procedure for the full spectral function as described in Section 4.1. However, we use the specified nonequilibrium distribution function $\bar{N}$ instead of a Bose distribution at given temperature. The iteration process then yields the fully self-consistent spectral function for this initial distribution and thus determines the initial Green function via

$$i\bar{G}^{<}(\vec{p}, p_0, t\!=\!0) \;=\; \bar{N}(\vec{p}, p_0, t\!=\!0)\; \bar{A}(\vec{p}, p_0, t\!=\!0)\,. \tag{7.3}$$

In principle one might choose the initialization – in particular the energy dependence of the distribution functions – in various ways. We employ here the simple description introduced above since it approximately reproduces the same equal-time (i.e. energy integrated) initial Green function as in the full Kadanoff-Baym calculation. However, with increasing coupling strength λ the spectral function achieves a considerable width and the on-shell values can be shifted. In this case the equal-time Green function deviates slightly in the low momentum region from the ‘quasiparticle’-like initialization (3.1) used for the Kadanoff-Baym calculation. This difference can be easily understood as follows:

For small coupling strength λ the spectral function is very narrow and located close to the bare on-shell energy $\omega_{\vec{p}}$. Therefore, when calculating the equal-time Green function by means of an energy integration, one can introduce an artificial factor $p_0/\omega_{\vec{p}}$ (which is approximately 1 in the region of considerable strength) without changing the integral sizeably. Using the normalization condition of the (p_0 weighted) spectral function (3.7), the energy integration can be preformed and one obtains equal-time Green functions in the ‘quasiparticle’ form (3.1). On the other hand, strong couplings lead to broad spectral functions such that the artificial factor $p_0/\omega_{\vec{p}}$ is no longer close to one. This comes about since i) the range of the spectral support is broad and thus the linear energy dependence of the factor is important and since ii) the spectral function is not located at the bare on-shell energy anymore, but slightly shifted to higher values. Thus the energy integration leads to somewhat different results as the ‘quasiparticle’ form when evaluating the energy integral. As we will see in the following, the equal-time Green functions – obtained within this scheme – show the same characteristics as those for the Kadanoff-Baym calculation, although they deviate for large couplings and small momenta. Nevertheless, they are useful for a comparison of the dynamics within the full quantum theory and the semiclassical approximation.

The initial distribution functions for the following studies are shown in Fig. 7.1 for polar symmetric settings as a function of the momentum coordinate p_x for $p_y = 0$. They are identical to those used in the first part of our investigations for polar symmetric systems within the full Kadanoff-Baym theory (c.f. Fig. 3.1 (upper plot)).

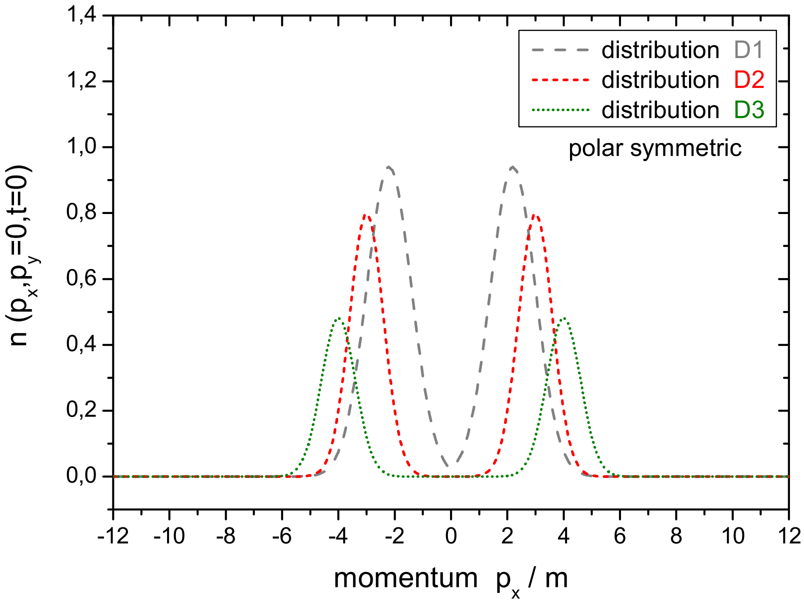

Figure 7.1: Initial momentum distributions for the initializations D1, D2 and D3. For the polar symmetrical settings in momentum space the distributions are shown as function of p_x (for $p_y = 0$).

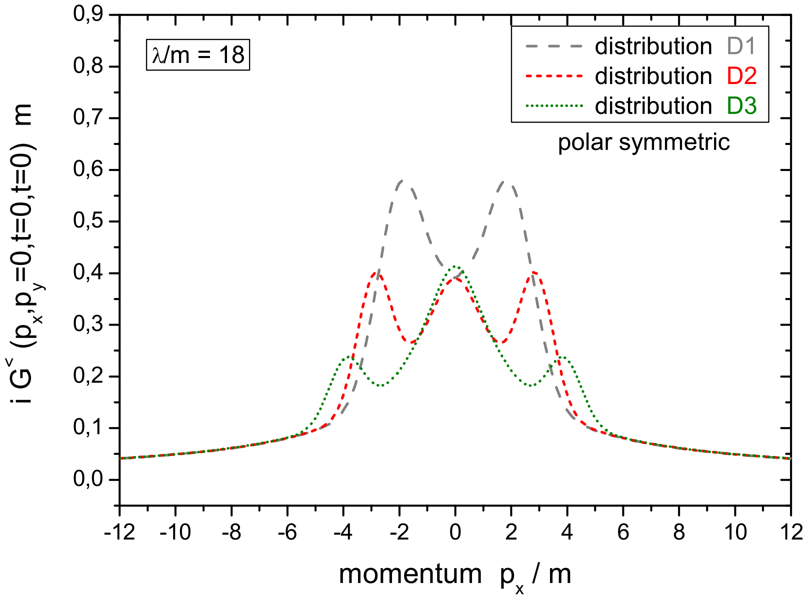

Figure 7.2: Initial equal-time Green functions for the initializations D1, D2 and D3. The equal-time Green functions are displayed for polar symmetric systems as a function of p_x (for $p_y = 0$) with coupling constant $\lambda/m = 18$.

The resulting initial equal-time Green functions – for the coupling constant $\lambda/m = 18$ – are displayed in Fig. 7.2. By comparison with the initial Green functions of the Kadanoff-Baym calculation (c.f. Fig. 3.1 (lower plot)) we find tiny deviations in the region of small absolute momenta. This is, of course, a consequence of the large coupling constant employed, which we use in order to compare to the calculations within the full quantum evolution for the same coupling strength. Since the initial states are very close to those used for the Kadanoff-Baym theory, we will also denote them as initializations D1, D2 and D3.

The advantage of the initialization prescription introduced above is that the actual spectral function – directly obtained by $\bar{A} = i\bar{G}^{>} - i\bar{G}^{<}$ from the Green functions – complies with the one determined from the self-energies (6.16) in accordance with the first order gradient expansion scheme. During the nonequilibrium time evolution this correspondence is maintained since the analytic expression for the spectral function already is a solution of the generalized transport equation itself. Furthermore, the real part of the retarded Green function, that enters the peculiar second Poisson bracket on the l.h.s. in (6.28), can be taken in the first order scheme (6.17) which simplifies the calculations sizeably.

We mention that other prescriptions are also possible for the calculation of $Re\,\bar{G}^{R}$:
1) One can determine it directly from $i\bar{G}^{\gtrless}$ by a Fourier technique similar to one used in the calculation of the self-consistent spectral functions in Section 4.1. Here the real part of the retarded Green function is obtained via inverse Wigner transformation with respect to the energy, multiplication by the (for retarded quantities characteristic) Θ-function in relative time and transformation back into phase-space.
2) One can also use dispersion relations with the spectral function to specify $Re\,\bar{G}^{R}$.
As we have checked in our actual simulations all prescriptions lead to practically identical results.

7.2 Numerical Study of Equilibration

Now we turn to the actual solutions of the generalized transport equation in the KB form (6.28). In Fig. 7.3 we show the time evolution of the equal-time Green function $iG^{<}(|\vec{p}|, t, t)$ for the polar symmetric initial states D1, D2 and D3 as specified above. We have displayed several momentum modes $|\vec{p}|/m =$ 0.0, 0.8, 1.6, 2.4, 3.2, 4.0 of the equal-time Green function on a logarithmic time scale. As in the full Kadanoff-Baym theory we find that for all initializations the quantum system approaches a stationary state for $t \to \infty$, i.e. all momentum modes approach a constant. However, the respective momentum modes of the different initializations do not achieve identical values for $t \to \infty$, as seen in particular for the low momenta $|\vec{p}|/m =$ 0.0, 0.8. This is not surprising since the various initializations – obtained within the self-consistent scheme described above – do not correspond to exactly the same energy. Thus the respective long-time limits should differ slighty. The small difference in energy is, of course, most prominently seen in the low momentum (energy) modes. Moreover, the dynamics within the generalized transport equation (6.28) is in general very similar

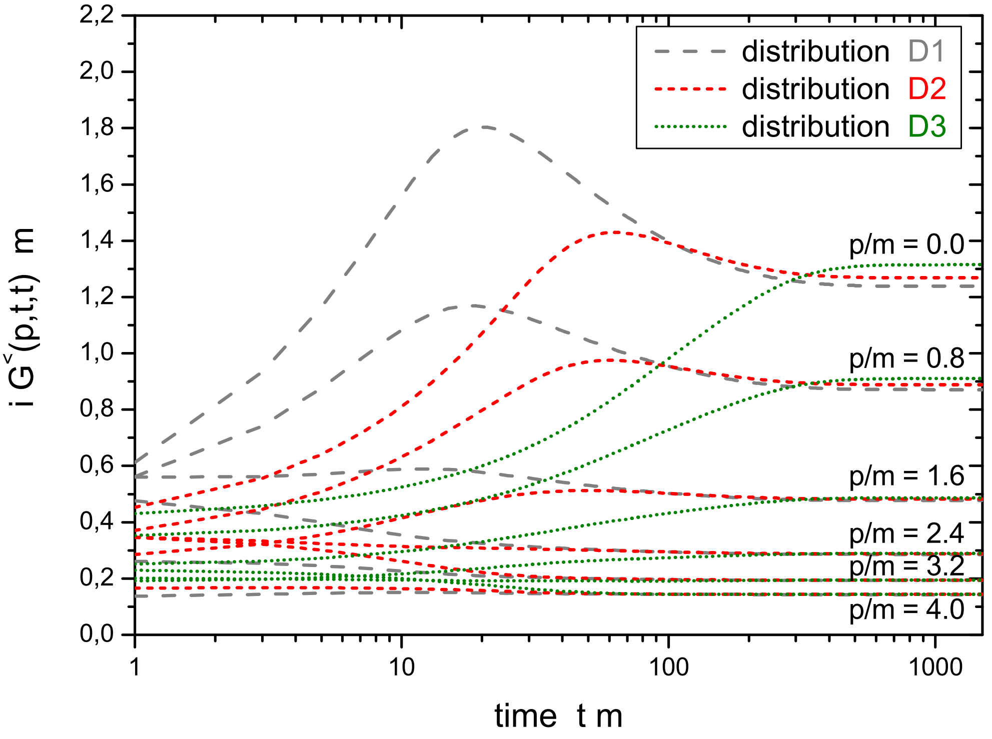

Figure 7.3: Evolution of several momentum modes $|\vec{p}|/m = 0.0, 0.8, 1.6, 2.4, 3.2, 4.0$ of the equal-time Green function on a logarithmic time scale for the different initializations D1, D2 and D3.

to the full Kadanoff-Baym theory. For all three initial states we find (apart from the very initial phase $t \cdot m < 1$) the same structures during the equilibration process. In particular for the initializations D1 and D2 the characteristic overshooting for the low momentum modes is seen as in the full quantum evolution. Even the positions of the maxima are in a comparable range: For the initialization D1 they are shifted to slightly larger times and are a little bit lower than in the full calculation; the same holds for the initial state D2. The initial distribution D3 yields a monotonous behaviour for all momentum modes within the generalized transport formulation which is again in a good agreement with the full dynamics.

Some comments are worthwhile with respect to the comparison performed above: The spectral function in the Kadanoff-Baym calculation is completely undetermined in the initial state; it develops during the very early phase to an approximate form (which in the following still evolves in time). In contrast to this, the spectral function in the generalized transport formulation (6.28) has a well-defined structure already from the beginning. This principle difference results from the fact, that we deal in the Kadanoff-Baym case with a true initial value problem in the two time directions. Thus the relative time integral – to obtain the spectral function as a function of energy by

Wigner transformation – is very small in the initial phase as discussed in Section 3.4. Consequently, the spectral shape in Wigner space is determined by the finite integration interval in time rather than by the interactions itself. On the other hand, we have used an infinite relative time range in deriving the generalized transport equation within the first order gradient expansion. Thus in this case we deal with a completely resolved spectral function already at the initial time, that clearly exhibits the incorporated physics. This demonstrates why both approaches can only be compared to a certain extend.

Nevertheless, the inclusion of the dynamical spectral function in terms of the generalized transport equation surpasses the shortcomings of the quasiparticle Boltzmann limit. Whereas the latter approach leads to a strictly monotonous evolution of the momentum modes, the inclusion of quantum effects in terms of a semiclassical approximation correctly yields the overshooting effects known from the solution of the full Kadanoff-Baym equation (Fig. 3.2).

Finally, concentrating on the very early time behaviour, we find a significant difference between the full and the approximate dynamics in the gradient scheme (6.28). For the generalized transport equation we find a monotonous evolution of the equal-time Green function momentum modes, whereas strong oscillations are observed in the initial phase for the solution of the full Kadanoff-Baym theory. Thus, with respect to the early time behaviour the generalized transport equation behaves much more like the Boltzmann approximation, which is a first order differential equation in time as well. However, the Kadanoff-Baym evolution is given by an integro-differential equation of second order in time. In this case the phase correlations between the Green functions $G^<_{\phi\phi}$, $G^<_{\pi\phi}$, $G^<_{\pi\pi}$ are kept and the instantaneous switching-on of the interaction results in an oscillatory behaviour of the single momentum modes. When including the collisional self-energies, i.e. on the three-loop level for the effective action, these oscillations are damped in time typically with the respective on-shell width for given momentum. If only the tadpole term is included, these oscillations are not damped and maintain forever. Therefore, the origin of the oscillatory behaviour can be traced back to the order of the underlying differential equation.

7.3 Evolution of the Spectral Function

Since the Green functions develop in time also the spectral properties of the system change as well. In Fig. 7.4 the time evolution of the spectral function for the initializations D1, D2 and D3 within the gradient scheme are displayed. We also focus on the spectral functions for two particular momentum modes $|\vec{p}|/m = 0.0$ (l.h.s.) and $|\vec{p}|/m = 2.0$ (r.h.s.) for various system times $t \cdot m = 5, 20, 60, 120, 240, 360, 480, 600$ up to the long-time limit. This representation corresponds to Fig. 3.5, where the respective evolution of the spectral function is studied for the full Kadanoff-Baym theory. We find that the time evolution of the spectral functions obtained from the generalized transport equation (6.28) is very similar to the one from the full quantum calculation. The zero-mode spectral function for the initial distribution D1 becomes sharper with

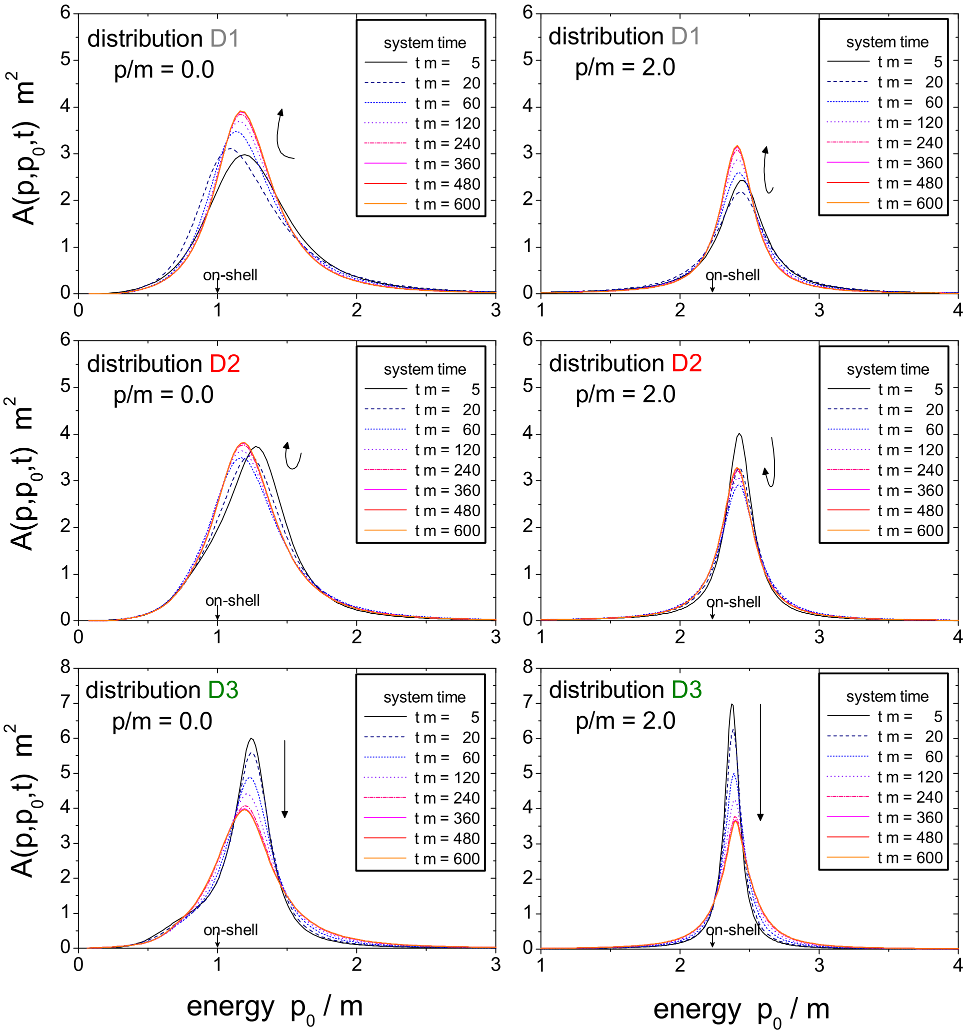

Figure 7.4: Time evolution of the spectral function $\bar{A}(\vec{p}, p_0, t)$ for the initial distributions D1, D2 and D3 (from top to bottom) with coupling constant $\lambda/m = 18$ for the two momentum modes $|\vec{p}|/m = 0.0$ (l.h.s.) and $|\vec{p}|/m = 0.0$ (r.h.s.). The spectral function from the transport eq. (6.28) is shown for times $t \cdot m = 5$, 20, 60, 120, 240, 360, 480, 600 as indicated by the different line types.

time and is moving to slightly higher energies. The opposite characteristics is observed for the zero-mode spectral function for the initialization D3, which broadens with time (reducing the peak correspondingly) and slowly shifts to smaller energies. Together with the weak evolution for the distribution D2 (which only slightly broadens at intermediate times and returns to a narrower shape at smaller energies in the long-time limit) the evolution of all three initializations in the semiclassical approximation is well comparable to the full Kadanoff-Baym dynamics (cf. Fig. 3.5). Furthermore, the maxima of the zero-mode spectral functions are located above the bare mass (as indicated by the on-shell arrow) for all initial states during the time evolution.

The spectral functions for the momentum mode $|\vec{p}|/m = 2.0$ are in a good agreement with the Kadanoff-Baym dynamics as well. Again we observe – for the initial distribution D1 – a narrowing of the spectral function, while for D3 the spectral func-

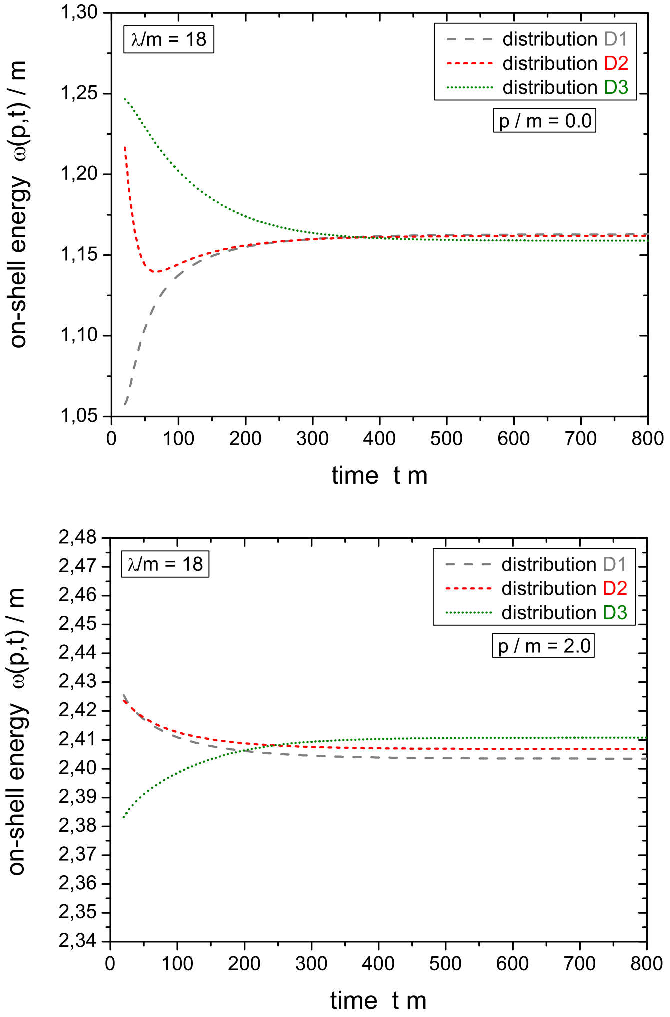

Figure 7.5: Time evolution of the on-shell energies $\omega(\vec{p},t)$ of the momentum modes $|\vec{p}|/m = 0.0$ and $|\vec{p}|/m = 2.0$ for the different initializations D1, D2 and D3 with $\lambda/m = 18$ in the semiclassical KB limit (6.28). The on-shell self-energies are extracted from the maxima of the time-dependent spectral functions.

tion broadens with time. Moreover, the width of the spectral function starting from distribution D2 shows a non-monotonous behaviour with a maximum at intermediate times.

In order to study the dynamics of the spectral function in a more quantitative manner we display in Fig. 7.5 the time evolution of the on-shell energies (as derived from the maxima of the spectral function) for the momentum modes $|\vec{p}|/m = 0.0$ (upper plot) and 2.0 (lower plot) for the initializations D1, D2 and D3 with $\lambda/m = 18$. By comparison with the corresponding results from the Kadanoff-Baym theory (cf. Fig. 3.6) we observe a close similarity of the evolutions within the full and the semiclassical KB scheme. The effective mass of the zero momentum mode decreases for initialization D3, passes a minimum for D2 and increases for the initial state D1. As familiar from

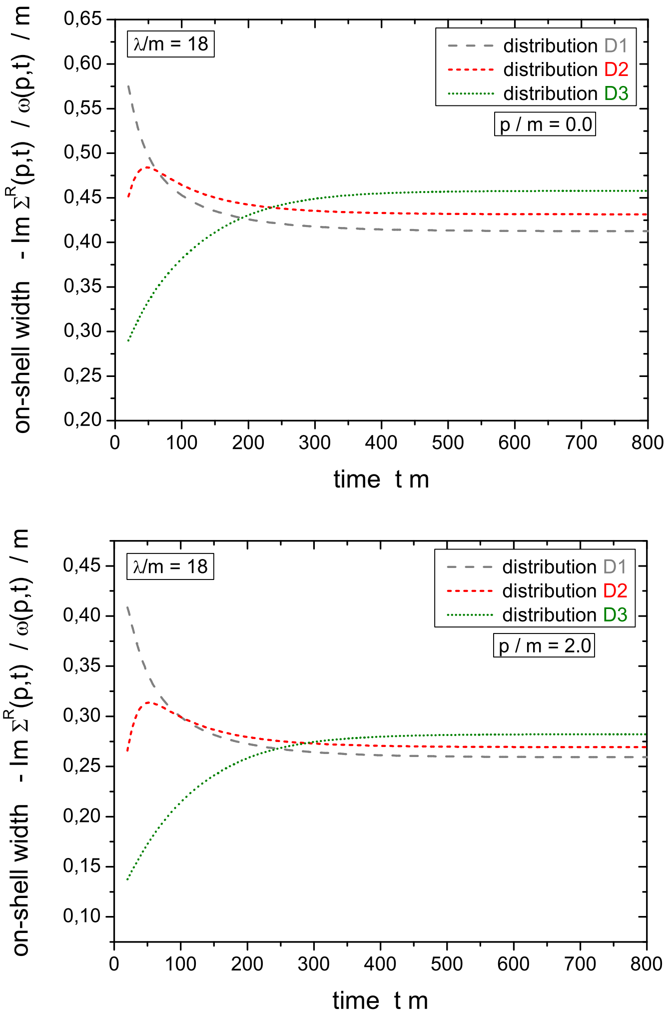

Figure 7.6: Time evolution of the on-shell widths $-Im\,\bar{\Sigma}^R(\vec{p},\omega(\vec{p},t),t)/\omega(\vec{p},t)$ of the momentum modes $|\vec{p}|/m = 0.0$ and $|\vec{p}|/m = 2.0$ for the different initializations D1, D2 and D3 with $\lambda/m = 18$ in the semiclassical transport eq. (6.28).

the Kadanoff-Baym calculations in Section 3.4 the behaviour of the on-shell energies is different for higher momentum modes. We find for the momentum mode $|\vec{p}|/m = 2.0$ a monotonous decrease of the on-shell energy for the initializations D1 and D2 and an increase for distribution D3. Altogether, the evolution of the on-shell energies for the higher modes is rather moderate compared to the lower ones in accordance with the dominant momentum contribution and the weakening of the retarded self-energy for larger modes.

Finally, the on-shell energies approach a stationary state for all modes and all initializations. However, the long-time limit of the equal momentum modes is not exactly the same for all initial distributions D1, D2 and D3. There is still a small difference due to the specific initial state generation from the given momentum distribution function (see discussion in Section 7.1).

Next we consider the time evolution of the on-shell width as determined by the imaginary part of the retarded self-energy at the maximum position of the spectral function. In Fig. 7.6 the on-shell width is displayed for the two momentum modes $|\vec{p}|/m = 0.0$ and $|\vec{p}|/m = 2.0$ for all three initial distributions D1, D2 and D3 with λ/m =18 as a function of time. For both momentum modes the on-shell width increases for the distribution D3, while it has a maximum at intermediate times ($t \cdot m \approx 40$) for the initialization D2. Thus the results – together with the reduction of the on-shell width for both momentum modes for the initialization D1 – is in good agreement with the results obtained for the full Kadanoff-Baym theory (cf. Fig. 3.7). However, the stationary values for the on-shell widths deviate again slightly in accordance with the preparation of the initial state in the gradient scheme.

Summarizing this Section we find that the main characteristics of the full quantum evolution of the spectral function are maintained in the semiclassical transport equation (6.28) as well. This includes the evolution of the on-shell energies as well as the width of the spectral function. Since the generalized transport equation is formulated directly in Wigner space one has access to the spectral properties at all times, whereas the very early times in the Kadanoff-Baym case have to be excluded due to the very limited support in the relative time interval $t_1 - t_2$.

7.4 Stationary State of the Semiclassical Evolution

As we have observed in the previous Sections the evolution within the generalized transport equation (6.28) leads to a stationary state for all three different initializations D1, D2 and D3. Thus we turn to the investigation of this long-time limit itself, here in particular for the initialization D2. In Fig. 7.7 we show the distribution function $\bar{N}$ of various momentum modes $|\vec{p}|/m = 0.0,\ 0.8,\ 1.6,\ 2.4,\ 3.2,\ 4.0$ for large times ($t \cdot m = 600$) as derived from the Green function itself and the spectral function via the relation $\bar{N} = i\bar{G}^{<}/\bar{A}$. The distribution function for a given momentum mode is calculated for all energies p_0 where the corresponding spectral function – as displayed in the lower part of Fig. 7.7 – exceeds a value of 0.5. Since the width of the late time spectral function decreases with increasing momentum, the energy range for which the distribution function is shown, is smaller for larger momentum modes. We find, that all momentum modes of $\bar{N}$ can be fitted at all energies by a single Bose function with a temperature $T/m = 1.827$ and a very small chemical potential $\mu/m = 0.000817$. Thus the generalized transport formulation (6.28) leads to a complete (off-shell) equilibration of the system very similar to the solution of the full Kadanoff-Baym equation (cf. Fig. 3.8 in Section 3.5). Furthermore, the long-time limit of the semiclassical time evolution exhibits a vanishing chemical potential μ/m in accordance with the properties of the neutral ϕ^4-theory. This might have been expected since in the generalized transport equation particle number non-conserving processes – which lead to the decrease of the chemical potential – are included by means of the dynamical spectral function. Thus the semiclassical approximation (6.28) solves the problems within the Boltzmann limit, which does not yield a full relaxation of the chemical potential, since only on-shell transitions of quasiparticles are taken into account.

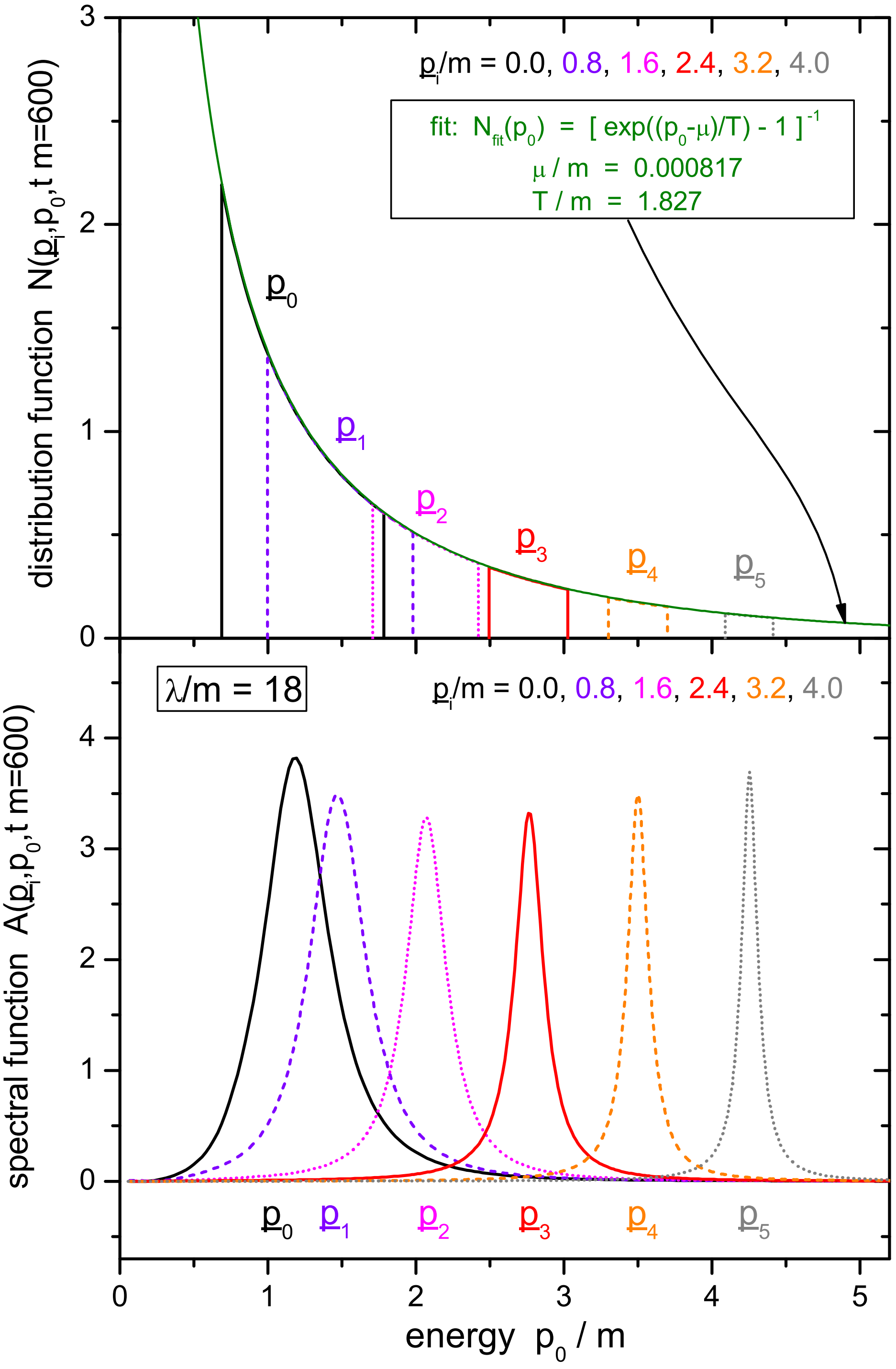

Figure 7.7: Spectral function $\bar{A}$ for various momentum modes as a function of energy p_0/m at the late time $t \cdot m = 600$ (lower part) for initial distribution D2 with coupling constant $\lambda/m = 18$. The corresponding distribution function $\bar{N}$ (at the same time for the same momentum modes) is shown in the upper part. All momentum modes can be fitted for all energies by a single Bose function of temperature $T/m = 1.827$ and a chemical potential μ/m close to zero.

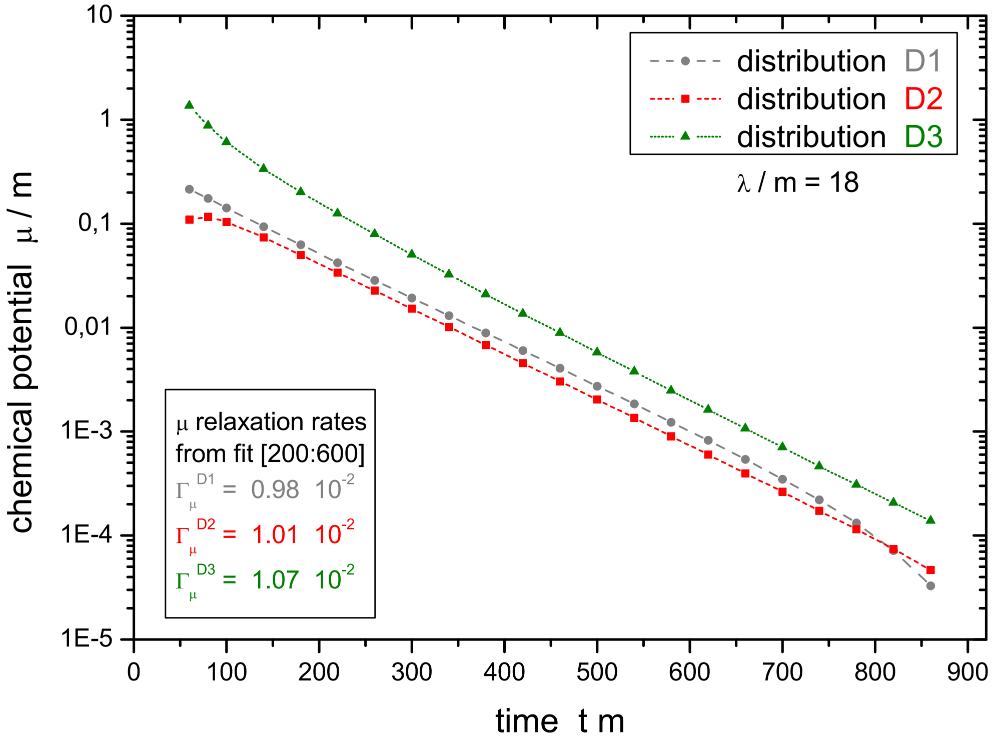

Figure 7.8: Relaxation of the chemical potential μ/m for the three initial distributions D1, D2, D3 within the generalized transport equation (6.28) in a logarithmic repesentation as a function of time. The decrease is approximately exponential in time $\propto \exp(-\Gamma_\mu \cdot t)$ and the relaxation rate Γ_μ is practically equal for all initializations.

After observing, that the chemical potential decreases to zero in the long-time limit, it is interesting to study the relaxation process itself. The relaxation of the chemical potential μ/m is shown for the three different initializations D1, D2 and D3 with coupling constant $\lambda/m = 18$ in Fig. 7.8. We see – as in the case of the Kadanoff-Baym evolution – that all initial states show an approximately exponential decrease in time. The relaxation rates – as determined from the slope of the exponential decline – are also approximately the same for all distributions. They are given by $\Gamma_\mu^{D1} \approx 0.98 \cdot 10^{-2}$ for distribution D1, $\Gamma_\mu^{D2} \approx 1.01 \cdot 10^{-2}$ for distribution D2 and $\Gamma_\mu^{D3} \approx 1.07 \cdot 10^{-2}$ for distribution D3. Thus the relaxation rates are in the same range as the ones found within the full Kadanoff-Baym theory. This is exactly the result one expects from the analytical estimate for the chemical potential relaxation rate. In Section 3.6 we have found that the relaxation rate Γ_μ can be explained within a linearized evolution equation including only equilibrium properties, i.e. the equilibrium spectral and (Bose) distribution function. It is appropriate for small deviations from the equilibrium state in terms of the chemical potential μ. In the present case of the generalized transport equation (6.28) we encounter exactly the same situation. We know from the validity of

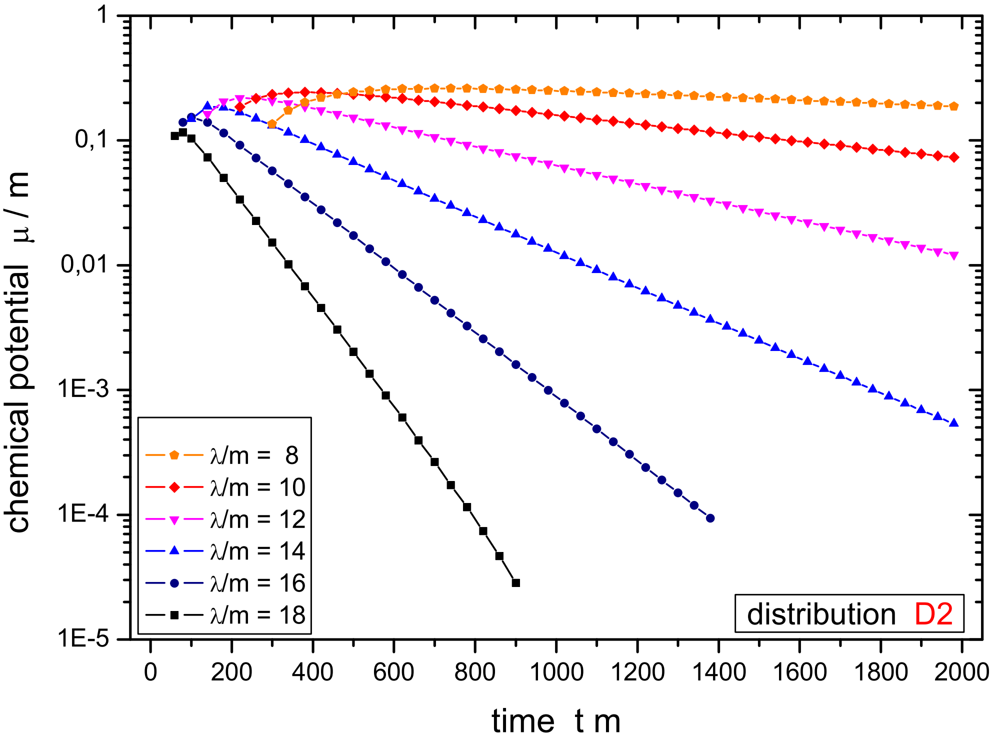

Figure 7.9: Relaxation of the chemical potential μ/m for initial distribution D2 with coupling constants $\lambda/m = 8, 10, 12, 14, 16, 18$ using the generalized transport equation (6.28).

the estimate that a linearized description is meaningful. Thus the evolution within the first order gradient equation should yield a comparable result as long as the equilibrium properties are nearly equal. This is indeed the case since the final temperatures for the various initial states are approximately the same (also compared to the Kadanoff-Baym case). They are given by $T_{eq}^{D1}/m \approx 1.819$, $T_{eq}^{D2}/m \approx 1.827$ and $T_{eq}^{D3}/m \approx 1.834$. Consequently, the same similarity holds for the spectral function, which is determined in equilibrium by the temperature T and the coupling strength λ. Therefore we can conclude, that the generalized transport equation (6.28) is sufficient to describe the correct relaxation of the chemical potential μ.

Finally, we study the relaxation of the chemical potential as a function of the coupling strength. To this aim we display in Fig. 7.9 the relaxation of the chemical potential μ for the initial distribution D2 for coupling constants $\lambda/m = 8, 10, 12, 14, 16, 18$ as obtained form the generalized transport equation (6.28). For all coupling constants λ the chemical potential μ is reduced exponentially in time $\propto \exp(-\Gamma_\mu \cdot t)$ and thus allows for the determination of a proper relaxation rate Γ_μ.

The results for the relaxation rates Γ_μ of the chemical potential as a function of the coupling strength λ are displayed in Fig. 7.10. They are scaled by the coupling

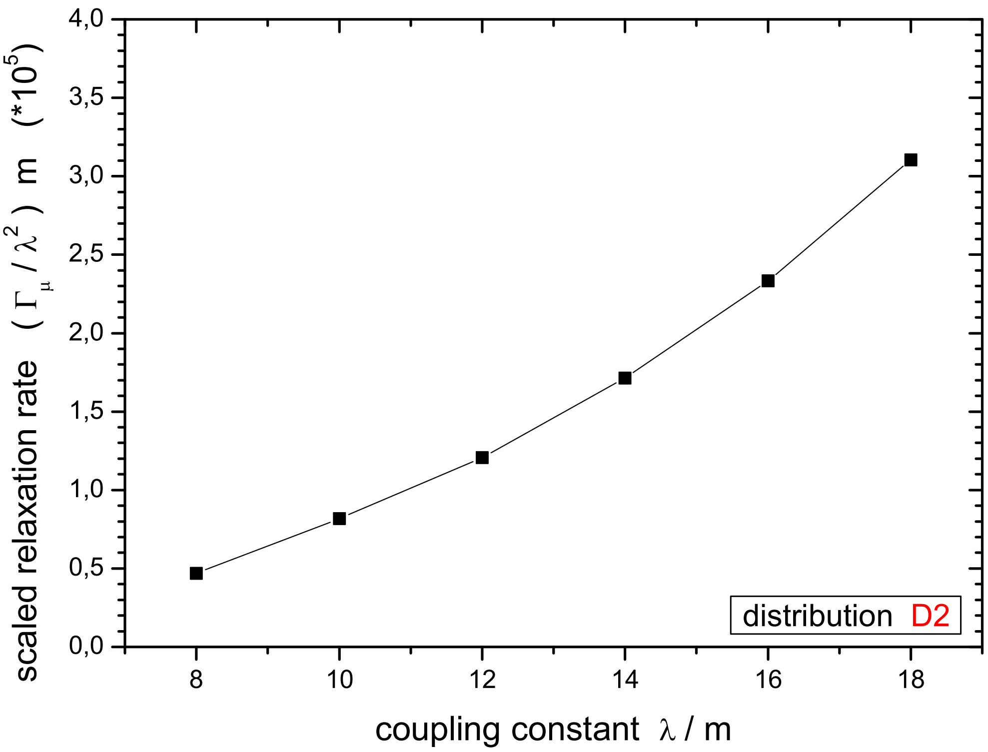

Figure 7.10: Scaled relaxation rate Γ_μ/λ^2 of the chemical potential as a function of the coupling strength λ/m for the initial distribution D2.

constant squared (λ^2) in order to take into account the overall coupling dependence of the collisional self-energy. We see that the relaxation rate Γ_μ increases much stronger than quadratically with the coupling strength. Whereas the relaxation is very weak for small and medium couplings $\lambda/m \leq 8$, it increases considerably for larger values of the interaction strength. By inspection of the analytical estimate for the relaxation rate of the chemical potential (3.30) we find an explanation for this strong dependence: At first here an overall factor of the coupling constant squared (λ^2) enters the expression for the relaxation rate, that stems from the collisional integral in terms of the scattering (sunset) self-energies. This factor, only, would yield a constant line in Fig. 7.10 and thus underestimate the observed behaviour significantly. Therefore, one has to keep in mind the additional λ dependence of the (equilibrium) spectral function that strongly influences the estimate for the relaxation rate since it appears in the energy-momentum integration weights several times. Thus the relaxation rate is determined explicitly (via the K_2-term (3.28)) and implicitly through the spectral functions in both contributions, K_1 (3.27) and K_2 (3.28), by the coupling strength λ in a nonlinear way.

We conclude that there might be a tiny relative shift of the different time scales of kinetic and chemical equilibration in dependence on the coupling strength. While the kinetic equilibration proceeds approximately with the coupling constant squared

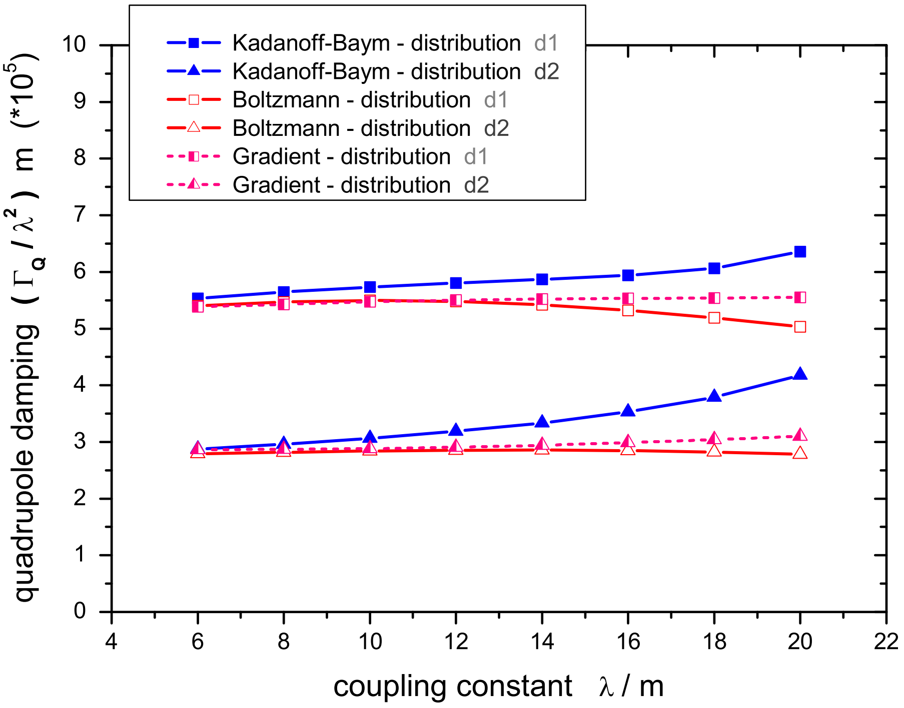

Figure 7.11: Scaled Relaxation rate for the generalized transport equation as a function of the coupling strength (half-filled symbols) for the initial distributions d1 (squares) and d2 (triangles). Additionally the results obtained within the Kadanoff-Baym (full symbols) and the Boltzmann calculation (open symbols) are shown for comparison.

(as indicated by the calculations for non-polar-symmetric systems), the chemical relaxation rate is a higher order process in λ as seen from Fig. 7.10. Thus the chemical equilibration should move with increasing coupling strength λ to earlier times relative to the kinetic one which – in its extreme case – might lead to a mixture of the different time scales.

7.5 Quadrupole Relaxation

In this Section we no longer restrict to polar symmetric systems and discuss the time evolution of more general initial distributions within the generalized transport approximation (6.28). We start with conditions similar to those employed in Section 5.2, but combined with the initialization scheme for the semiclassical limit. Again – as in the full Kadanoff-Baym and the Boltzmann case – the decrease of the quadrupole moment of the distribution is approximately exponential in time ($\propto \exp(-\Gamma_Q \cdot t)$) and thus allows for the extraction of a quadrupole damping rate Γ_Q. The scaled quadrupole damping rates – as obtained for the two initial distributions d1 and d2 - are displayed in Fig. 7.11 as a function of the coupling strength λ/m. The calculations show that the quadrupole relaxation rates within the semiclassical approximation (6.28) for both initial distributions d1 and d2 is well within in the range of the full Kadanoff-Baym and the on-shell Boltzmann case. Additionally, the quadrupole relaxation rate is rather flat in the coupling λ when divided by the coupling constant squared (λ^2) as already observed for the other two evolution schemes.

7.6 Validity of the Gradient Approximation

As we have seen in the previous Sections the generalized transport equation (6.28) leads to a good agreement with the Kadanoff-Baym dynamics. This indicates that the semiclassical limit can be applied without loosing essential features of the full quantum dynamics for homogeneous systems (in particular D1, D2 and D3). We recall, that the underlying assumption for the validity of the first order gradient expansion scheme – which has been used to derive the generalized transport equation – is that all functions are slowly evolving in the mean space and time coordinates. Thus, in comparison to the first order time derivatives, the second order time derivatives should be small, such that they can be neglected to a good approximation. In this Section we will study now this criterion in a more quantitative way. To this aim we consider as a relative measure the energy-momentum integrals over the absolute value of first and second order time derivatives of various functions entering the generalized transport equation. Explicitly this measure is given at time t by

$$M_{F}^{1/2}(t) \; = \; \int \frac{d^D p}{(2\pi)^D} \; \left| \, \partial_t^{(1/2)} \; \bar{F}(\vec{p}, p_0, t) \, \right| \tag{7.4}$$

for an arbitrary function $\bar{F}$ in Wigner space. In the following we take into account the time derivatives of the Green functions and the self-energies, i.e.

$$\bar{F} \; \in \; \{ \, i\bar{G}^<, \, i\bar{\Sigma}^<, \, Re\,\bar{G}^R, \, Re\,\bar{\Sigma}^R \, \} \, . \tag{7.5}$$

The time evolution of this measures is shown in Fig. 7.12 for the first and the second order time derivatives of the Green function and in Fig. 7.13 for the collisional and the retarded self-energies. The calculation has been performed for the initial distribution D2 with a coupling strength of $\lambda/m = 18$. For the Green functions as well as the self-energies the second order time derivatives are about one order of magnitude smaller than the first order expressions. Thus the underlying assumption of the first order gradient expansion is fulfilled very well indicating that the results obtained within the semiclassical scheme should match with those for the full quantum evolution to a large extent. This is exactly what we have found from the explicit comparison of the evolution of the equal-time Green functions as well as the spectral functions in Sections 7.2 and 7.3.

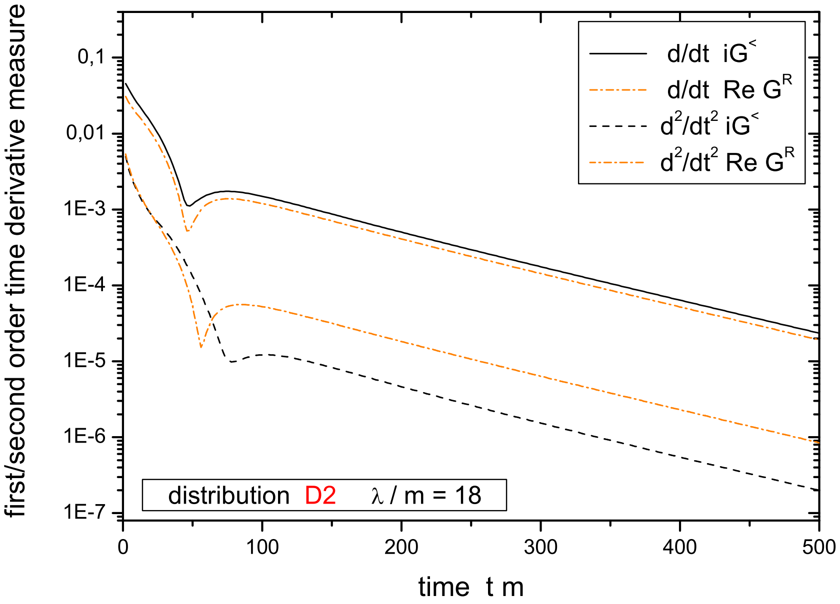

Figure 7.12: Time evolution of the first/second order time derivative measure for the Green functions functions $i\bar{G}^{<}$ and $Re\,\bar{G}^{R}$ for initial distribution D2 with coupling constant $\lambda/m = 18$. During the whole evolution the second order time derivatives are more than an order of magnitude smaller than the first order derivatives supporting the validity of the gradient expansion.

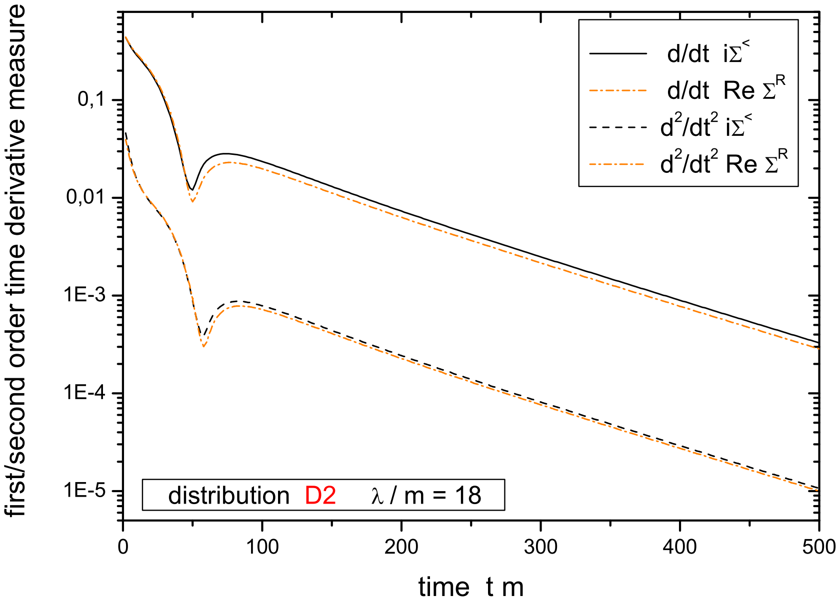

Figure 7.13: Time evolution of the first/second order time derivative measure for the functions $i\bar{\Sigma}^{<}$ and $Re\,\bar{\Sigma}^{R}$ for initial distribution D2 with coupling constant $\lambda/m = 18$. During the whole evolution the second order time derivatives are significantly smaller than the first order contributions.

7.7 Generalized Transport in Botermans-Malfliet Form

In this Section we will perform a detailed comparison of the generalized transport equation (in the original *Kadanoff-Baym* (KB) form) (6.28) with the modified *Botermans-Malfliet* (BM) form (6.34). As discussed in detail in Section 6.3 the latter form results from the replacement of the collisional self-energy by $i\bar{\Sigma}^< = i\bar{G}^< \cdot \bar{\Gamma}/\bar{A}$ in the second Poisson bracket on the l.h.s. of the original kinetic equation (6.28). This is done in order to obtain a consistent first order equation in the gradients and to achieve consistency of the resulting transport equation with the corresponding generalized mass-shell relation.

In Fig. 7.14 we compare the time evolution within the generalized transport equation in the KB form to the consistent equation in BM form. In this respect several momentum modes of the equal-time Green function are displayed evolving in time from an initial distribution D2 for a coupling constant $\lambda/m = 16$. We find that the deviations between both approximations (KB and BM) are rather moderate. Only for very small momentum modes $|\vec{p}|/m \leq 1.6$ deviations between both calculational modes are visible. For the very low momentum modes the range of difference starts at $t \cdot m \approx 10$ and extends to $t \cdot m \approx 100$ for the non-zero modes. For the zero momentum mode the deviation lasts even longer. In this region the semiclassical transport in the BM form is slightly slower than in the original KB choice. Nevertheless, also the BM form exhibits the typical overshooting behaviour of the low momentum modes beyond the stationary limit as observed for the KB form. However, the maxima are shifted slightly to later times. Finally both gradient approximations converge in the long-time limit to very similar configurations.

We recall that the relation $i\bar{\Sigma}^< = i\bar{G}^< \cdot \bar{\Gamma}/\bar{A}$ is valid exactly in equilibrium, only. Otherwise the difference is at least of gradient order which justifies this replacement inside Poisson bracket terms as in the Botermans-Malfliet formulation. Thus the differences resulting from an exchange of the terms should become smaller when performed at later time, i.e. closer to equilibrium. In this respect we show in Fig. 7.15 calculations that start with a propagation in terms of the transport equation in KB form and then change to the BM form at a given time $t_{BM} \cdot m = 10, 20, 40, 60$. Furthermore, for the initial distribution D2 at $\lambda/m = 16$ also the full evolution within the BM choice is displayed ($t_{BM} \cdot m = 0$, solid lines). For the low lying momentum modes $|\vec{p}| = 0.0, 0.8$ the direct use of the Botermans-Malfliet transport equation yields the respective low lying curves. All other lines with $t_{BM} \cdot m > 0$ follow the results of the original (KB) gradient form – as given in Fig. 7.14 – until the switch to the Botermans-Malfliet type is performed. Thus the results for later switching times are (in the intermediate time regime) slightly higher than the ones obtained by an earlier change of the propagation scheme. This indicates the small delay of the evolution in the BM form in comparison to the original (KB) choice. Nevertheless, all respective curves join for very late times and approach a very similar final state. This, of course, corresponds to the very similar calculations already obtained for the complete evolution within either the KB or the BM form. The higher momentum modes a rather insensitive to the switching time for

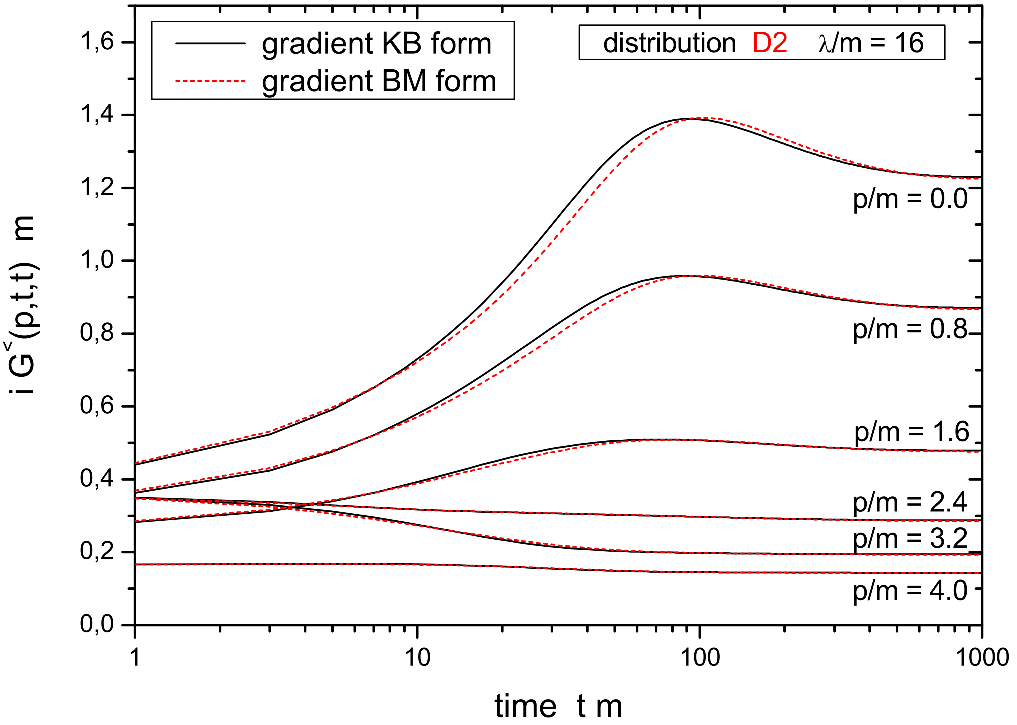

Figure 7.14: Time evolution of various equal-time Green function momentum modes within the generalized transport equation (original KB form, solid lines) and within the Botermans-Malfliet (BM) form (dashed lines) for initial distribution D2 with coupling constant $\lambda/m = 16$.

the propagation method.

As the final part of the comparison we investigate the approximation $i\bar{\Sigma}^< \rightarrow i\bar{G}^< \cdot \bar{\Gamma}/\bar{A}$ quantitatively, Thus we introduce a measure for the absolute strength of the collision term by integrating the collision rates over energy and momentum. Since the collision term vanishes, if the above substitution holds exactly, i.e. in equilibrium, the absolute size gives an idea about the validity of this replacement at the zero order level. Explicitly the measure reads:

$$M_{col}(t) \;=\; \int \frac{d^D p}{(2\pi)^D}\; \frac{1}{|\,2p_0\,|} \left|\; i\bar{\Sigma}^< \, i\bar{G}^> \;-\; i\bar{\Sigma}^> \, i\bar{G}^< \right| . \tag{7.6}$$

Furthermore, we define a measure for the deviation of the second Poisson bracket in the original and in the consistent Botermans-Malfliet formulation. It is given by the integration over the absolute differences of the Poisson terms as

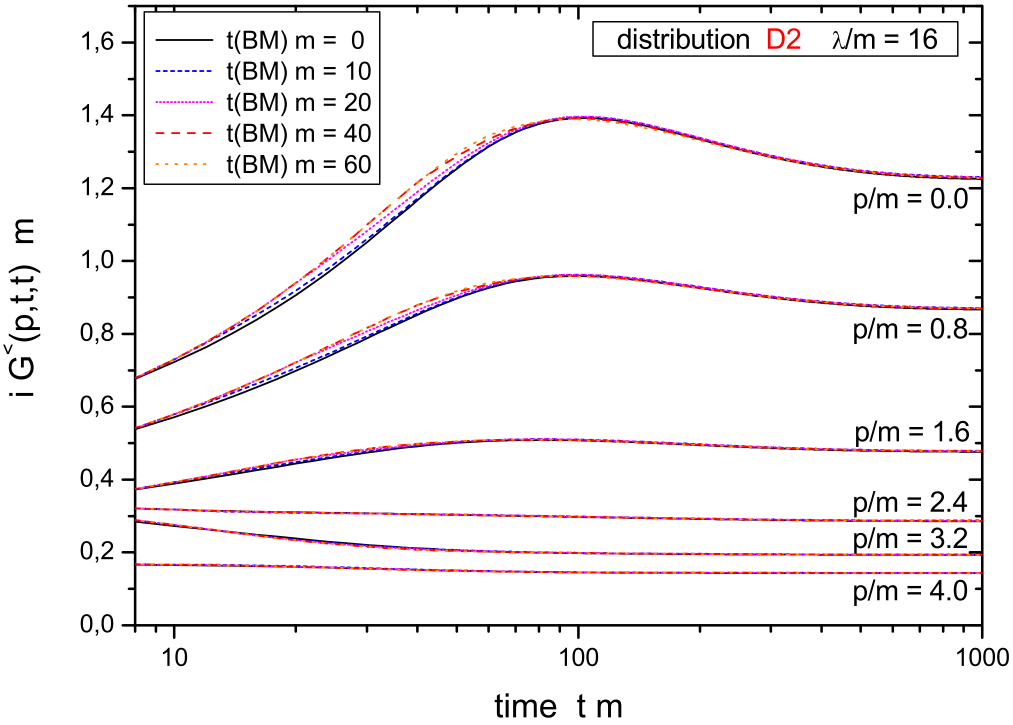

Figure 7.15: Time evolution of various equal-time Green function momentum modes for an initial distribution D2 with coupling constant $\lambda/m = 16$. The propagation is performed within the original (KB) generalized transport equation up to times $t_{BM} \cdot m = 0,\, 10,\, 20,\, 40,\, 60$ and then continued within the consistent generalized transport equation in BM form for later times.

$$M_{off}(t) \;=\; \int \frac{d^Dp}{(2\pi)^D}\;\frac{1}{\mid 2p_0 \mid}\;\left| \,\{\, i\bar{\Sigma}^< \,,\, Re\, \bar{G}^R \,\} \;-\; \{\, i\bar{G}^< \,\frac{\bar{\Gamma}}{\bar{A}} \,,\, Re\, \bar{G}^R \,\} \,\right| \;. \qquad (7.7)$$

With respect to the generalized transport equation (6.28) we include in both cases the additional factor $1/(2p_0)$. In Fig. 7.16 we display the time evolution of the measure (7.6) (solid line) and the measure (7.7) (dashed line). The calculation has been performed for the initial state D2 with a coupling constant $\lambda/m = 16$. We find that both measures decrease as a function of time in accordance with the equilibration of the system. Additionally, the contribution from the difference of the Poisson brackets (7.7) is always smaller than the one stemming from the collision term (7.6). This indicates that the replacement of the collisional self-energy $i\bar{\Sigma}^< \rightarrow i\bar{G}^< \cdot \bar{\Gamma}/\bar{A}$ is more reliable when it takes place at the gradient level in accordance with the assumption of Botermans and Malfliet. However, the relative suppression is not very large.

In summarizing this Chapter we point out that the approximation of the full Kadanoff-Baym dynamics by the generalized transport equations in Kadanoff-Baym

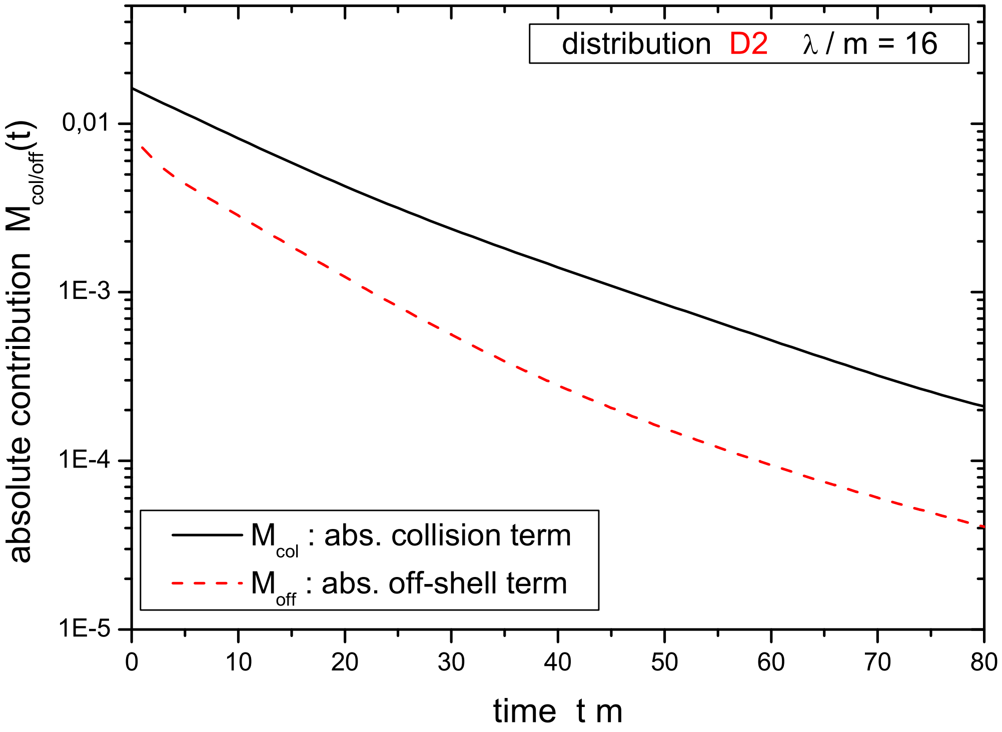

Figure 7.16: Time evolution of the measure functions for the collision term (7.6) and the difference of the second Poisson bracket in standard (KB) and consistent (BM) form (7.7) for initial distribution D2 with coupling constant $\lambda/m = 16$. Both contributions decrease in time in accordance with the equilibration of the system. The Poisson contribution (dahed line) is always significantly smaller than that of the collision term (solid line).

(6.28) or Botermans-Malfliet form (6.34) holds very well for the different momentum modes of the Green function $i\bar{G}^<$ itself. Slight deviations are only visible for the zero momentum mode at early to intermediate times (Figs. 3.2, 7.3 and 7.14) for a logarithmic representation of the time axis. Consequently, the characteristic features of quantum equilibration obtained for the full Kadanoff-Baym theory are retained in the generalized transport limits. The validity of these transport equations – based on a first order gradient expansion – could be shown explicitly, since second order gradient terms turned out to be smaller by more than an order of magnitude (cf. Figs. 7.12 and 7.13).

Chapter 8

Application of Semiclassical Transport to Heavy-Ion Collisions

In this Chapter we will use the generalized transport equation (6.34) in order to investigate experimental heavy-ion collisions at intermediate and high energies. As indicated by several experiments, strong modifactions of the spectral properties are observed for particles in the dense and hot medium. Thus it is interesting to see, if quantum off-shell effects lead to an improved description of the experimental results.

8.1 Testparticle Representation

The starting point for the following off-shell dynamics is the generalized transport equation in consistent first order gradient expansion, i.e. the Botermans-Malfliet form (6.34). As a first step we are interested in the collisionless off-shell propagation of the particles in the medium. The collisions between the particles are treated in transport codes separately and will be lateron incorporated explicitly by taking into account the appropriate quantum transition rates. Thus we consider the off-shell transport of particles with vanishing collision term, which we rewrite in the following form:

$$
\begin{aligned}
2\, p^{\mu}\, \partial^x_{\mu}\, i\bar{G}^{<} \;\; - \;\; & \partial^x_{\mu} \left[\left(\partial^{\mu}_p\, Re\, \bar{\Sigma}^R \; + \; \frac{p^2 - m^2 - Re\, \bar{\Sigma}^R}{\bar{\Gamma}}\; \partial^{\mu}_p\, \bar{\Gamma} \right) \, i\bar{G}^{<} \right] \\
+ \;\; & \partial^{\mu}_p \left[\left(\partial^x_{\mu}\, Re\, \bar{\Sigma}^R \; + \; \frac{p^2 - m^2 - Re\, \bar{\Sigma}^R}{\bar{\Gamma}}\; \partial^x_{\mu}\, \bar{\Gamma} \right) \, i\bar{G}^{<} \right] \; = \; 0\,.
\end{aligned}
\tag{8.1}
$$

Here we omit an explicit representation of the local part of the self-energy $\bar{\Sigma}^{\delta}$, since it can be incorporated – by the replacement $Re\, \bar{\Sigma}^R \to \bar{\Sigma}^{\delta} + Re\, \bar{\Sigma}^R$ – within the real part of the retarded self-energy. In order to obtain an approximate solution to this equation we use a testparticle ansatz for the (real and positive semidefinite) Green function $i\bar{G}^{<}$, i.e.

$$i\bar{G}^{<}(\vec{p},p_0,\vec{x},t) \;\sim\; \sum_{i=1} \frac{1}{2p_0}\, \delta^{(d)}(\vec{x}-\vec{x}_i(t))\;\; \delta^{(d)}(\vec{p}-\vec{p}_i(t))\;\; \delta(p_0-\epsilon_i(t))\,. \tag{8.2}$$

Thus the Green function is represented by a system of testparticles (numbered by the index i) which are located at time t at positions $\vec{x}_i(t)$, have momenta $\vec{p}_i(t)$ and energy $\epsilon_i(t)$. Since we are interested in the description of realistic heavy-ion collisions, we will consider the case of $d=3$ spatial dimensions. The testparticle ansatz (8.2) is inserted in the equation of motion (8.1), which has been rearranged such that the general property of the δ-distribution $f(x)\,\delta(x-x_i)=f(x_i)\,\delta(x-x_i)$ can be exploited within the derivative terms. Since these inner terms only depend on the general testparticle coordinates, the outer derivatives act only on the product of δ-functions themselves. We obtain for the individual contributions

$$\begin{aligned}
2\,p_0\,\partial_t\, i\bar{G}^{<} \;&=\; \sum_i \,[\,(-\dot{\vec{x}}_i)\;\; \vec{\nabla}_x\,\delta^{(d)}(\vec{x}-\vec{x}_i)\;\; \delta^{(d)}(\vec{p}-\vec{p}_i)\;\; \delta(p_0-\epsilon_i) \\
&\qquad +(-\dot{\vec{p}}_i)\;\; \delta^{(d)}(\vec{x}-\vec{x}_i)\;\; \vec{\nabla}_p\,\delta^{(d)}(\vec{p}-\vec{p}_i)\;\; \delta(p_0-\epsilon_i) \\
&\qquad +(-\dot{\epsilon}_i)\;\; \delta^{(d)}(\vec{x}-\vec{x}_i)\;\; \delta^{(d)}(\vec{p}-\vec{p}_i)\;\; \partial_{p_0}\,\delta(p_0-\epsilon_i)\,]\,,
\end{aligned} \tag{8.3}$$

$$2\,\vec{p}\,\vec{\nabla}_x\, i\bar{G}^{<} \;=\; \sum_i \frac{\vec{p}_i}{\epsilon_i}\;\; \vec{\nabla}_x\,\delta^{(d)}(\vec{x}-\vec{x}_i)\;\; \delta^{(d)}(\vec{p}-\vec{p}_i)\;\; \delta(p_0-\epsilon_i)\,, \tag{8.4}$$

$$\partial_{p_0}\,\left(\partial_t\, Re\,\bar{\Sigma}^{R}\cdot i\bar{G}^{<}\right) \;=\; \sum_i \frac{1}{2\epsilon_i}\;\; \partial_t\, Re\,\bar{\Sigma}^{R}_{(i)}\;\; \delta^{(d)}(\vec{x}-\vec{x}_i)\;\; \delta^{(d)}(\vec{p}-\vec{p}_i)\;\; \partial_{p_0}\,\delta(p_0-\epsilon_i)\,, \tag{8.5}$$

$$\begin{aligned}
\partial_t\,\left(\partial_{p_0}\, Re\,\bar{\Sigma}^{R}\cdot i\bar{G}^{<}\right) \;&=\; \sum_i \,[\,\frac{-\dot{\vec{x}}_i}{2\epsilon_i}\;\; \partial_{\epsilon_i}\, Re\,\bar{\Sigma}^{R}_{(i)}\;\; \vec{\nabla}_x\,\delta^{(d)}(\vec{x}-\vec{x}_i)\;\; \delta^{(d)}(\vec{p}-\vec{p}_i)\;\; \delta(p_0-\epsilon_i) \\
&\qquad +\frac{-\dot{\vec{p}}_i}{2\epsilon_i}\;\; \partial_{\epsilon_i}\, Re\,\bar{\Sigma}^{R}_{(i)}\;\; \delta^{(d)}(\vec{x}-\vec{x}_i)\;\; \vec{\nabla}_p\,\delta^{(d)}(\vec{p}-\vec{p}_i)\;\; \delta(p_0-\epsilon_i) \\
&\qquad +\frac{-\dot{\epsilon}_i}{2\epsilon_i}\;\; \partial_{\epsilon_i}\, Re\,\bar{\Sigma}^{R}_{(i)}\;\; \delta^{(d)}(\vec{x}-\vec{x}_i)\;\; \delta^{(d)}(\vec{p}-\vec{p}_i)\;\; \partial_{p_0}\,\delta(p_0-\epsilon_i) \\
&\qquad +\frac{1}{2\epsilon_i}\;\; \partial_t\,\partial_{\epsilon_i}\, Re\,\bar{\Sigma}^{R}_{(i)}\;\; \delta^{(d)}(\vec{x}-\vec{x}_i)\;\; \delta^{(d)}(\vec{p}-\vec{p}_i)\;\; \delta(p_0-\epsilon_i)\,]\,,
\end{aligned} \tag{8.6}$$

$$\vec{\nabla}_p \left(\vec{\nabla}_x Re\, \bar{\Sigma}^R \cdot i\bar{G}^< \right) = \sum_i \frac{1}{2\epsilon_i} \, \vec{\nabla}_{x_i} \, Re\, \bar{\Sigma}^R_{(i)} \, \delta^{(d)}(\vec{x}-\vec{x}_i) \, \vec{\nabla}_p \, \delta^{(d)}(\vec{p}-\vec{p}_i) \, \delta(p_0-\epsilon_i), \tag{8.7}$$

$$\vec{\nabla}_x \left(\vec{\nabla}_p Re\, \bar{\Sigma}^R \cdot i\bar{G}^< \right) = \sum_i \frac{1}{2\epsilon_i} \, \vec{\nabla}_{p_i} \, Re\, \bar{\Sigma}^R_{(i)} \, \vec{\nabla}_x \, \delta^{(d)}(\vec{x}-\vec{x}_i) \, \delta^{(d)}(\vec{p}-\vec{p}_i) \, \delta(p_0-\epsilon_i) \tag{8.8}$$

and the analogous contributions for the terms with width $\bar{\Gamma}$. Here we have omitted the time index for the testparticle coordinates $\vec{x}_i \equiv \vec{x}_i(t)$, $\vec{p}_i \equiv \vec{p}_i(t)$ and $\epsilon_i \equiv \epsilon_i(t)$. The notation $F_{(i)}$ implies that the function is taken at the coordinates of the testparticle at time t, i.e. $F_{(i)} \equiv F(\vec{p}_i(t), \epsilon_i(t), \vec{x}_i(t), t)$. The equations of motions for the testparticles inbetween collisions are obtained by comparison of the coefficients of the linear independent contributions for each single testparticle

$$\vec{\nabla}_x \, \delta^{(d)}(\vec{x}-\vec{x}_i) \;\; \delta^{(d)}(\vec{p}-\vec{p}_i) \;\; \delta(p_0-\epsilon_i) \, , \tag{8.9}$$

$$\delta^{(d)}(\vec{x}-\vec{x}_i) \;\; \vec{\nabla}_p \, \delta^{(d)}(\vec{p}-\vec{p}_i) \;\; \delta(p_0-\epsilon_i) \quad \text{and}$$

$$\delta^{(d)}(\vec{x}-\vec{x}_i) \;\; \delta^{(d)}(\vec{p}-\vec{p}_i) \;\; \partial_{p_0} \, \delta(p_0-\epsilon_i(t)) \, .$$

In the most general case – where the collisional self-energies depend on four-momentum p, the spatial coordinates $\vec{x}$ and time t – the equations of motion for the testparticles read

$$\frac{d\vec{x}_i}{dt} = \frac{1}{1-C_{(i)}} \frac{1}{2\epsilon_i} \left[2\vec{p}_i + \vec{\nabla}_{p_i} Re\, \bar{\Sigma}^R_{(i)} + \frac{\epsilon_i^2 - \vec{p}_i^{\,2} - m^2 - Re\, \Sigma^R_{(i)}}{\bar{\Gamma}_{(i)}} \;\; \vec{\nabla}_{p_i} \bar{\Gamma}_{(i)} \right] , \tag{8.10}$$

$$\frac{d\vec{p}_i}{dt} = \frac{-1}{1-C_{(i)}} \frac{1}{2\epsilon_i} \left[\vec{\nabla}_{x_i} Re\, \bar{\Sigma}^R_{(i)} + \frac{\epsilon_i^2 - \vec{p}_i^{\,2} - m^2 - Re\, \bar{\Sigma}^R_{(i)}}{\bar{\Gamma}_{(i)}} \;\; \vec{\nabla}_{x_i} \bar{\Gamma}_{(i)} \right] , \tag{8.11}$$

$$\frac{d\epsilon_i}{dt} = \frac{1}{1-C_{(i)}} \frac{1}{2\epsilon_i} \left[\frac{\partial Re\, \bar{\Sigma}^R_{(i)}}{\partial t} + \frac{\epsilon_i^2 - \vec{p}_i^{\,2} - m^2 - Re\, \bar{\Sigma}^R_{(i)}}{\bar{\Gamma}_{(i)}} \;\; \frac{\partial \bar{\Gamma}_{(i)}}{\partial t} \right] . \tag{8.12}$$

In eqs. (8.10)-(8.12) a common multiplication factor $(1 - C_{(i)})^{-1}$ appears, which contains the energy derivatives of the retarded self-energy

$$C_{(i)} = \frac{1}{2\epsilon_i} \left[\frac{\partial}{\partial \epsilon_i} Re\, \bar{\Sigma}^R_{(i)} + \frac{\epsilon_i^2 - \vec{p}_i^{\,2} - m^2 - Re\, \bar{\Sigma}^R_{(i)}}{\bar{\Gamma}_{(i)}} \;\; \frac{\partial}{\partial \epsilon_i} \bar{\Gamma}_{(i)} \right] . \tag{8.13}$$

It yields a shift of the system time t to the 'eigentime' of particle i defined by $\tilde{t}_i = t/(1-$

$C_{(i)}$). As the reader immediately verifies, the derivatives with respect to the 'eigentime', i.e. $d\vec{x}_i/d\tilde{t}_i$, $d\vec{p}_i/d\tilde{t}_i$ and $d\epsilon_i/d\tilde{t}_i$ then emerge without this renormalization factor for each testparticle i when neglecting higher order time derivatives in line with the first order semiclassical approximation scheme. The correction factor is a generalization of the quasiparticle renormalization factor in the case of finite width. In the limiting case of particles with vanishing gradients of the width $\bar{\Gamma}$ the equations of motion (8.10)-(8.12) reduce to the well-known transport equations of the quasiparticle picture [14].

Following Ref. [34] we take $\bar{m}^2 = p^2 - Re\,\bar{\Sigma}^R$ as an independent variable instead of p_0, itself. This then fixes the energy (for given $\vec{p}$ and $\bar{m}^2$) to

$$p_0^2 \;=\; \vec{p}^{\,2} \;+\; \bar{m}^2 \;+\; Re\,\bar{\Sigma}^R(\vec{p}, \bar{m}^2, x)\,. \tag{8.14}$$

In particular we are interested in the evolution of the mass parameter $\bar{m}$ of the testparticles in time. Alternatively, one can directly study the time evolution of the deviation of the actual mass parameter $\bar{m}$ from the bare mass m which is given by the mass-function (6.18) at the testparticle coordinates,

$$\bar{M}_{(i)} \;=\; \bar{m}^2_{(i)} - m^2 \;=\; \epsilon_i^2 - \vec{p}_i^{\,2} - Re\,\bar{\Sigma}^R_{(i)} - m^2\,. \tag{8.15}$$

We obtain the time evolution of the off-shell mass (squared) difference $\bar{M}_{(i)}$ by inserting the equations of motion for the testparticles (8.10)-(8.12) [34, 35]

$$\frac{d\bar{M}_{(i)}}{dt} = \frac{\bar{M}_{(i)}}{\bar{\Gamma}_{(i)}}\,\frac{d\bar{\Gamma}_{(i)}}{dt} \qquad \text{or} \qquad \frac{d\bar{m}_i^2}{dt} = \frac{\bar{m}_i^2 - m^2}{\bar{\Gamma}_{(i)}}\,\frac{d\bar{\Gamma}_{(i)}}{dt}\,. \tag{8.16}$$

Thus the evolution of the off-shellness $\bar{M}$ is directly determined by the time evolution of the width $\bar{\Gamma}$ together with the ratio of both quantities. In (8.16) – as well as in the equation of motion of the testparticles – the characteristic combination $\bar{M}/\bar{\Gamma}$ appears as a weighting factor for the changes in the imaginary part of the retarded self-energy. It can be traced back to the second Poisson bracket in the consistent transport equation in the collisionless limit (8.1). Thus the peculiar second Poisson bracket of the generalized semiclassical transport theory provides the evolution of the off-shellness of a nonequilibrium system.

Similar equations of motion for the testparticles (8.10)-(8.12) have been also derived by Leupold for the case of nonrelativistic bosonic or fermionic systems [32]. They lead to a comparable evolution of the off-shell masses, however, determined by the nonrelativistic width and the respective mass-function.

8.2 Model Studies

In this part we will explore the physical implications of the equations of motion (8.10)-(8.12) for the testparticles. Thus we consider the propagation of particles in a time-dependent complex potential of Woods-Saxon form in space. For the present investigation we discard an explicit dependence of the self-energy on the momenta and the energy, which will be investigated lateron. For the retarded self-energy we assume the form

$$\bar{\Sigma}^R(\vec{x}) \; = \; Re\,\bar{\Sigma}^R(\vec{x}) \; - \; \frac{i}{2}\bar{\Gamma}(\vec{x}) \; = \tag{8.17}$$

$$2p_0 \left[\frac{V_0}{1+\exp\{(|\,\vec{x}\,| - R)/a_0\}} - i \left(\frac{W_0}{1+\exp\{(|\,\vec{x}\,| - R)/a_0\}} + \frac{\Gamma_V}{2} \right) \right]$$

allowing for a non-vanishing vacuum width Γ_V. Throughout the model studies (to be presented below) we use $R = 5$ fm, $a_0 = 0.6$ fm. The distribution function is represented in terms of the testparticle distribution (8.2), where $\vec{x}_i(t)$, $\vec{p}_i(t)$ and $\bar{m}_i^2(t)$ are the corresponding solutions of the equations of motion (8.10)-(8.12). In the case (8.17) all derivatives with respect to energy and momentum vanish such that (8.10)-(8.12) reduce to

$$\frac{d\vec{x}_i}{dt} \; = \; \frac{\vec{p}_i}{\epsilon_i}\,, \tag{8.18}$$

$$\frac{d\vec{p}_i}{dt} \; = \; -\frac{1}{2\epsilon_i}\vec{\nabla}_{x_i} Re\,\bar{\Sigma}^R_{(i)} \; + \; \frac{\bar{m}_i^2 - m^2}{\bar{\Gamma}_{(i)}} \; \frac{1}{2\epsilon_i}\vec{\nabla}_{x_i}\bar{\Gamma}_{(i)}\,, \tag{8.19}$$

$$\frac{d\bar{m}_i^2}{dt} \; = \; \frac{\bar{m}_i^2 - m^2}{\bar{\Gamma}_{(i)}} \; \frac{d\bar{\Gamma}_{(i)}}{dt}\,. \tag{8.20}$$

In the following we will also use the notation $M^2 \equiv \bar{m}^2$ for the general off-shell mass and $M_0^2 \equiv m^2$ for the respective bare mass squared of the particles.

We initialize all testparticles i with a fixed energy p_0 at some distance ($|\,\vec{x}(t\!=\!0)\,| \approx$ 15 fm) on the negative z-axis with a three-momentum vector in positive z-direction. The initial mass parameters $M_i(t=0)$ are selected according to the vacuum width Γ_V which might be arbitrarily small, but finite. The particles are then propagated in time according to eqs. (8.18) - (8.20). In Fig. 8.1 (upper part) the results for $p_{i0}(z(t))$, $M_i(z(t)) \equiv \bar{m}_i(z(t))$ and $p_{iz}(z(t))$ are displayed as a function of $z(t)$ instead of the time t. We show the evolution of 21 testparticles with mass parameters, that are initially separated by $\Delta M = 0.05 \cdot \Gamma_V$ around the vacuum value of $M_0 \equiv m = 0.7$ GeV. The potential has a non-vanishing imaginary part ($W_0 = 70$ MeV, $\Gamma_V = 0.8$ MeV) whereas the real part is vanishing ($V_0 = 0$ MeV) (see Fig. 8.1 (lower part)). One recognizes that the differences between the mass parameters increase when reaching the potential region, which corresponds directly to a broadening of the spectral function. The same spreading behavior is observed for the three-momentum of the testparticles, such that the energy p_0 is conserved throughout the whole calculation (upper line). When leaving

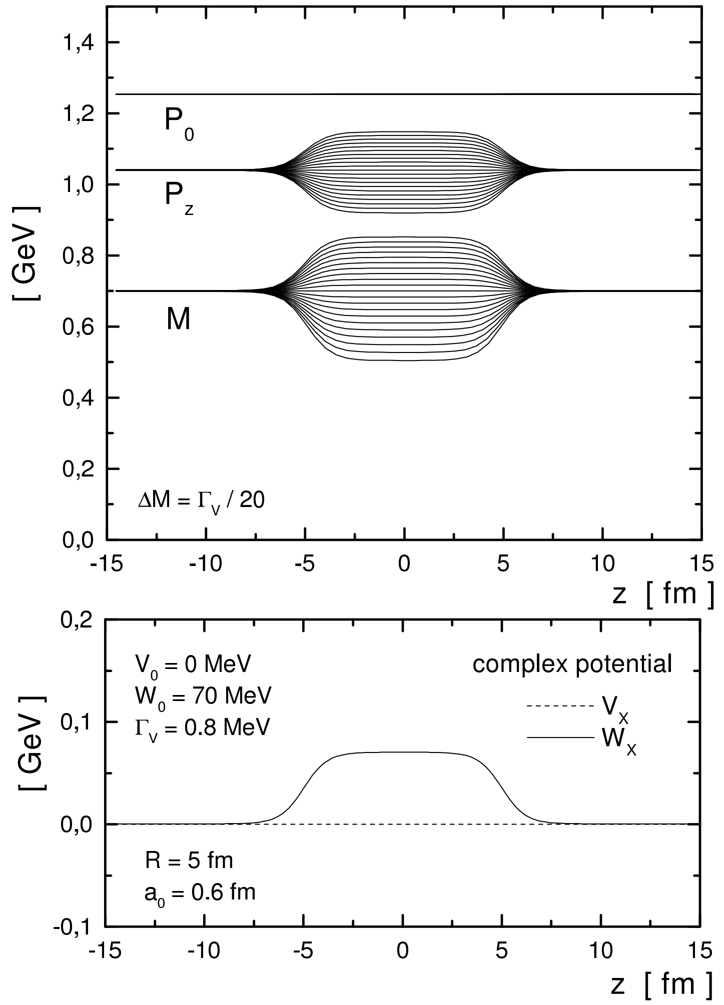

Figure 8.1: upper part: p_{i0}, p_{iz} and M_i as a function of $z(t)$ for a purely imaginary potential $W_0 = 70$ MeV (lower part). The vacuum width is $\Gamma_V = 0.8$ MeV and the initial separation in mass of the testparticles is given by $\Delta M = 0.05 \cdot \Gamma_V$ around the mean value of $M_0 = 0.7$ GeV.

the potential region the splitting decreases and the correct asymptotic solution for the spectral function is restored.

As a next step we present in Fig. 8.2 (upper part) a calculation where we additionally allow for a non-vanishing real part of the potential (i.e. $V_0 = -20$ MeV, Fig. 8.2 (lower part)). While the spreading of the mass parameter is not affected by this change, we find a shift of the testparticle momenta where the real part of the potential deviates from zero, since here the particles are accelerated.

In the next example of this model study we show in Fig. 8.3 (upper part) the case of a broad vacuum spectral function entering a (time-independent) nonrelativistic potential with $V_0 = -20$ MeV and $W_0 = 100$ MeV. The vacuum width is chosen as $\Gamma_V = 160$ MeV, while 11 testparticle trajectories are shown with an initial separation

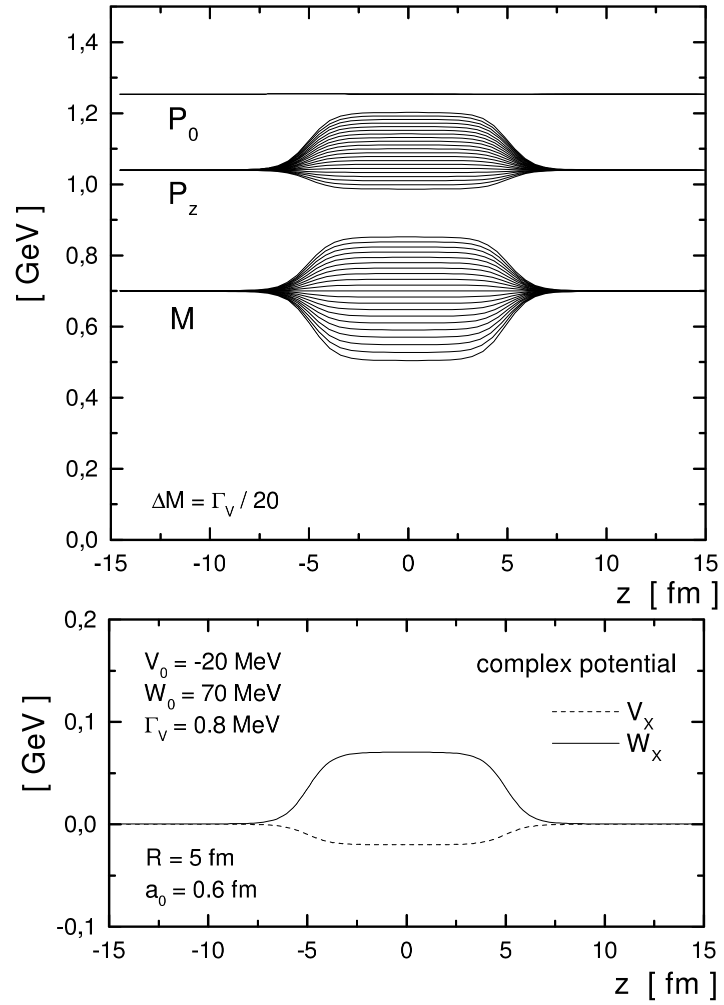

Figure 8.2: upper part: p_{i0}, p_{iz} and M_i as a function of $z(t)$ for a complex potential with $V_0 = -20$ MeV, $W_0 = 70$ MeV (lower part). For the vacuum width and the initial mass separation we have used the same values as in Fig. 8.1.

of the masses $\Delta M = 0.05 \cdot \Gamma_V$. One observes that the spectral function is further broadened in the complex potential zone and reaches its initial dispersion in mass again after passing the diffractive and absorptive area.

The question remains if the testparticle distribution (8.2) reproduces the local splitting in mass as expected due to quantum mechanics, i.e. in our case a Breit-Wigner distribution

$$F(\bar{m}) \; = \; \frac{1}{2\pi} \frac{\Gamma_V}{(\bar{m} \, - \, m)^2 \, + \, \Gamma_V^2/4} \tag{8.21}$$

with a local width $\bar{\Gamma}(\vec{x}) = 2 \; W_0(z) + \Gamma_V$. This is demonstrated in Fig. 8.4, where

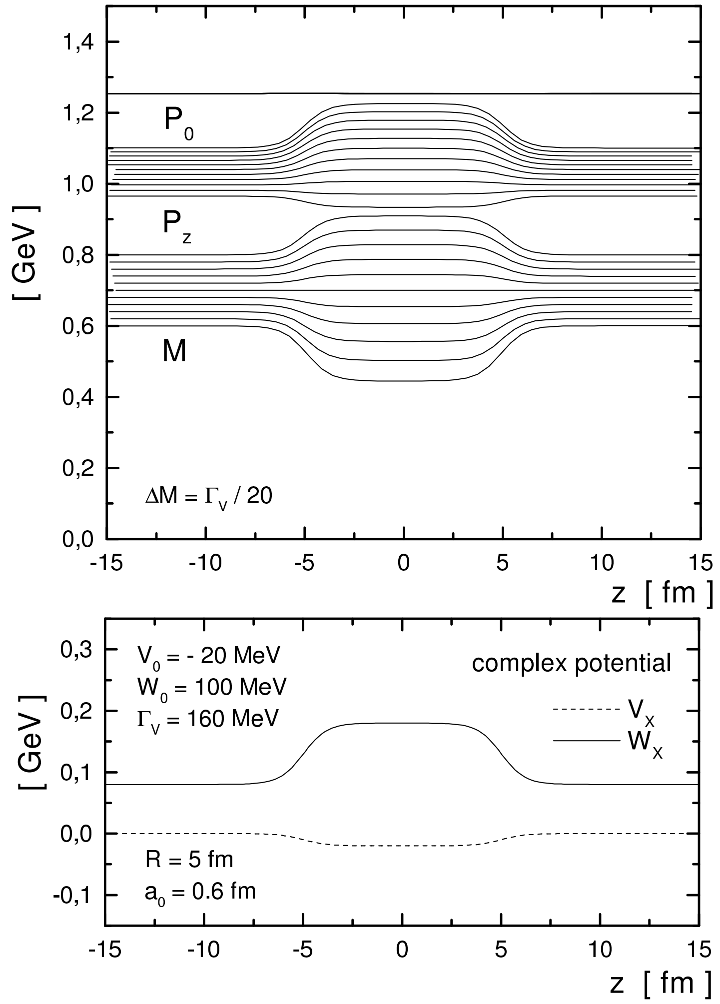

Figure 8.3: upper part: p_{i0}, p_{iz} and M_i as a function of $z(t)$ for a broad vacuum spectral function in a time-independent potential $V_0 = -20$ MeV, $W_0 = 100$ MeV (lower part). We have chosen a vacuum width $\Gamma_V = 160$ MeV and an initial mass separation of $\Delta M = 0.05 \cdot \Gamma_V$ around $M_0 = 0.7$ GeV for the testparticle trajectories displayed.

we show the spectral function as a function of mass M from the testparticle evolution at fixed coordinate z in comparison to the quantum Breit-Wigner distribution with local width $\bar{\Gamma}(\vec{x})$ (full lines) for a pure imaginary potential with parameters $W_0 = 50$ MeV and vacuum width $\Gamma_V = 2$ MeV. The differences to the exact results in Fig. 8.4 are practically not visible for all values of z from - 8 fm to 8 fm. The width of the distribution increases from 1 MeV in the vacuum ($z = \pm$ 8 fm) to 102 MeV ($= 2\ W_0 +\ \Gamma_V$) in the center of the absorptive potential ($z = 0$). Thus our off-shell quasiparticle propagation is fully in line with the quantum mechanical result at least for quasi-stationary quantum states.

Next we step to more general potentials that include a dependence on the momentum $\vec{p}$ and the energy p_0 as well. The retarded self-energy is chosen of the type:

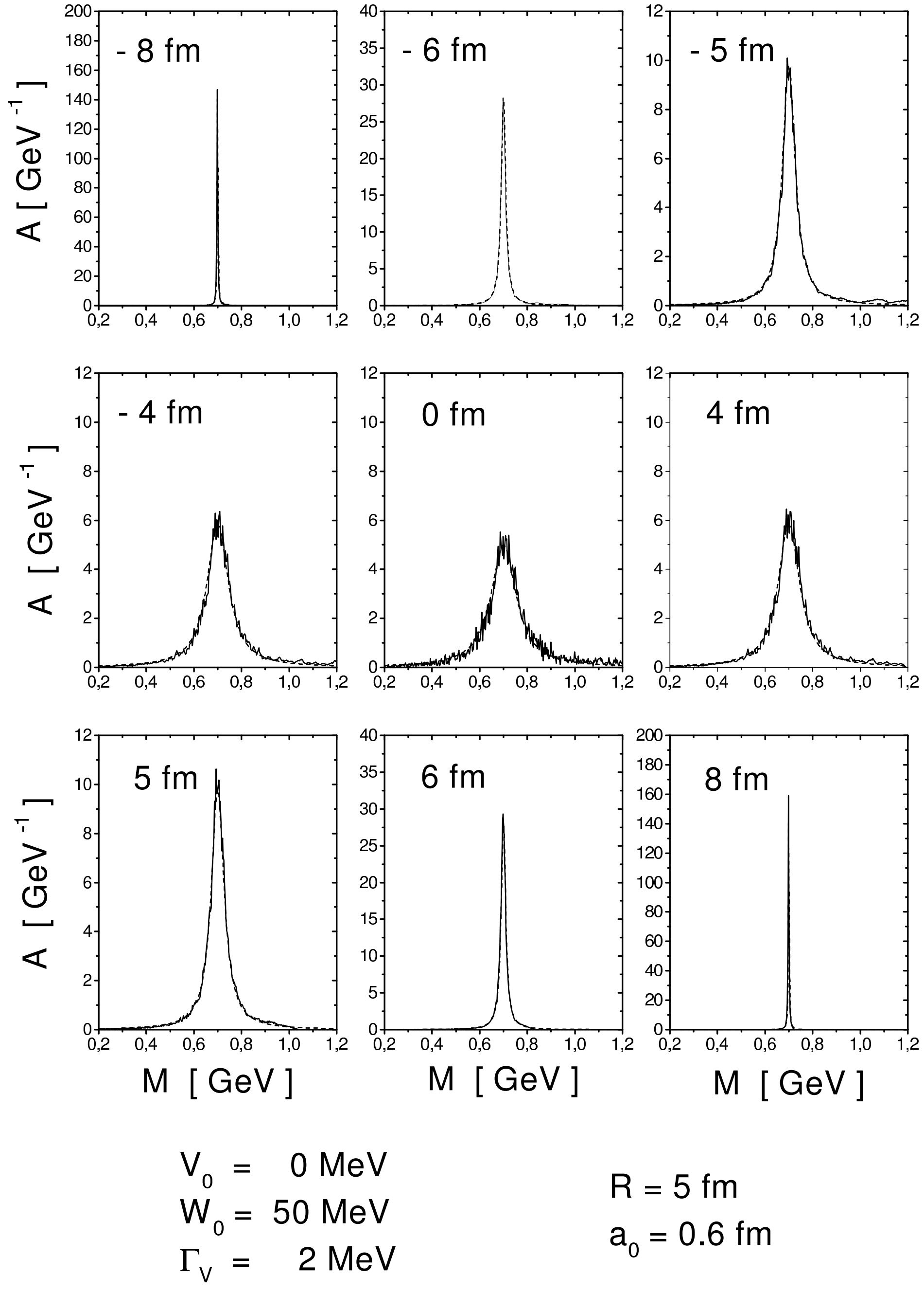

Figure 8.4: The spectral distribution at different coordinates z from the testparticle distribution in comparison to the analytical result (solid lines) for $V_0 = 0$, $W_0 = 50$ MeV and $\Gamma_V = 2$ MeV. The analytical result is practically identical to the histograms from the testparticle distribution and thus hardly visible.

$$\bar{\Sigma}^R(\vec{p},p_0,\vec{x}) \;=\; Re\,\bar{\Sigma}^R(\vec{p},p_0,\vec{x}) \;-\; \frac{i}{2}\bar{\Gamma}(\vec{p},p_0,\vec{x}) \;= \tag{8.22}$$
$$\frac{V(p_0,\vec{p})}{1+\exp\{(|\,\vec{x}\,|-R)/a_0\}} \;-\; i\left(\frac{W(p_0,\vec{p})}{1+\exp\{(|\,\vec{x}\,|-R)/a_0\}} + \frac{\Gamma_V}{2}\right)$$

again with a constant (relativistic) vacuum width Γ_V. While the spatial extension of the potential is given as in the first model case by a Woods-Saxon shape (with parameters $R = 5$ fm and $a_0 = 0.6$ fm) its momentum dependence for the real as well as for the imaginary part is introduced by

$$V(p_0,\vec{p}) \;= C_V\,\frac{\Lambda_V^2}{\Lambda_V^2-(p_0^2-\vec{p}^2)}\,, \qquad W(p_0,\vec{p}) \;= C_W\,\frac{\Lambda_W^2}{\Lambda_W^2-(p_0^2-\vec{p}^2)}\,. \tag{8.23}$$

Here the constants C_V (C_W) give the 'strength' of the complex potential while Λ_V (Λ_W) play the role of cutoff-parameters. Due to the structure in the denominator of (8.23) the momentum-dependent part of this potential is explicitly Lorentz-covariant.

In our simulation we propagate the testparticles with different initial mass parameters M_i, which are shifted relative to each other by $\Gamma_V/(20$ GeV) around a mean mass of 1.0 GeV. For each testparticle a momentum in positive z-direction is attributed such that all of them have initially the same energy $p_0 = 2.0$ GeV. All testparticles are again initialized on the negative z-axis with ($|\,\vec{x}_i(t=0)\,| \approx 15$ fm) and then evolved in time according to the full equations of motion (8.10), (8.11) and (8.16).

In our first simulation with the energy-momentum dependent trial self-energy (8.22) we consider a purely imaginary potential with a strength of $C_W = 0.6$ GeV^2 and a cutoff-parameter $\Lambda_W = 2.0$ GeV. The evolution in energy p_{0i}, momentum p_{zi} and in the mass parameter M_i for all testparticles is shown in Fig. 8.5 (upper part) as a function of $z(t)$. When the testparticles enter the potential region, their momenta and mass parameters are modified. As already shown for the momentum-independent case, the imaginary potential leads to a spreading of the trajectories in the mass parameter M_i which in turn reflects a broadening of the spectral function. The relation between the imaginary self-energy and the spreading in mass is fully determined by relation (8.16). Since we have chosen a potential with no explicit time dependence, the energy of each testparticle is a constant of time. According to the explicit momentum dependence of our 'trial' potential each single testparticle is affected with different strength. Since the imaginary potential is strongest for small momenta (which correspond to the highest lines in the lower graph of Fig. 8.5), the momentum and mass coordinates of those testparticles are changed predominantly which are initialized with the lowest momenta (i.e. with the largest masses). As a result one observes a rather asymmetric distribution in the mass parameters (and in the momenta) in the potential zone. This is different from the case of momentum-independent potentials which yield a nearly equidistant spreading of the mass trajectories. For $z(t) \gg R$ the mass and momentum coordinates of the testparticles return to the proper asymptotic value.

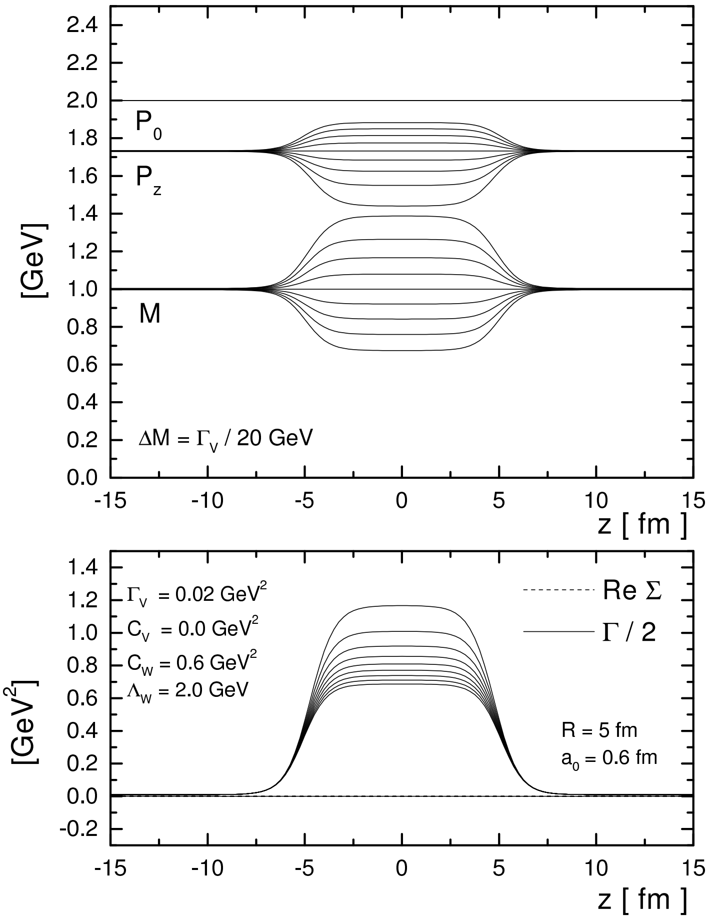

Figure 8.5: upper part: p_{i0}, p_{iz} and M_i as a function of $z(t)$ for a momentum-dependent imaginary potential with $C_W = 0.6$ GeV^2 and $\Lambda_W = 2.0$ GeV (lower part). The vacuum width is chosen as $\Gamma_V = 0.02$ GeV^2 and the initial separation in the mass parameter of the testparticles is $\Delta M = \Gamma_V/20$ around $M_0 = 1.0$ GeV.

In the next example we allow for an addititonal real part of the self-energy. The calculation is performed with the parameters $C_V = -0.3$ GeV^2, $C_W = 0.6$ GeV^2 and $\Lambda_V = \Lambda_W = 2.0$ GeV. The momentum-dependent real part (lower part of Fig. 8.6) causes – as also observed for the momentum independent case (cf. Fig. 8.2) – an additional shift of the testparticle momenta. Since the real part of the potential is larger for small initial momenta, these testparticle momenta are shifted up somewhat more than for particles with larger momenta. This gives rise to a reduction of the asymmetry introduced by the momentum-dependent imaginary part of the self-energy (upper part of Fig. 8.6). As observed for the momentum-independent self-energy the mass parameters of the testparticles are only weakly influenced by the real part of the potential.

To summarize our model results for the simple complex potential of the Woods-Saxon type, we find a spreading of the mass trajectories of the testparticles in the potential region. This resembles the broadening of the spectral function due to the

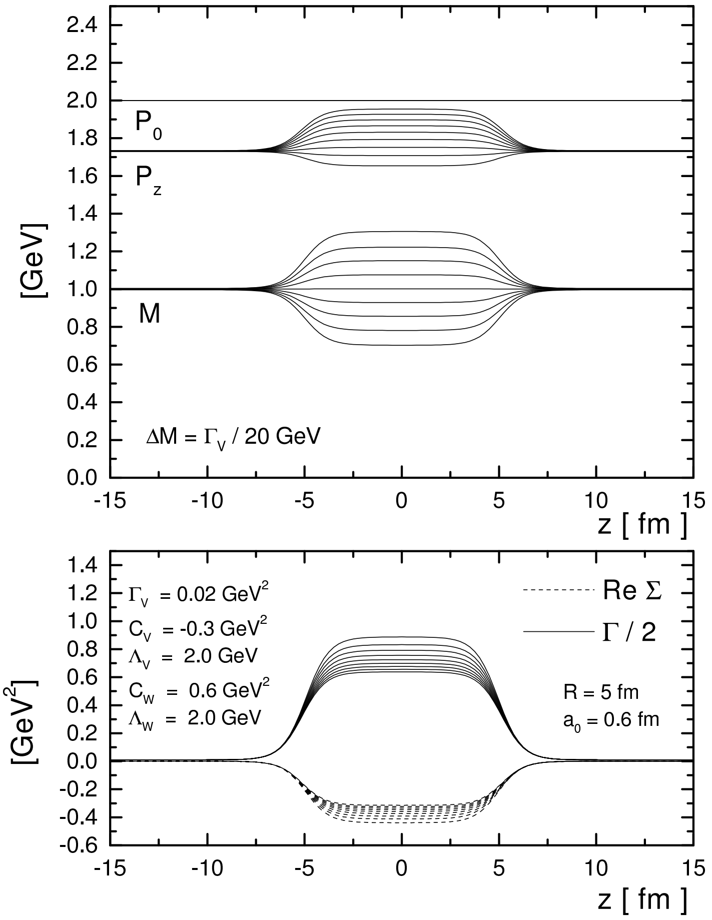

Figure 8.6: upper part: p_{i0}, p_{iz} and M_i as a function of $z(t)$ for a momentum-dependent complex potential with $C_V = -0.3$ GeV^2, $\Lambda_V = 2.0$ GeV, $C_W = 0.6$ GeV^2 and $\Lambda_W = 2.0$ GeV (lower part). For the vacuum width and the initial mass separation the same values are used as in Fig. 8.5.

space-time dependent imaginary part of the potential in line with quantum mechanics. When leaving the potential regime the correct asymptotic solutions for the spectral function are restored. We, furthermore, find that the energy conservation is guaranteed on the single-particle level during the propagation, if $\partial/\partial t \; \bar{\Gamma} = 0$. The model studies have also shown, that momentum-dependent potentials can lead to a more asymmetrical spreading in mass which can be reduced by a non-vanishing real part of the self-energy. Nonetheless, we observe that for the momentum-dependent case the correct limit for the spectral function is assumed as well for large distances relative to the potential range.

8.3 Application to Heavy-Ion Collisions

In this Section we will investigate realistic heavy-ion collisions within the off-shell treatment derived above. At first we briefly describe some essential features of the implementation of the off-shell extension into a general transport code appropriate for nucleus-nucleus collisions at intermediate and high energies. Finally, we will show some results obtained within the generalized transport scheme in order to point out the effects of the off-shell dynamics.

While, so far, we have only considered the collisionless propagation of particles in a medium, we now turn to the explicit inclusion of scattering processes among the particles. The collision term of the Kadanoff-Baym equation can only be worked out in more detail by giving explicit approximations for the self-energies $\bar{\Sigma}^{\gtrless}$. A corresponding collision term can be formulated in full analogy to Refs. [14, 98], e.g. from Dirac-Brueckner theory, and implementing detailed balance as

$$\begin{aligned} I_{coll}(\vec{p},\bar{m}^2,x) \;=\; & Tr_2\, Tr_3\, Tr_4\;\; A(\vec{p},\bar{m}^2,x)\; A(\vec{p}_2,\bar{m}_2^2,x)\; A(\vec{p}_3,\bar{m}_3^2,x)\; A(\vec{p}_4,\bar{m}_4^2,x) \qquad (8.24)\\ & \times\; \left| T((\vec{p},\bar{m}^2)+(\vec{p}_2,\bar{m}_2^2) \rightarrow (\vec{p}_3,\bar{m}_3^2)+(\vec{p}_4,\bar{m}_4^2)) \right|^2_{\mathcal{A},\mathcal{S}}\;\; \delta^{(4)}(p+p_2-p_3-p_4)\\ \times\; & \big[\, N(\vec{p}_3,\bar{m}_3^2,x)\; N(\vec{p}_4,\bar{m}_4^2,x)\; \bar{f}(\vec{p},\bar{m}^2,x)\; \bar{f}(\vec{p}_2,\bar{m}_2^2,x)\\ & \qquad - N(\vec{p},\bar{m}^2,x)\; N(\vec{p}_2,\bar{m}_2^2,x)\; \bar{f}(\vec{p}_3,\bar{m}_3^2,x)\; \bar{f}(\vec{p}_4,\bar{m}_4^2,x)\,\big]\;. \end{aligned}$$

As in the usual on-shell formulation of quantum-transport theory the distribition functions $N(\vec{p},\bar{m}^2,x)$ enter the collision term together with the respective Bose-enhancement or Pauli-blocking factors $\bar{f}(\vec{p},\bar{m}^2,x) = 1+\eta\, N(\vec{p},\bar{m}^2,x)$ with $\eta = \pm 1$ for bosons/fermions. Additionally, the spectral functions A of the participating particles are taken into account, which change in time due to the actual interaction. In eq. (8.24) the trace over particles 2, 3, 4 is given explicitly for fermions as

$$Tr_2 \;=\; \sum_{\sigma_2,\tau_2} \frac{1}{(2\pi)^4} \int d^3p_2\; \frac{d\bar{m}_2^2}{2\sqrt{\vec{p}_2^{\,2}+\bar{m}_2^2}}\,, \tag{8.25}$$

where σ_2, τ_2 denote the spin and isospin of particle 2. In case of bosons we have

$$Tr_2 \;=\; \sum_{\sigma_2,\tau_2} \frac{1}{(2\pi)^4} \int d^3p_2\; \frac{dp_{0,2}^2}{2} \tag{8.26}$$

in accordance with the normalization conditions for the bosonic (scalar) spectral function A_B

$$\int \frac{dp_0^2}{4\pi} \, A_B(p,x) = 1 \, , \tag{8.27}$$

whereas for fermions the corresponding relation is

$$\int \frac{dp_0}{2\pi} \, A_F(p,x) = 1 \, . \tag{8.28}$$

We mention that the spectral function A_F in case of fermions in (8.24) is obtained by considering only particles of positive energy and assuming the spectral function to be identical for spin 'up' and 'down' states [35]. Furthermore, the off-shell in-medium scattering amplitude T enters the collision term. Here the indices $\mathcal{A}, \mathcal{S}$ stand for the antisymmetric/symmetric matrix element in case of fermions/bosons.

Neglecting the 'gain-term' in eq. (8.24) one recognizes that the collisional width of the particle in the rest frame is given by

$$\Gamma_{coll}(\vec{p}, \bar{m}^2, x) \; = \; Tr_2 \, Tr_3 \, Tr_4 \;\; A(\vec{p}_2, \bar{m}_2^2, x) \; A(\vec{p}_3, \bar{m}_3^2, x) \; A(\vec{p}_4, \bar{m}_4^2, x) \tag{8.29}$$

$$\times \;\; \left| \, T((\vec{p}, \bar{m}^2) + (\vec{p}_2, \bar{m}_2^2) \to (\vec{p}_3, \bar{m}_3^2) + (\vec{p}_4, \bar{m}_4^2)) \, \right|^2_{\mathcal{A},\mathcal{S}} \;\; \delta^{(4)}(p + p_2 - p_3 - p_4) \tag{8.30}$$

$$\times \;\; N(\vec{p}_2, \bar{m}_2^2, x) \; \bar{f}(\vec{p}_3, \bar{m}_3^2, x) \; \bar{f}(\vec{p}_4, \bar{m}_4^2, x) \; . \tag{8.31}$$

Here as in eq. (8.24) local on-shell scattering processes are assumed for the transitions $p + p_2 \to p_3 + p_4$. The extension of eq. (8.24) to inelastic scattering processes (e.g. $NN \to N\Delta$) or ($\pi N \to \Delta$ etc.) is straightforward when exchanging the elastic transition amplitude T by the corresponding inelastic one and taking care of Pauli-blocking or Bose-enhancement for the particles in the final state. We note, that for bosons a Bose-enhancement factor is neglected in the following calculations since their actual phase-space density is small for the systems of interest.

For particles of infinite life time in vacuum – such as protons – the collisional width (8.29) has to be identified with twice the imaginary part of the self-energy. Thus the transport approach determines the particle spectral function dynamically via (8.29) for all hadrons if the in-medium transition amplitudes T are known *in their full off-shell dependence*. Since this information is not available for configurations of hot and dense matter, which is the major subject of future development, a couple of assumptions and numerical approximation schemes have to be invoked in actual applications. Since in binary collisions due to energy and momentum conservation – once the final masses are fixed – only the final scattering angle $\Omega = (\cos\theta, \phi)$ is undetermined, we can replace the amplitude squared in (8.29) as

$$|T(\vec{q})|^2_{\mathcal{A},\mathcal{S}} \; = \; \frac{4\pi^2}{\mu^2} \, \frac{d\sigma}{d\Omega}(\sqrt{s}) \, , \tag{8.32}$$

where $\vec{q}$ is the momentum transfered in the collision at invariant energy $\sqrt{s}$ and μ is the reduced mass of the scattering particles. The differential cross section $d\sigma/d\Omega$ or $T(\vec{q})$ in principle should be evaluated in the Brueckner approach, however, in practice effective parametrizations are employed [14].

The following dynamical calculations are based on the conventional HSD (hadron string dynamics) transport approach [27, 99], which has been successfully applied to heavy-ion collisions from GANIL up to RHIC energies [100]. For the investigations with energies up to 100 A MeV (GANIL energies) essentially the nucleon degrees of freedom are important, since inelastic processes such as $NN \to N\Delta \to \pi N$, $\pi N \to \Delta$ are suppressed. The real part of the nucleon self-energy is determined as in Ref. [27] and includes an explicit momentum dependence of the scalar and vector self-energies for nucleons in order to be appropriate also for relativistic reactions. For the imaginary part of the retarded self-energy we assume for the low GANIL energies an energy-momentum independent form. Since this is no longer adequate for relativistic systems, we will incorporate an additional momentum dependence beginning with the SIS energy regime (1-2 A GeV). However, we will discard in all cases the explicit dependence of the self-energy on the energy p_0. This approximation implies that the correction factors $(1-C_{(i)})^{-1}$ in the testparticle equations of motion (8.10)-(8.12) are equal to 1 and thus do not contribute.

The collisions of nucleons are described by the closest distance criterion of Kodama et al. [101] in the individual NN c.m.s., i.e.

$$|\,\vec{x}_1 - \vec{x}_2\,| \leq \sqrt{\sigma\,|\,\vec{p}_1 - \vec{p}_2\,|\,/\,\pi}\,, \tag{8.33}$$

where σ denotes the total cross section of the process, which is written here as a function of the three-momentum difference in the c.m.s. In the case of nucleon-nucleon collisions the Cugnon parametrization [102] for the in-medium NN differential cross section $d\sigma/d\Omega(\sqrt{s'})$ is used by identifying (in the NN c.m.s.)

$$s' - 4m_N^2 \;=\; s - 4\bar{m}^2 \;=\; 4\vec{p}^{\,2}, \tag{8.34}$$

where m_N is the nucleon vacuum mass, $\bar{m}$ the actual off-shell mass and $\sqrt{s'}$ the invariant energy of a nucleon-nucleon collision in the vacuum with the same cms-momentum $\vec{p}$. The final nucleon states are selected by Monte-Carlo according to the local spectral function $\bar{A}$ determined by the collisional width $\Gamma_{coll}((\vec{p}), x)$ (8.29), while the angular distribution in the c.m.s. is taken the same as for on-shell nucleons. This recipe for off-shell nucleon-nucleon scattering is practically an *ad-hoc* assumption and has to be controlled by off-shell matrix elements of the nucleon Brueckner T-matrix in the medium.

According to eq. (8.24) the nucleons can change their virtual mass $\bar{m}$ in the scattering process $1 + 2 \to 3 + 4$, while keeping the energy and momentum balance. This

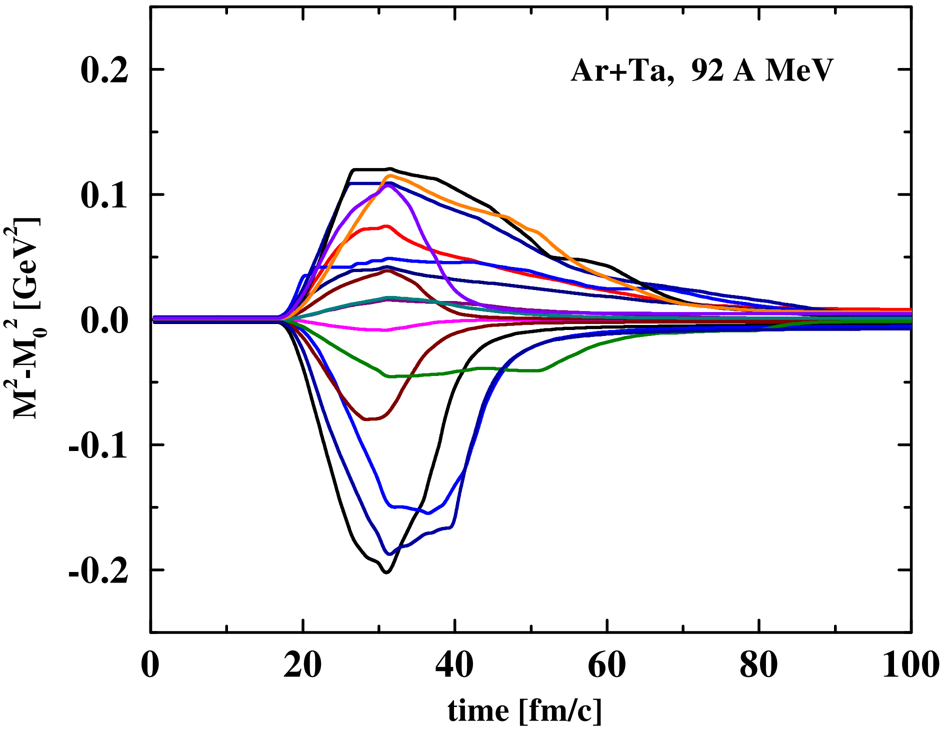

Figure 8.7: The nucleon off-shell propagation in mass $M_i^2(t) - M_0^2$ as a function of time for 16 randomly chosen testparticles. The system is $Ar + Ta$ at 92 A MeV and impact parameter $b = 1$ fm.

process is technically handled by selecting the final nucleon masses by Monte Carlo according to the local Breit-Wigner distribution. However, our Monte Carlo simulations showed that this change of virtuality for elastic collisions has a minor effect on the observables.

Apart from the description of particle propagation and rescattering the results of the transport approach also depend on the initial conditions, $\vec{x}_i(t=0)$, $\vec{p}_i(t=0)$, $\bar{m}_i^2(t=0)$. In view of nucleus-nucleus collisions, i.e. two nuclei impinging towards each other with a laboratory momentum per particle p_{lab}/A, the nuclei can be considered as in their respective groundstate, which in the semiclassical limit is given by the local Thomas-Fermi distribution [14]. Additionally the virtual mass $\bar{m}_i^2$ has been determined by Monte-Carlo according to the Breit-Wigner distribution (8.21) assuming an in-medium width $\Gamma_0 = 1$ MeV. For the vacuum width of the nucleons we have also used $\Gamma_V = 1$ MeV which implies that nucleons propagating to the continuum in the final state of the reaction achieve their vacuum mass on the 0.1 % level.

Our first applications we devote to nuclear reactions at GANIL energies (92 - 95 A MeV), since here the more recent measurements have lead to conflicting results between different transport approaches [103]. We start with the reaction $Ar + Ta$ at 92 A MeV. As an exemplary study of the off-shell dynamics we present in Fig. 8.7 for some

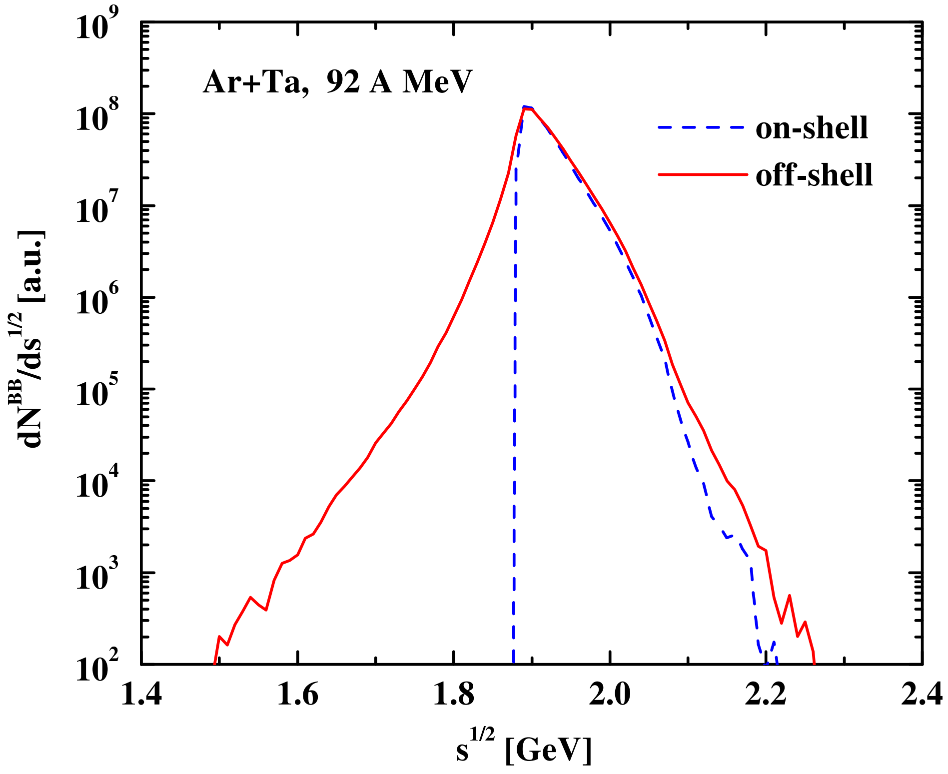

Figure 8.8: The number of baryon-baryon (BB) collisions as a function of the invariant energy $\sqrt{s}$ for $Ar + Ta$ at 92 A MeV integrated over all impact parameters. The solid line is obtained from including the off-shell propagation in the transport approach while the dashed line stands for the result in the on-shell limit.

randomly chosen testparticles i their off-mass-shell behaviour $M_i^2(t) - M_0^2$ ($\bar{m} \equiv M$, $m \equiv M_0$) as a function of time in a central collision ($b = 1$ fm). It is seen that during the maximum overlap of the nuclei at $t \approx 30$ fm/c the off-shellness reaches up to 0.2 GeV^2, however, in analogy to the model studies the nucleons become practically on-shell for $t \geq 90$ fm/c. The finite width at the end of the calculation presented here is due to the fact, that the collisional width Γ_{coll} is still different from zero. The fluctuations in $M_i^2(t) - M_0^2$ in time give some idea about the numerical accuracy of the calculation for the space-time derivative of $\Gamma(x)$; the functions become smoother when increasing the number of testparticles/nucleon furtheron (≥ 1000).

We continue with qualitative investigations, that allow to extract the physics more clearly. In Fig. 8.8 we display the number of baryon-baryon collisions $dN^{BB}/d\sqrt{s}$ as a function of the invariant energy $\sqrt{s}$ for $Ar + Ta$ at 92 A MeV integrated over all impact parameters. The dashed line shows the result for the on-shell transport approach (starting at $2m_N$) whereas the solid line corresponds to the off-shell result, which extends down to $\sqrt{s} \approx 1.5$ GeV. Note, that elastic collisions of off-shell nucleons can occur below $\sqrt{s} = 2m_N$ due to their dynamical virtuality in mass.

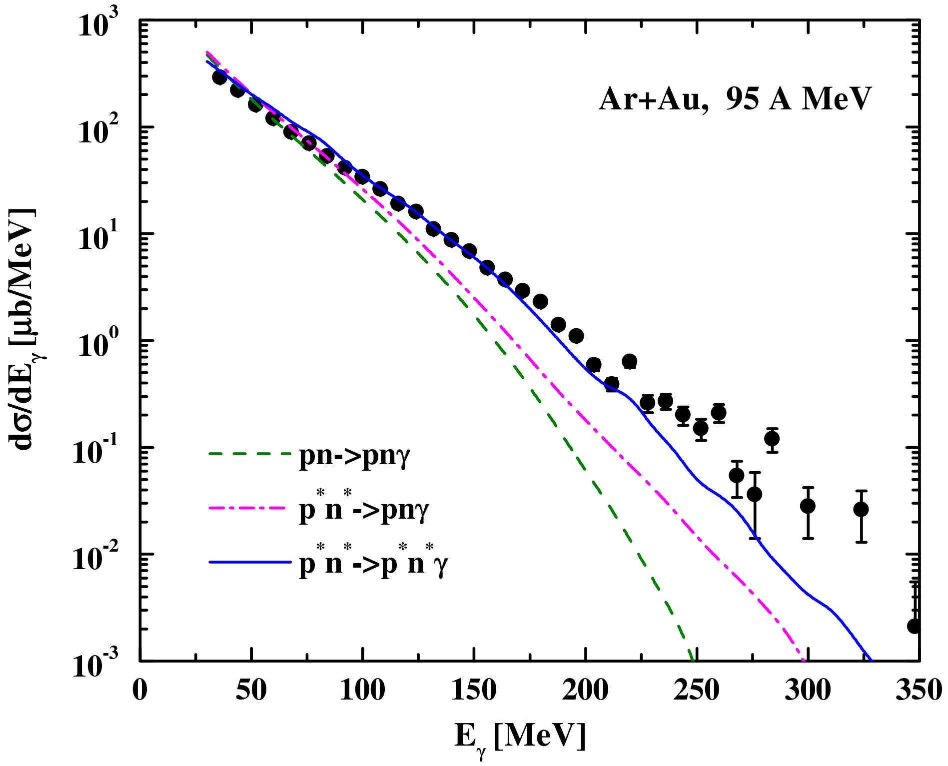

Figure 8.9: The inclusive differential photon spectra for $Ar + Au$ at 95 A MeV within various limits in comparison to the data from Ref. [104]. The dashed line is obtained in the on-shell propagation limit including on-shell nucleons in the final state, too. The dash-dotted line results from the off-shell propagation, however, including on-shell nucleons in the final production channel. The solid line results from the off-shell propagation of nucleons including also off-shell nucleons in the final channel.

The latter $\sqrt{s}$ distribution can approximately be tested experimentally by hard photon spectra, a question that has been explored by the TAPS collaboration for $Ar + Au$ at 95 A MeV [104, 105]. In order to test the off-shell transport approach we have performed calculations for this system, too, using the parametrizations (4.13) of Ref. [14] for the elementary differential photon cross section in proton-neutron (pn) collisions. Note, that the elementary photon bremsstrahlung in pn collisions is at best known within a factor of 2 (cf. the discussion in Ref. [14]). Fig. 8.9 displays the results of our bremsstrahlung calculations in comparison to the data from Ref. [104]. The dashed line corresponds to the conventional on-shell calculation and is practically identical to the BUU analysis performed by Holzmann et al. [105], but underestimates the high energy photon yield dramatically. This situation does not improve very much when including the off-shell propagation of nucleons for the initial channel (dash-dotted line), however, still requiring that the nucleons in the final state are on-shell, too. Denoting off-shell nucleons by an extra * this corresponds to the individual reactions $p^* + n^* \to p + n + \gamma$, whereas the dashed line is obtained from the channel $p + n \to p + n + \gamma$.

On the other hand, the energetic photons are produced very early in the collision phase where the virtual mass distribution of nucleons – determined by $\Gamma_{coll}(x)$ (8.29) – becomes very broad. Thus including this virtuality in mass also in the final state, where the masses are selected by Monte-Carlo according to (8.21) with a local width $\Gamma(x)$, we self-consistently can sum the individual channels $p^* + n^* \to p'^* + n'^* + \gamma$. The result of such calculations is shown in Fig. 8.9 by the solid line which comes quite close to the experimental data [104]. We note that in the latter calculations we have averaged the photon yield over 10 MeV bins to reduce the statistical fluctuations emerging from the Monte-Carlo final state selection. Whereas in Ref. [105] the high energy photon yield has been tentatively attributed to very high momentum components in the initial phase-space distribution – which semiclassically are not bound – our present results indicate that this yield might be almost entirely explained (without introducing any additional assumptions) by the off-shell transport approach. It is presently unclear, if the missing high energy photon yield should be attributed to three-body reaction channels [106, 107], to the contribution of the $\Delta \to \gamma N$ channel [108] or to the secondary $\pi N \to \gamma N$ channel [109, 110].

Whereas for energies up to 100 A MeV (GANIL energies) essentially the nucleon degrees of freedom were important, we have to take into account inelastic processes in the SIS regime (up to 2 A GeV). Thus the actual 'recipies' for the creation of nucleon and meson resonances involved have to be specified. We will only briefly mention the main assumptions entering the calculation. For a detailed discussion of this issue we refer the reader to Ref. [35]. For the production of resonances – by employing the usual Breit-Wigner cross section – we take into account not only the (mass-dependent) vacuum width Γ_V but the width caused by collisions Γ_{coll} as well. The (two-body) decay of resonances is treated as in the standard on-shell picture but corrected by the appropriate phase-space factors. Thus the ratio of the two-body phase-space integrals evaluated with the general off-shell masses of the emerging particles to the integrals calculated with the usual on-shell values enters explicitly. The masses of the outgoing particles are selected by Monte-Carlo according to the local spectral functions with a total width, which is self-consistently determined by (8.29) in its full space-time and momentum dependence.

In case of meson production by off-shell baryon-baryon or meson-baryon collisions one has to fix the mass differential cross sections, that depend on the particles in the entrance channel and especially on the available energy. Far above the thresholds the mass differential cross sections are approximated by the standard on-shell cross section in terms of the excess energy above the threshold weighted by the meson spectral functions for given total width. Close to the threshold, however, a constant matrix element is assumed which is multiplied by the available phase-space for the outgoing off-shell particles. Again we refer the reader to a more detailed study of the implementation of the off-shell transitions to Ref. [35], where the reasonability of the assumptions is discussed as well. In a more recent work [37] the concept has been improved significantly by incorporating off-shell G-matrix elements in order to describe antikaon production in nucleus-nucleus collisions at SIS energies.

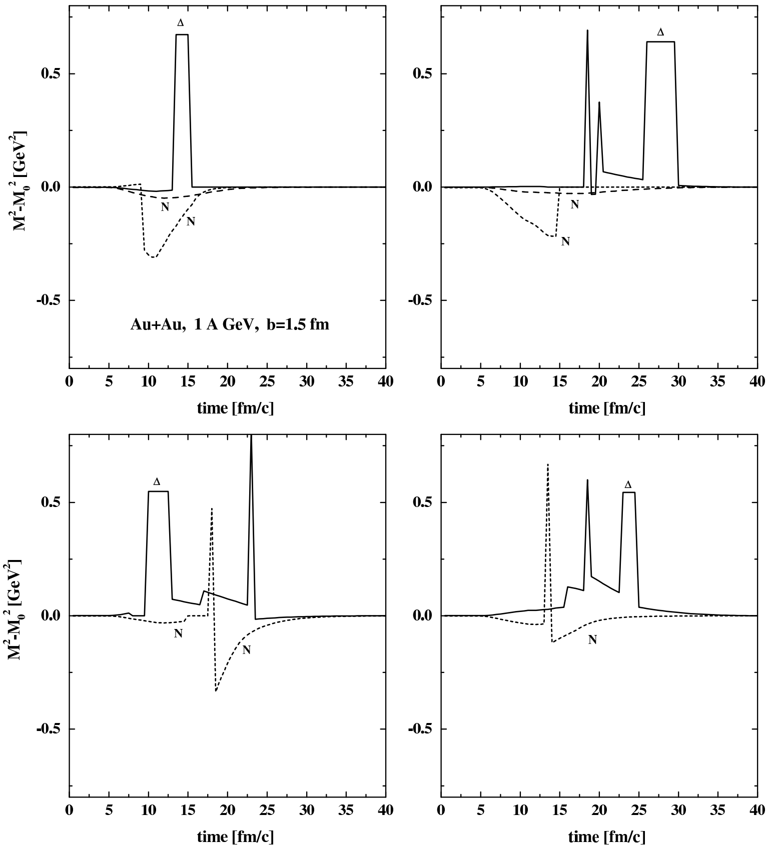

Figure 8.10: Some randomly chosen examples for the baryon off-shell propagation in mass in $Au + Au$ collisions at 1 A GeV and $b = 1.5$ fm. The sudden spikes correspond to Δ or N^* excitations, that decay again after a few fm/c to off-shell nucleons and a pion.

We now proceed to nuclear reactions at SIS energies (1 - 2 A GeV) that have been analysed within conventional transport models to a large extent (cf. Ref. [27] and Refs. cited therein). In order to show the qualitative changes relative to the case of lower bombarding energies we present in Fig. 8.10 the off-mass-shell behaviour $M_i^2(t) - M_0^2$ for some randomly chosen testparticles i as a function of time in a central $Au + Au$ collision ($b = 1.5$ fm) at 1 A GeV. It is seen that during the collision of the nuclei from $t \approx 7 - 25$ fm/c the off-shellness of baryons reaches up to 0.8 GeV^2, however, the nucleons become practically on-shell for $t \geq 35$ fm/c. The individual sudden high mass excitations and subsequent decays correspond essentially to Δ and N(1440) baryons. Nucleons in their decay may be off-shell, but propagate again to their on-shell mass in the continuum.

The corresponding baryon spectral distribution is shown in Fig. 8.11 as a function of the invariant mass for the latter reaction at times of 0, 5, 10, 20, 40 and 60 fm/c. Apart from a broadening of the nucleon spectral function at the initial time steps one

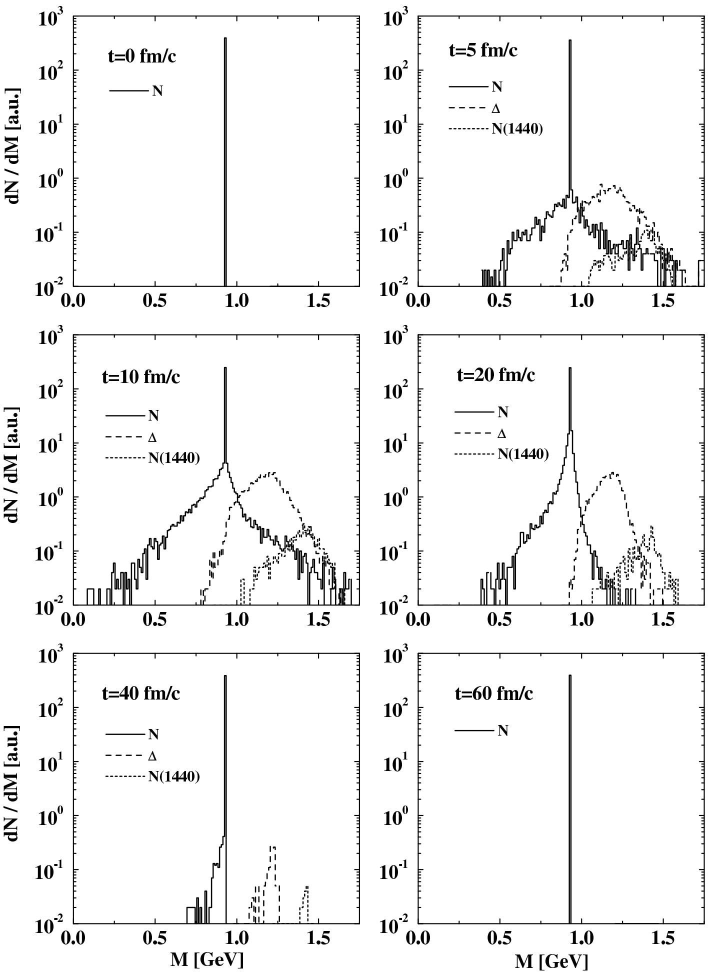

Figure 8.11: The baryon distribution in mass M for $Au + Au$ at 1 A GeV and $b = 1.5$ fm for times of 0, 5, 10, 20, 40 and 60 fm/c. The dashed and dotted lines stand for Δ and $N(1440)$ resonances, respectively.

observes that the high mass tail is completely covered by the Δ and N(1440) excitations. This is different from the results at GANIL energies since in the latter case the Δ excitation was dynamically suppressed and the high mass tail of the spectral function dominated by nucleons. In fact, in 1 A GeV $Au + Au$ collisions the resonance high mass spectrum in the off-shell calculations is only slightly enhanced as compared to the on-shell calculations (without explicit representation). Note that at t = 60 fm/c all resonances have decayed and the nucleons have become on-shell again.

Without going into detail we want to summarize the findings of the application of the on-shell transport to heavy-ion collisions in the SIS energy regime. A detailed discussion and representation is given in [35]. We find that the off-shell propagation of nucleons practically does not change the rapidity distributions dN/dy and has only a minor effect on the transverse momentum spectra of protons within the statistics reached except for the very high momentum tails. The distribution of baryon-baryon collisions in the invariant energy $\sqrt{s}$ is found to be also enhanced only for high invariant energies since here the collisions with or between resonances – which are only slightly affected in their high mass spectrum – dominate the spectrum. Again except for high momentum tails there is no dramatic change in the pion and K^+ spectra at SIS energies for $Au + Au$ at 1.0 A GeV and $Ni + Ni$ at 1.8 A GeV, our results being well in line with the data of the KaoS Collaboration. This no longer holds for the K^- spectra from $Ni + Ni$ collisions at 1.8 A GeV which are enhanced by a factor of ~ 2 relative to the on-shell calculation within the statistics reached. We attribute this enhancement to a broad spectral function of antikaons at high baryon density and to the 'subthreshold' energy of 1.8 A GeV considered. Antikaons couple strongly to nucleons and thus achieve a large collisional width in the nuclear medium. Thus off-shell antikaons might be produced at far subthreshold energies, become asymptotically on-shell and thus enhance the K^- yield.

As mentioned above the situation has been improved more recently by taking into account a coupled-channel G-matrix approach for the determination of the in-medium properties of the antikaons as well as off-shell transition matrix elements [37]. The full in-medium calculations agree well with the K^- spectra in semi-central $Ni{+}Ni$ collisions at 1.93 A GeV, which are underestimated by a factor of 2 for free transition matrix elements. However, the actual results show a strong sensitivity on the many-body scheme involved, especially on the dressing of the pion. In all limits considered [37] no convincing description could be obtained of all spectra measured at GSI simultaneously.

At AGS energies (2 - 11 A GeV) the particle production in the HSD approach essentially occurs via the excitation and decay of strings which can be viewed as continuum excitations of hadrons. Any spectral broadening of the 'continuum' thus is not likely to be seen in the asymptotic particle spectra of pions, kaons or antikaons especially since they are most abundantly produced far above the individual NN or πN thresholds. Indeed, we have found almost negligible deviations between the off-shell and the on-shell propagation in the rapidity spectra of these particle species for $Au + Au$ collisions at 11.3 A GeV [35].

Furthermore, we have investigated equilibration times for nuclear matter configurations – modelling intermediate and high energy nucleus-nucleus collisions – within the semiclassical off-shell transport approach [36]. In this case the transport equations are solved for a finite box in coordinate space employing periodic boundary conditions. We have found that the equilibration times within the off-shell approach are approximately the same as within the on-shell limit for the momentum configurations considered. Moreover, it has been demonstrated [36] that the off-shell HSD approach reproduces the 'proper' spectral functions for nucleons and Δ's, which in equilibrium are given analytically once the collisional width $\Gamma_{coll}(\vec{p}, M)$ is known as a function of the 3-momentum $\vec{p}$ and invariant mass M.

We conclude this Chapter by noting that the Botermans-Malfliet form of the semiclassical generalized transport equation (6.34) allows for an explicit solution within the generalized testparticle representation (8.2). The corresponding testparticle equations of motion (8.10)-(8.12) provide transparent extensions of the on-shell testparticle dynamics by including additionally the off-mass-shell dynamics (8.16), which is directly determined by the total width $\bar{\Gamma}(p,x)$ or equivalently the imaginary part of the retarded self-energy. The extended testparticle equations of motion can be incorporated in present transport codes like HSD without any severe problems, however, the off-shell transition rates have to be specified in addition. These off-shell rates might be determined by on-shell rates, that are corrected by phase-space [34, 35, 36] or explicitly from in-medium G-matrix calculations [37]. Both ways have been persued in the last years showing that the off-shell dynamics in nucleus-nucleus collisions leaves its traces essentially in the high momentum spectra of particles as well as in the differential spectra of produced photons or mesons close to threshold energies.

Chapter 9

Summary and Outlook

In this thesis the problem of nonequilibrium dynamics of strongly interacting quantum fields has been addressed, which is a genuine problem in practically all branches of physics that either involve strong couplings or long time phase-coherences between amplitudes such as two-point Green functions. The quantum evolution of systems far from equilibrium has been based on the Kadanoff-Baym equations within a self-consistent scheme for the self-energies from a 2PI effective action for self-interacting quantum fields. In particular we have investigated the question, to what extent approximate solutions based i) on a generalized semiclassical off-shell transport equation or ii) the classical on-shell Boltzmann equation compare with the exact solution of the respective Kadanoff-Baym equations.

In detail we have studied the quantum time evolution of ϕ^4-field theory for homogeneous systems in 2+1 space-time dimensions for far-from-equilibrium initial conditions [111]. The three-loop approximation for the CTP 2PI effective action has been employed, i.e. the tadpole and sunset self-energies (cf. Fig. 2.3). The tadpole contribution corresponds to a dynamical mass term whereas the sunset self-energy is responsible for dissipation and an equilibration of the system. Since both self-energies are ultraviolet divergent they had to be renormalized by including proper counterterms (cf. Appendix B). The numerical solutions for different initial configurations out of equilibrium (with the same energy density) show, that the asymptotic state achieved for $t \to \infty$ is the same for all initial conditions. In fact, we have shown that this asymptotic state corresponds to the exact off-shell equilibrium state of the system obeying the equilibrium Kubo-Martin-Schwinger (KMS) relations among the various two-point functions. Hence, within these approximations, the Kadanoff-Baym equations manifest irreversibility as expected from its coarse graining nature by expressing the n-body dynamics in terms of two-point functions, only.

During the equilibration process we have identified three different stages which are related to i) the initial build-up of correlations, ii) a kinetic thermalization and finally iii) a chemical equilibration. We find that the correlations are formed at very short times scales and are practically independent from the coupling strength involved. This result is in agreement with earlier studies of the nonrelativistic Kadanoff-Baym theory in the nuclear physics context [63]. We have, furthermore, observed that during the second phase of kinetic equilibration the time evolution of the occupation numbers of states (momentum modes) may be non-monotonic; here a memory to the initial configuration is kept in the full off-shell dynamics. This is not observed in the kinetic on-shell Boltzmann description. In the final state, which is achieved by chemical equilibration, we have demonstrated that the distribution functions can adequately be described by thermal Bose functions employing a temperature T and chemical potential μ as Lagrange parameters. Since the ϕ^4-theory does not include an explicitly conserved quantum number, the chemical potential μ has to vanish in thermal equilibrium. This limit is achieved dynamically within the Kadanoff-Baym scheme by off-shell $1 \leftrightarrow 3$ transitions that violate particle number conservation as recently conjectured in [48]. Such processes are inhibited in the Boltzmann limit due to the restriction to number-conserving $2 \leftrightarrow 2$ on-shell scattering processes. The approach to chemical equilibrium, moreover, is found to be well described in an approximate scheme that only involves small deviations from the equilibrium state.

The spectral ('off-shell') distributions of the excited quantum modes have been evaluated by a Fourier transformation with respect to the time difference $t - t'$ from the retarded Green functions. For the systems investigated we have found no universal time evolution for the spectral functions, however, they differ only in the phase of kinetic nonequilibrium and rather fast approach the thermal equilibrium shapes. The width of the spectral functions increases with the coupling strength λ employed in the interacting theory.

Furthermore, a detailed comparison of the full quantum dynamics to approximate schemes like that of a standard kinetic (on-shell) Boltzmann equation has been performed for the ϕ^4-field theory. Our analysis shows that the consistent inclusion of the dynamical spectral function has a significant impact on relaxation phenomena. We find that far off-shell $1 \leftrightarrow 3$ processes are also responsible for an increase of the quadrupole relaxation rate in case of larger couplings λ relative to the Boltzmann limit, which is attributed again to the fact that the latter transitions are missed in the Boltzmann approximation. Nevertheless, the relaxation is rather adequately described in the Boltzmann limit for small and moderate couplings, such that the full off-shell dynamics has only a small effect on the relaxation processes in momentum space. We have shown additionally, that the relaxation rates can also approximately be determined by a simple relaxation ansatz with satisfying results. These studies demonstrate, that quantum-field theoretical problems behave very much like (semi-)classical many-body systems.

Moreover, it has been seen, that the monotonous evolution within the number conserving Boltzmann limit does not approach the correct equilibrium state, but shows a finite chemical potential in the stationary limit. This, of course, is a shortcoming of the on-shell approximation, which in principle can be cured by inclusion of higher order processes.

In order to improve the standard on-shell (or quasiparticle) transport theory we have derived generalized off-shell transport equations from the Kadanoff-Baym equations in phase-space representation by restricting to first order derivatives in x and p. In fact, it could been shown explicitly, that second order derivatives (of self-energies and Green functions) are smaller than the first order derivatives by at least an order of magnitude. As a consequence the dynamics within the generalized transport formulation shows a very similar structure as the full quantum solution. This is clearly seen for the propagation of the equal-time momentum modes of the Green functions and the evolution of the spectral function for all configurations considered. It includes, in particular, the overshooting behaviour of the low momentum equal-time modes, which occurs at intermediate times depending on the initial distribution. Furthermore, the evolution within the generalized transport equation leads to a stationary state in the long time limit, which exhibits a full off-shell equilibration with vanishing chemical potential. Even the relaxation rates of the chemical potential obtained from the semiclassical evolution agree very well with those of the full Kadanoff-Baym theory. The dependence of the relaxation rate on the coupling constant is rather non-trivial, since it is strongly affected by the equilibrium spectral function as seen from the analytical estimate. Thus we conclude that the inclusion of the dynamical spectral function – as inherent in the semiclassical approximation of the KB equations – surpasses the shortcomings of the on-shell Boltzmann limit.

Moreover, we have shown that the generalized transport equation in Kadanoff-Baym (KB) form and in Botermans-Malfliet (BM) form lead to comparable results for the time evolution of the initial configurations considered. Only for the time-dependent occupation of low momentum modes slight differences have been observed. This is a typical quantum phenomenon related to the large de Broglie wavelength of the low momentum modes.

The generalized transport equation in BM form is used for the off-shell description of realistic heavy-ion collisions [34, 35, 36] since it allows for a solution within an extended testparticle ansatz. The resulting equations of motion in 8-dimensional phase-space include additional terms with space-time and energy-momentum derivatives of the imaginary part of the self-energies, that are not contained in the conventional on-shell limit of quasiparticles. It is found that the off-shellness in the particle mass is directly connected to the total width of the particle in the medium (eq. (8.16)).

The off-shell dynamics has been incorporated in the HSD transport approach and applied to heavy-ion collisions from GANIL to AGS energies. In this context we have discussed some details of the implementation, partly focussing on the importance of the self-consistent dynamical width, which results from collisions of the particles in the dense and/or hot medium. The consequences of the off-shell extension have been exemplified for single testparticle trajectories and the spectral function for model cases as well as nucleus-nucleus reactions at different energies. The main effects of the off-shell dynamics show up in the subthreshold production of particles and in a modification of the $\sqrt{s}$ distribution of the collisions, which yields a change (hardening) of the transverse momentum spectra.

Furthermore, we have introduced an efficient method for the calculation of self-consistent spectral functions in thermal equilibrium. The iteration scheme proposed automatically preserves the underlying normalization and analyticity condition. In this context we have briefly considered the case of massless fields ($m \to 0$) in the original Lagrangian as well. In principle, we find no qualitative difference in the dynamics of massless fields compared to the one with finite mass for moderate couplings due to the generation of a dynamical mass by the leading tadpole diagram. However, close to a critical coupling we obtain a substantial decrease of the pole mass for the zero momentum mode, which is accompanied by a large increase of the width. Simultaneously the occupation number of the lowest mode changes drastically while the occupation of the higher momentum modes remain about the same. We address this effect as due to the onset of Bose condensation, where our successive iteration scheme breaks down. In order to study the Bose condensation in more detail one has to include explicitly non-vanishing field expectation values [55] in the self-consistent dynamics. This task we leave for future investigations.

There are further questions, that should be settled in the future. First of all, a solution of the generalized BM transport equation in testparticle form for the ϕ^4-theory is desirable in order to finally show, that a description on the basis of the testparticle equations of motion (8.10, 8.11 and 8.16) leads to the same results as the direct integration of the transport equations in Chapter 7. Additionally, appropriate off-shell transport equations in the case of gauge-field theories like Quantum-Electrodynamics (QED) or Quantum-Chromodynamics (QCD) should be studied within the same framework as developed in this work. We note, however, that this additionally requires to solve the problem of gauge constraints like Slavnov-Taylor identities, which is a separate problem of highly complex nature.

Appendix A

Numerical Implementation

For the solution of the Kadanoff-Baym equations we have developed a computer program which differs in several points from the approach presented in Refs. [67, 68]. Instead of solving the second order differential equation (2.22) we generate a set of first order differential equations for the Green functions in the Heisenberg picture,

$$\begin{aligned} i\,G^{<}_{\phi\phi}(x_1,x_2) &= \; <\phi(x_2)\,\phi(x_1)> \,=\, i\,G^{<}(x_1,x_2)\;, \qquad \text{(A.1)} \\ i\,G^{<}_{\pi\phi}(x_1,x_2) &= \; <\phi(x_2)\,\pi(x_1)> \,=\, \partial_{t_1}\, i\,G^{<}_{\phi\phi}(x_1,x_2)\;, \\ i\,G^{<}_{\phi\pi}(x_1,x_2) &= \; <\pi(x_2)\,\phi(x_1)> \,=\, \partial_{t_2}\, i\,G^{<}_{\phi\phi}(x_1,x_2)\;, \\ i\,G^{<}_{\pi\pi}(x_1,x_2) &= \; <\pi(x_2)\,\pi(x_1)> \,=\, \partial_{t_1}\,\partial_{t_2}\, i\,G^{<}_{\phi\phi}(x_1,x_2)\;, \end{aligned}$$

with the canonical field momentum $\pi(x) = \partial_{x_0}\phi(x)$. The first index π or ϕ is always related to the first space-time argument. Exploiting the time-reflection symmetry of the Green functions some of the differential equations are redundant. The required equations of motion are given as

$$\begin{aligned} \partial_{t_1}\, G^{<}_{\phi\phi}(\vec{p},t_1,t_2) &= G^{<}_{\pi\phi}(\vec{p},t_1,t_2)\;, \qquad \text{(A.2)} \\ \partial_{t}\, G^{<}_{\phi\phi}(\vec{p},t,t) &= 2\,i\,Im\{\,G^{<}_{\pi\phi}(\vec{p},t,t)\,\}\;, \\ \\ \partial_{t_1}\, G^{<}_{\pi\phi}(\vec{p},t_1,t_2) &= -\,\Omega^2(t_1)\;G^{<}_{\phi\phi}(\vec{p},t_1,t_2) \;+\; I^{<}_{1}(\vec{p},t_1,t_2)\;, \\ \partial_{t_2}\, G^{<}_{\pi\phi}(\vec{p},t_1,t_2) &= G^{<}_{\pi\pi}(\vec{p},t_1,t_2)\;, \\ \partial_{t}\, G^{<}_{\pi\phi}(\vec{p},t,t) &= -\,\Omega^2(t)\;G^{<}_{\phi\phi}(\vec{p},t,t) \;+\; G^{<}_{\pi\pi}(\vec{p},t,t) \;+\; I^{<}_{1}(\vec{p},t,t)\;, \\ \\ \partial_{t_1}\, G^{<}_{\pi\pi}(\vec{p},t_1,t_2) &= -\,\Omega^2(t_1)\;G^{<}_{\phi\pi}(\vec{p},t_1,t_2) \;+\; I^{<}_{1,2}(\vec{p},t_1,t_2)\;, \\ \partial_{t}\, G^{<}_{\pi\pi}(\vec{p},t,t) &= -\,\Omega^2(t)\;2\,i\,Im\{\,G^{<}_{\pi\phi}(\vec{p},t,t)\,\} \;+\; 2\,i\,Im\{\,I^{<}_{1,2}(\vec{p},t,t)\,\}\;, \end{aligned}$$

where $t = (t_1 + t_2)/2$ is the mean time variable. Thus we explicitly consider the propagation in the time diagonal direction as in Ref. [62]. In the equations of motion (A.2) the current (renormalized) effective energy including the time dependent tadpole contribution enters,

$$\Omega^2(t) \;=\; \vec{p}^{\,2} \;+\; m^2 \;+\; \delta m^2_{tad} \;+\; \delta m^2_{sun} \;+\; \bar{\Sigma}^{\delta}(t)\,. \qquad \text{(A.3)}$$

The evolution in the t_2 direction has not be taken into account for $G^<_{\phi\phi}$ and $G^<_{\pi\pi}$ since the Green functions beyond the time diagonal ($t_2 > t_1$) are determined via the time-reflection symmetry $G^<_{\phi\phi/\pi\pi}(\vec{p}, t_1, t_2) = -[\,G^<_{\phi\phi/\pi\pi}(\vec{p}, t_2, t_1)\,]^*$ from the known values for the lower time triangle in both cases. Since there is no time reflection symmetry for the $G_{\pi\phi}$ functions, they have to be calculated (and stored) in the whole t_1, t_2 range. However, we can ignore the evolution of $G_{\phi\pi}$ since it is obtained by the relation $G^<_{\phi\pi}(\vec{p}, t_1, t_2) = -[\,G^<_{\pi\phi}(\vec{p}, t_2, t_1)\,]^*$. The correlation integrals in (A.2) are given by

$$\begin{aligned} I_1^<(\vec{p}, t_1, t_2) \;=\;& -\int_0^{t_1} dt' \;\; [\Sigma^>(\vec{p}, t_1, t') - \Sigma^<(\vec{p}, t_1, t')] \;\; G^<_{\phi\phi}(\vec{p}, t', t_2) \qquad \text{(A.4)} \\ & + \int_0^{t_2} dt' \;\; \Sigma^<(\vec{p}, t_1, t') \;\; \left[\, G^<_{\phi\phi}(-\vec{p}, t_2, t') - G^<_{\phi\phi}(\vec{p}, t', t_2) \,\right] \;, \end{aligned}$$

$$\begin{aligned} I_{1,2}^<(\vec{p}, t_1, t_2) \;\equiv\;& \partial_{t_2}\, I_1^<(\vec{p}, t_1, t_2) \qquad \text{(A.5)} \\ =\;& -\int_0^{t_1} dt' \;\; [\Sigma^>(\vec{p}, t_1, t') - \Sigma^<(\vec{p}, t_1, t')] \;\; G^<_{\phi\pi}(\vec{p}, t', t_2) \\ & + \int_0^{t_2} dt' \;\; \Sigma^<(\vec{p}, t_1, t') \;\; \left[\, G^<_{\pi\phi}(-\vec{p}, t_2, t') - G^<_{\phi\pi}(\vec{p}, t', t_2) \,\right] \;. \end{aligned}$$

In (A.2) and (A.5) one can replace $G^<_{\phi\pi}(\vec{p}, t_1, t_2) = -[\,G^<_{\pi\phi}(\vec{p}, t_2, t_1)\,]^*$ such that the set of equations is closed in the Green functions $G^<_{\phi\phi}$, $G^<_{\pi\phi}$ and $G^<_{\pi\pi}$.

The disadvantage, to integrate more Green functions in time in this first order scheme, is compensated by its good accuracy. As mentioned before, we especially take into account the propagation along the time diagonal which leads to an improved numerical precision. The set of differential equations (A.2) is solved by means of a 4th order Runge-Kutta algorithm. For the calculation of the self-energies we apply a Fourier-method similar to that used in Ref. [59, 62]. The self-energies (2.24), furthermore, are calculated in coordinate space where they are products of coordinate space Green functions (that are available by Fourier transformation) and finally transformed to momentum space.

Appendix B

Renormalization of ϕ^4-Theory in 2+1 Dimensions

In 2+1 space-time dimensions both self-energies (cf. Fig. (2.3)) incorporated in the present case are ultraviolet divergent. Since we consider particles with a finite mass no problems arise from the infrared momentum regime. The ultraviolet regime, however, has to be treated explicitly.

For the renormalization of the divergences we only assume that the time-dependent nonequilibrium distribution functions are decreasing for large momenta comparable to the equilibrium distribution functions, i.e exponentially. Thus we can apply the conventional finite temperature renormalization scheme. By separating the real-time (equilibrium) Green functions into vacuum ($T = 0$) and thermal parts it becomes apparent, that only the pure vacuum contributions of the self-energies are divergent. For the linear divergent tadpole diagram we introduce a mass counterterm (at the renormalized mass m) as

$$\delta m^2_{tad} \;=\; \int \frac{d^2p}{(2\pi)^2}\,\frac{1}{2\omega_{\vec{p}}}\,, \qquad\qquad \omega_{\vec{p}} = \sqrt{\vec{p}^2 + m^2}\,, \tag{B.1}$$

that cancels the contribution from the momentum integration of the vacuum part of the Green function.

In case of the sunset diagram only the logarithmically divergent pure vacuum part requires a renormalization, while it remains finite as long as at least one temperature line is involved. Contrary to the case of 3+1 dimensions it is not necessary to employ the involved techniques developed for the renormalization of self-consistent theories (in equilibrium) in Refs. [78, 79]. Since the divergence only appears (in energy-momentum space) in the real part of the Feynman self-energy Σ^c at $T = 0$ (and equivalently in the real part of the retarded/advanced self-energies $\Sigma^{R/A}$), it can be absorbed by another mass counterterm

$$
\begin{aligned}
\delta m^2_{sun} &= -Re\,\Sigma^c_{T=0}(p^2) \;=\; -Re\,\Sigma^{R/A}_{T=0}(p^2) \qquad\qquad (B.2)\\
&= \frac{\lambda^2}{6}\int\frac{d^2q}{(2\pi)^2}\int\frac{d^2r}{(2\pi)^2}\;\frac{1}{4\,\omega_{\vec q}\,\omega_{\vec r}\,\omega_{\vec q+\vec r-\vec p}}\;\frac{\omega_{\vec q}+\omega_{\vec r}+\omega_{\vec q+\vec r-\vec p}}{[\,\omega_{\vec q}+\omega_{\vec r}+\omega_{\vec q+\vec r-\vec p}\,]^2-p_0^2}
\end{aligned}
$$

at given 4-momentum $p = (p_0, \vec p)$ and renormalized mass m.

In summary, we replace the non-renormalized mass m^2 contained in the original Lagrangian (2.1) by $m_B^2 = m^2 + \delta m^2_{tad} + \delta m^2_{sun}$ with the mass counterterms given by (B.1) and (B.2). Thus the divergent part of both diagrams is subtracted. The finite part is fixed such that for the vacuum case ($n(\vec p) \equiv 0$) both renormalized self-energies vanish at the renormalized mass m.

In Figs. B.1 and B.2 we demonstrate the applicability of the renormalization prescription. To this aim we display two momentum modes $|\vec p|/m = 0.0$ (upper plots) and $|\vec p|/m = 2.0$ (lower plots) of the equal-time Green function $iG^<(|\vec p|, t, t)$ for various momentum cut-offs p_{max}/m = 6, 8, 10, 12, 14, 16, 18, 20, 22, 24 with (cf. Fig. B.1) and without (cf. Fig. B.2) renormalization of the sunset self-energy. For both cases the renormalization of the tadpole diagram has been used. We mention, that a non-renormalization of the tadpole self-energy has even more drastic consequences in accordance with the linear degree of divergence. For the non-renormalized calculations – with respect to the sunset diagram – we observe that both momentum modes do not converge with increasing momentum space cut-off. In fact, all lines tend to infinity when the maximum momentum is enlarged (since the gridsize of the momentum grid is kept constant). Although the divergence (as a function of the momentum cut-off) is rather weak – in accordance with the logarithmic divergence of the sunset self-energy in 2+1 space-time dimensions – a proper ultraviolet limit is not obtained.

This problem is cured by the sunset mass counterterm (B.2) as seen from Fig. B.1. For the momentum mode $|\vec p|/m = 2.0$ the calculations converge to a limiting curve with increasing momentum cut-off. Even for the more selective case of the $|\vec p|/m = 0.0$ mode of the equal-time Green function the convergence is established. We point out that this limit is obtained for the unequal-time Green functions as well (not shown here explicitly). In fact, it turns out that the equal-time functions provide the most crucial test for the applicability of the renormalization prescription, since the divergent behaviour appears to be less pronounced for the propagation along a single time direction t_1 or t_2. Thus we can conclude, that the renormalization scheme introduced above, i.e. including mass counterterms for the divergent tadpole and sunset self-energies, leads to ultraviolet stable results.

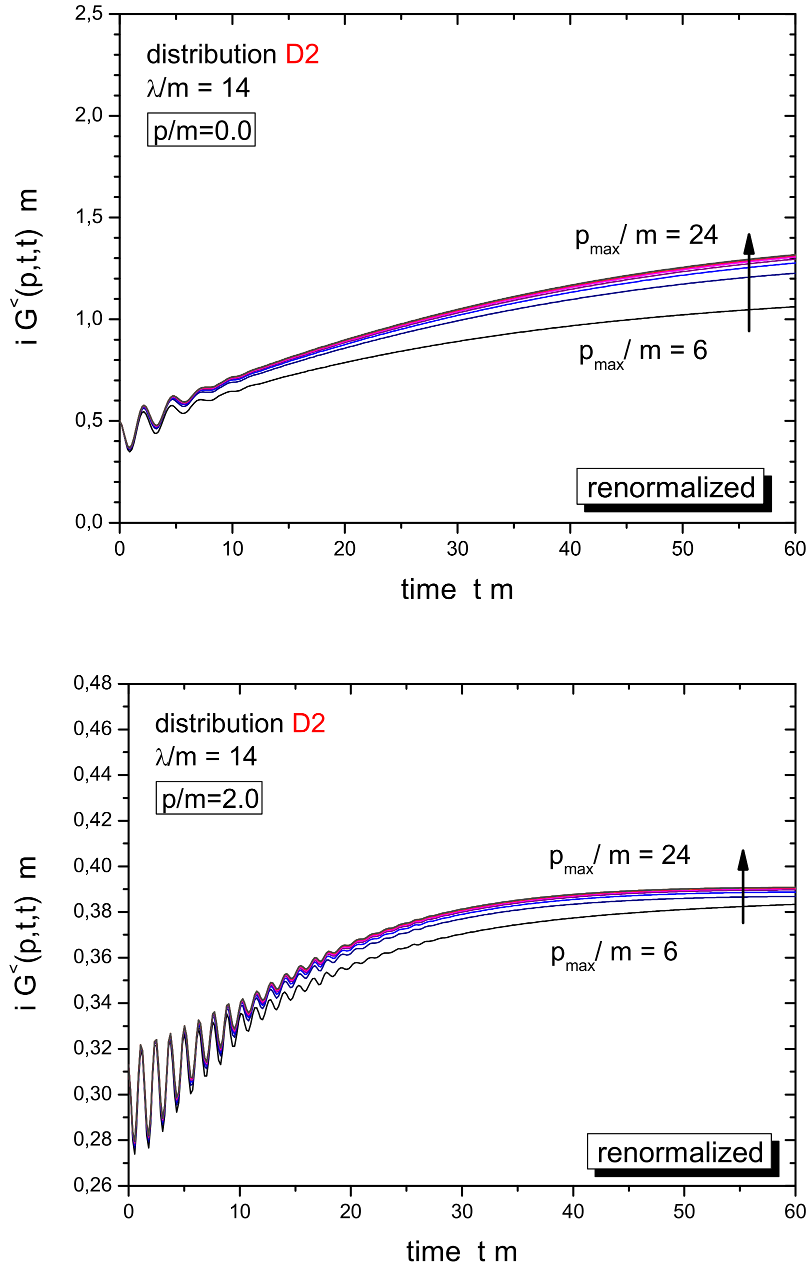

Figure B.1: Time evolution of two momentum modes $|\vec{p}\,|/m = 0.0$, $|\vec{p}\,|/m = 2.0$ of the equal-time Green function starting from the initial distribution D2 (as specified in Section 3.1) with coupling constant $\lambda/m = 14$. With the renormalization of the sunset diagram a proper limit is obtained when increasing the momentum cut-off $p_{max}/m =$ 6, 8, 10, 12, 14, 16, 18, 20, 22, 24.

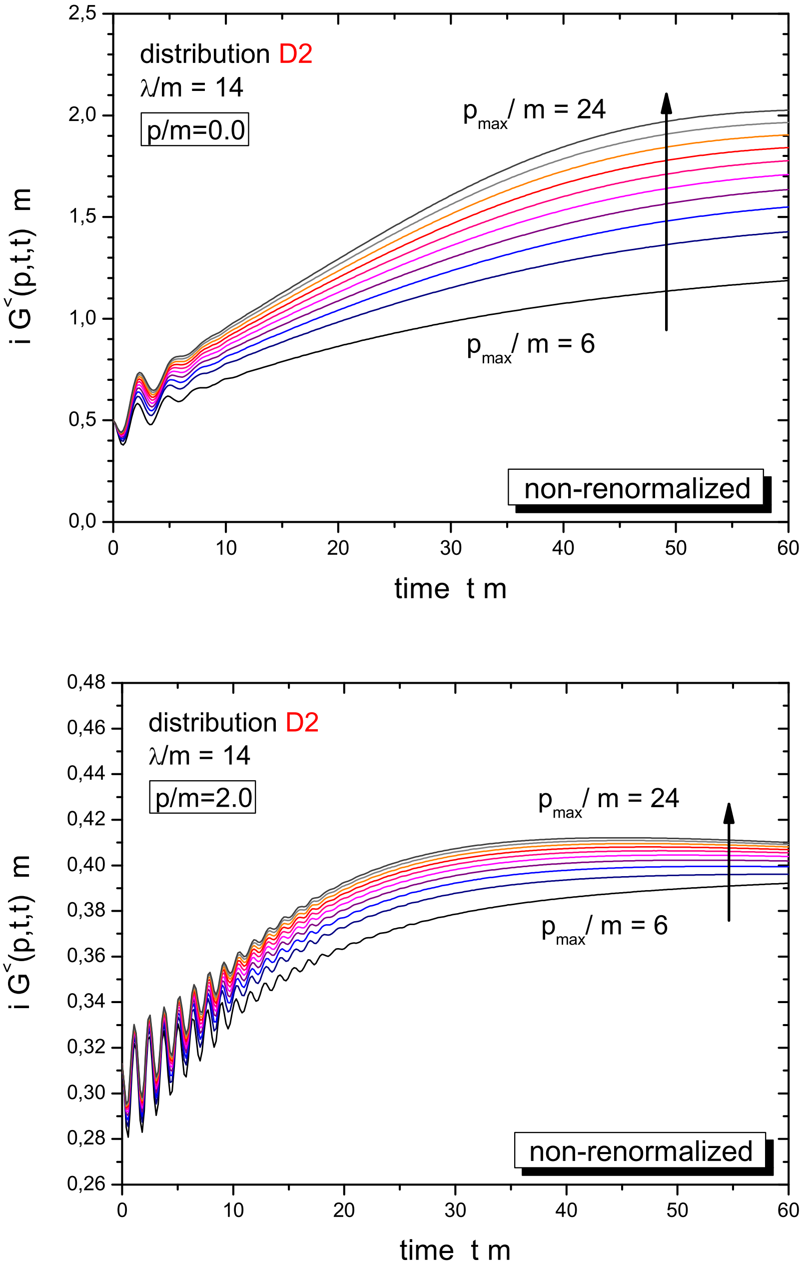

Figure B.2: Time evolution of two momentum modes $|\vec{p}\,|/m = 0.0$, $|\vec{p}\,|/m = 2.0$ of the equal-time Green function starting from the initial distribution D2 with coupling constant $\lambda/m = 14$. Without the renormalization of the sunset diagram the curves tend to infinity when enlarging the ultraviolet cut-off.

Appendix C

General Initial Conditions

In Section 3.1 we briefly have described our choice for the initial conditions for the full dynamical equations; i.e. we have taken some particular initial momentum distribution of interest, $n(\vec{p}, t=0)$, which is then inserted in the standard quasiparticle expressions (compare (5.1)):

$$\begin{aligned}
G^{\gtrless}_{\phi\phi,qp}(\vec{p}, t=0, t'=0) &= \frac{-i}{2\omega_{\vec{p}}} \; \{ \, n(\mp\vec{p}) \;\; + \;\; [\, n(\pm\vec{p}) + 1 \,] \} \\
G^{\gtrless}_{\phi\pi,qp}(\vec{p}, t=0, t'=0) &= \frac{1}{2} \; \{ \mp n(\mp\vec{p}) \;\; \pm \;\; [\, n(\pm\vec{p}) + 1 \,] \, \} \\
G^{\gtrless}_{\pi\phi,qp}(\vec{p}, t=0, t'=0) &= \frac{1}{2} \; \{ \pm n(\mp\vec{p}) \;\; \mp \;\; [\, n(\pm\vec{p}) + 1 \,] \, \} \\
G^{\gtrless}_{\pi\pi,qp}(\vec{p}, t=0, t'=0) &= \frac{-i \, \omega_{\vec{p}}}{2} \; \{ \, n(\mp\vec{p}) \;\; + \;\; [\, n(\pm\vec{p}) + 1 \,] \, \} \, .
\end{aligned} \tag{C.1}$$

We note that for the energy $\omega_{\vec{p}}$ in the above expression we have taken the on-shell energy with the bare mass. This straightforward procedure, though, is not the most general form for initial conditions within the standard Kadanoff-Baym scheme. In principle, there exist *four* independent real valued numbers for characterizing the most general initial condition instead of the two distributions $n(\vec{p}, t=0)$ and $n(-\vec{p}, t=0))$ in (C.1). To this aim we first remark that the formal solution of the Kadanoff-Baym equations (2.15), including all boundary conditions at the initial time t_0, can be cast in the form [11]

$$
\begin{aligned}
G^{<}_{\phi\phi}(\vec{x}_1,t_1;\vec{x}_2,t_2) \; = & \qquad\qquad\qquad\qquad (C.2) \\
\int\limits_{t_0=0}^{\infty} dt'\, dt'' \int d^3x'\, d^3x''\, & G^{\mathrm{R}}(\vec{x}_1,t_1;\vec{x}',t')\; \Sigma^{<}(\vec{x}',t';\vec{x}'',t'')\; G^{\mathrm{A}}(\vec{x}'',t'';\vec{x}_2,t_2) \\
+ \int d^3x'\, d^3x'' \Bigg[& G^{\mathrm{R}}(\vec{x}_1,t_1;\vec{x}',t_0=0)\;\; G^{<}_{\pi\pi}(\vec{x}',t_0;\vec{x}'',t_0)\;\; G^{\mathrm{A}}(\vec{x}'',t_0;\vec{x}_2,t_2) \\
& - G^{\mathrm{R}}(\vec{x}_1,t_1;\vec{x}',t_0=0)\;\; G^{<}_{\pi\phi}(\vec{x}',t_0;\vec{x}'',t_0)\;\; \frac{\partial}{\partial t_0''}\, G^{\mathrm{A}}(\vec{x}'',t_0'';\vec{x}_2,t_2) \\
& - \frac{\partial}{\partial t_0'}\, G^{\mathrm{R}}(\vec{x}_1,t_1;\vec{x}',t_0')\;\; G^{<}_{\phi\pi}(\vec{x}',t_0;\vec{x}'',t_0)\;\; G^{\mathrm{A}}(\vec{x}'',t_0;\vec{x}_2,t_2) \\
& + \frac{\partial}{\partial t_0'}\, G^{\mathrm{R}}(\vec{x}_1,t_1;\vec{x}',t_0')\;\; G^{<}_{\phi\phi}(\vec{x}',t_0;\vec{x}'',t_0) \frac{\partial}{\partial t_0''}\;\; G^{\mathrm{A}}(\vec{x}'',t_0'';\vec{x}_2,t_2) \Bigg]_{t_0=t_0'=t_0''=0} .
\end{aligned}
$$

This relation is sometimes denoted as a *generalized fluctuation-dissipation theorem* in the literature [5, 8, 11, 15]. G^{R} and G^{A} represent the self-consistently dressed retarded and advanced propagator, respectively, within the real-time formalism (2.18, 2.19). Since the Kadanoff-Baym equations are second order differential equations in time for both time arguments in case of a relativistic bosonic theory, (C.2) obviously has to contain four independent initial real valued quantities. It is straightforward to show that $iG^{<}_{\phi\phi}(\vec{p},t,t)$ and $iG^{<}_{\pi\pi}(\vec{p},t,t)$ are real valued, whereas $iG^{<}_{\phi\pi}(\vec{p},t,t)$ and $iG^{<}_{\pi\phi}(\vec{p},t,t)$ are related to each other by complex conjugation; hence we get two further real quantities for the initial conditions. Furthermore, due to the equal-time commutation relations, one first notes that i) $G^{<}_{\phi\phi}(\vec{p},t,t) = G^{<}_{\phi\phi}(-\vec{p},t,t))$, $G^{<}_{\pi\pi}(\vec{p},t,t) = G^{<}_{\pi\pi}(-\vec{p},t,t))$ and ii) $G^{<}_{\phi\pi}(\vec{p},t,t)) = G^{<}_{\pi\phi}(-\vec{p},t,t)) - 1$. Hence, for a real relativistic field theory for scalar bosons all the various Green functions for equal times at momentum $-\vec{p}$ are directly related to those at momentum $\vec{p}$. In total, this proves that apart from the two distributions $n(\vec{p})$ and $n(-\vec{p})$ there exist two further independent quantities for the initial Green functions (C.1). One is allowed, for example, to freely choose the real and imaginary part of $G^{<}_{\phi\pi}(\vec{p},t,t))$ instead of those stated in (C.1). In more physical terms, the four initial conditions correspond to the amplitudes and the phases of the two momentum modes $\vec{p}$ and $-\vec{p}$. The ansatz in (C.1) represents a statistically averaged distribution for the phases.

Inspecting further the formal solution (C.2), one notices that all the various terms containing the four initial conditions and contributing to $G^{<}_{\phi\phi}$ are damped by the retarded and advanced propagator for times $t_1, t_2 > t_0 = 0$ and thus will die out on a timescale of the inverse damping width (3.8). Correspondingly, this is also the timescale of dephasing and decoherence of the initial modes if particular phases would have been chosen initially. As an example, some moderate initial oscillations in the equal-time Green function can be seen in Fig. 3.2 and in Fig. B.1. The modes need ‘some time’ to acquire their characteristic spectral dressing and collective phase correlations, before the further (and rather smooth) dynamics proceeds. This time is indeed roughly the inverse damping width for the various modes. The destruction of initial (phase) correlations resembles the old conjecture of Bogolyubov [112] that the initial conditions do vanish after some finite time and do not show up any further in the subsequent dynamics of the system.

As a final remark we note, that one can principally also take care of higher order initial correlations within the dynamical prescription, which are *not* incorporated in (C.2) and in the standard Kadanoff-Baym equations [8, 113, 114, 115]. We recall that the standard real-time prescription stems from a perturbative Wick-type expansion, which is valid for a special initial density operator of single-particle (Gaussian) type. The Kadanoff-Baym equations then correspond to self-consistent and resummed Dyson-Schwinger equations in real-time for a given set of skeleton-type diagrams. On the other hand, there might (or should) exist initial correlations *beyond* the single-particle mean-field (or Gaussian) level. As we have discussed in section 3.3, some particular higher order correlations – in this case due to the quantal collisions – will be generated dynamically during the course of the evolution. Hence, in principle, such correlations should also be taken care of in the beginning of the evolution. This is not a simple task, though: These non-trivial correlations lead to non-zero expectation values of normal-ordered operators, which can be taken care of by defining new types of contractions, which couple the time evolution of the system also to those higher order correlations. For details of such a procedure we refer the interested reader to Refs. [8, 113, 114, 115].

Bibliography

[1] J. Schwinger, J. Math. Phys. 2 (1961) 407.

[2] P. M. Bakshi and K. T. Mahanthappa, J. Math. Phys. 4 (1963) 1, 12.

[3] L. V. Keldysh, Zh. Eks. Teor. Fiz. 47 (1964) 1515; Sov. Phys. JETP 20 (1965) 1018.

[4] R. A. Craig, J. Math. Phys. 9 (1968) 605.

[5] K. Chou, Z. Su, B. Hao, and L. Yu, Phys. Rept. 118 (1985) 1.

[6] L. P. Kadanoff and G. Baym, *Quantum statistical mechanics*, Benjamin, New York, 1962.

[7] D. F. DuBois in *Lectures in Theoretical Physics*, edited by W. E. Brittin (Gordon and Breach, NY 1967), pp 469-619.

[8] P. Danielewicz, Ann. Phys. (N.Y.) 152 (1984) 239.

[9] E. Calzetta and B. L. Hu, Phys. Rev. D 37 (1988) 2878.

[10] H. Haug and A. P. Jauho, *Quantum Kinetics in Transport and Optics of Semiconductors*, Springer, New York, 1999.

[11] C. Greiner and S. Leupold, Ann. Phys. 270 (1998) 328.

[12] W. Cassing, Z. Physik A 327 (1987) 447.

[13] W. Cassing, K. Niita, and S. J. Wang, Z. Physik A 331 (1988) 439.

[14] W. Cassing, V. Metag, U. Mosel, and K. Niita, Phys. Rept. 188 (1990) 363.

[15] B. Bezzerides and D. F. DuBois, Ann. Phys. 70 (1972).

[16] P. Lipavský, V. Špička, and B. Velický, Phys. Rev. B 34 (1986) 6933.

[17] V. Špička and P. Lipavský, Phys. Rev. Lett. 73 (1994) 3439; Phys. Rev. B 52 (1995) 14615.

[18] W. Botermans and R. Malfliet, Phys. Rept. 198 (1990) 115.

[19] S. Mrówczyński and P. Danielewicz, Nucl. Phys. B 342 (1990) 345.

[20] A. Makhlin, Phys. Rev. C 52 (1995) 995; A. Makhlin and E. Surdutovich, Phys. Rev. C 58 (1998) 389.

[21] K. Geiger, Phys. Rev. D 54 (1996) 949; Phys. Rev. D 56 (1997) 2665.

[22] D. A. Brown and P. Danielewicz, Phys. Rev. D 58 (1998) 094003.

[23] J. P. Blaizot and E. Iancu, Nucl. Phys. B 557 (1999) 183.

[24] Y. B. Ivanov, J. Knoll, and D. N. Voskresensky, Nucl. Phys. A 657 (1999) 413.

[25] J. Knoll, Y. B. Ivanov, and D. N. Voskresensky, Ann. Phys. 293 (2001) 126.

[26] R. Rapp and J. Wambach, Adv. Nucl. Phys. 25 (2000) 1.

[27] W. Cassing and E. L. Bratkovskaya, Phys. Rept. 308 (1999) 65.

[28] G. Agakichiev et al, Phys. Rev. Lett. 75 (1995) 1272.

[29] P. A. Henning, Phys. Rept. 253 (1995) 235; Nucl. Phys. A 582 (1995) 633.

[30] Y. B. Ivanov, J. Knoll, and D. N. Voskresensky, Nucl. Phys. A 672 (2000) 313.

[31] Y. B. Ivanov, J. Knoll, and D. N. Voskresensky, Phys. Atom. Nucl. 66 (2003) 1902.

[32] S. Leupold, Nucl. Phys. A 672 (2000) 475; Nucl. Phys. A 695 (2001) 377.

[33] M. Effenberger, E. L. Bratkovskaya, and U. Mosel, Phys. Rev. C 60 (1999) 044614; M. Effenberger and U. Mosel, Phys. Rev. C 60 (1999) 051901.

[34] W. Cassing and S. Juchem, Nucl. Phys. A 665 (2000) 377.

[35] W. Cassing and S. Juchem, Nucl. Phys. A 672 (2000) 417.

[36] W. Cassing and S. Juchem, Nucl. Phys. A 677 (2000) 445.

[37] W. Cassing, L. Tolos, E. L. Bratkovskaya, and A. Ramos, Nucl. Phys. A 727 (2003) 59.

[38] J. W. Negele, Rev. Mod. Phys. 54 (1982) 913.

[39] F. Cooper, S. Habib, Y. Kluger, E. Mottola, J. P. Paz, and P. R. Anderson, Phys. Rev. D 50 (1994) 2848.

[40] D. Boyanovsky, H. J. de Vega, and R. Holman, Phys. Rev. D 51 (1995) 734; F. Cooper, Y. Kluger, E. Mottola, and J. P. Paz, Phys. Rev. D 51 (1995) 2377.

[41] D. Boyanovsky, H. J. de Vega, R. Holman, D.-S. Lee, and A. Singh, Phys. Rev. D 51 (1995) 4419.

[42] D. Boyanovsky, M. D'Attanasio, H. J. de Vega, R. Holman, and D.-S. Lee, Phys. Rev. D 52 (1995) 6805.

[43] D. Boyanovsky, H. J. de Vega, R. Holman, and J. F. J. Salgado, Phys. Rev. D 54 (1996) 7570.

[44] D. Boyanovsky, H. J. de Vega, R. Holman, S. P. Kumar, and R. Pisarski, Phys. Rev. D 57 (1998) 3653.

[45] D. Boyanovsky, I. D. Lawrie, and D.-S. Lee, Phys. Rev. D 54 (1996) 4013.

[46] D. Boyanovsky, H. J. de Vega, R. Holman, S. P. Kumar, R. D. Pisarski, and J. Salgado, Phys. Rev. D 58 (1998) 125009.

[47] D. Boyanovsky, H. J. de Vega, R. Holman, and M. Simionato, Phys. Rev. D 60 (1999) 065003.

[48] E. A. Calzetta and B. L. Hu, *arXiv:hep-ph/0205271*.

[49] C. de Dominicis and P. Martin, J. Math. Phys. 5 (1964) 14.

[50] J. M. Cornwall, R. Jackiw, and E. Tomboulis, Phys. Rev. D 10 (1974) 2428.

[51] S. Sengupta, F. C. Khanna, and S. P. Kim, *arXiv:hep-ph/0301071*.

[52] A. Peter, W. Cassing, J. M. Häuser, and A. Pfitzner, Nucl. Phys. A 573 (1994) 93.

[53] S. J. Wang, W. Zuo, and W. Cassing, Nucl. Phys. A 573 (1994) 245.

[54] J. M. Häuser, W. Cassing, A. Peter, and M. H. Thoma, Z. Phys. A 353 (1995) 301.

[55] A. Peter, W. Cassing, J. M. Häuser, and M. H. Thoma, Z. Phys. C 71 (1996) 515.

[56] A. Peter, W. Cassing, J. M. Häuser, and M. H. Thoma, Z. Phys. A 358 (1997) 91.

[57] J. M. Häuser, W. Cassing, S. Leupold, and M. H. Thoma, Ann. Phys. 265 (1998) 155.

[58] S. Juchem, W. Cassing, and J. M. Häuser, Eur. Phys. J. A 2 (1998) 355.

[59] P. Danielewicz, Ann. Phys. (N.Y.) 152 (1984) 305.

[60] C. Greiner, K. Wagner, and P.-G. Reinhard, Phys. Rev. C 49 (1994) 1693.

[61] C. Greiner, K. Wagner, and P.-G. Reinhard, 'Finite Memory in the collision process of a fermionic system and its effect on relativistic heavy ion collisions', Proc. of the NATO Advanced Study Institute on 'Hot und Dense Matter', Bodrum, Turkey, 1993, eds. W. Greiner, H. Stöcker und A. Gallmann, NATO ASI Series B, Physics, Vol. 335, plenum press (1994).

[62] H. S. Köhler, Phys. Rev. C 51 (1995) 3232.

[63] H. S. Köhler and K. Morawetz, Eur. Phys. J. A 4 (1999) 291; Phys. Rev. C 64 (2001) 024613.

[64] L. Banyai, D. B. Tran Thoai, E. Reitsamer, H. Haug, D. Steinbach, M. U. Wehner, M. Wegener, T. Marschner, and W. Stoltz, Phys. Rev. Lett. 75 (1995) 2188; L. Banyai, Q. T. Vu, B. Mieck, and H. Haug, Phys. Rev. Lett. 81 (1998) 882; Q. T. Vu, H. Haug, W. A. Hügel, S. Chatterjee, and M. Wegener, Phys. Rev. Lett. 81 (2000) 3508.

[65] A. Wackert, A. Jauho, S. Rott, A. Markus, P. Binder, and G. Döhler, Phys. Rev. Lett. 83 (1999) 836.

[66] K. Morawetz, *Nonequilibrium at short time scales – Formation of correlations*, Springer, Berlin, 2003.

[67] J. Berges and J. Cox, Phys. Lett. B 517 (2001) 369.

[68] G. Aarts and J. Berges, Phys. Rev. D 64 (2001) 105010.

[69] J. Berges, Nucl. Phys. A 699 (2002) 847.

[70] K. B. Blagoev, F. Cooper, J. F. Dawson, and B. Mihaila, Phys. Rev. D 64 (2001) 125003.

[71] A. V. Ryzhov and L. G. Yaffe, Phys. Rev. D 62 (2000) 125003.

[72] G. Aarts, D. Ahrensmeier, R. Baier, J. Berges, and J. Serreau, Phys. Rev. D 66 (2002) 045008.

[73] F. Cooper, J. F. Dawson, and B. Mihaila, Phys. Rev. D 67 (2003) 056003.

[74] B. Mihaila, Phys. Rev. D 68 (2003) 036002.

[75] L. M. A. Bettencourt, K. Pao, and J. G. Sanderson, Phys. Rev. D 65 (2002) 025015.

[76] M. Salle, J. Smit, and J. C. Vink, Phys. Rev. D 64 (2001) 025016.

[77] M. Salle and J. Smit, Phys. Rev. D 67 (2003) 116006.

[78] H. van Hees and J. Knoll, Phys. Rev. D 65 (2002) 025010.

[79] H. van Hees and J. Knoll, Phys. Rev. D 65 (2002) 105005.

[80] J. M. Luttinger and J. C. Ward, Phys. Rev. 118 (1960) 1417.

[81] G. Baym, Phys. Rev. 127 (1962) 1391.

[82] E. Fick and G. Sauermann, *The Quantum Statistics of Dynamic Processes*, Vol. 86, Springer Series in Solid-State Sciences (1990).

[83] J. Rau and B. Müller, Phys. Rept. 272 (1996) 1.

[84] R. Kubo, J. Phys. Soc. Japan 12 (1957) 570; C. Martin and J. Schwinger, Phys. Rev. 115 (1959) 1342.

[85] N. P. Landsman and C. G. van Weert, Phys. Rept. 145 (1987) 141.

[86] R P. Parwani, Phys. Rev. D 45 (1992) 4695.

[87] S. Jeon, Phys. Rev. D 52 (1995) 3591.

[88] E. Wang and U. Heinz, Phys. Rev. D 53 (1996) 899.

[89] T. Nishikawa, O. Morimatsu, and Y. Hidaka, *arXiv:hep-ph/0302098.*

[90] J. Lehr, M. Effenberger, H. Lenske, and U. Mosel, Phys. Lett. B 483 (2000) 324; J. Lehr, H. Lenske, S. Leupold, and U. Mosel, Nucl. Phys. A 703 (2002) 393.

[91] R. D. Pisarski, Nucl. Phys. A 525 (1991) 175c.

[92] R. Balian and C. DeDominicis, Nucl. Phys. 61 (1960) 502.

[93] G. Aarts, Phys. Lett. B 518 (2001) 315.

[94] D. Yu. Grigoriev and V. A. Rubakov, Nucl. Phys. B 299 (1988) 6719; D. Yu. Grigoriev, V. A. Rubakov, and M. E. Shaposhnikov, Nucl. Phys. B 326 (1989) 737.

[95] G. Aarts and J. Smit, Phys. Lett. B 393 (1997) 395; W. Buchmüller and A. Jakovac, Phys. Lett. B 407 (1997) 39.

[96] A. H. Mueller and D. T. Son, *arXiv:hep-ph/0212198.*

[97] S. Mrówczyński, Phys. Rev. D 56 (1997) 2265.

[98] W. Cassing and S. J. Wang, Z. Phys. A 337 (1990) 1.

[99] W. Ehehalt and W. Cassing, Nucl. Phys. A 602 (1996) 449.

[100] W. Cassing, E. L. Bratkovskaya, and S. Juchem, Nucl. Phys. A 674 (2000) 249.

[101] T. Kodama, S.B. Duarte, K.C. Chung, R. Donangelo, and R.A.M.S. Nazareth, Phys. Rev. C 29 (1984) 2146.

[102] J. Cugnon, D. Kinet, and J. Vandermeulen, Nucl. Phys. A 379 (1982) 553.

[103] M. Germain, Ch. Hartnack, J. L. Laville, J. Aichelin, M. Belkacem, and E. Suraud, Phys. Lett. B 437 (1998) 19.

[104] R. Holzmann et al., Phys. Rev. Lett. 72 (1994) 1608.

[105] R. Holzmann et al., Proc. of the 7th International Conference on Nuclear Reaction Mechanisms, Varenna, June 6-11, 1994, ed. by E. Gadioli, p. 261.

[106] A. Bonasera, F. Gulminelli, and J. Molitoris, Phys. Rep. 243 (1994) 1.

[107] A. Bonasera and F. Gulminelli, Phys. Lett. B 259 (1991) 399; B 275 (1992) 24.

[108] M. Prakash, P. Braun-Munzinger, J. Stachel, and N. Alamanos, Phys. Rev. C37 (1988) 1959.

[109] K. K. Gudima et al., Phys. Rev. Lett. 76 (1996) 2412.

[110] G. Martinez et al., Preprint SUBATECH 1999.

[111] S. Juchem, W. Cassing, and C. Greiner, *arXiv:hep-h/0307353*, submitted to Phys. Rev. D, in press.

[112] N. Bogolyubov, J. Phys. (USSR) 10 (1946) 257; J. Phys. (USSR) 10 (1946) 265.

[113] S. Fujita, Phys. Rev. A 4 (1971) 1114.

[114] A. G. Hall, J. Phys. A 8 (1975) 214.

[115] P. A. Henning, Nucl. Phys. B 337 (1990) 547.

Deutsche Zusammenfassung

Nichtgleichgewichts-Vielteilchentheorie oder Quantenfeldtheorie ist von großer Bedeutung in der Untersuchung von Transportvorgängen in vielen Bereichen der Physik, in der Kernphysik, in der kosmologischen Teilchenphysik und auch in der Physik der kondensierten Materie. Der multidisziplinäre Aspekt ergibt sich dabei aus dem gemeinsamen Interesse, die verschiedenen Relaxationsphänomene von dissipativen Quantensystemen zu verstehen. In der aktuellen Kernphysik bildet vor allem das Verständnis der Dynamik von Schwerionenkollisionen bei verschiedenen Einschussenergien eine große Motivation für die Untersuchung von Vielteilchen-Quantensystemen oder Quantenfeldtheorien außerhalb des Gleichgewichts. Der Anfangszustand einer solchen Schwerionenreaktion stellt dabei einen extremen Nichtgleichgewichtszustand dar, während der Endzustand zumindest einen gewissen Grad an Thermalisierung aufweisen kann. Tatsächlich zeigen sich bei den Experimenten am Relativistic Heavy-Ion Collider (RHIC) in Brookhaven, der die zur Zeit höchsten Einschussenergien liefert, erste Hinweise – wie der Aufbau eines kollektiven Flusses verbunden mit der Erzeugung von großen Drücken – für eine frühe Thermalisierung des Systems. Für eine vollständiges Verständnis solcher Phänomene ist eine ab initio Beschreibung der Dynamik von Quantenfeldtheorien außerhalb des Gleichgewichts unerlässlich.

Für eine theoretische Untersuchung der Nichtgleichgewichts-Vielteilchenphysik von Quantensystemen stellt die Formulierung auf dem geschlossenen Zeitpfad (CTP oder Schwinger-Keldysh Formalismus) eine geeignete Basis dar. Die bedeutsamste Rolle spielen hierbei die resultierenden Dyson-Schwinger Gleichungen für die Einteilchen-Green-Funktionen, die sogenannten Kadanoff-Baym Gleichungen. Sie beschreiben die kausale Evolution des Systems als ein Ensemblemittel über die Anfangsdichtematrix, die den Ausgangszustand des Systems auch weitab vom Gleichgewicht charakterisiert. Die in die Kadanoff-Baym Gleichung eingehenden Selbstenergien können aus einer zweiteilchen-irreduziblen (2PI) Effektiven Wirkung abgeleitet werden. Aufgrund der Konstruktion dieses Funktionals und somit auch der Selbstenergien mittels selbstkonsistenter Green-Funktionen bleiben die fundamentalen globalen Symmetrien der zugrundeliegenden Theorie erhalten und die thermodynamische Konsistenz gewahrt. Entscheidenden Einfluss auf das Äquilibrierungsverhalten hat die explizite Berücksichtigung von Kollisionsprozessen, wie schon Untersuchungen von Schwerionenreaktionen bei niedrigen Energien gezeigt haben. Hier ist eine volle zeitabhängige Hartree- oder Hartree-Fock Beschreibung nicht in der Lage, die Reaktionsdynamik mit ansteigender Einschussenergie hinreichend gut zu beschreiben, so dass zusätzlich Boltzmann-ähnliche Kollisionsterme in Betracht gezogen werden müssen. Ähnliche Resultate zeigen sich auch bei der nichtperturbativen Untersuchung von Phasenübergängen zweiter Ordnung von Quantenfeldtheorien außerhalb des Gleichgewichts. Geht man in der Kadanoff-Baym Gleichung über eine mean-field Beschreibung hinaus und bezieht in den Selbstenergien Stoßprozesse ein, so führt dies zu Dissipation und zur Brechung der Zeitumkehrinvarianz. Diese makroskopische Irreversibilitiät entsteht letztlich durch das Abschneiden der (exakten) Martin-Schwinger Hierarchie für Green-Funktionen und einer Reduktion der vollen n-Teilchendynamik auf das Zweiteilchen-Niveau.

Ein weiterer wichtiger Aspekt des CTP-Formalismus liegt in der Tatsache, dass dieser einen Ausgangspunkt für die Ableitung generalisierter Transportgleichungen darstellt. So können on-shell Boltzmann Gleichungen aus der vollen Kadanoff-Baym Theorie unter bestimmten Näherungen abgeleitet werden, die insbesondere in praktischen Untersuchungen von Nichtgleichgewichtssystemen eine vorrangige Rolle spielen. Darüberhinaus können über eine Gradiententenentwicklung der vollen Kadanoff-Baym Gleichung (und den Verzicht auf eine zusätzliche Quasiteilchen-Annahme) off-shell Erweiterungen formuliert werden. Neben Anwendungen in der Plasmaphsik und der Festkörperphysik sind diese generalisierten off-shell Transportgleichungen insbesondere von Relevanz für die Simulation von Schwerionenkollisionen. Hier besitzen Teilchen wie die Δ-Resonanz oder das ρ-Meson große Zerfallsbreiten im Vakuum, während andere Hadronen aufgrund der Stöße im Medium eine nichtvernachlässigbare Kollisionsbreite aufweisen können. Eine Beschreibung in Form von on-shell Quasiteilchen wird daher fragwürdig und eine explizite Berücksichtigung der dynamischen Spektralfunktion notwendig. Aus diesem Grund ist die konsistente Formulierung des Quantentransports von extrem kurzlebigen Teilchen jenseits der Quasiteilchenannahme von großer Bedeutung.

Obwohl die Analogie zwischen den Kadanoff-Baym Gleichungen und der Boltzmann Näherung offensichtlich ist, ist der Zusammenhang alles andere als trivial. Die volle Quantenevolution enthält viel mehr Information als die on-shell Boltzmann Gleichung, da sie die komplette Dynamik der Spektralfunktion berücksichtigt. Eine zufriedenstellende Antwort auf die Frage, inwieweit die Quantendynamik das Äquilibrierungsverhalten beeinflusst, läßt sich dementsprechend nur aus der vollständigen Lösung sowohl der Kadanoff-Baym als auch der Boltzmann Gleichung erhalten.

In der vorliegenden Arbeit wurde die Quanten-Zeitentwicklung am Beispiel der relativistischen ϕ^4-Theorie in 2+1 Raumzeit Dimensionen für Anfangszustände weitab vom Gleichgewicht für räumlich homogene Systeme untersucht. Die hierbei verwendete Kadanoff-Baym Gleichung beinhaltet die volle Nichtgleichgewichts-Quantendynamik auf dem Einteilchen-Niveau, d.h. bei Beschränkung auf Zweipunkt(Green)-Funktionen. Die kausale Evolution ist nicht-lokal in der Zeit, sondern wird auch beeinflusst durch Konfigurationen in der Vergangenheit, aufgrund der auftretenden memory(-Gedächtnis)-Integrale. Weiterhin enthält die Kadanoff-Baym Gleichung sowohl die statistische wie auch die volle spektrale Information des sich entwickelnden Systems. Die Näherungen an die exakte Theorie entstehen lediglich durch den Ansatz für die Selbstenergiebeiträge. Im vorliegenden Fall wurde eine Drei-Loop-Approximation bezüglich der zweiteilchen-irreduziblen Effektiven Wirkung (definiert auf dem geschlossenen Zeitpfad) benutzt, so dass die selbstkonsistenten tadpole- und sunset-Selbstenergien die Zeitentwicklung des Systems steuern. Der tadpole-Beitrag führt dabei zu einer dynamisch generierten effektiven Masse, während die sunset-Selbstenergie Stoßprozesse miteinbezieht und somit für den dissipativen Charakter verantwortlich ist, der zu einer vollständigen Äquilibrierung des Systems führt. Da beide Selbstenergien ultraviolett divergent sind, mußten sie durch die Einführung von geeigneten Massengegentermen renormiert werden.

Für die Untersuchungen der skalaren ϕ^4-Theorie in 2+1 Raumzeit Dimensionen

sind – abgesehen von der Tatsache, dass dieser Quantenfeldtheorie per se von Interesse ist – hauptsächlich zwei Aspekte von Vorteil:
1) In 1+1 Dimensionen finden on-shell Streuprozesse aufgrund von Energie- und Impulserhaltung nur (kol-)linear statt. Entsprechend führen on-shell Stöße somit nicht zu einer Veränderung der Impulsverteilung; eine Äquilibrierung wird ausschließlich durch off-shell Kollisionen bewirkt, was einer eher ungewöhnlichen Situation entspricht. In 2+1 Dimensionen tragen sowohl on-shell als auch off-shell Prozesse zu einer Äquilibrierung der Impulsverteilung bei. Aus diesem Grund stellt die ϕ^4-Theorie in 2+1 Dimensionen ein geeignetes quantenfeldtheoretisches Modellsystem dar, um die Unterschiede zwischen der vollen Kadanoff-Baym Dynamik und Näherungsverfahren, wie z.B. dem Boltzmann Grenzfall, zu untersuchen.
2) Die Divergenzstruktur der ϕ^4-Theorie in 2+1 Dimensionen erlaubt ein kontrolliertes Renormierungsverfahren. Beide berücksichtigten Selbstenergien enthalten nur Vakuumanteile der Green-Funktionen und können über Massengegenterme renormiert werden. In 3+1 Dimensionen divergieren dagegen Klassen von Diagrammen, die zudem Nicht-Vakuumanteile der Green-Funktionen beinhalten. Hier müssen im Prinzip Renormierungsverfahren für selbstkonsistente Näherungen angewandt werden, die bisher nur für den thermischen Gleichgewichtsfall entwickelt worden sind.

Die Lösung der vollen Kadanoff-Baym Gleichung wurde zunächst für verschiedene Anfangszustände untersucht, die durch die gleiche Gesamtenergie gekennzeichnet sind. Dabei zeigte sich, dass die Zeitentwicklung der unterschiedlichen Initialisierungen gleicher Energie im Langzeitlimes auf ein und denselben Endzustand hinausläuft. Der resultierende gemeinsame asymptotische Zustand entspricht dabei dem exakten off-shell Gleichgewichtszustand. Dies konnte explizit durch das Erfüllen der Kubo-Martin-Schwinger (KMS) Gleichgewichtsrelationen durch die verschiedenen Zweipunkt-Funktionen nachgewiesen werden.

Die Zeitentwicklung des Systems konnte weiterhin durch drei verschiedene Stufen gekennzeichnet werden. Zunächst werden i) Anfangskorrelationen aufgebaut, danach folgt ii) eine kinetische Thermalisierung bevor schließlich iii) eine chemische Äquilibrierung stattfindet. Die erste Phase der Entwicklung ist bestimmt durch ein Anwachsen der anfänglich verschwindenden Korrelationsenergie. Diese Korrelationen werden auf sehr kurzen Zeitskalen erzeugt, die näherungsweise unabhängig sind von der verwendeten Kopplungsstärke. Zusätzlich werden die in einzelnen Impulsmoden der gleichzeitigen Green-Funktion auftretenden Anfangsoszillationen entsprechend der selbstkonsistenten Breite gedämpft. Die zeitliche Entwicklung der Besetzungszahlen der Impulszustände kann dabei in der zweiten Phase der kinetischen Äquilibrierung nicht-monoton verlaufen, so dass im Rahmen der vollen off-shell Dynamik stets ein gewisses Gedächtnis des Ausgangszustandes gewahrt bleibt. In der on-shell Boltzmann Näherung hingegen tritt dieses nicht-monotone Verhalten nicht auf.

Die letzte Phase der Zeitentwicklung ist charakerisiert durch die Abnahme des chemischen Potentials. Da die (neutrale) ϕ^4-Theorie keine erhaltenen Quantenzahlen beinhaltet, muss das chemische Potential im thermischen Gleichgewichtszustand verschwinden. Dies geschieht dynamisch innerhalb der Kadanoff-Baym Zeitentwicklung durch off-shell $1 \leftrightarrow 3$ Übergänge, die die Teilchenzahl verändern. Die Wichtigkeit der einbezogenen Spektralfunktion läßt sich hierbei aus einer Abschätzung für die chemische Relaxationsrate (für kleine Abweichungen vom Gleichgewichtszustand) ablesen. Im Gegensatz hierzu ist die Boltzmann Näherung auf teilchenzahlerhaltende $2 \leftrightarrow 2$ on-shell Streuprozesse beschränkt, wodurch der resultierende Endzustand der Zeitentwicklung durch ein endliches chemisches Potential gekennzeichnet ist. Die asymptotische Verteilungsfunktion der Kadanoff-Baym Zeitentwicklung kann für alle Impulse und Energien durch ein und dieselbe thermische Bose-Verteilung bei einer Temperatur T und einem nahezu verschwindenden chemischen Potential μ beschrieben werden, d.h. sowohl für die on-shell Energien als auch im off-shell Bereich. Aus diesem Grund entspricht dieser Langzeitlimes einem thermischen Gleichgewichtszustand unter Erfüllung der zugehörigen KMS-Relationen.

Die zeitliche Entwicklung der Spektralfunktion zeigte weiterhin kein universelles Verhalten; alle untersuchten Anfangszustände lieferten unterschiedliche Spektralfunktionen bis in den Bereich der kinetischen Äquilibrierung. Im Verlauf der kinetischen Äquilibrierungsphase nahmen die Spektralfunktionen jedoch eine Struktur ähnlich dem Gleichgewichtszustand an, was sich insbesondere in den gleichen Relaxationsraten für das chemische Potential für die verschiedenen Anfangsverteilungen äußerte.

Als zweiter Schwerpunkt der vorliegenden Arbeit wurde die Zeitentwicklung der Kadanoff-Baym Gleichung mit Näherungsverfahren verglichen und dabei zunächst die on-shell Boltzmann Approximation untersucht. Hierbei zeigte sich, dass die konsistente Berücksichtigung der dynamischen Spektralfunktion einen deutlichen Einfluss auf das Relaxationsverhalten hat. So bedingen nichtteilchenzahlerhaltende off-shell Prozesse für große Kopplungsstärken ein Anwachsen der Quadrupol-Relaxationsrate im Kadanoff-Baym Fall relativ zur Boltzmann Näherung. Auf der anderen Seite lassen sich die Relaxationsraten für kleinere und mittlere Kopplungen recht gut mit der on-shell Boltzmann Näherung abschätzen, so dass der Schluss naheliegt, dass sich quantenfeldtheoretische Probleme sehr ähnlich zu (semi-)klassischen Vielteilchensystemen verhalten. Wie schon erwähnt, weist die Boltzmann Rechnung jedoch noch weitere Unzulänglichkeiten auf. Zum einen findet innerhalb der teilchenzahlerhaltenden Boltzmann Näherung keine Relaxation des chemischen Potentials statt. Somit konvergiert die Zeitentwicklung für $t \to \infty$ nicht gegen den korrekten Gleichgewichtszustand der skalaren Theorie, sondern weist ein endliches chemisches Potential auf. Zum anderen erfolgt die Evolution der Impulsmoden der gleichzeitigen Green-Funktion in der Boltzmann Näherung stets in monotoner Weise und steht damit im Gegensatz zu dem beobachteten Überschwingen für bestimmte Anfangsverteilungen in der vollen Kadanoff-Baym Rechnung.

Um die Beschreibung mittels genäherter Methoden zu verbessern, wurden – über die Quasiteilchen-Boltzmann Gleichung hinaus – generalisierte off-shell Transportgleichungen abgeleitet, die sich aus der Kadanoff-Baym Gleichung in Phasenraumdarstellung durch eine Gradientenentwicklung der ersten Ordnung ergaben. Es zeigte sich für die untersuchten Systeme, dass die generalisierten Transportgleichungen eine sehr ähnliche Zeitentwicklung wie die volle Kadanoff-Baym Theorie liefern. Dies beinhaltet die Evolution der einzelnen Moden der gleichzeitigen Green-Funktion, die auch für die generalisierten quantenkinetischen Gleichungen bei mittleren Zeiten für kleine

Impulse nicht-monoton verlaufen. Desweiteren findet man in der zeitlichen Entwicklung der Spektralfunktion innerhalb der semiklassischen Näherung dieselben Charakteristika wie in der vollen Theorie. Schließlich führt auch die generalisierte Transportgleichung im Grenzfall großer Zeit zu einem stationären Zustand, der einem (off-shell) Gleichgewichtszustand mit verschwindendem chemischen Potential entspricht. Die zugehörigen Relaxationsraten stimmen ebenfalls sehr gut mit denen der vollen Kadanoff-Baym Gleichung überein. Sie weisen eine starke, nichttriviale Abhängigkeit von der Kopplungskonstanten auf, da die Relaxation des chemischen Potentials maßgeblich von der (Gleichgewichts-)Spektralfunktion beeinflusst wird, wie eine analytische Abschätzung belegt. Zusammenfassend ist zu sagen, dass durch die Miteinbeziehung der dynamischen Spektralfunktion im Rahmen der generalisierten Transportgleichung eine verlässliche Näherungslösung der vollen Kadanoff-Baym Gleichung erreicht wird.

Neben der zunächst verwendeten generalisierten Transportgleichung (in der Kadanoff-Baym (KB) Form) wurde zusätzlich die Botermans-Malfliet (BM) Form untersucht, die sich aus ersterer durch eine zusätzliche Konsistenzforderung bezüglich der ersten Gradientenordnung ergibt. Die detaillierten Rechnungen zeigten, dass in beiden semiklassischen Näherungen die Zeitentwicklung in sehr ähnlicher Weise erfolgt, wobei nur leichte Differenzen in der Besetzung der Niedrigimpulsmoden auftraten.

Die generalisierte Transportgleichung in BM Form bildete außerdem den Ausgangspunkt für eine Einbeziehung der off-shell Dynamik in die Beschreibung realistischer Schwerionenkollisionen. Im Rahmen eines Testteilchen-Ansatzes liessen sich Evolutionsgleichungen für die Off-shellness der Teilchen, d.h. die Abweichung des quadrierten Viererimpulses von der Massenschale, herleiten, die entscheidend von der Veränderung der Breite bestimmt wird und über den Imaginärteil der (retardierten) Selbstenergie gegeben ist. Die off-shell Dynamik wurde in das bestehende HSD Transportmodell implementiert und auf Schwerionenreaktionen von GANIL bis AGS Energien (0.1 - 10 A GeV) angewandt. Die Effekte der off-shell Erweiterung wurden hierbei für Modellstudien anhand von einzelnen Testteilchentrajektorien und der resultierenden Spektralfunktion diskutiert. In Kern-Kern Reaktionen äußert sich die Miteinbeziehung der off-shell Eigenschaften hauptsächlich in der Erzeugung von Teilchen unterhalb der (Vakuum-)Schwelle (relativ zu Nukleon-Nuleon Stößen) und einer Modifikation der $\sqrt{s}$-Verteilung der Kollisionen, die eine Veränderung oder Härtung der Transversalimpulsspektren mit sich bringt.

Neben der Dynamik von Systemen abseits des Gleichgewichts wurde in dieser Arbeit auch eine effiziente Methode zur Berechnung von selbstkonsistenten Spektralfunktionen bei endlicher Temperatur vorgestellt, die automatisch die zugehörigen Normierungs- und Analyzitätsbedingungen erfüllt. In diesem Zusammenhang wurde ebenfalls der masselose Fall der ϕ^4-Theorie in 2+1 Dimensionen untersucht. Für große Kopplungen ist eine starke Reduktion der Polmasse der Impuls-Nullmode zu beobachten, die von einem deutlichen Anwachsen der Breite begleitet wird; zudem wächst die Besetzungszahl der Nullmode, im Gegensatz zu den restlichen energetischeren Moden, deutlich an. Dieses Verhalten läßt sich als der Beginn einer Bose Kondensation interpretieren.

Danksagung

Zum guten Schluss dieser Arbeit möchte ich mich natürlich noch bei all denen bedanken, die auf direkte oder indirekte Weise zu ihrem Gelingen beigetragen haben.

Zuallererst gebührt mein Dank Prof. Dr. Dr. Wolfgang Cassing für die intensive Betreuung und seine ständige Bereitschaft zu Diskussionen. Insbesondere für die interessante Themenstellung möchte ich mich an dieser Stelle bedanken.

Prof. Dr. Ulrich Mosel danke ich für die Aufnahme an sein Institut.

Außerdem möchte ich Prof. Dr. Carsten Greiner für sein reges Interesse an dieser Arbeit danken. Seine vielfältigen Anregungen haben zu ihrem Gelingen mit beigetragen.

Ein ganz herzlicher Dank geht an meine beiden 'Kommunarden' Gunnar Martens und Dr. Stefan Leupold für die vielen fachlichen, semi-fachlichen und fachfremden Diskussionen, die ich mit ihnen am Institut und auf unserem kleinen Hof an der schönen Wieseck führen durfte.

Insbesondere Dr. Gregor Penner, Marcus Post, Christoph Keil und meinem Zimmerkollegen Dr. Peter Watson möchte ich für die nette Atmosphäre am Institut danken.

Christoph Keil, Frank Frömel, Prof. Dr. Horst Lenske sowie Dr. Frank Hofmann und Dr. Jochen Geiss sei weiterhin für den Computerservice gedankt.

Elke Jung möchte ich für die vielfache administrative Unterstützung danken.

Ganz herzlich möchte ich mich bei meinen Eltern bedanken, die mir auf all meinen Wegen und so auch auf diesem immer voll und ganz den Rücken gestärkt haben.

Schließlich gilt mein ganz besonderer Dank Yvonne Stadach. Ohne ihre Rücksichtnahme und Motivation wäre diese Arbeit nicht zustandegekommen.